Department of Materials
Imperial College London

Investigation Of The Oxidation Behaviour Of The Polycrystalline Co-Ni Base Superalloys

Farah Binti Ismail

Submitted in part fulfilment of the requirement for the degree of doctor philosophy in materials engineering at Imperial College London
Doctor of Philosophy
February 2017

Declaration of Originality

I herewith declare that the material presented in this thesis is of my own work and, where appropriate, that the work of others has been correctly referenced.

Copyright Declaration

The copyright of this thesis rests with the author and is made available under a Creative Commons Attribution Non-Commercial No Derivatives licence. Researchers are free to copy, distribute or transmit the thesis on the condition that they attribute it, that they do not use it for commercial purposes and that they do not alter, transform or build upon it. For any reuse or redistribution, researchers must make clear to others the licence terms of this work

Dedication

For my father

قُلْ هَلْ يَسْتَوِي الَّذِينَ يَعْلَمُونَ وَالَّذِينَ لَا يَعْلَمُونَ ۗ إِنَّمَا يَتَذَكَّرُ أُولُو الْأَلْبَابِ

Are those equal, those who know and those who do not know?

Only the men of understanding are mindful.

(Az-Zumar [39:9])

Preface

This thesis is submitted for the degree of Doctor of Philosophy at Imperial College London.

Parts of the present study have been published and are detailed below:

F. Ismail, V. A. Vorontsov, T.C. Lindley, M.C. Hardy, D. Dye, B. A. Shollock. Alloying Effects on Oxidation Mechanisms in Polycrystalline Co-Ni Base Superalloys. *Corrosion Science*, 116:44-52, 2017.

F. Ismail, M. C. Hardy, T. C. Lindley, D. Dye, B. A Shollock. Oxidation of Polycrystalline Co-Al-W Superalloys for Gas Turbine Applications. in Proceedings of The 9th International Charles Parsons Turbine and Generator Conference. Loughborough, UK, 15 – 17 Sept. 2015.

Other contributing paper related to this thesis:

M. Knop, P. Mulvey, F. Ismail, A. Radecka, K.M. Rahman, T.C. Lindley, B.A. Shollock, M.C. Hardy, M.P. Moody, T.L. Martin, P.A.J. Bagot, D. Dye. New Polycrystalline Co-Ni Superalloy. *JOM*, 66:2495-2501, 2014.

Abstract

The initial study reported here focused on the oxidation of Co-Al-W alloys containing nickel (29-34 at. %) and chromium (12-17 at. %) additions with the objective of improving the oxidation resistance of these alloys at high temperatures (800-850 °C) for high-pressure turbine discs. Starting with the analysis in the as-atomised powder, the material was then consolidated using hot-isostatic pressing (HIP) and a two-stage HIP was performed to optimise the precipitation of carbides. Solution heat-treated and aged samples were studied in terms of the effects of additional alloying elements on the alloys' oxidation behaviour after high temperature exposures. Isotopic oxidation tracer experiments were carried out at 800-850 °C in isotopically enriched oxygen ($^{16}O^-$ and $^{18}O^-$) to elucidate the oxidation mechanisms.

Oxidation mechanisms in alloys with different Co-Ni ratio and Cr, Al contents were investigated in polycrystalline cobalt-base superalloys. Various characterisation techniques were used to investigate the oxidation mechanisms such as FEG-SEM, STEM with EDX, high resolution TEM, FIB-SEM, and FIB-SIMS were applied.

The various phases present in the initial and oxidised microstructures have been established, together with the oxidation behaviour of the alloy. After oxidation at 800 °C for 200 hours, the alloys exhibit a multi-layered structure, consisting of an outer oxide scale with a continuous alumina layer at the oxide-alloy interface. The bulk metal consisting of a cobalt solid solution containing secondary phases (Co_3W and CoAl), carbides precipitates (Ta-Zr carbides) and fine γ' ($Co_3(Al-W)$) precipitates. The oxidation behaviour on shot-peened surfaces was studied and it was found that shot-peening does not affect the oxidation resistance directly but it does alter the sub-surface region causing recrystallisation and thus opening up diffusion paths for cations/anions diffusions.

The study of oxygen transport mechanisms using $^{18}O_2$ as a tracer element has revealed that an outer chromium-rich oxide layer formed at the metal surface during the initial oxidation and continuous inner alumina layer is primarily formed subsequently. This alumina layer appears to effectively block the diffusion of oxygen to the metal/oxide interface and oxidation proceeds by outward cation diffusion. This study demonstrates that protective oxide scales can be formed in cobalt-base superalloys.

Acknowledgements

I would like to start by thanking my academic supervisors Prof. Barbara Shollock, Prof. David Dye and Prof. Trevor Lindley for their support and guidance throughout my PhD studies. I would also like to thank my industrial supervisor, Dr. Mark Hardy from Rolls-Royce plc for the opportunity to conduct this invaluable research with Rolls-Royce plc. I would like to acknowledge my sponsor, Majlis Amanah Rakyat (Malaysian Government Sponsor) and EPSRC.

I would like to express my gratitude to my PhD examiners, Dr. Catherine Rae and Dr, Mark Wenman for their time to valuable inputs.

I am grateful to have the opportunity to work with my brilliant colleagues in my research group who supported my work and my thesis. Sincere thanks to Vassili Vorontsov, Mezan Rahman, Ioannis Bantounas, Sophia Yan, Matthias Knop, Paul Mulvey, Daniella Proprentner, Ben Foss, Jine-Sung Jung, Martin Weiser, Claire Trant, Anna Radecka and Lucy Reynolds.

I would also like to acknowledge Dr. Richard Chater for his guidance in SIMS, Dr. Mahmoud Ardakani, Dr. Ecaterina Ware, Dr. Richard Beanland and Steven Hindmarsh for their support in TEM and FIB. I would also like to thank Dr. Dan Child from Rolls-Royce plc for his guidance in shot-peening.

Special thanks to my best friends, for always being there, anywhere in the world for me, at every stage of my life, to Aideeni Megat and Amira Samsudin, thank you.

Lastly, I would like to thank my family, my mum, my sisters, my brother and Ross for the love, strength and tremendous support.

Table of Contents

Declaration of Originality 2

Copyright Declaration 3

Dedication 4

Preface 6

Abstract 7

Acknowledgements 8

Table of Contents 9

1 Introduction 14

1.1 Turbine Disc Materials Requirements 14

1.2 High temperature oxidation 16

1.3 Thesis Structure 16

2 Literature Review 19

2.1 The Gas Turbine 19

2.1.1 Gas turbine materials 20

2.2 Designing Polycrystalline Disc Alloys 24

2.2.1 Turbine disc requirements 24

2.2.2 High-temperature materials 27

2.2.3 Alloying elements and their effects on microstructure of superalloys 28

2.2.4 Carbide precipitates in superalloys 31

2.3 Processing and Manufacturing of Turbine Disc 35

2.3.1 Powder Metallurgy 35

2.3.2 Characterisation of powder particles 37

2.3.3 Methods to reduce the PPB 39

2.4 High Temperature Oxidation 41

2.4.1 General principle of oxidation 41

2.4.2 Oxidation of nickel base superalloys 47

2.4.3 Spallation of oxide scale 49

2.4.4 Transition of metastable Al_2O_3 to α-Al_2O_3 51

2.4.5 Tracer study of oxide scale formation 53

2.4.6 The combined two-stage oxidation and SIMS technique 56

2.4.7 The effect of surface treatment (shot-peening) on oxidation 57
2.5 Development of Cobalt-Base Superalloys 61
2.5.1 Conventional cobalt base alloys 61
2.5.2 The discovery of γ/γ' cobalt base superalloy 62
2.5.3 Phase stability in cobalt-base superalloys 64
2.5.4 Oxidation of Co-Al-W superalloys 66
2.6 Alloying of Co-Al-W Superalloys 71
2.6.1 Elemental effects on properties 71
2.6.2 Summary of alloying additions effects on Co-Al-W superalloy 73
2.7 Concluding Remarks 76
3 Materials and Characterisation Techniques 78
3.1 The V208 Alloys Series 78
3.1.1 Materials and specimen 78
3.1.2 Sample preparation for oxidation experiments 79
3.2 The Two-Stage Oxidation Experiments 80
3.2.1 Isotopic oxidation experiments 80
3.2.2 Heating and cooling rate 82
3.2.3 Long-term oxidation in air 82
3.3 The Two-Stage HIP Process for the As-Atomised Powder 83
3.3.1 Two-stage HIP 83
3.4 Effect of Shot-Peening on Oxidation 85
3.5 Scanning Electron Microscopy 86
3.5.1 FEG-SEM with EDX 86
3.5.2 Quantification of Oxidation Products - The Damage Depth Analysis 88
3.5.3 Energy-selective Backscatter (EsB) mode in FIB-SEM 89
3.6 Focused Ion Beam (FIB) Techniques 93
3.6.1 Overview of instrumentation 93
3.6.2 Alloy cross-section preparation by FIB 94
3.6.3 FIB-SIMS elemental mapping of oxide scales 96
3.7 Transmission Electron Microscopy (TEM) 99
3.7.1 FIB in-situ lift out 99
3.7.2 TEM examination 101
3.7.3 High-resolution TEM 101
4 The V208 Series – Overview 103
4.1 Introduction 103
4.1.1 Mechanical testing 104

4.1.2 Comparisons of the as-received microstructures 106
4.1.3 Phase equilibria in the bulk 107
4.2 The As-Atomised Powder Particles 109
4.2.1 Carbide precipitates 110
4.3 The Two-Stage HIP Powder Processing 115
4.4 Oxidation Behaviour of the V208 Alloy Series 118
4.5 Discussion 121
4.5.1 The effect of alloying additions on the oxidation behaviour 121
4.5.2 The effect of alloying additions on phase stability in the bulk 123
4.6 Conclusions 124
5 Specific V208 alloys – The Variation of Co:Ni Ratio and Chromium and Aluminium Contents on the Oxidation Behaviour 126
5.1 Introduction 126
5.1.1 Alloys characteristics in the as-received condition 127
5.1.2 The surface oxide morphology 134
5.2 Oxidation of the Specific V208 Alloys 135
5.2.1 Oxide cross-section morphologies 135
5.2.2 Spallation behaviour of surface scale 137
5.3 Selected Alloy – 15Cr-10Al 139
5.3.1 Long-term oxidation 139
5.3.2 FIB-SIMS elemental mapping of $^{16}O^-$ and $^{18}O^-$ 140
5.3.3 Isotopic fraction (f) maps and intensity peaks 142
5.3.4 STEM-EDX analysis 143
5.3.5 High resolution TEM examination 145
5.4 Discussion 148
5.4.1 The effect of Cr:Al ratio in Co-Ni base superalloys in terms of phase stability and oxidation resistance 149
5.4.2 Mechanism of oxide formation in Co-Ni base superalloys 150
5.5 Conclusions 152
6 Specific V208 alloys - The Effect of Shot-Peening on the Oxidation Behaviour 154
6.1 Introduction 154
6.2 Oxide Cross-Section Morphology 155
6.3 FIB-SIMS Analysis 159
6.3.1 Elemental mapping of $^{16}O^-$ and $^{18}O^-$ 159
6.3.2 Isotopic fraction map 165
6.4 Discussion 169

6.4.1 The effect of chromium and aluminium content 170
6.5 Conclusion 173
7 Conclusions and Further Work 175
7.1 Suggestion for Further Work 177
References 179

1 Introduction

The first requirements for jet engines in the 1940s was speed, and the first applications for the jet engine was military aircraft [1]. The civil aircraft only started its demand during the post war, particularly in North America where companies like General Electric and Pratt & Whitney came to dominate the jet engine market. In the 1950s, the civil aircraft main requirements were economy and power. However, this is not to say that the passenger aircraft did not demand speed. The popularity of Concorde proved that speed is still desirable for civil aircraft. Concorde entered the market in 1976 with its first installation with Air France and British Airways, equipped with lower fuel consumption and three times the speed of Frank Whittle's first patented turbojet in 1928 [1]. The Concorde aircraft flew twice the speed of sound for three to four hours per day for 27 years. Nevertheless, the real challenge for the civil transportation was not to go faster, but bigger and cheaper to run. On top of that, quieter and cleaner engines were preferred.

1.1 Turbine Disc Materials Requirements

One of the major challenges for aero engine designers today is to find the optimum balance between fuel economy, noise and emissions [2]. These requirements are now coupled with the demand for extended service life at lower operating cost. Currently, nickel-base superalloys are commonly used for various components in the hotter parts of gas turbine engine, for example turbine vanes, blades and discs, due to their superior creep and fatigue properties at high temperature [3]. These components must withstand high mechanical loading in corrosive and oxidative environments at high temperatures - up to 1100 °C in the case of the high-pressure single crystal nickel superalloy turbine blades, while the operating temperatures of the rim sections of high-pressure polycrystalline nickel superalloy turbine discs have continued to challenge materials and design engineers as temperatures now approach 750 °C [3]. An increase of 30 - 50 °C in temperature capability for the discs is highly desirable and is a target for commercial aircraft engine manufacturers such as Rolls-Royce Plc.

In designing high-pressure turbine discs, emphasis is made on yield stress and tensile strength of a material. Although the operating temperature is lower than turbine blades, the discs are subjected to rotational speeds in excess of 10,000 rpm, and the bore of the discs are subjected to stresses around 1000 MPa [2]. The yield strength of the current nickel turbine disc alloys is influenced by the proportions of precipitate strengthening phase, γ', and thus the concentration of elements which promote these phases should be considered to achieve the optimum strength. According to Reed [2], the fraction of γ' strengthening phase should be in the range of 40 - 55%, which can be achieved through heat treatments and adding γ' forming elements such as aluminium, titanium, and tantalum.

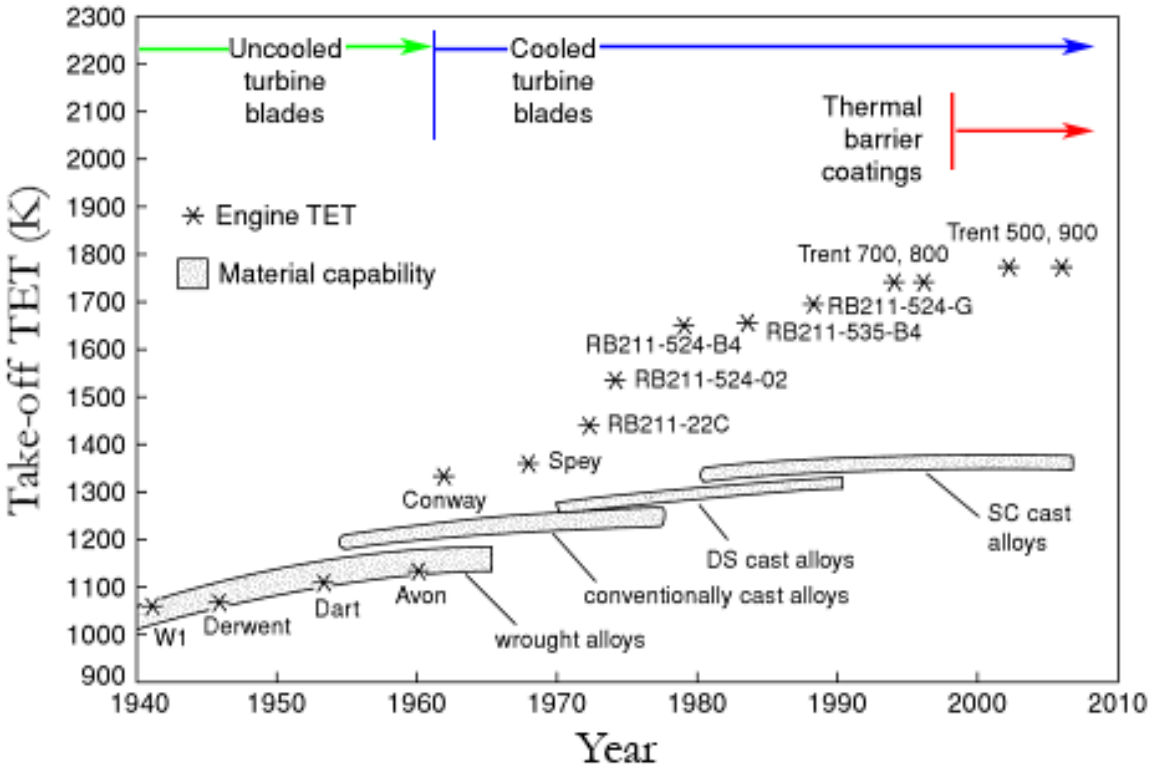


Figure 1.1: Evolution of Rolls-Royce civil aircraft engine with turbine entry temperature (TET) capability since 1940s. Figure adapted from [4].

Over 50 years, the performance of an engine can be improved if the turbine entry temperatures (TET), which is the temperature of the hot gases entering the turbine stage, can be raised. Figure 1.1 represents the temperature improvements in TET of large aeroengines since Whittle's first engine in 1940 [2]. This increasing demand is viewed as an incentive for an engine manufacturer to enhance the temperature capability of superalloys. To meet the demand of increased TET and high mechanical loading, a new generation of nickel-base superalloys is now being produced through powder metallurgy (P/M). Alloy RR1000 is a P/M alloy developed by Rolls-Royce plc and is the current benchmark for this study.

In 2006, a new class of cobalt-base alloys was reported with strengths similar to nickel-base superalloys [5]. This new class of high temperature alloys has the potential to replace nickel-base superalloys for load-bearing components for high temperature applications. Furthermore, the basic advantage of cobalt is that it has a higher melting temperature than nickel – 1495 °C as opposed to 1455 °C. This, in turn, can allow an increase in the operating temperature of the turbine discs. The aim of this research is to develop the early work of Sato et al. [5] in understanding the new Co-Al-W ternary system for polycrystalline disc applications.

1.2 High temperature oxidation

In order for these new cobalt-base alloys to be used in the hot section in gas turbines, they must display acceptable properties at high temperature over long periods of time. With the increase in turbine entry temperature (TET), the lifetime of high temperature materials can be significantly decreased by oxidation as it impairs the mechanical properties, particularly by reducing the load-bearing cross section through loss of metal or by altering the strength of the surface and increasing the probability of fatigue crack initiation. High temperature oxidation and corrosion resistance have led to the need to design a material that can form a stable protective oxide layer, such as aluminium oxide (Al_2O_3), to withstand the high temperature environment. The study of oxidation behaviour in cobalt-base superalloys is vital as it is still relatively poor compared to the nickel-base superalloys.

The oxidation behaviour of cobalt-base superalloys can to be improved by suitable alloying strategies. For this, alloying elements, such as chromium and nickel, have been added to the Co-Al-W ternary system in varying amounts. Since the current understanding of the oxide formation mechanism in Co-Al-W alloys is limited, there is a need to focus on the difference in oxidation sequence with varying amounts of alloying elements at high temperature. The aim of this PhD research is to evaluate the effects of alloying elements, in particular, cobalt and nickel ratio and chromium and aluminium content, on the oxidation behaviour of Co-Al-W superalloys. This research will investigate systematically the effect of additions of alloying elements on the oxidation mechanism of the cobalt-base superalloys and the changes to the underlying microstructures at temperatures ranging from 800 °C to 850 °C. In addition, the effect of surface stress on the oxidation behaviour of cobalt base superalloys is studied in the later chapter.

1.3 Thesis Structure

The thesis consists of seven chapters where the initial section comprises a literature review and experimental procedure. The literature review (Chapter 2) aims to give a general information on the current powder metallurgy nickel base superalloys for disc applications, followed by a description of

the oxidation behaviour of superalloys and the specific Co-Al-W superalloys. The elemental effects on basic properties of cobalt base superalloys were consolidated to predict the behaviour of the current alloys studied. Oxygen tracer experiments are reviewed with respect to oxidation mechanism studies. On top of that, in an attempt to get better understanding of carbides in P/M alloys, various studies starting from the as-atomised powder particles characteristics to hot isostatic pressing process (HIP) are described in this chapter.

Chapter 3 describes the experimental procedures employed in the current investigation. It explains the specific methodologies used for conducting the various micro-analytical characterisation techniques.

The subsequent thesis chapter reports and discusses the V208 alloy series in terms of their basic microstructural stability to preliminary selection of the best overall oxidation performance. Work conducted on the characterisation of the carbides particles in the as-atomised stage is presented and optimisation of the HIP route for these research alloys.

The following chapter looks at the down-selected alloys from the V208 series. The chapter initially compares the oxidation behaviour of these alloys at 200 hours and 300 hours followed by long term oxidation of a specific alloy, which possess the best oxidation resistance. The results and analysis of the study on the oxidation behaviour of these alloys includes aspects such as oxide layer microstructure, recrystallisation, spallation and aluminium-depletion in the substrate. The effect of Cr:Al ratio in these alloys in terms of their damage depth will be discussed later in this chapter (Chapter 5).

Chapter 6 looks at the effect of shot-peening specimens for high temperature oxidation. The chapter includes results from the focused ion beam (FIB) secondary ion mass spectroscopy (SIMS) elemental mapping of these alloys after thermal exposure and surface stress. Based on the $^{16}O^-$ and $^{18}O^-$ distributions in the elemental mapping, the isotopic fraction (f) of oxygen-18 were calculated and mapped to study the mechanism of oxide formation.

A conclusions and further work chapter (Chapter 7) highlights the lessons learnt as part of the four-year study and highlights the keys areas in which total understanding is lacking and requires future research.

2 Literature Review

2.1 The Gas Turbine

The basic operation of gas turbine engines is to generate thrust through a propulsion system. The most widely used form of propulsion system for modern aircraft is the gas turbine engine. Figure 2.1 (a) represents the schematic layout of a gas turbine engine with all the core components of a compressor, combustion chamber and power turbine, which drives the compressor. All gas turbines run based on the Brayton cycle as illustrated in Figure 2.1 (b). The basis of understanding of the engine operation involves a series of processes called a cycle. A thermodynamic process in a gas, such as heating or compressing, creates a series of work and processes, in which the state is changed during each process, but the gas eventually returns to its original state.

The variation of the state of gas from inlet to exit of gas turbine is annotated from 1 → 6. The starting point, which is the inlet condition of a gas turbine engine, is in the same state as the surrounding air. In cruising flight, the inlet slows the air stream as it is brought to the compressor front at 2. The pressure and temperature of the gas increases slightly, entropy remains the same.

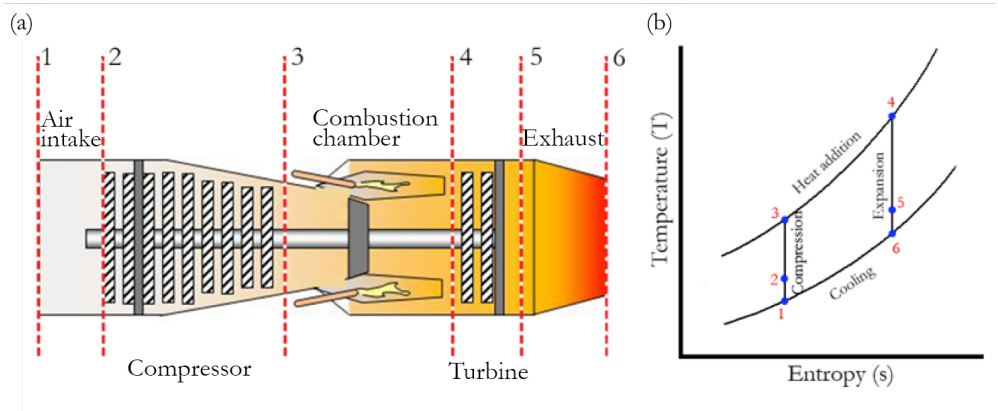


Figure 2.1: (a) The basic schematic of a gas turbine layout with the variation of stages that corresponds to (b) the temperature-entropy diagram for the Brayton cycle. Figure adapted from [6].

Next, as the gas flow is compressed, the temperature and pressure continues to rise in order to move to a sustainable combustible stage. The combustion process in the combustion chamber occurs at a constant pressure from 3 → 4 as the fuel is injected. Here the temperature increases to a very high level. From 4 → 5, the hot exhaust is passed to the turbine stage. The turbine converts the energy from the combustor into mechanical energy to drive the compressor, driven accessories and ultimately the fan to produce engine thrust. At this stage, the temperature and pressure of the gas reduces. In the last section, the nozzle brings the gas back to free stream pressure from 5 → 6, which produces a high velocity jet. This is again a constant entropy process, where internal energy of the gas gets converted into kinetic energy where the pressure expands to the surrounding pressure. Externally, the flow of the gas returns to the free stream conditions, which completes the cycle.

2.1.1 Gas turbine materials

The components that make up the arrangement in the gas turbine engine require high temperature capabilities. The components that make up the hottest sections of the gas turbine engine require superior high temperature strength, creep and oxidation resistance. The civil aeroengine nowadays is moving towards higher thrust and better fuel economy. Since the capability of the gas turbine is limited by the operating conditions of the materials used, hence, there is the need to push the performance of these materials towards higher temperature capabilities. Figure 2.2 illustrates the materials used in the Trent 800 engine.

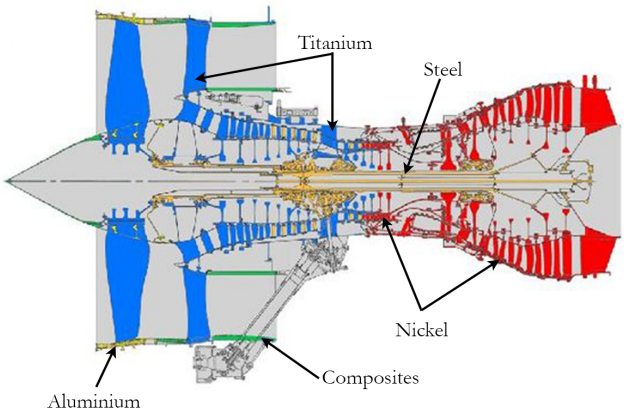


Figure 2.2: Illustration of material usage in the Trent 800 engine. Figure adapted from [7].

The first few stages of the gas turbine engine such as the fan section and the low-pressure compressor typically made from a titanium-base alloy. Note that in most large civil aeroengines, such as the Trent engine produced by Rolls-Royce plc, the engine contains approximately eight stages of

compressors, in which the first half (low/intermediate-pressure compressor) uses titanium-base alloys and the back end of the compressor stage (high-pressure compressor) uses nickel-base alloys. Titanium alloys are useful when weight is a consideration and good specific strength and fatigue resistance, but their poor high-temperature oxidation resistance limits their applications to 700 ºC [8]. At the high-pressure compressor stage, the temperature is usually up to 600 ºC but it can be as high as 650 ºC in which case the use of nickel-base alloys is essential [3].

Following the compressor stage, the combustion chamber that has the highest operating temperature of typically 1426 ºC (1700 K), which often exceeds the melting temperature of most alloys, is mostly made from advanced nickel-base superalloys with thermal barrier coatings (TBC). Finally, the turbine sections and exhaust nozzle, which have an operating temperature of up to 1327 ºC (1600 K) and eight stages of both high pressure followed by intermediate and low pressure turbine stages. Due to the high operating temperature of this section, nickel–base superalloys dominate due to their exceptional properties at elevated temperatures.

Figure 2.3 illustrates the typical variation of pressure and temperature profile in a gas turbine engine. Note that the current study is focusing on the development of the next generation alloy for disc applications in the high-pressure turbine (HPT) and high-pressure compressor (HPC) stage where the current alloy used in the civil aircraft is the polycrystalline nickel-base superalloys. Based on this diagram, the operating temperature for the high-pressure compressor (HPC) and high-pressure turbine (HPT) disc is between 650 -750 ºC [3].

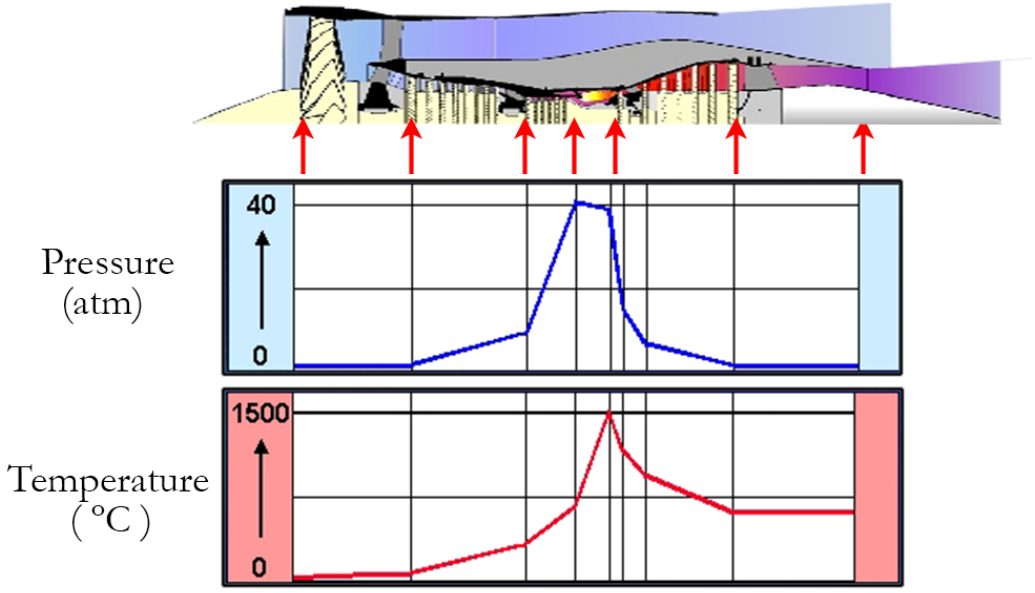


Figure 2.3: The pressure and temperature profile in each stages of the turbofan engine. Figure adapted from [7].

In 2014, Rolls-Royce plc announced the new future product technology called the Advance™ and UltraFan™ to meet the target of reducing the CO_2 emissions by 75 % per passenger per kilometer, in which the strategy is by introducing the three-shaft between the intermediate-pressure and high-pressure shafts for Advance™ and a power gearbox between the fan and intermediate pressure compressor for UltraFan™. The new engine also benefits from lightweight materials by replacing the titanium fan blades to composite carbon-titanium fan blade with titanium leading edge. Advance™ will offer at least 20 % better fuel burn per passenger per kilometer than the first generation of Trent engine and will be ready for service from the end of this decade. UltraFan™ is expected to offer at least 25 % improvement in fuel burn per passenger per kilometre and should be ready for service from 2025 onwards [9]. Furthermore, additional benefits in performance can be achieved through improved aerodynamic aircraft design using lighter composite and lightweight alloys.

This new engine development is the outcome from the recent ACARE Flightpath 2050 [10], where all the European's stakeholders in aviation industry come together in a high level group to develop a vision to develop Europe's aviation system and industry by 2050. The main goals include protecting the environment by specifying a 75 % reduction in CO_2 emissions and 90 % reduction in NOx emissions. The noise emissions are targeted to be reduced by 65 %. Fuel and noise efficiency are continuously improved by substantial development in vehicle and engine. In parallel, the air traffic control system is optimized to provide the most efficient fuel and time consumption and associated atmospheric emissions and also to address noise. This includes the introduction of fuel cells and battery-powered vehicles for ground operations at airports and also emission-free aircraft movements when taxiing [10].

Since the material used in the turbine section of the engine limits the maximum temperature at which the gas turbine engine can operate, there is a need to push the operating temperature of a material in the gas turbine engine, which would allow the engine core to run hotter, increasing the overall thermal efficiency of the engine. Moreover, the need for high efficiency in the engine becomes more important as fuels become more costly. The Airbus A380 aircraft, which is a fairly new addition to the aeroengine industry in this decade, has contributed to the ever-increasing efficiency of fuel consumption, which need less than 3 litres of fuel per passenger per 100 km in a standard cabin configuration [11]. Whereas, that the average fuel consumption for the world's fleet before then was around 5 litres.

The current nickel-base superalloys used for the hot rotative parts in gas turbine engine have almost reached their maximum capability. Material improvements and new material development are now being done simultaneously and research are currently focusing on the use of composite materials and advanced metal alloys. The discovery of the new polycrystalline $L1_2$ cobalt-base superalloys in 2006 has opened up a new window for the next generation alloy development, but first, the criteria of a turbine disc are discussed in order to meet the basic requirements. The next generation alloy development is a long and continuous process.

2.2 Designing Polycrystalline Disc Alloys

2.2.1 Turbine disc requirements

Turbine discs, where the dovetail of the blades are attached, are subjected to the radial forces pulled by the blades and body forces resulting from the rotation [3]. In addition to that, thermal load from the transient and a steady-state temperature variation within the discs also contributes to the additional stress. The thermal loads are caused by the disc heating and cooling which cause a radial temperature gradient within the disc and in turn cause thermal loading [12]. Typically the temperature is not higher than the compressor discharge temperature where materials suitable for applications below 750 ºC (at the rim) are generally chosen.

Advanced turbine engine configurations using higher temperature combustor and airfoil concepts require compressor and turbine disc, as shown in Figure 2.4, which can withstand temperatures higher than 500 - 650 °C at the bore and up to 700 – 750 ºC at the rim of high-pressure turbine discs, and materials suitable for application below these temperatures are typically chosen. A current objective of engine manufacturers is to develop a disc alloy that will enable operation at temperatures up to 800 °C. Some advanced powder metallurgy nickel-base superalloys such as ME3, Alloy 10, and LSHR have been designed for higher working temperatures ranging from 650 °C to 700 °C [13]. It is crucial to note that an increase in 30 °C in temperature capability compared to the currently used coarse grain RR1000, the material used for Rolls-Royce Trent 1000 engine, nickel-base superalloy is highly desirable, without coating the disc rim and diaphragm.

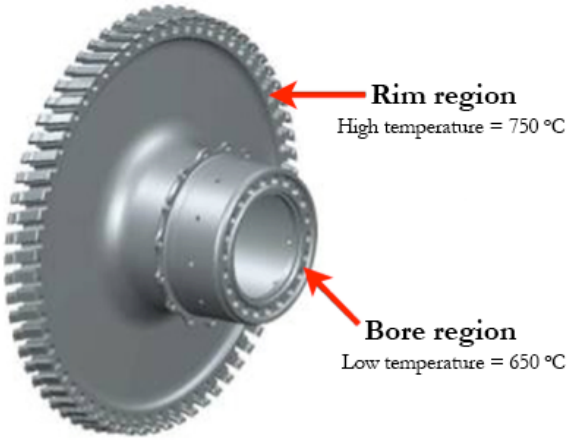


Figure 2.4: Schematic of a typical high pressure turbine disc highlighting the general operating conditions.

Disc failures, although very uncommon, results in the release of pieces from the turbine at high velocities. In general, the important characteristics that a turbine disc should have are tensile and fatigue strength. Therefore, a good fracture toughness and low crack growth rate are the desirable properties for a superior disc material [2]. It is highly important for the rotor designer to avoid the discs bursting due to the catastrophic failure that it could create.

It is worth noting that turbine disc components are deemed safety critical parts due to the inability to contain the component in the event of a failure. Unlike the fan loss, which can be 'contained' within the engine casing, the mass and energy within a turbine disc will result in a catastrophic failure with ejection of larger fragments of disc from the engine likely [14]. The 'uncontained' engine failure is likely to be a violent one, and can be much more serious because engine debris exits at high velocities giving potential danger to the pressurised aircraft structure, adjacent engines, and possibly directly to the aircraft passengers or a person on the ground.

According to the European Aviation Safety Agency (EASA) design specifications for large aeroplanes (CS-25.903), for turbine engine installations; 'Design precautions must be taken to minimise the hazards to the aeroplane in the event of an engine rotor failure or of a fire originating within the engine which burns through the engine case' [15]. However, this is not the case in the past 10 years, where many evidence of 'uncontained' disc failure have been reported.

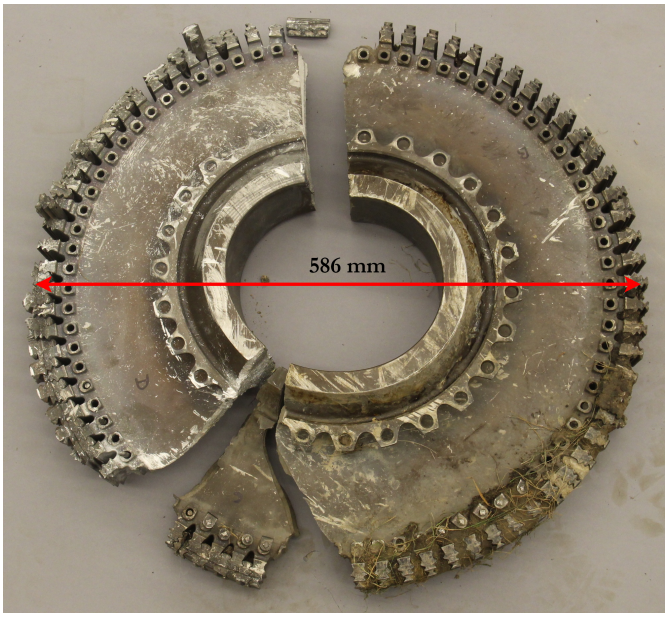


Figure 2.5: Recovered stage 2 HPT disc from American Airlines flight 383 incident. Figure retrieved from NTSB press release [16].

On 28th October 2016, a 19-year-old disc violently broke apart inside the engine of an American Airlines Group Inc. taking off from Chicago's O'Hare International Airport. Carey et al. reported that the engine was caught on fire and resulted in an aborted takeoff and evacuation of the passengers [17]. The 'uncontained' failure of a stage 2 disc (see Figure 2.5) in the HPT section of a General Electric's CF6-80 engine was described to have pieces flying through in a distance of a third of a mile from the plane. The cause of such failure was due to fatigue cracking initiating at an internal inclusion near the forward side of the hub's inner bore, according to the National Transport Safety Board (NTSB), USA [16].

The material that is used for the disc alloy is different from the blade (polycrystalline vs. single crystal). The nickel-base polycrystalline alloys have been used for the past decades due to their exceptional strength and environmental resistance at high temperatures. The 'uncontained' disc failure is usually extensive and is critical for safety of the passenger onboard. Optimisation of the properties of the disc material by adding suitable alloying elements, which will make the alloy system more complex, can mitigate the likelihood of this failure.

The next sub-chapter will discuss the alloy chemistry of the current nickel-base superalloys and the requirements for the next generation turbine discs materials.

2.2.2 High-temperature materials

High temperature materials have to withstand mechanical loading in a highly corrosive, oxidising environment. According to Reed [2], a desirable characteristic for high temperature materials is the ability to withstand loading at an operating temperature close to its melting point. When the operating temperature (T_{oper}) and melting temperature (T_m) ratio is greater than 0.6, the material can be classified as a high temperature material. In general, base elements for high temperature alloys have to possess melting points above approximately 1400 °C in order to ensure sufficient creep strength.

Given these considerations, nickel-base alloys have emerged as the ones chosen for high temperature applications [2]. Cobalt is the only other metal to display a density and cost that are comparable to nickel, with cobalt having a slightly higher melting point by 40 °C over nickel [5]. Starting with the requirement for the operating temperature for the next generation of turbine discs alloys to be 800 °C, and using as a guide the melting temperature of cobalt (1493 °C);

$$\tau = T_{oper} / T_m \qquad \text{Equation 2.1}$$

$$\tau = (800 + 273) / (1493 + 273)$$

$$\tau \approx 0.61$$

This shows that these new cobalt alloys could form a new class of high temperature alloys for disc applications. Other metals such as titanium and iron are also the basis of high temperature materials with exceptional strength. However, titanium is limited to lower temperature applications (typically in compressor region) because titanium is combustible under certain conditions of temperature, pressure and oxygen concentration. Also, steel is limited due to its lower corrosion resistance and it is unstable at high temperatures (where crystal structure changes from BCC to FCC as temperature rises). The main reason why cobalt-base alloys have not found extensive use is their lower strength compared to nickel-base alloys [5], [18]. In addition, cobalt-base alloys tend to be more expensive than the nickel-base alloys [2]. The nickel-base alloys show the highest temperature/strength combination of all cast and wrought superalloys, making them ideal for use in many applications, for example, in aircraft engines and industrial gas turbines, nuclear reactors, and the oil and gas industry [18], [19].

As many as 14 alloying elements are added to superalloys in varying amounts to major amounts to nickel-base superalloys [20]. Currently, nickel-base superalloys are selected when the highest temperatures between 1204 – 1371 ºC need to be achieved, and strength is a consideration. The γ'

precipitates in nickel-base superalloys provide most of the strengthening and result in useful operating temperatures up to 90 % of the melting point.

Cobalt-base superalloys are typically strengthened by carbides and solid-solution hardeners, there are no intermetallic compounds that have the same degree of utility as the γ' precipitates then [20]. The cobalt-base superalloys originate in the Stellite® alloys patented in the early 1900s by Elwood Haynes [21]. Back in the days before the discovery by Sato et al., cast and wrought cobalt superalloys continue to be used because:

- Cobalt alloys have higher melting point than nickel alloys (50 ºC more) which gives them more room for higher operating temperature [2].
- Cobalt alloys gives superior resistance to hot corrosion due to their high chromium content [21].
- Cobalt alloys have better thermal fatigue resistance and weldability over nickel alloys [3].
- Cobalt was added to nickel alloys in considerable volume fraction – the decision to reduce this was due to strategic supply.

2.2.3 Alloying elements and their effects on microstructure of superalloys

Most superalloys contain a variety of elements in a large number of combinations to produce a specific effect on the desired properties. Superalloys, mostly in nickel-base, usually consist of following phases [2], [3], [20]:

- **Austenitic FCC matrix** phase gamma (γ), which is a nonmagnetic phase that usually contains elements such as nickel, cobalt, iron, chromium, molybdenum and tungsten.
- **Secondary phases intermetallic** compound gamma prime (γ' - Ni_3X), which is an primitive cubic ordered phase that is coherent to the γ matrix. Elements such as aluminium, titanium, niobium (γ" - Ni_3Nb), tantalum and chromium usually form the spherical/cuboidal shaped γ'.
- **Secondary phase carbides** MC, $M_{23}C_6$, M_6C and M_7C_3 (rare) where carbon between 0.002 – 0.2 wt. % combines with reactive elements such as titanium, tantalum, hafnium and niobium as the M (metal).
- **Borides** may be formed on the grain boundaries when boron segregates and generally favourable for creep-rupture properties.

- **Topologically Close Packed (TCP)** phases such as Laves, σ and μ which usually form with excessive amount of refractory elements.

Grain boundary strengtheners - Carbides provide limited strengthening indirectly by stabilising the grain boundaries against excessive shear. Other elements such as boron, zirconium and hafnium were added to promote grain boundary effect other than precipitation or carbide formation [20].

Unfavorable tramp elements – Carbides, borides and magnesium were added for tramp-element control. The tramp elements such as silicon, phosphorous, sulphur, lead, bismuth, tellurium, selenium, and silver, often in amounts as low as one-part-per-million level, are responsible for property level reductions in superalloys but they are invisible optically or with an electron microscope [20]. The use of microprobe and Auger spectroscopic analysis can detect these elements decorating the grain boundaries at high local concentrations.

Elements responsible for brittle phase – The formation of TCP phases such as Laves, σ and μ is often caused by elements such as cobalt, molybdenum, tungsten and chromium. Although these elements are added for their favourable alloying potential, an excessive addition, together with long-term heat treatment during service or high temperature may result in low ductility (brittle) and can cause loss of mechanical properties due to TCP precipitation [3], [20].

Elements for oxidation resistance – Chromium will promote the formation of chromia (Cr_2O_3) on the outer scale protecting the surface from high-temperature degradation. Further oxidation will induce a more protective oxide, alumina (Al_2O_3) that is more stable at high temperature [2], [18], [20].

Alloy density - Alloying additions considerably influence the density of superalloys; higher aluminium, titanium and chromium contents reduce the density, whereas the solid solution strengtheners tungsten and tantalum increase it [22].

Table 2.1 summarises the effect of several alloying elements on the nickel and cobalt base superalloys. Note that not all of this elemental effect occur necessarily in a given alloy. New discoveries might not be presented in this table but the purpose of this summary is to depict the major alloying elements and their known effect in a basic superalloy system. The major alloying elements that are present in nickel base superalloys are also illustrated in Figure 2.6 where the height of the element blocks indicate the amounts that may be present.

Table 2.1: The role of alloying elements on nickel and cobalt base superalloys. Table adapted from [22].

Elements	**Effets on nickel-base superalloys**	**Effects on cobalt-base superalloys**
Chromium	- Oxidation and hot corrosion resistance - Solid solution strengthening	- Oxidation and hot corrosion resistance; - Forms M_7C_3 and $M_{23}C_6$ carbides
Molybdenum, Tungsten	- Solid solution strengthening - Forms M_6C carbides	- Solid solution strengthening - Forms M_6C carbides - Forms intermetallic compound Co_3X
Aluminium	- Forms γ' – $Ni_3(Al, Ti)$ - Oxidation resistance	- Oxidation resistance - Forms intermetallic compound CoAl
Titanium	- Forms γ' – $Ni_3(Al, Ti)$ - Forms MC carbides	- Forms MC carbides - Forms intermetallic compound Co_3Ti
Tantalum, Niobium	- Solid solution strengthening - Forms MC carbides - Enhances oxidation resistance	- Solid solution strengthening - Forms MC and M_6C carbides - Forms intermetallic compound Co_2X
Boron, Zirconium	- Improve rupture life through increase ductility - Boron forms borides	- Improve rupture life through increase ductility
Hafnium	- Hafnium forms MC carbides	-
Cobalt	- Raises γ' solvus temperature	-
Nickel	-	- Stabilises FCC form of matrix - Forms intermetallic Ni_3Ti

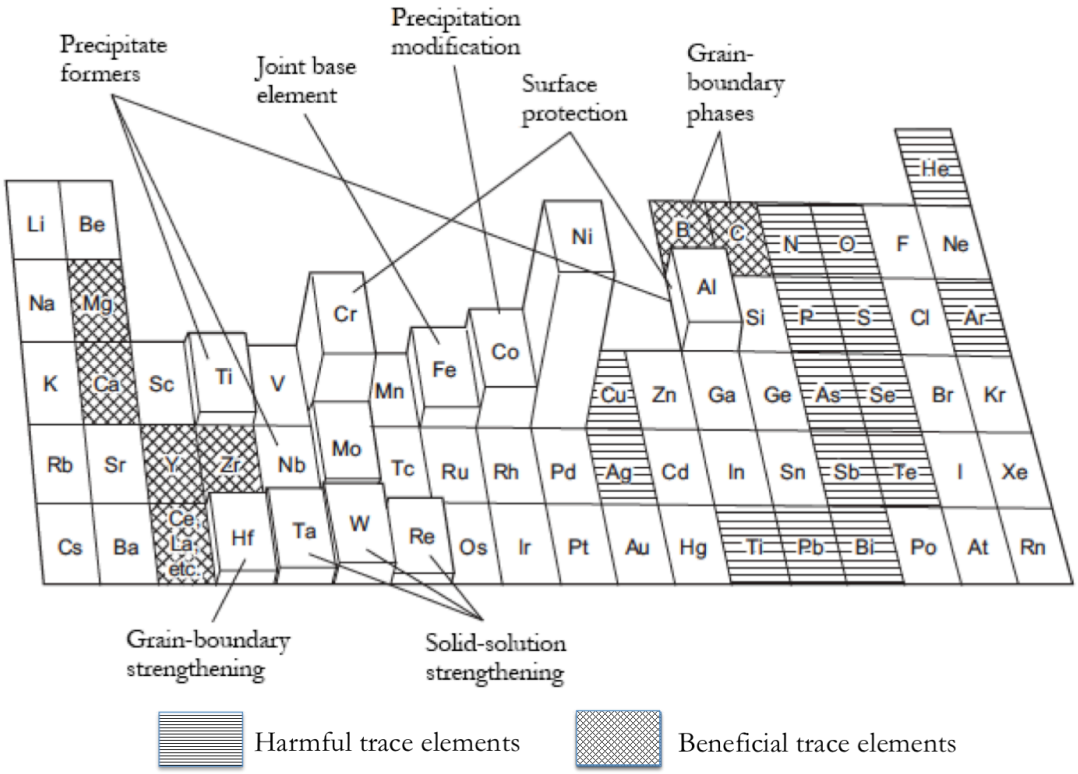


Figure 2.6: Periodic table of elements highlighting the alloying elements used in nickel-base superalloys. The level of each element indicates the amount that may be present in wt. %. Figure adapted from [23].

2.2.4 Carbide precipitates in superalloys

The combination of carbon at 0.002 – 0.2 wt. % with reactive or refractory metals forms carbides. During solidification at high temperature of more than 1038 ºC, the most common carbides in nickel-base superalloys, which is MC carbides precipitates from the super-saturated solid solution [2]. These MC carbides are in FCC close packed structure in the form of random cubic or script morphology along the grain boundaries. In many cases, the carbides exist jointly, however, they usually follow a sequential reaction in the solid state following breakdown of the MC carbides which are normally formed at the molten state [20].

MC carbides such as TiC and HfC are among the most stable compounds in nature and the order of formation for these carbides is [20]:

$$HfC \rightarrow TaC \rightarrow NbC \rightarrow TiC$$

Recent alloys that contain high tantalum content contain MC carbides that are reportedly not easy to decompose during processing or solution treatment in the range of 1200 – 1260 ºC [20]. During heat

treatment, MC which is a high-temperature carbide begins to decompose and form $M_{23}C_6$ along the grain boundaries or in the matrix. With enough chromium content, the MC carbides react with γ matrix to form $M_{23}C_6$ carbides:

$$MC + \gamma = M_{23}C_6 + \gamma'$$

Where M in MC carbides is usually titanium, molybdenum, niobium or hafnium and M in $M_{23}C_6$ carbides is usually chromium. An example of MC carbide decomposition is as follows [24]:

$$(Ti, Mo)C + (Ni, Cr, Al, Ti) \rightarrow Cr_{21}Mo_2C_6 + Ni_3(Al, Ti)$$

$M_{23}C_6$ carbides are found primarily at grain boundaries and can be in the form of globular, discontinuous, rounded or blocky. Some $M_{23}C_6$ carbides can be found in script-like morphology along the grain boundaries. This carbide is formed with moderate-to-high chromium content during lower temperature heat treatment (760 – 816 ºC) [3]. Although, in some instances, they may form at temperature as high as 982 ºC from degeneration of MC carbides and from available soluble residual carbon in the alloy matrix [20].

He et. al. has performed a study on the nucleation of carbides, primarily the $M_{23}C_6$ carbides during creep tests and the preferential precipitation sites can be seen in Figure 2.7. After multiple creep tests were performed at 800 ºC/550 MPa between 40 – 800 hours, the $M_{23}C_6$ carbide nucleated mainly at the grain boundaries, sub-boundaries, MC carbide site as well as on the surface of γ/γ' eutectic [25]. During high temperature creep tests, most of the primary MC carbide gradually decomposes to form M_6C carbide, the size and amount of MC carbide decreases with increasing exposure time, and an increase in temperature resulted in further changes in MC carbide morphology [25]. It is worth noting that in this study, the creep test temperature is too low to completely dissolve all the MC carbides.

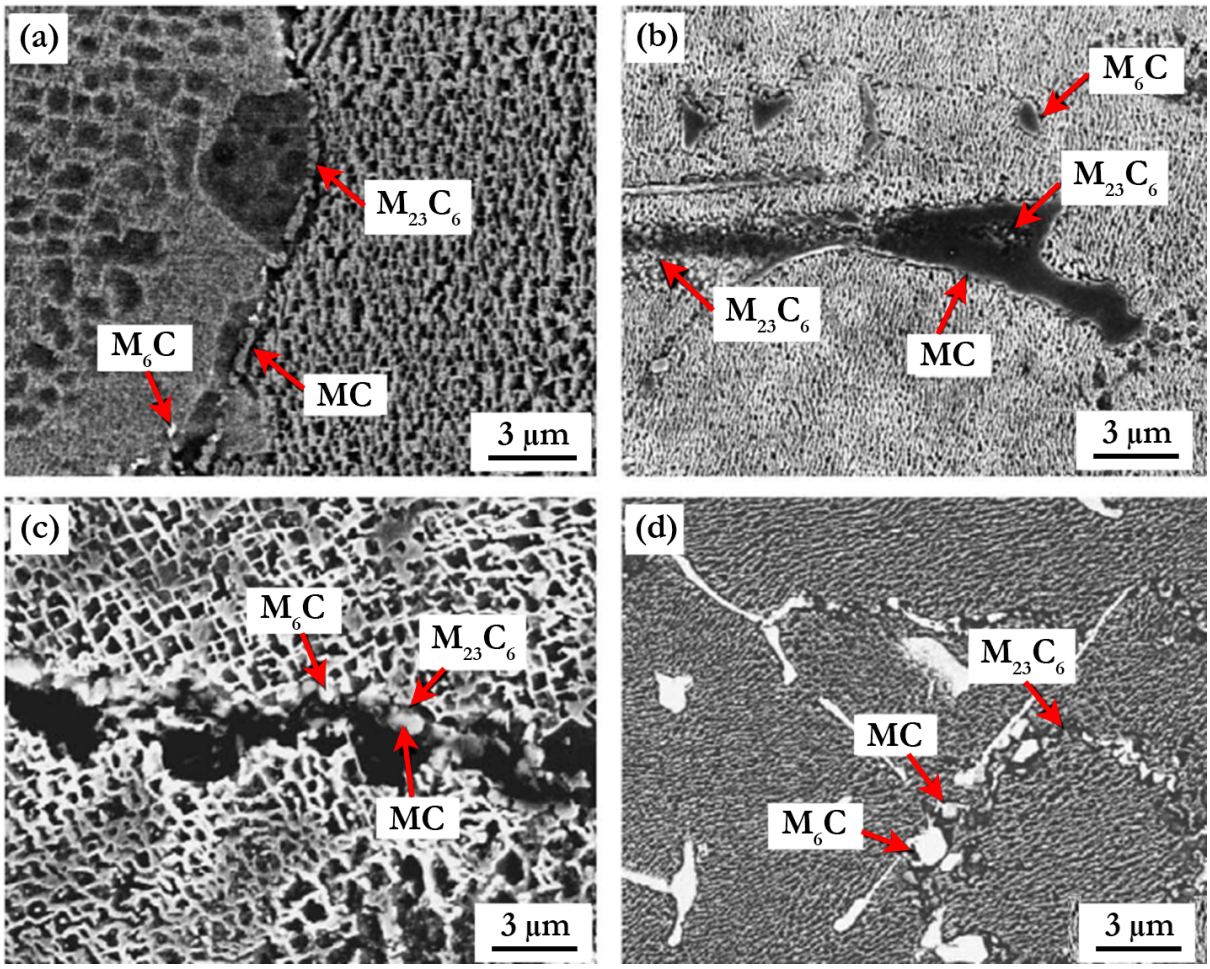


Figure 2.7: SEM micrographs showing the morphology of MC, M_6C and $M_{23}C_6$ after various creep tests showing the preferential nucleation of $M_{23}C_6$ carbides at (a) surface of γ/γ' eutectic (b) grain boundary MC carbide (c) grain boundary (d) sub-boundary. Figure adapted from [25].

M_6C carbides are typically made of molybdenum or tungsten with elemental content (M in the alloy) of more than 6 -8 at. % and formed at intermediate temperature between 815 – 980 ºC [20]. Since M_6C carbides are formed at higher temperature than the $M_{23}C_6$ carbides they are more stable and hence, their use is more commercially important than the latter as a grain boundary precipitates. This carbide also precipitates in blocky form in grain boundaries and less often in a Widmanstätten intergranular morphology [20]. The formation reaction of M_6C carbide is similar to that of the $M_{23}C_6$ but with higher molybdenum or tungsten [2]:

$$MC + \gamma \rightarrow M_6C + \gamma'$$

Where the M is generally molybdenum, tungsten, cobalt, tantalum or chromium and the possible reaction is as follows [24]:

$$(Mo, Ti)C + (Ni, Co, Al, Ti) \rightarrow Mo_3(Ni, Co)_3C + Ni_3(Al,Ti)$$

It is known that some morphology of carbides is detrimental for rupture life and ductility, for example, the continuous grain boundary $M_{23}C_6$, cellular-discontinuous grain boundary $M_{23}C_6$ and Widmanstätten M_6C [20][18]. The blocky shaped $M_{23}C_6$ at grain boundaries, however, have a beneficial effect on rupture strength [18]. When the $M_{23}C_6$ carbide is formed, there will be a depletion of chromium around the precipitate, hence, in this area, it is difficult to form a protective oxide, namely Cr_2O_3, due to lack of chromium [26].

2.3 Processing and Manufacturing of Turbine Disc

2.3.1 Powder Metallurgy

Powder metallurgy (P/M), since its appearance in the 1960s, is used when conventional cast or wrought components are not meeting the performance requirement of the application [3]. Such failure of a component is related to the segregation, which results in poor mechanical properties by reducing the ductility and toughness of the material during consolidation. The disadvantage of this route is the higher cost, but the heavily alloyed grades of superalloys such as Rene 95 and Astroloy require minimal levels of segregation during melt processing [27]. Therefore, the need for powder metallurgy for the production of some high-refractory superalloy components such as turbine discs became apparent in the 1970s [28].

The disc of a turbine engine is machined from forgings. The manufacturing route for producing the particular materials in this study in which the alloy is made is by vacuum induction melting (VIM) then a P/M route is applied as shown in Figure 2.8 [29]. Since the material used in this study contains high alloying elements, the P/M route is chosen to eliminate any segregation in the bulk. Although the method is more expensive, P/M yields cleaner results because of the reduced ceramic inclusions [28].

The first step in the producing a P/M product is melting the raw materials via VIM processing. The VIM process uses induction coil heating to melt the alloy in a ceramic crucible to which the alloying elements are added [20]. Clearly the cleanliness of the melt is important since any contamination will be inherited by the powder. The ingot is then poured into a tundish and passes through a ceramic nozzle with a continuous stream of gas at high pressure is delivered to the stream of molten metal arriving at the nozzle [27]. The molten metal will then disintegrate and solidify into fine spherical particles of diameter 30 – 300 μm. This procedure, which is called the atomisation process, is designed to be long enough to allow complete solidification of particles before they reach the outlet of the chamber. The alloy powder is then sieved for quality control of the particle sizes.

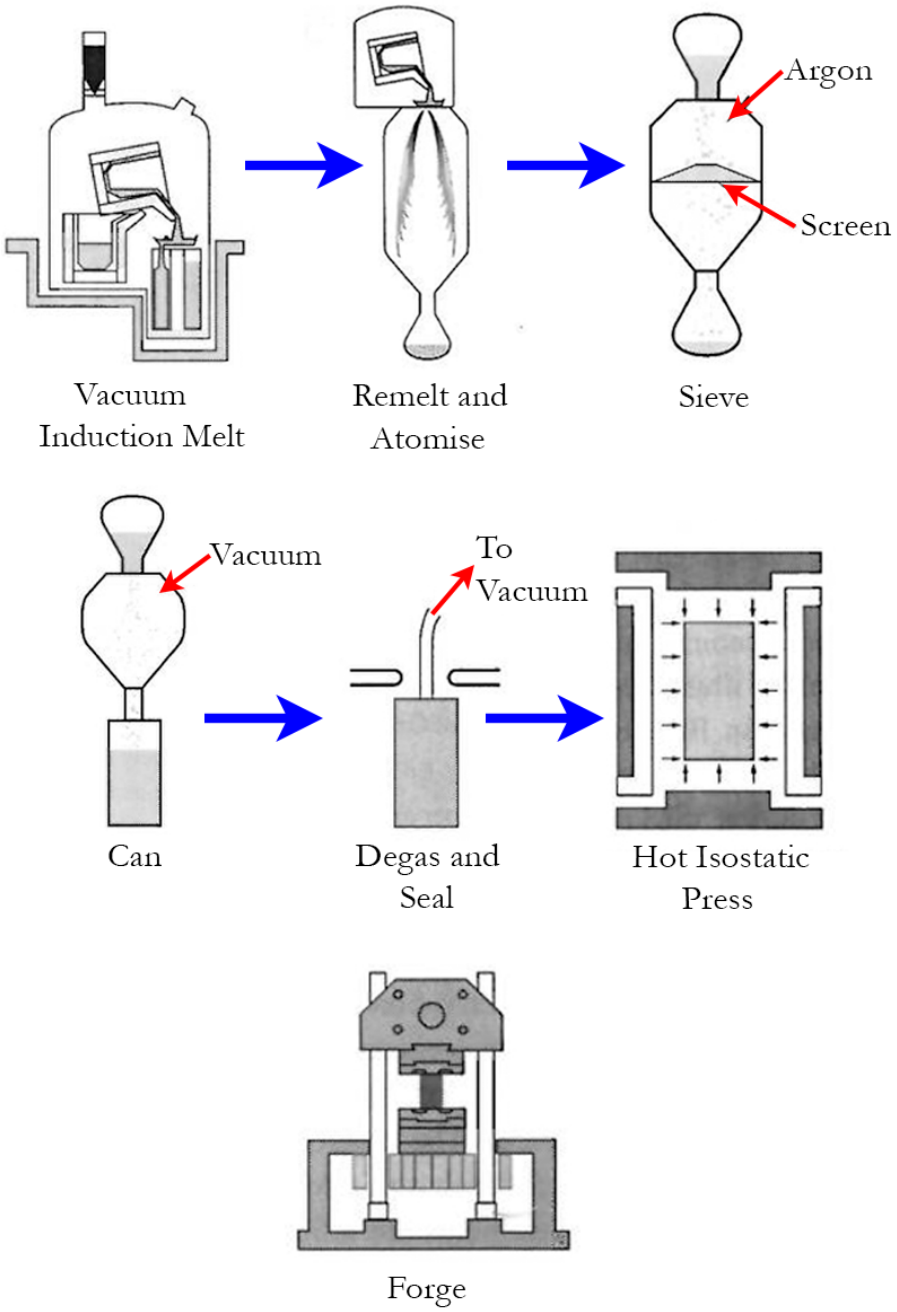


Figure 2.8: Illustration of sequence used for the production of forged superalloys via powder metallurgy. Figure adapted from [29].

The powder particles that solidify will produce a thin oxide layer on the surface, this layer of oxide needs to be controlled to minimise the prior-particle boundaries (PPB). The use of ceramic crucible and filters, which contains non-metallic inclusions, could also influence the cleanliness of the powder surface [30]. This oxide film is inevitable. Therefore, the main challenge is to ensure good bonding between the PPB by bringing the particles into contact at high temperature and pressure with mechanical deformation [30].

The atomised powders are then packed in a steel can ready for hot isostatic pressing (HIP). Upon completion of filling, the containers are de-gassed either at ambient or elevated temperature where hot de-gassing can provide benefits in minimising the levels of entrapped argon within the powder blend [31]. The sealed container is then placed into a HIP vessel in which the densification is taking place in an argon atmosphere. The HIP container is heated just below the γ'-solvus temperature of the alloy. The finished product is called a HIP compact. Isothermal forging is then applied to the HIP compact to deform into a disc shape before machining into a final product.

2.3.2 Characterisation of powder particles

The surface of powder particles needs to be controlled by controlling the amount of carbon or other refractories including the cleanliness of the atomisation chamber. Since the surface is the preferential site for the PPB and oxides to form, optimisation of the processing and heat treatment is studied. It is generally believed that PPBs are caused by atomic segregation and particle contamination. Together resulting in precipitation at PPB either in the form as carbides, oxides, oxy-carbides, or perhaps as oxy-carbonitrides [32].

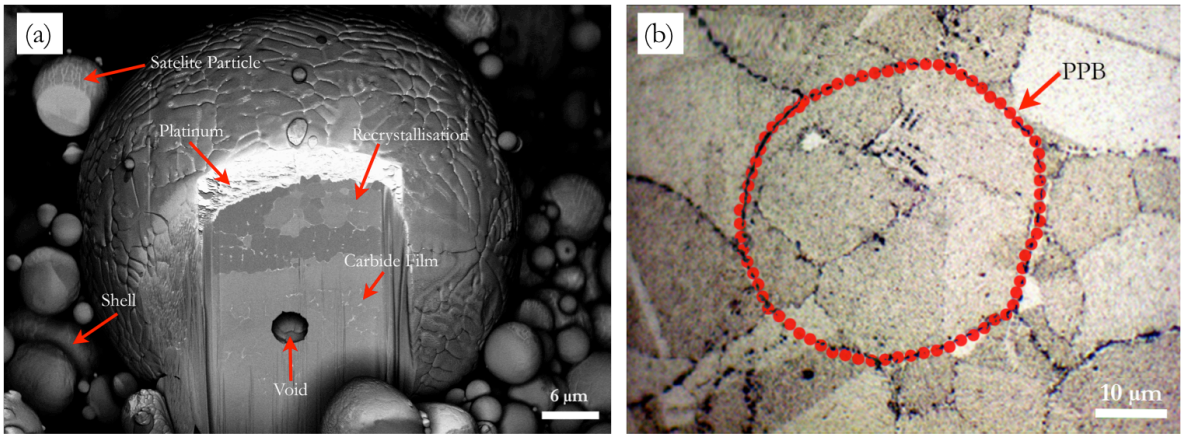


Figure 2.9: (a) EsB-SE micrograph of FIB cross section Co-Ni alloy in the as-atomised state showing the defects in and around a large particle (b) SEM image of as-HIPed nickel base superalloy highlighting the PPB, figure adapted from [33].

The as-atomised powder is varied in size and usually has a dendritic structure depending on the cooling rate. Figure 2.9 (a) shows a selected powder particle from a Co-Ni base superalloy, which will be studied later in the results chapter. Note that the bright and dark contrast in energy selected back-scatter electron (EsB) mode corresponds to the composition of heavy and light elements, respectively. The as-atomised powder in Figure 2.9 (a) is selected to show most of the possible defects that a powder particle possesses after solidification. Such defects are satellite particles, shell,

void and recrystallization. Carbide films and segregation of elements (heavy elements) were found at the surface as well as interdendritic region, respectively.

Based on previous studies [34], [35], segregation of various alloying elements on the powder surface during solidification is due to the solidification kinetics and the degree of solidification depends on the cooling rate and particle size. For example, a high carbon content in the bulk and a high oxygen content in the atmosphere can increase the PPB decoration and further reduce the ductility and toughness of the consolidated product [34]. Pores or hollow particles can also be found in the powder and these are due to entrapped gas (argon) or solidification shrinkage. However, their presence in the as-atomised stage is not detrimental to the final microstructure, as the pores will close during consolidation at high temperature [36].

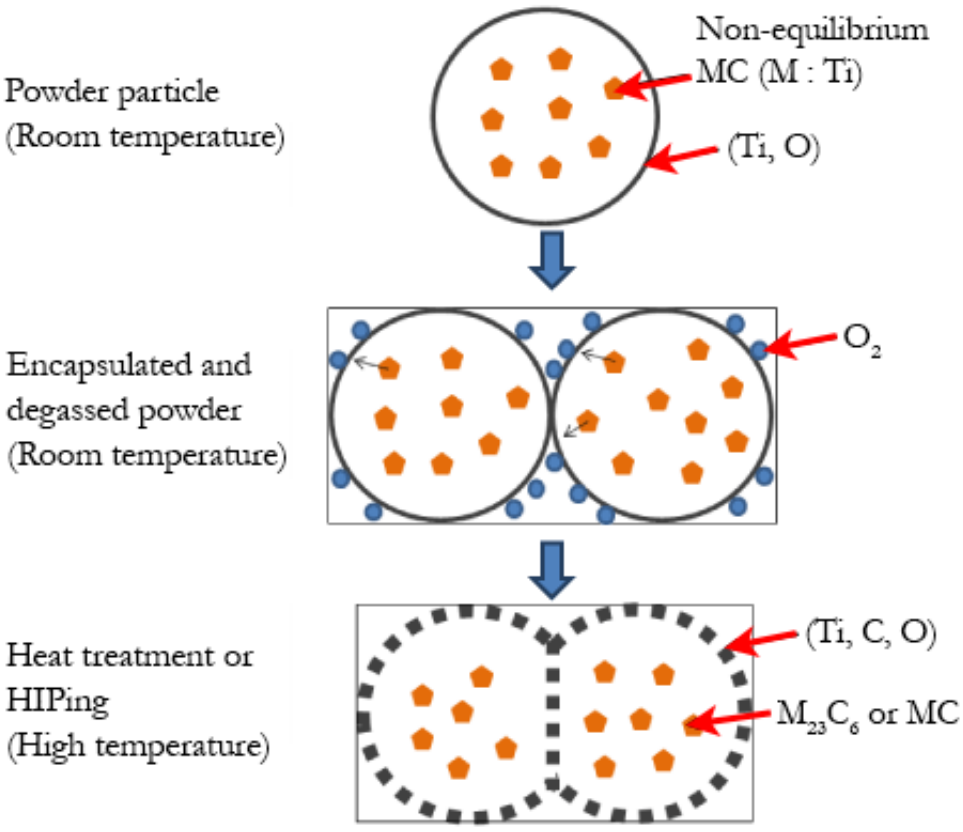


Figure 2.10: Schematic diagram of PPB nucleation in nickel base superalloys. Figure adapted from [37].

A recent work done by Bai et al. on the formation of PPB from room temperature to high temperature and during HIPing has been reviewed and the PPB formation mechanisms are presented in Figure 2.10. This interesting finding shows that at room temperature, carbides formed both on the

surface and within the powder interior can be observed in interdendritic regions [28]. In the interior region, the non-equilibrium metallic carbides MC, such as TiC, NbC, MoC were detected [38].

When the powder is being compressed, oxygen is being absorbed at the powder surface and reacts with elements such as aluminium and titanium to form an oxide layer of alumina, Al_2O_3 or titanium dioxide, TiO_2 [38]. This preliminary surface oxidation induces further precipitation of MC and $M_{23}C_6$ when heat-treatment is applied due to these specific oxides particles, which act as a nuclei for the reaction to take place [38]. Aubin et al. suggested that elements such as titanium and carbon within the powder particles migrated to the surface during the early stage of compaction in HIPing due to the oxides on the outside of the particles [34].

2.3.3 Methods to reduce the PPB

Many efforts have been done to reduce the formation of PPB on the powder particle surface such as optimising the heat-treatment and the proportion of alloying elements.

Heat treatment - Qiu et al. studied the microstructure evolution of RR1000 when the powder was annealed at high temperatures [32]. They found that above 900 ºC, very fine precipitates were formed on the particle surface and the precipitates coarsened and become more discrete with increasing temperature up to 1200 ºC. They also found that the precipitates on the surface were rich in hafnium, zirconium and oxygen but no hafnium was found on the surface before heat treatment, in the as-received condition. This indicates that the hafnia (HfO_2), which formed on the surface, originates from the diffusion of hafnium from the interior of particles to the surface [39].

Zhang et al. made the same statement when he found that powder heat treatment could reduce PPB [40]. The ultimate mechanism of powder heat treatment is based on the control of carbide precipitation. Dahlen et al. suggested that in order to reduce the PPB on the surface, stabilisation of MC and $M_{23}C_6$ carbides at the interior of the powder particles through heat treatment was necessary [41]. Furthermore, HIPing at super-solvus temperatures could also result in reduced density of PPB by transforming grains within the original powder particles to grow beyond the precipitates of PPB, thus resulting in larger grains with serrated boundaries [39].

Composition of carbide formers – Ma et al. performed a study on the effect of hafnium content on the formation of hafnia. The findings suggested that at 0.3 wt. %, the formation of MC PPB was supressed but at higher hafnium content, 0.6 wt. %, more MC carbides precipitate at the PPB [42]. It is thought that more oxide nuclei are formed at PPB when the hafnium concentration increases in the alloy, this promotes the precipitation of PPB carbides [37].

The same situation also occurs in martensitic stainless steel, where Norell et al. found in gas atomised particles that certain elements would segregate to the surface to form oxides. In martensitic steel, manganese and chromium are the strong oxide formers. Even though the amount of manganese added in the steel was as little as 0.48 wt.%, the surfaces showed extensive manganese oxide [43]. The authors explain that this shows liquid state diffusion must have taken place.

The two-stage HIP – Many have applied a two-stage HIP treatment to study the evolution of carbide precipitates and the PPB. For example, Dahlen et al. has managed to form stable $M_{23}C_6$ precipitates at the pre-compaction stage in Astroloy [41]. The carbides formed are coarser and stable but with less particle to particle contact. It is during the second stage of HIP that the MC carbides form but the formation is slower due to more carbon being tied up in the $M_{23}C_6$ carbides. He also suggested that better results could be achieved if the powders undergo a heat treatment process without any HIP compaction. This two-stage HIP is useful as a selective method to precipitate the favorable carbides since carbon cannot be removed from the alloys due to the beneficial effect of $M_{23}C_6$ grain boundary carbides that create serrations to hinder grain boundary sliding and improve creep resistance [3]. In other way suggested by Allen et al. for IN100, the powders could be heat treated at higher temperature (> 1150 ºC) to precipitate coarse and stable MC carbides [44]. These would then be stable enough to withstand the following HIP.

One interesting paper by Thamburaj et al. also suggested that the two-stage HIP is successful in removing the PPB and produces a random carbide distribution because the final HIP was performed at sub-solvus temperature, retaining the fine grain size [45]. The two-stage HIP was performed at 950 ºC for 2 hours followed by a final HIP at 1115 °C for 3 hours for the alloy Nimonic alloy [45].

The two-stage HIP was proven to work for alloy Rene 95 by Hu et al. who suggested that a high temperature pre-heat treatment is applied prior to HIP. During this stage, non-equilibrium carbides can be transformed into stable MC carbides and this effect can be used to suppress the formation of PPB carbides [46].

2.4 High Temperature Oxidation

2.4.1 General principle of oxidation

Thermodynamics of oxidation- Oxidation reaction is defined as the loss of electrons when a metal combines with an atom or with a molecular group [47]. When a metal is oxidised, oxygen, which is the other species, is reduced (gains electrons). The equation of a metallic oxidation of a single metal reaction is given in the following:

$$M(s) + O_2(g) \rightarrow MO_2(s) \qquad \text{Equation 2.2}$$

Where M: metal and M_xO_y is the oxide product. Note that pure metal oxidized more rapidly than alloys.

In general, high temperature oxidation of metals is controlled by thermodynamic and kinetic factor. In order to understand the behaviour of complex alloy system such as nickel base and cobalt base superalloys, there is the need to understand the oxidation mechanisms of a pure metal. At constant temperature and pressure, the driving force for oxidation to occur, called the Gibbs free energy, G is defined as [48]:

$$G = H - TS \qquad \text{Equation 2.3}$$

Where H: enthalpy, S: entropy and T: absolute temperature. By taking in mind that the temperature is constant, a reaction to change the thermodynamic properties of both enthalpy and entropy becomes:

$$\Delta G = \Delta H - T\Delta S \qquad \text{Equation 2.4}$$

A spontaneous high temperature oxidation can only occur if the change in Gibbs free energy is negative, $\Delta G < 0$. Thermodynamic equilibrium is reached when $\Delta G = 0$, whereas, a non-spontaneous oxidation which is thermodynamically unfavourable happens when the change in Gibbs free energy is positive, $\Delta G > 0$.

Thermodynamically, in order for an oxide to form on the surface of a metal, the oxygen potential in the environment should be higher than the oxygen partial pressure in equilibrium with the oxide. The standard free energy for the oxidation reaction in Equation 2.4 can be written as [49]:

$$\Delta G = -RTln\left(\frac{a_{MO_2}}{a_M p_{(O_2)}}\right) \qquad \text{Equation 2.5}$$

Where a_{MO_2} is the activities of the oxide, a_M is the activities of the metal and $p_{(O_2)}$ is the partial pressure of oxygen in gas. It is assumed that in the ideal behaviour the value of the activities are unity.

Assuming that unit activity of the metal and oxide, the equation becomes:

$$\Delta G = -RT \ln p_{O_2} \qquad \text{Equation 2.6}$$

A plot of the standard free energies for the formation of important oxides is given in Ellingham-Richardson diagram in Figure 2.11. This diagram is used to obtain the information of partial pressure of oxygen required for any metal to form oxide at any temperature [50]. The plot is the standard free energy for the formation of oxides as a function of temperature. Note that the diagram does not take reaction kinetics into account.

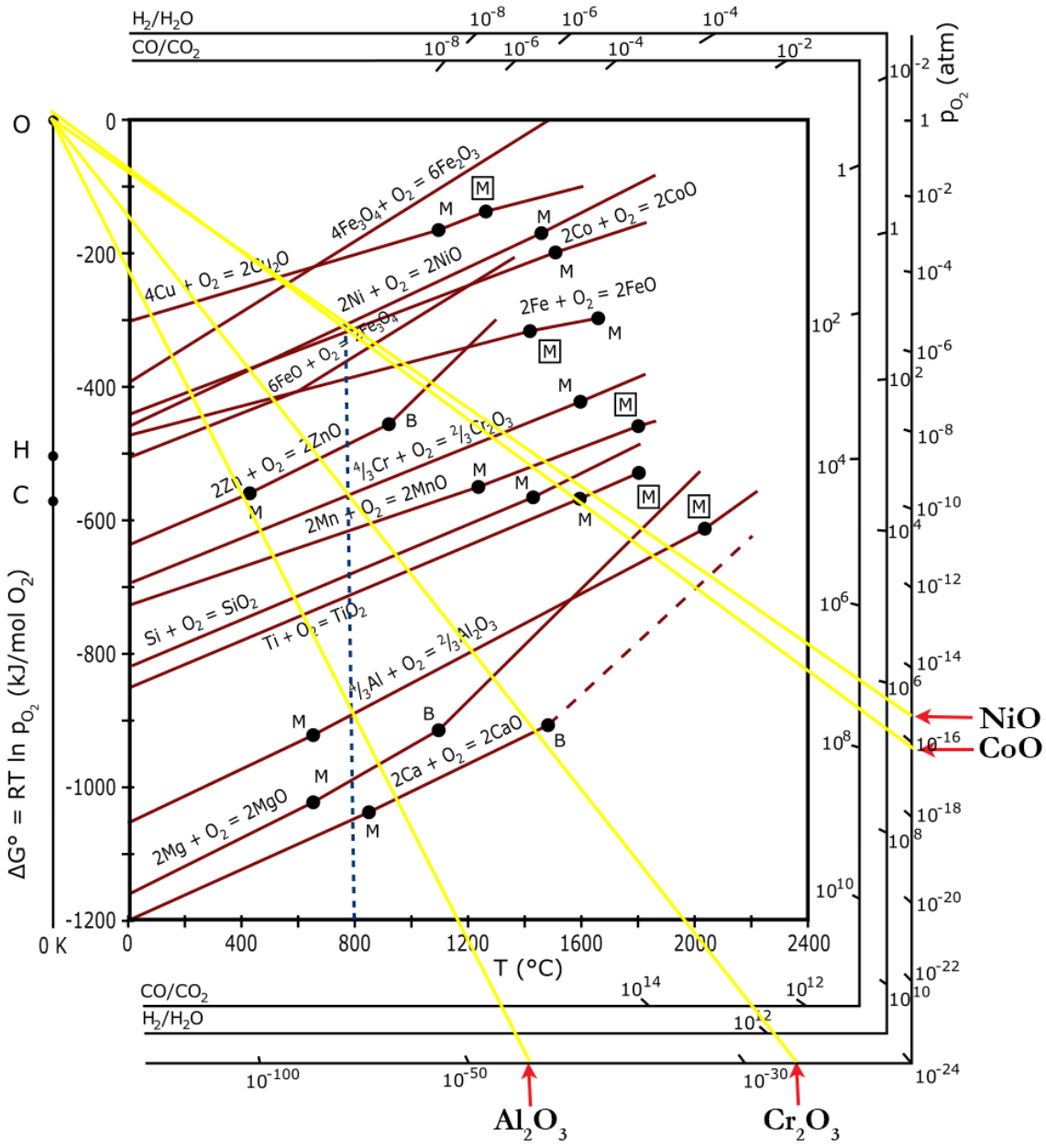


Figure 2.11: Ellingham-Richardson diagram of some important oxides. Figure adapted from [50].

As marked in the diagram, the partial pressure of a particular metal oxide is determined by drawing a diagonal line across to intercept with a vertical line of the corresponding oxidation temperature. The line that crosses the p_{O_2} on the right hand side of the diagram corresponds to the equilibrium partial pressure of oxygen for the oxide to form. An illustration of the possible oxides (with relevant alloying elements) in the current Co-Ni base superalloys at 800 ºC, which are shown in Figure 2.11 by the intercepting yellow lines with the respective oxides. The oxides plotted on the top in the diagram are easier to form (at low p_{O_2}) than those plotted at the lower region. Hence, by taking the partial

pressure number of each possible oxide, the sequence of oxide formation in the Co-Ni base superalloys at 800 ºC should be as follows:

$$NiO \rightarrow CoO \rightarrow Cr_2O_3 \rightarrow Al_2O_3$$

Note that the Ellingham-Richardson diagram only corresponds to the favourable types of oxides that could form under certain temperature and partial pressure of oxygen. It does not take the kinetics of oxidation into account, which means that even the formation of a specific oxide is thermodynamically favourable, the oxides could take a very long time to form; i.e: the oxidation kinetics can be slow [49]. The protectivity of some oxides differs from one another, for example, Cr_2O_3 and Al_2O_3 are well known in an alloy system to have slow growth rates [20].

Kinetics of oxidation – At a constant temperature and in the same gas atmosphere throughout the whole oxidation test, isothermal oxidation is taking place. As time increases, the oxide thickness increases and therefore, the mass changes, the material most commonly experiences a weight gain due to the addition of oxygen atoms into the material. Moreover, the weight of the material could be decreased due to spallation of oxide scales. The weight change behaviour of an oxidised metal could be categorised as:

- Logarithmic weight gain
- Parabolic weight gain
- Linear weight gain
- Weight loss

The four different kinetics of oxidation that metals obeyed by metals during isothermal oxidation can be seen in Figure 2.12. Typical non-protective oxides that form volatile oxides when metal oxidized usually show a linear weight loss [51]. Oxidation of metals that shows a positive weight gain may be linear, logarithmic or parabolic. In the case of logarithmic growth of the oxide, the typical oxidation mechanism usually occurs at temperatures below 500 ºC and, therefore, is not relevant for elevated temperatures and in this study [52]. The linear oxidation however, is observed in oxidation of iron and magnesium at temperatures 1000 ºC and 500 ºC, respectively. These types of oxides are unable to grow a protective barrier from oxygen to diffuse in to the metal surface [51].

The most desirable oxidation trend of metals at high temperatures is the parabolic kinetics, where the oxide film remains intact on the metal surface forming a uniform and continuous barrier to protect the diffusion of anions (oxygen) through the film. Based on the curve in Figure 2.12, the oxidation process is taking place rapidly in the beginning but slows down as the metal is forming a protective oxide layer and prevents it from further oxidation. The oxidation that follows parabolic laws does not stop entirely, but the rate of oxidation slows down over time.

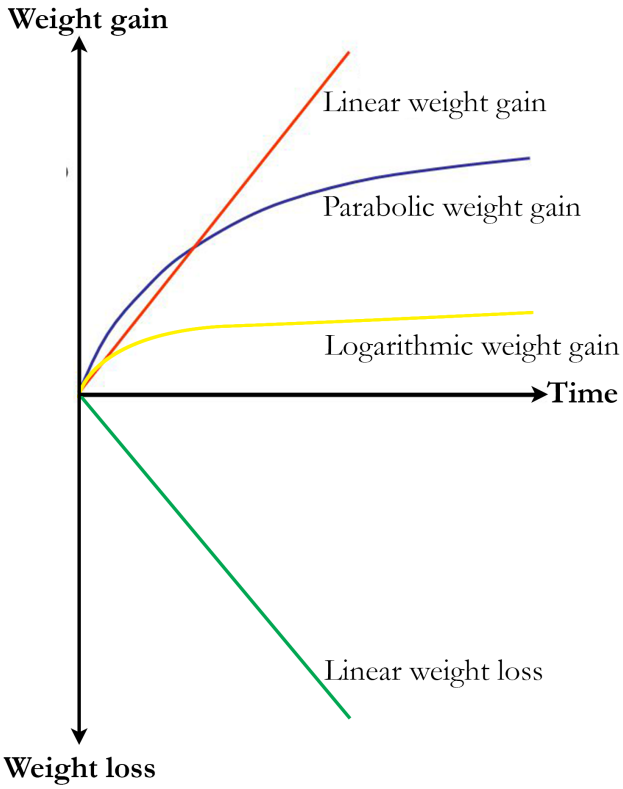


Figure 2.12: Isothermal oxidation weight change behaviour showing weight gain and weight loss with different kinetic forms. Figure adapted from [51].

The parabolic oxidation law can be expressed as follows [3]:

$$dx/_{dt} = {k_p}/_{x} \qquad \text{Equation 2.7}$$

Where k_p is the parabolic rate constant with units of cm²/sec. The equation can be integrated into:

$$x_t^2 - x_{t_0}^2 = 2k_p(t - t_0) \qquad \text{Equation 2.8}$$

Where t is oxidation time and t_0 is the time at which the diffusion control begins. The initial oxide thickness is denoted as $x_{t_0}^2$ at $t = 0$ and x_t^2 is the final oxide thickness.

The thicknesses in Equation 2.8 can also be written in terms of mass change per unit area, $\frac{\Delta m}{A}$ as follows:

$$\left(\frac{\Delta m}{A}\right)_t^2 - \left(\frac{\Delta m}{A}\right)_{t_0}^2 = 2k'_p(t - t_0) \qquad \text{Equation 2.9}$$

Where the unit for k_p is g^2/cm^4 and is often used to compare the oxidation rates in metallic oxides for some popular oxides as shown in Figure 2.13. The use of the parabolic rate constant is convenient to compare the growth rate of some important oxides in an alloy system. For example, at a given temperature, the rate constant for Al_2O_3 is lower than that of Cr_2O_3. This means that Al_2O_3 grows more slowly than Cr_2O_3 and produces a thin and compact layer on the surface. The high rate constant for other oxides above, such as FeO and CoO means that thicker oxides are grown on the metal surface.

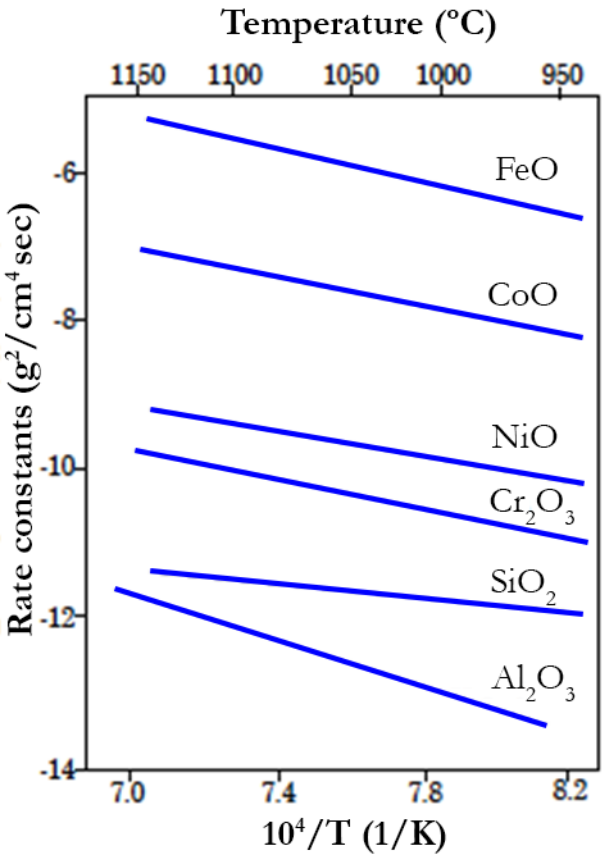


Figure 2.13: The rate constants for some important oxides as a function of temperature. Figure adapted from [3]

The principle oxides that might form in a superalloy system are based on elements added to the base metal such as chromium and aluminium for the purpose of improving the oxidation resistance (chromium) and precipitation strengthening (aluminium). Typical oxides formed in a nickel base superalloys are [20]:

- Chromium oxide (Cr_2O_3)
- Aluminium oxide (Al_2O_3)
- Nickel oxide (NiO)

- Cobalt oxide (CoO)
- Spinel ($NiO - CrO_2$)

Oxidation of alloys is different than oxidation of pure metals where various elements in an alloy system have a different alloy affinity and diffusion rate. During the initial stage of oxidation, virtually all oxides that are stable thermodynamically will form but one is likely to be dominant [20]. For example, in nickel base superalloy, NiO may form initially when oxidised, but only one or two oxide is stable across the entire surface. That dominant oxide in nickel base superalloys is Cr_2O_3 or Al_2O_3, depending on the chemistry of the alloy [20].

2.4.2 Oxidation of nickel base superalloys

To understand the formation of a protective alumina scale on nickel-base superalloys, there is a need to examine the oxidation mechanism of nickel-chromium-aluminium (Ni-Cr-Al) system at high temperature. In general, Cr_2O_3 and Al_2O_3 are the two most important oxides since they are regarded as the most protective oxides in superalloys. However, their growth is dependent on the optimum amount of chromium, aluminium and supply of oxygen. Chromia usually forms and is most protective at temperatures below 871 ºC, whilst alumina is protective at temperatures above the evaporation point of chromia [20].

According to Pettit and Giggins, the oxidation mechanism of Ni-Cr-Al ternary system can be classified into one of three categories based on three types of mechanisms (Type I, Type II and Type III) of oxide formation based on Figure 2.14 [53]. Type I alloys are high in nickel with a small amount of chromium and aluminium. In the case of Type II alloys, they are relatively chromium rich and low in aluminium. Finally, the higher amounts of both chromium and aluminium are assigned to Type III alloys [53].

The oxide phases formed are determined by the composition of the alloy, as shown in Figure 2.14 (a). At the beginning of oxidation of any Ni-Cr-Al alloy, the rapid diffusion of oxygen converts the surface layer of the alloy to oxide. As shown in Figure 2.14 (a), the initial oxidation is preceded by the formation of $Ni(Cr, Al)_2O_4$ spinels followed by a rapid outward-growing NiO scale where the composition of this layer is determined by the composition of the alloy [53]. A significant amount of Cr_2O_3 and Al_2O_3 would be formed depending on the amount of each element in the alloy. As the oxidation process continues, the diffusion of oxygen into the alloy precipitates Cr_2O_3 and Al_2O_3 as shown in Figure 2.14 (b). The oxidation of aluminium requires very little oxygen activity compared to chromium; i.e: particles of Al_2O_3 extends deeper into the alloy than particles of Cr_2O_3 [53].

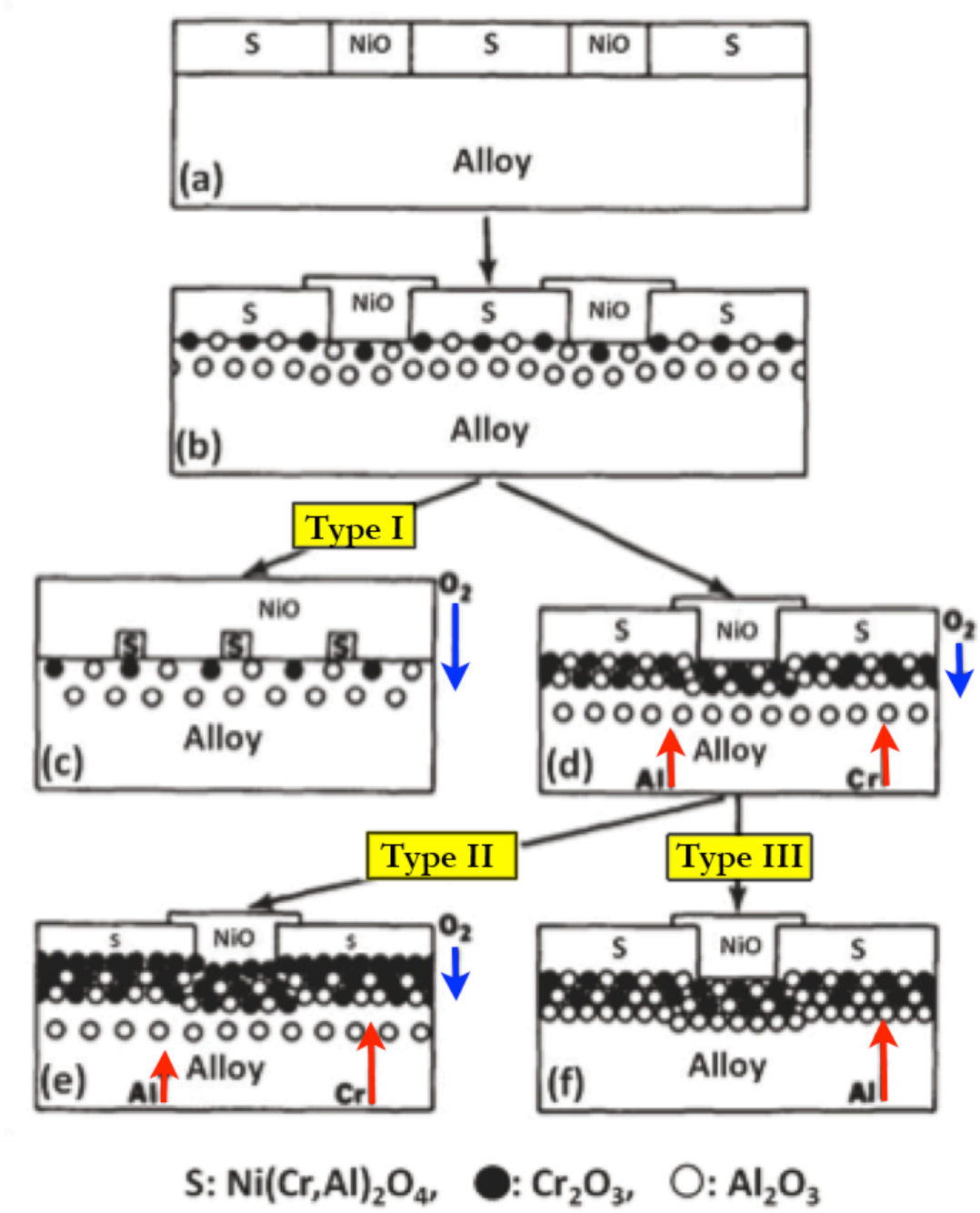


Figure 2.14: Schematic diagram of the oxidation mechanisms for Ni-Cr-Al alloys. Figure adapted from [53].

Type I – This type of alloy shows the instance of internal oxidation where chromium and aluminium continue to oxidise internally because there is not enough layers of Cr_2O_3 and Al_2O_3 to restrict the movement of oxygen into the alloy. In the external scale, the growth of NiO completely envelops other diffusion of phases in the external scale as shown in Figure 2.14 (c) [53].

Type II – This type of alloys shows a good example where the combined volume fraction of Cr_2O_3 and Al_2O_3 is sufficient to inhibit the movement of oxygen from the external scale into the alloy. Initially, the scale structure is composed of external NiO and $Ni(Al,Cr)_2O_4$ scale and Cr_2O_3 and Al_2O_3 sub-scale such as the Group I, with enough oxidation time, the sub-scale Cr_2O_3 is transformed into a continuous scale due to the sufficient amounts of chromium in the alloy as shown in Figure 2.14 (d). Since the formation of these oxides are continuous, there is a reduction in the flux of oxygen into the alloy and it establishes a lower oxygen activity over the alloy than that established by the NiO external scale [53]. However, the flux of oxygen is still sufficient to oxidize the aluminum internally but not the chromium as shown in Figure 2.14 (e). It is only when the Cr_2O_3 scale becomes continuous that a steady-state oxidation reaction is achieved and controlled by the transport of chromium to form Cr_2O_3.

Type III – In the case of this type of alloy, the same mechanism follows as in Type II alloy where there is a duplex layer of Cr_2O_3 and Al_2O_3 on the surface that limits the activity of oxygen as shown in Figure 2.14 (f). However, this type of alloy contains sufficient amounts of aluminium that is best capable of resisting high temperature oxidation due to the exclusive formation of a compact and adherent alumina oxide underneath the chromium oxide layer. As usual, the steady-state conditions are reached when the Al_2O_3 layer becomes continuous and the oxidation reaction is controlled by transport through the Al_2O_3 scale.

This famous study by Pettit and Giggins [53] is called the 'selective oxidation' which means that in Ni-Cr-Al ternary system, chromium allows a continuous layer of Al_2O_3 to be formed on Ni-Cr-Al alloys at lower aluminium concentrations than would be necessary if the chromium were not present in the alloy by contributing to the volume fraction of precipitated oxide which reduces the movement of oxygen into the alloy.

Also, in the same Ni-Cr-Al ternary system, an initial suggestion called 'the third element effect' by Wagner [54] suggested that the third element, chromium, in M-Al alloys (M as metal), acts as a getter for oxygen in the alloy during the initial stage, lowering the oxygen solubility in the alloy and preventing internal oxidation of the more reactive component, aluminium, producing external Al_2O_3 layers at lower aluminium levels than in binary M-Al alloys.

2.4.3 Spallation of oxide scale

Under some circumstances, the adherent external scale gets weaker and spallation starts to occur. One of the desired properties of the oxide scale is good adherence to the alloy surface, besides having slow growth rate. This phenomenon usually takes place during cooling when stress develops

in the scale as a result of the thermal expansion difference between the scale and the metal surface [55]. Generally, the main cause of surface oxide spallation results from the compressive stress in the oxide scale whilst cooling down.

The stresses cause the scale to spall away through delamination of oxide or cracking. The spallation of oxides is unlikely to happen under tensile stress condition. Spallation is most likely to occur under compressive in-plane stress in the oxide layer during cooling from high temperature [56]. The morphology of the oxides such as sub-surface curvature, internal oxidation or the dissolution of oxygen within the alloy substrate are the main causes of tensile stress in the oxide scale [57].

There have been many reports on spallation of oxides at high temperature, but the most interesting study was reviewed by Evans et al. where modes of spallation were classified into two principal routes as shown in Figure 2.15. According to Evans et. al, under compressive conditions, spallation may result either from the growth of a tensile, wedge crack along the interface or by buckling and cracking of the oxide layer [58].

Route I (thick oxide, strong interface) – Oxide scale spalled via wedging where compressive shear cracking initially occurs in the oxide with strong oxide/alloy interface strength, compared to the oxide as shown in Figure 2.15 (a). It is presumed that the formation of shear cracks within the oxide layer is presumably nucleated at the pre-existing defects [58]. Later, wedges develop at the adjacent oxide layer by differential contraction as a result of further cooling of the sample as shown in Figure 2.15 (b). Subsequently, decohesion at the interface is shown in Figure 2.15 (c).

Route II (thin oxide, weak interface) – This route of spallation is opposite to Route I, where a relatively weak interface as depicted in Figure 2.15 (e) by poor adherence of oxide scale to the metal surface. Such weakness can be essential to the system and could arise from the accumulation of voids, growth of interfacial cavities or the segregation of impurities to this region such as sulphur [58]. The buckling of the oxides initiates from a poorly adherent region as shown in Figure 2.15 (f). Later, the docohesion propagates laterally along the interface of the oxide/alloy as shown in Figure 2.15 (g). The presence of such an interfacial zone of low strength can result in buckling of the oxide layer.

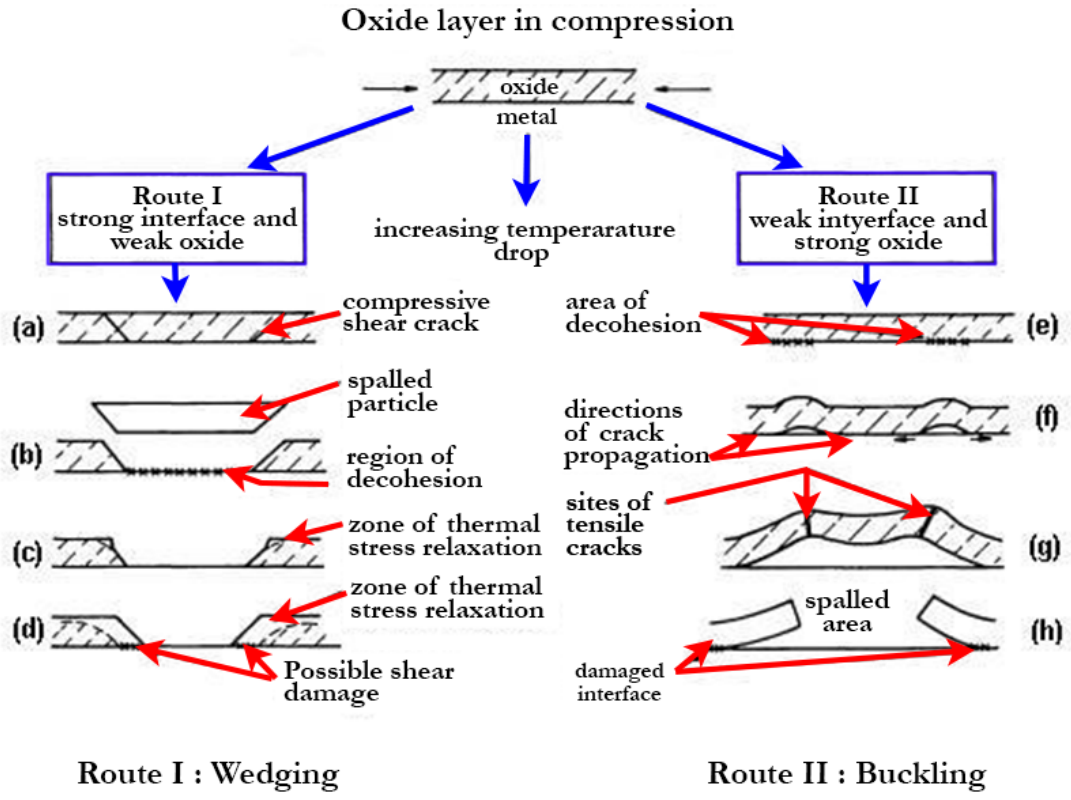


Figure 2.15: The main routes to the spallation of oxide scale grown on the surface of alloy. Figure adapted from [58], [59].

2.4.4 Transition of metastable Al_2O_3 to α-Al_2O_3

The oxidation resistance of high-temperature alloys is ideal when it forms of a protective oxide such as alumina. Ideally, the oxide layer should be highly stable, continuous, slow growing, free from cracks or pores, adherent and coherent [60]. There are several types of alumina that can form during high temperature oxidation, some of which are metastable and exist in various forms, such as cubic γ-Al_2O_3, tetragonal δ- Al_2O_3 and monoclinic θ-Al_2O_3. An α- Al_2O_3, however, is a stable and desirable oxide in hexagonal-close-packed structure which comes close to satisfying these earlier requirements; the slow growth rate is related to its highly stoichiometric structure [60]. The schematic diagram is plotted by Garigga-Majo et al. in Figure 2.16 which shows the time-temperature transformation (TTT) diagram for high temperature oxidation in β-NiAl alloy. The proposed transformation sequence from metastable alumina to α- Al_2O_3 is as follows [61]:

$$\gamma\text{-}Al_2O_3 \rightarrow \delta\text{-}Al_2O_3 \rightarrow \theta\text{-}Al_2O_3 \rightarrow \alpha\text{-}Al_2O_3$$

Oxidation at higher temperatures should always involve transition aluminas which may be observed during the initial stages of oxidation [60]. Transitional aluminas are formed dependent on various

parameters such as temperature and time. Doychak et al. suggested that the oxidation of β-NiAl can be divided into three stages; 1) transient stage where fast diffusion of aluminium by outward cation diffusion is producing δ- Al_2O_3 and θ-Al_2O_3 after 1 hour of oxidation at 1100 ºC, 2) transformation stage where metastable aluminas transformed into α-Al_2O_3 by nucleation process and 3) mature stage where the transformation from γ-Al_2O_3 to α-Al_2O_3 is complete [61].

Kear et al. have also studied the transient oxidation but in Ni-Cr-Al alloys at 1000 ºC where the first phases to form have been identified as $Ni(Cr, Al)_2O_4$ and NiO as plotted in Figure 2.16. The NiO grows rapidly and Cr_2O_3 forms beneath it and eventually becomes continuous. Below the Cr_2O_3 layer, Al_2O_3 develops as a metastable phase [62]. It is thought that the transformation of the metastable Al_2O_3 to α-Al_2O_3 occurs upon its integration into the external scale [62].

It is therefore, known from many previous studies that the transition of metastable aluminas are only occurring at the early stages of oxidation. Based on Figure 2.16, 28 hours of oxidation at 1100 ºC is sufficient to produce a stable α-Al_2O_3. It is therefore, noted in this particular study on cobalt base superalloys, that a stable, slow-growing protective α-Al_2O_3 will eventually grow after high temperatures and prolonged oxidation time (200 hours).

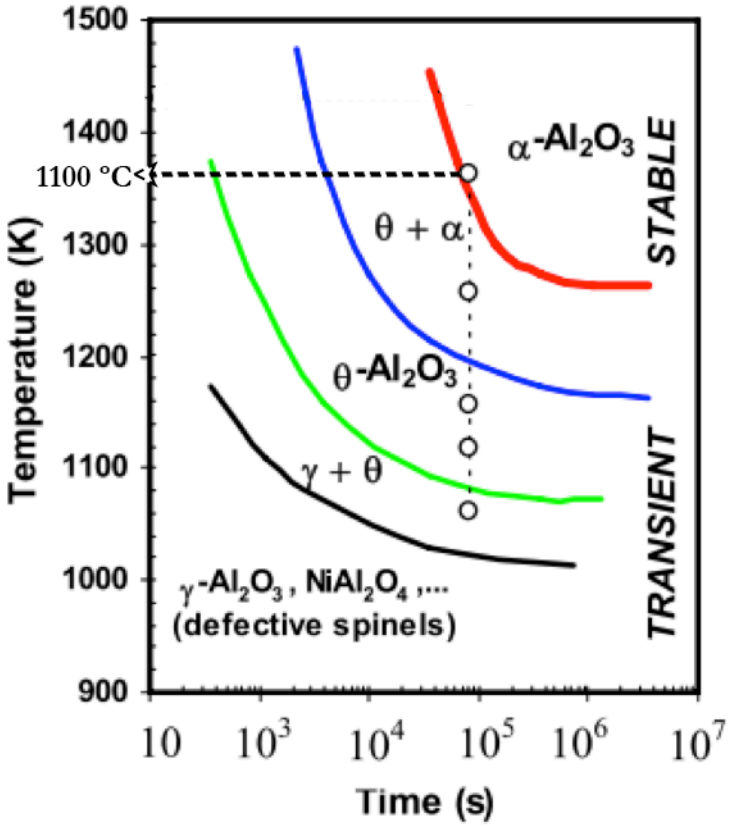


Figure 2.16: Schematic TTT diagram for the high temperature oxidation β-NiAl alloy. Figure adapted from [63].

2.4.5 Tracer study of oxide scale formation

Tracer experiments using standard Secondary Ion Mass Spectrometry depth profiling (dynamic SIMS) have been broadly used for the study of high-temperature oxidation particularly on alumina-forming alloys [60], [61], [64]–[68]. The idea of tracer distribution study to investigate the transport mechanism in oxides grown in alloys system is useful to understand the mechanism of oxide scale formation. The oxide grown with $^{16}O_2$ gas forms the initial scale and subsequently a new oxide forms with the $^{18}O_2$ gas. The word 'tracer' or 'marker' is usually corresponds to the location of the $^{18}O^-$ in second stage of oxidation [69].

The main principle in the two-stage oxidation is to oxidise the sample first under $^{16}O_2$ atmosphere, then the reaction chamber is evacuated and $^{18}O_2$ is introduced for the second step of the oxidation test. Then the sample is studied under Secondary Ion Mass Spectroscopy (SIMS) analysis to understand the oxide growth mechanism by examining the distributions of the oxygen isotopes in the $^{16}O_2$ and $^{18}O_2$ exposures.

The typical shape of $^{16}O^-$ and $^{18}O^-$ tracer concentration profiles for various transport mechanisms were presented by Chevalier et. al as shown in Figure 2.17. If outward cation (metal) transport is the primary mechanism, the tracer concentration will form a new oxide at the gas-oxide interface as shown in Figure 2.17 (a). If the transport mechanism is inward anion (oxygen), three types of profiles are possible depending on the transport pathway. In Figure 2.17 (b), the anion transport through cracks or pores is forming the new oxide at the metal-oxide interface. The same goes for the case in Figure 2.17 (c) where the new oxide is forming at the metal-oxide interface but this time via grain boundaries. No significant $^{18}O^-$ enriched oxide forms at the metal-oxide interface when anion transport proceeds via much slower bulk diffusion as illustrated in Figure 2.17 (d). When the anionic-cationic growth do not share the same path as shown in Figure 2.17 (e), the new oxides will form at both gas-oxide and metal-oxide interfaces. However, when both anionic-cationic growth are happening in the same path, the reaction product is expected to form within the pre-existing scale during the second stage of the oxidation as shown in Figure 2.17 (f).

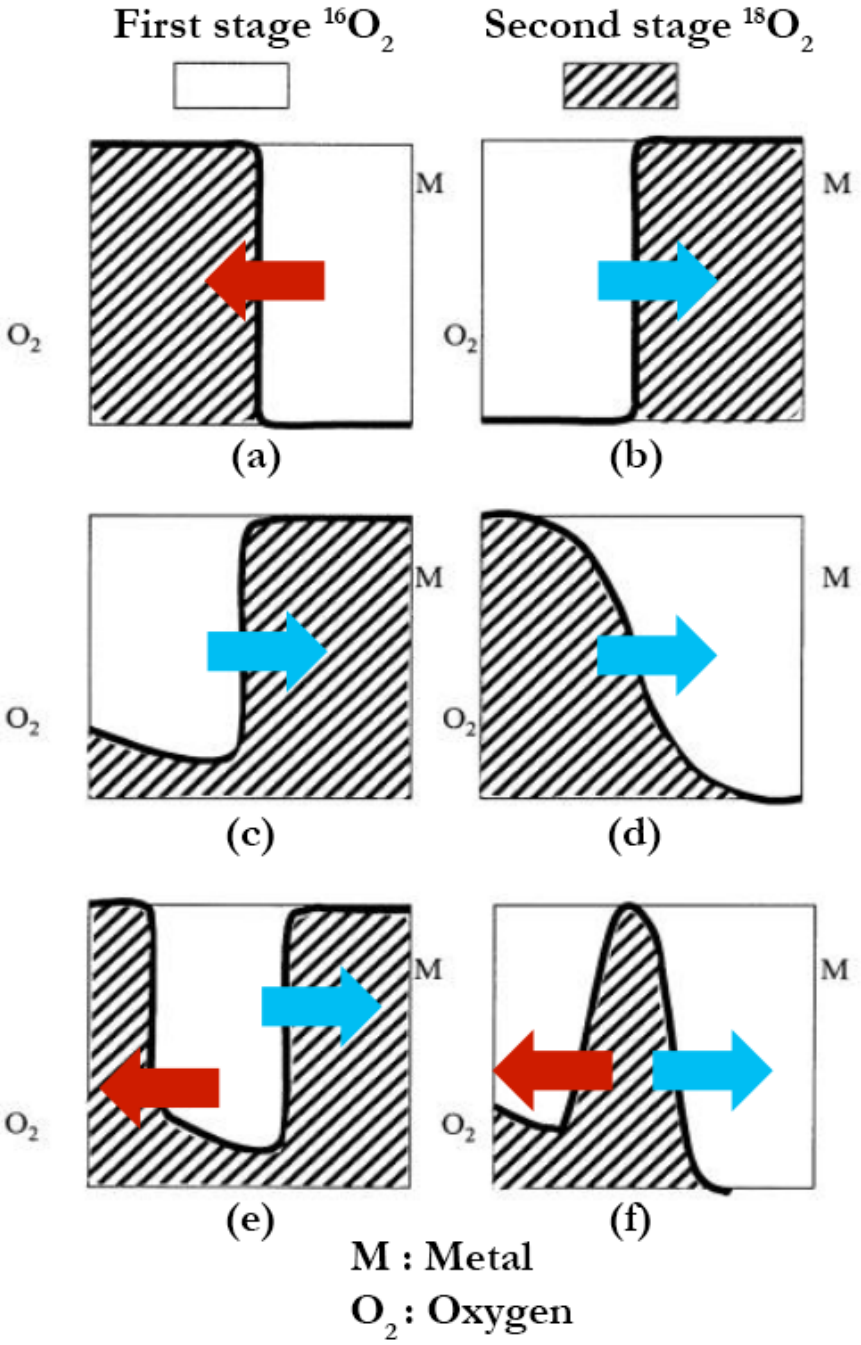


Figure 2.17: Schematic tracer concentration profiles for various transport mechanisms. (a) Outward cation transport. (b) Inward anion transport via cracks (c) Inward anion transport via grain boundaries (d) Inward anion transport via lattice (e) Mixed anion-cation transport via different paths (f) Mixed anion-cation transport via the same paths. Figure adapted from [69].

2.4.6 The combined two-stage oxidation and SIMS technique

SIMS depth profiling is an extremely useful technique for analysing the tracer oxygen diffusion mechanisms in an alloy system, as it is able to distinguish all the isotopes in the periodic table. The three principles of oxide growth mechanisms that were discussed earlier: a) outward cationic growth b) inward anionic growth c) mixed anionic-cationic growth, can be characterised by using in-situ micro-machining via focused ion beam (FIB ion milling) and directly analyzing by using high-resolution SIMS. In the past decade, SIMS mass spectrometry has been implemented on FIB instruments, so that micro machining (FIB ion milling) and SIMS analyses can be conducted in the same instrument.

An example of a two-stage oxidation experiment to study the oxide growth mechanism using $^{16}O^-$ and $^{18}O^-$ tracer study has been done on RR1000 at 800 ºC for 120 hours as shown in Figure 2.18. The elemental maps correspond to exposures in $^{16}O_2$ for 72 hours during the first stage followed by 48 hours in $^{18}O_2$. The SIMS maps revealed some interesting features with respect to the oxidation of this nickel base alloy. First, the map of $^{16}O^-$ revealed the existence of the external scale with the internal oxides directly beneath in the base alloy. The intensity of $^{16}O^-$ at the internal oxide is indicating an inward diffusion of oxygen via grain boundaries during oxide growth. Moreover, the inward transport results in new oxide formation as seen in the $^{18}O^-$ map at the oxide-metal interface. It can be summed up that in the region of the external scale closest to the oxide-gas interface, the oxide is composed of mostly ^{18}O, whereas in the region closest to the oxide-metal interface, the oxides contain a mixture of ^{16}O and ^{18}O species. Therefore, the mechanism of oxidation in this case is transport taking place through the external scale to form the new oxide at the oxide-alloy interface, but at the same time new oxide also forms at the gas-oxide interface [70].

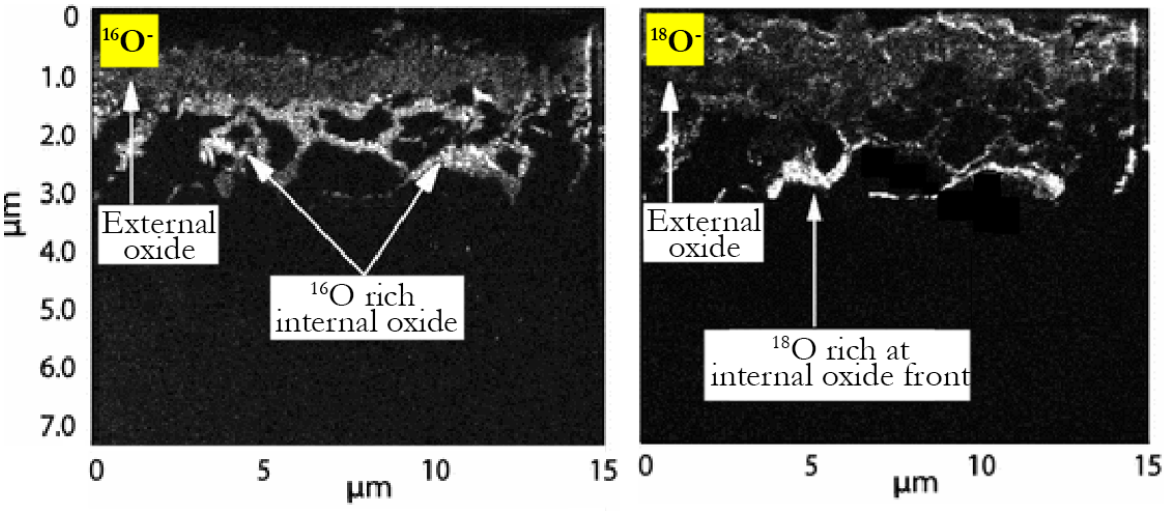


Figure 2.18: FIB-SIMS elemental mapping of $^{16}O^-$ and $^{18}O^-$ after two-stage oxidation experiment carried out for RR1000 at 800 ºC for 120 hours. Figure adapted from [70]

Focused ion beam (FIB) – The microscope system works in principally the same way as conventional SIMS, but in this case the FIB200 is using a gallium Ga^+ liquid metal ion gun (LMIG), which operates at 30 keV. The size of the beam can be changed depending on the beam current used and typically a beam current of 7 nA is used for the purpose of material removal (milling craters) whilst a finer beam current of 1nA is sufficient to polish the metallic oxide surface of a material in this study. A thin layer of platinum (approximately 1.5 µm thick) is typically used to protect the oxide surface during milling as well as to prevent surface charging. In a standard SIMS depth profiling, a single primary ion gun generates the secondary ions to characterise the surface composition and at the same time, erodes the sample with a high current density to get in-depth information [71].

The FIB technique is a useful method in this study in terms of analysing the microstructural evolution of the oxide during high-temperature exposure by examining the thickness, the porosity, the diffusion of cations/anion, the chemical composition and the distribution of the different phases present in the multilayer oxides. In the case of thin oxides, for instance, cobalt-base superalloys are well known to have a good oxidation resistance, the FIB milling of a crater at an angle (45 to 60 º) is beneficial to stretch the thin oxide, making it more prominent for further SIMS analysis.

2.4.7 The effect of surface treatment (shot-peening) on oxidation

The general definition of shot peening is a cold working process to create plastic deformation used to produce a compressive residual stress layer near the surface of metals [72]. Such compressive residual stress is resistance to fatigue crack initiation. It is thought that the crack growth performance can be improved by modifying the surface or sub-surface of alloy. Therefore, by plastically deforming the

materials surface by impacting some small, round metallic particles is sufficient to create plastic deformation [73]. It is well known that shot peening a surface is a low cost method that creates a large compressive residual stress on the surface and this compressive residual stress contributes to the increased fatigue strength of material [73].

The current turbine disc material is required to withstand higher temperatures and stresses, and it has been established that shot-peening, in general, can extend the service life of the critical components. Since this is the normal required condition for a turbine disc, there is the need to study the effect of shot peening on the surface in a high temperature oxidation environment, especially the effects on growth of some specific oxides at high temperature. Previous studies have been done proving the negative effect of applied stress and surface roughness on the increase of oxidation rates [74], [75]. However, there have also been a few claims that shot peening has a beneficial effect on oxidation resistance by enhancing the chromium diffusivity to produce an early formation of Cr_2O_3 in iron-nickel base alloy (Incoloy 800H) and nickel base superalloy (RR1000) [76]–[79].

A good example to represent the morphology of surface scale and sub-surface oxide before and after shot-peening can be seen in Figure 2.19 [70]. The micrographs demonstrate the severity of oxidation on in the extent of external scales where TiO_2 and Cr_2O_3 are present. In the case shot peening, the damage occurred in the sub-surface region as seen in Figure 2.19 (b). This sub-surface damage can be detrimental to the oxidation resistance. The evidence in the shot-peening condition proves that there is a severe grain boundary internal oxidation in the sub-surface region. Shot-peening has been reported to increase the oxidation rates in alloys where protective oxide scales are normally found, such as RR1000, as reported by Cruchley et al. [78]. According to his investigations, the weight gain kinetics on oxidised RR1000 increased at temperatures 700 – 750 ºC [79].

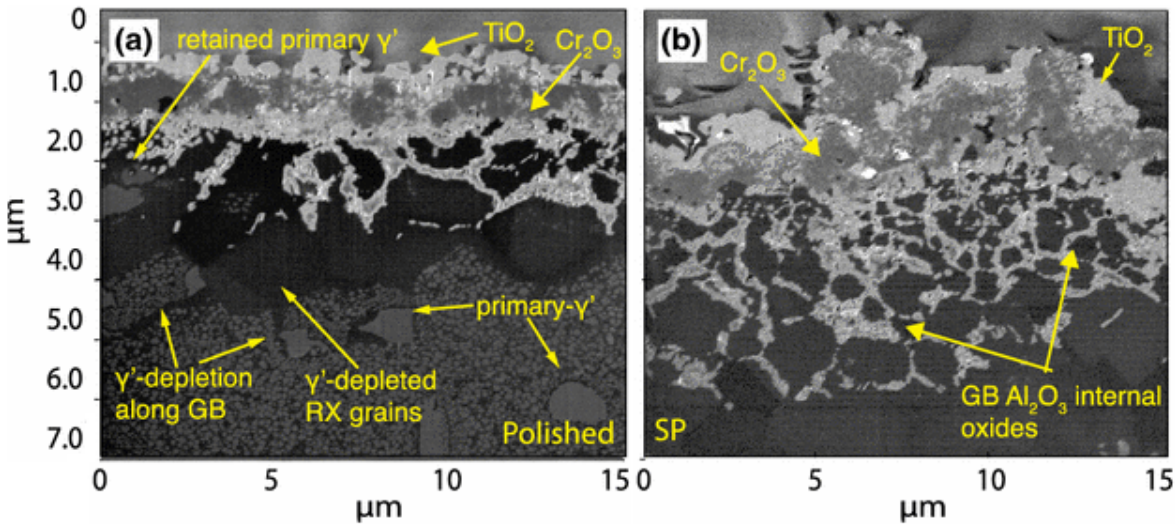


Figure 2.19: Cross sections of oxidised RR1000 at 800 ºC for 120 hours (a) polished specimen (b) shot-peened specimen. Figure adapted from [70].

Since there was more than one element oxidising in RR1000, the reported mass gain by Cruchley et al. could possibly be from the enhanced formation of the external scale (Cr_2O_3). Due to this concern, the subsequent study was focused on the extent of Cr_2O_3 growth at oxidising temperatures between 700 – 800 ºC [80]. Therefore, Figure 2.20 is plotted to compare the Cr_2O_3 growth rate in all three temperatures for both polished and shot-peened conditions. Note that the scatter represents 50 measurements taken from each sample with ± 1 standard deviation.

The trend from Figure 2.20 shows that at both 700 and 750 ºC, both shot-peened conditions yield a higher Cr_2O_3 growth than that of the polished conditions. Conversely, the trend at 800 ºC shows the opposite, where shot-peening provides benefits to oxidation resistance in terms of the rate of chromia growth. Recrystallisation in the sub-surface region and sub-surface oxide penetration at a deeper depth via grain boundaries were also reported in the shot-peened condition.

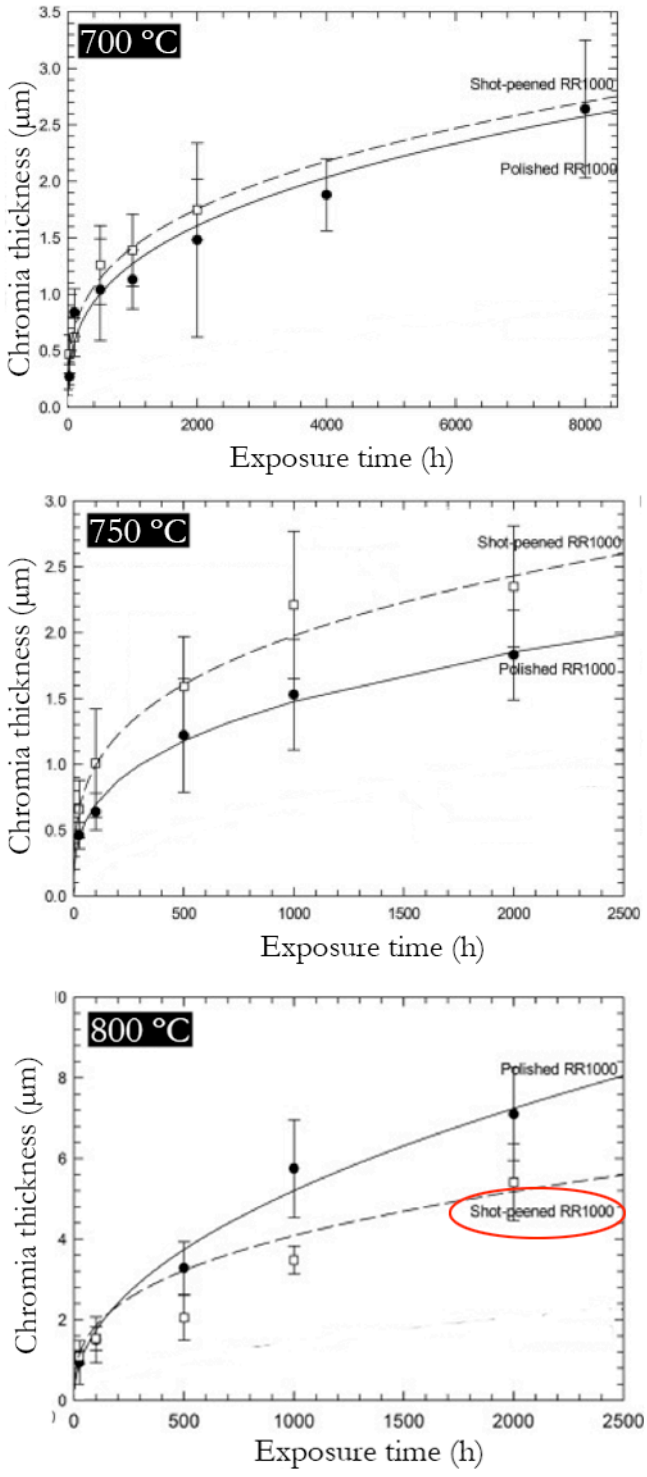


Figure 2.20: Plot of chromia thickness against exposure time at three different oxidation temperatures for both shot-peened and polished conditions. Figure adapted from [80].

2.5 Development of Cobalt-Base Superalloys

2.5.1 Conventional cobalt base alloys

Superalloys are generally divided into three classes; nickel-base superalloys, cobalt-base superalloys, and iron-base superalloys. Since the first nickel-base superalloy, known as "80/20" nickel-chromium, developed by Bedford and Pilling and Merica in the 1930s, the demand for increased engine efficiency has pushed the nickel-base superalloys to their mechanical and thermal limits [18]. Nickel-base superalloys were developed for high temperature applications for a number of reasons; first, these alloys form a stable face-centred cubic (FCC) solid solution which is tough and ductile; second, diffusion rates for FCC metals, such as nickel, are low which leads to high temperature microstructural stability; finally, it is moderate in cost compared to other platinum group metals [2]. The most important strengthening phase for nickel-base superalloys is the stable $L1_2$ type intermetallic compound, Ni_3Al, which precipitates as a cuboidal intermetallic γ' phase in the FCC γ nickel solid solution.

With an atomic number of 27, cobalt falls between iron and nickel. The melting point of cobalt is 1493 ºC and its density is 8.85 g/cm^3, which is similar to that of nickel (8.902 g/cm^3). Cobalt is ferromagnetic. At temperatures below 417 ºC, cobalt is a hexagonal closed-packed (HCP) structure, but above that temperature above its melting point, cobalt is a FCC structure [23].

The early cobalt-base superalloys, in the 1920s, depended solely on solid-solution strengthening, interaction between hard carbides and alloy imperfections such as dislocations and stacking faults for high temperature strength [81]. They are typically used in high corrosive environment or high stress applications [82]. Co–Cr and Co–Cr–W alloys were developed for applications in aggressive environments and as wear-resistant materials [3], and the cobalt-base superalloy, Stellite 21, was the first turbine vane material utilised in jet engines [19].

These cobalt alloys did not form the $L1_2$ type precipitates, but instead relied on carbides (MC, M_6C, and $M_{23}C_6$) to produce similar strengthening effects [18]. The carbides in the early cobalt base superalloys are divided into two groups; chromium-rich and refractory elements rich carbides. The chromium rich carbides are usually in the form of M_3C_2, M_7C_6 and $M_{23}C_6$ [20]. Chromium can be substituted with refractories such as molybdenum, cobalt or tungsten. The M_7C_6 carbides form when there is a shortage of chromium in the alloy system. Then, this carbide can form $M_{23}C_6$ with further ageing or during service [82]. Refractory element rich carbides are typically in the form of MC or M_6C in cobalt base superalloys. The main strengthening carbide is MC, where it is normally formed during cooling with elements such as hafnium, zirconium, tantalum, niobium or titanium [82].

The conventional cobalt base superalloys are strengthened by $L1_2$ Co_3X, which are called the geometrically close packed phase (GCP). They are coherent with the FCC γ phase, similar to γ' in nickel base superalloys. The Co_3X phases are commonly Co_3Al [83], [84], Co_3W [85], [86], Co_3Ti [87], [88], and Co_3Ta [89]. Co_3Ti is the only stable $L1_2$ structure in cobalt base superalloy binary system but applications are limited to 750 ºC due to their lower strength [18]. The lattice misfit in cobalt base superalloy is high, more than 1 %. Since the lattice misfit provides growth and coalescence of the γ' precipitates as it gives larger surface energy for coarsening, the desirable number should be in between -0.1 to 0.5 %, such as in nickel [2]. Therefore, cobalt base superalloy are not widely used in high temperature applications due to instability of γ' phase. Their applications are restricted to static components such as vanes or combustion chambers, where superior oxidation resistance and weldability are desired [23], [87].

2.5.2 The discovery of γ/γ' cobalt base superalloy

With the development of nickel-base superalloys strengthened by the γ' $Ni_3(Al, Ti)$ phase, the possibilities of precipitation hardening using geometrically close-packed phases that have the form A_3B have been investigated by many researchers. The latest cobalt superalloys based on the Co-Al-W system are similar to the precipitation strengthened nickel-base superalloys, having a FCC gamma (γ) cobalt solid solution matrix strengthened with precipitates of gamma-prime (γ') $Co_3(Al,W)$ phase, which is an intermetallic compound with an ordered $L1_2$ structure [5].

In 2006, Sato et. al published a paper in Science, where they have identified cobalt-base superalloys showing a high-temperature strength greater than those of conventional nickel-base superalloys [5]. The stable ternary compound with $L1_2$ structure $Co_3(Al, W)$ formed as γ' precipitates, in the composition of Co-9Al-7.5W (at. %). Novel γ'-strengthened cobalt-base superalloys (see Figure 2.21) possess very similar γ/γ' microstructures when compared to conventional nickel base superalloys [5]. The cuboidal γ'-phase distributes homogeneously within the γ matrix and the precipitates align along the [001] directions as shown in Figure 2.21 (a).

The authors claimed that the new $L1_2$ phase consists of Co_3Al phase stabilised by the addition of tungsten and no other elements such as chromium or molybdenum exhibit the same effect. The ternary phase diagram in Figure 2.21 (c) shows at 900 ºC that there is a small phase field of γ' between the γ (A1) matrix phase, CoAl (B2) phase and Co_3W (DO_{19}) phase.

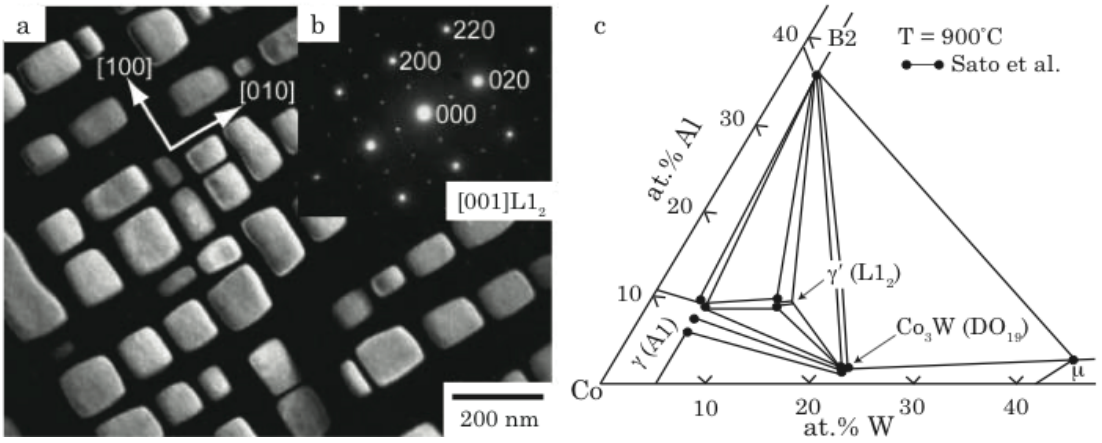


Figure 2.21: a) Electron micrographs of Co-9Al-7.5W (at. %) aged at 900°C for 72 h. b) Selected area diffraction pattern. c) Isothermal section diagram of the Co-Al-W ternary system at 900°C. Figures adapted from Sato et al. [5].

Similar to nickel-base superalloys, the atoms that construct the basic alignment of FCC crystal structure is cobalt as shown in Figure 2.22. When more than one element is present in the FCC crystal structure, the structure becomes ordered FCC. In this case, similar to Ni_3Al in nickel base superalloys, the γ' phase exhibits the LI_2 crystal structure, where the aluminium and tungsten atoms are situated at the corners of the unit cell and the cobalt atoms are at the face centres. Figure 2.22 shows a classic example of ordering. Ordering is a very important trait in the strengthening of superalloys [20].

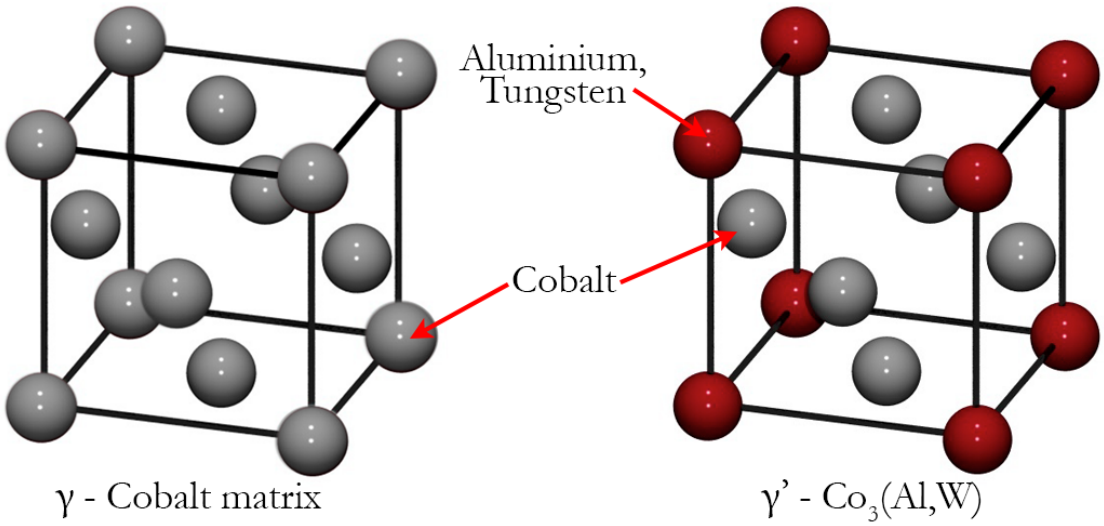


Figure 2.22: Unit cell of the FCC γ matrix on the left consists of cobalt atoms and the $L1_2$ structure of the γ' on the right consists of Co_3(Al, W).

As the γ' phase is embedded coherently in the FCC γ matrix, the lattice misfit is relatively low, approximately 0.53% [5]. Therefore, this promising novel class of high temperature alloy is currently being investigated intensely. However, it is noted that this γ' phase field is really small, an incorrect ratio of aluminium and tungsten can exhibit the unwanted B2-CoAl and DO_{19}-Co_3W phases. Similar to nickel base superalloys, these types of phases are detrimental to the mechanical properties of the alloy. Nevertheless, since its discovery, this promising alloy provides a possible breakthrough in the development of high temperature alloys, especially with the demand of increasing operating temperature as well as nickel reaching its limit in the superalloys future applications. The development of this alloy is still in the early stages. Much research has been done since its discovery to find the optimum alloying compositions to achieve excellence in both mechanical and environmental properties.

2.5.3 Phase stability in cobalt-base superalloys

There are several metastable intermetallic phases that can be found in the Co-Al-W alloys, namely, Co_7W_6 (μ), CoAl (B2), and Co_3W (DO_{19}). Sato et. al claimed that the γ′ in the ternary Co-Al-W system is stable at 900 ºC but metastable at 1000 ºC, where these secondary phases Co_7W_6 (μ), CoAl (B2), and Co_3W (DO_{19}) co-exists with the γ matrix or γ'.

Shinagawa et al. observed that the γ′ phase is metastable between 900°C to 1000°C, where a transformation from a matrix (γ) containing γ′ and μ-phase (Co_7W_6) to a matrix (γ) containing intermetallic β-phase (CoAl) and χ-phase (Co_3W) takes place between these temperatures [90]. Such secondary phases in the system may be detrimental to the mechanical properties of the alloy and so it is important to understand the effect of other additions on the phase equilibria. The equilibrium reaction at 900 ºC in the Co-Al-W ternary system is presented in Figure 2.23.

At 1000 ºC, Miura et al. reported that the Co-Al-W ternary system consists of two three phase regions; Co-CoAl+Co_7W_6 and Co-Co_7W_6-Co_3W as shown in Figure 2.23. The reaction starts from the eutectic and occurs in both binary system; L → Co-Al and L → Co-W at 1400 ºC. The other three phase region Co-Co_7W_6-Co_3W was the product of Co-Co_7W_6 → Co_3W at 1093 ºC as shown in Figure 2.23. Sato et al. has predicted the existence of γ' in the ternary Co-Al-W system is obtained from the ternary peritectoid reaction of Co-CoAl-Co_7W_6 with another peritectoid reaction of Co-Co_7W_6-Co_3W producing $Co_3(Al,W)$. In between the formation, there is a complicated sequence of reactions as shown in Figure 2.23.

The ternary Co-Al-W system involves a complicated sequence of reactions and four three-phase regions can be expected in the ternary alloy:

- $Co + CoAl + Co_3(Al,W) = \gamma + \beta + \gamma'$
- $Co + Co_3W + Co_3(Al,W) = \gamma + \chi + \gamma'$
- $CoAl + Co_7W_6 + Co_3W = \beta + \mu + \chi$
- $CoAl + Co_3W + Co_3(Al,W) = \beta + \chi + \gamma'$

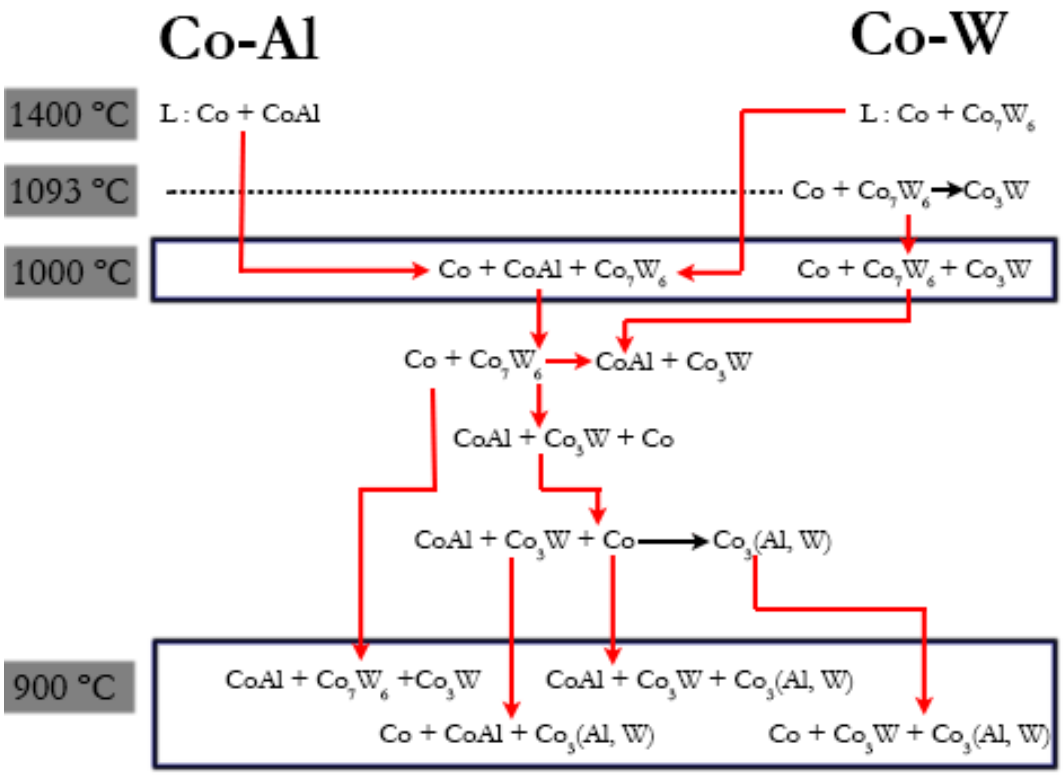


Figure 2.23: The sequence for the reaction in the Co-Al-W binary system at 900 ºC. Figure adapted from [91]

Kobayashi et al. [92], proved that γ' formed with a coarsened shape and in contact with CoAl and Co_3W after a 900 ºC for 500 hours of heat treatment as shown in Figure 2.24. The prolonged heat treatment from 500 hours to 2000 hours has produced a metastable phase of Co_3W, which is a cause of a decrease in aluminium content due to oxidation at high temperature. The aluminium-depleted region is transformed from γ/γ' phase into γ/Co_3W phase as shown in Figure 2.24. With a further 2000 hours of heat treatment the fraction reduced significantly. γ' became metastable and decomposed into CoAl and Co_3W, as shown in Figure 2.24.

It is crucial to control the ratio of aluminium and tungsten in the ternary cobalt system. Oohashi et al. investigated the effect of tungsten concentrations in Co-Al-W system [93]. The variation of tungsten between 9, 11.5 and 11.75 at. % shows no detrimental secondary phases but at 12 at. % of tungsten and heat-treated at 900 ºC for 168 hours produced the CoAl and Co_3W phases.

Many have studied the effects of other elements in the production of these secondary phases. Chromium, tantalum, molybdenum, manganese, iron, and silicon were the few elements that were added in the ternary system in a little amount (2 at. %) [83], [94]–[96]. All of these elements exhibit γ + γ' + CoAl + Co_3W after aged at 900 ºC for 168 hours in the ternary Co-8.8Al-9.8W [97].

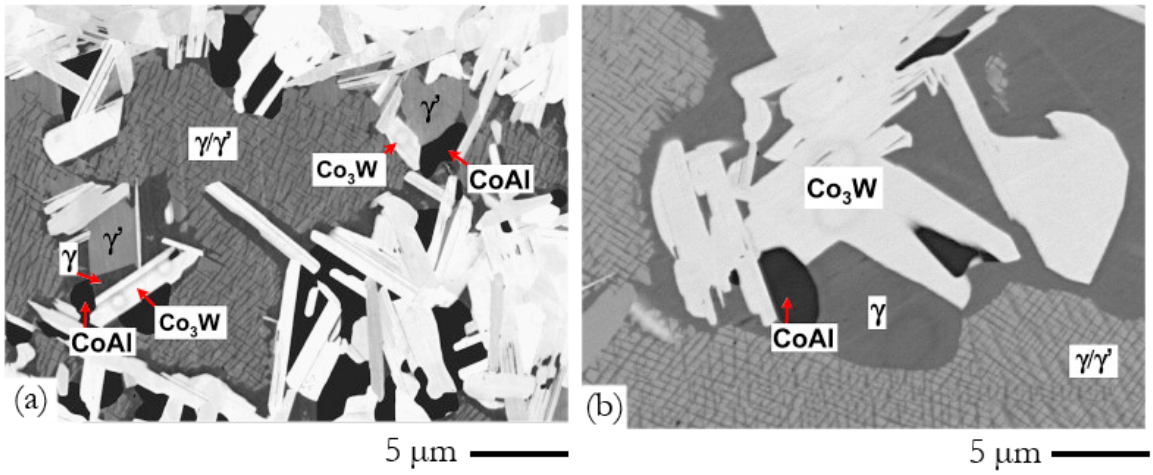


Figure 2.24: Back-scattered electron image of the diffusion-couple heat treated alloy (Co-27Al and Co-15W at.%) at 900 ºC for a) 500 h and b) 2000 h. Figure adapted from [92].

2.5.4 Oxidation of Co-Al-W superalloys

High temperature oxidation resistance is another important design factor for the Co-Al-W alloys for use in high temperature applications. The oxidation of nickel-base superalloys have been studied comprehensively, and aluminium and chromium are the key elements that form protective oxide layers that prevent further oxidation [18], [81]. Very little research has been carried out concerning the oxidation behaviour of the new γ'–strengthened cobalt base superalloys. It is reported that the Co-Al-W base superalloys typically form cobalt-rich oxides CoO, Co_3O_4, and $CoWO_4$ that are non-protective and have a high tendency for spallation after exposure in air at 800°C [95], [98], [99]. However, the aluminium content is very important in forming the slow-growing, high stability and compact scale of alumina (Al_2O_3) [98], [100].

In recent studies, chromium was added to improve the oxidation resistance of this alloy, as it is known that chromium forms a protective chromia layer (Cr_2O_3), but too large an addition of chromium was found to destabilise the γ/γ' microstructure [98]. Shinagawa et al. [90] reported that the addition of nickel can stabilise the γ/γ' microstructure by widening the γ' phase in the Co-Al-W system, allowing, more chromium to be added to the system without compromising the stability of the γ' phase.

Isothermal oxidation experiments have been carried out by previous studies at 800, 900, and 1000 ºC [94], [95], [101]. Oxidation of Co-Al-W superalloys at high temperatures in air takes place in two stages, a brief transient period at the beginning of exposure followed by a steady-state oxidation period [98]. According to Klein et al., at both 800 and 900 ºC, oxidation is likely to happen based on the oxide kinetics rather than thermodynamics. The transient oxide period at 900 ºC consists of cobalt oxide (CoO) instead of Co_3O_4 at 800 ºC. The outward diffusion of the cations to form a thick, compact and adherent oxide layers on the surface is limited as time increases. The same goes to the mass gain. This proved that the Co-Al-W superalloys formed protective oxide layers, which decelerated the kinetics of oxidation after the transient period.

At steady state conditions, several oxides co-exist and may be divided into different scale layers as shown in Figure 2.25. The outermost oxide layer is usually Co_3O_4, a stable oxide layer with spinel structure, which usually forms at temperatures in the range of 600 - 800 °C [13]. At higher temperatures, Co_3O_4 decomposes to CoO, which has a rock salt structure and is stable at temperatures up to 900 °C [102]. The middle oxide layer is a mixed oxide containing Co, Al and W, whereas the inner oxide layer is a thin layer of Al_2O_3. The highlighted region in Figure 2.25 (b) is the γ'-depleted region where needle-like shaped intermetallic compounds (Co_3W) are formed within the γ matrix as a result of decomposition of the Co_3(Al, W) precipitates to form the alumina scale [103]. Oxidation at 800 °C leads to the formation of a protective inner Al_2O_3 layer whereas oxidation at 900 °C leads to the formation of a discontinuous Al_2O_3 layer. The example is shown in Figure 2.25 where transformation in alloy Co-9Al-9W-0.12B from a two-phase γ/γ' to a two-phase γ/Co_3W microstructure takes place at 800 ºC for 500 hours [98], [100].

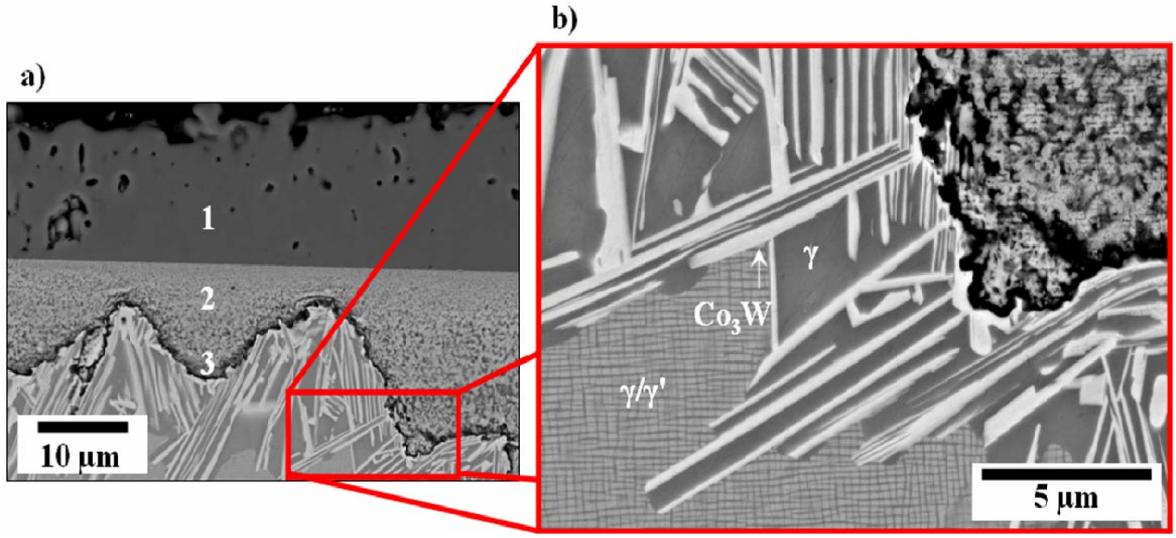


Figure 2.25: Oxidation of Co-Al-W showing (a) three layers of oxides typically found in the ternary Co_3(Al, W) system (b) γ'-depleted area showing the matrix (γ), the precipitation strengtheners (γ'), and the secondary phase (μ: Co_3W). Figure adapted from [98].

Note that in Figure 2.25, the thickness of the outer scale (CoO) is substantial and grows up to approximately 50 μm. Since the non-protective CoO is formed on the surface, the mass gain increases as the isothermal oxidation time increases [94].

There are three types of cobalt oxides that could exist at high temperatures, such as CoO, Co_3O_4, Co_2O_3, which are not protective and result in poor oxidation and corrosion resistance [95]. Under a specific partial pressure, the cobalt base alloys are inclined to form Co_3O_4 at lower temperature (600 – 800 °C), which has been found by many previous studies in Co-Al-W base alloys [94], [95]. However, at higher oxidation temperature (more than 900 °C), Co_3O_4 is unstable and decomposes into CoO, shown in Figure 2.25. The final type of cobalt oxide is Co_2O_3, which is unstable and typically obtained electrochemically under careful conditions [104]. No previous studies in Co-Al-W alloys have yielded this type of oxide.

Many cobalt-base alloys use formation of chromia (Cr_2O_3) to achieve good oxidation resistance. Chromia scale, however, is not protective above 980 °C due to the decomposition of Cr_2O_3 into CrO_3. Al_2O_3 is a more stable oxide and has slower growth rate than Cr_2O_3 . The relative oxide stabilities can be predicted using the Ellingham-Richardson diagram in Figure 2.11. To interpret this diagram, some of the important oxides that may form in the studied alloys are CoO, NiO, Cr_2O_3, and Al_2O_3. In view of the equilibrium oxygen partial pressure at 800 °C, where the oxidation temperature in this study is based on, the sequence of formation of scales in these particular alloys are NiO, followed by CoO, then Cr_2O_3, and lastly Al_2O_3. This corresponds to previous studies in nickel base

superalloys where similar sequence of scales have been found, except for NiO, and according to Klein et al., the NiO or nickel-rich oxides are formed at the oxide-alloy interface.

Yan et al. has performed a series of isothermal oxidation experiments on Co-7Al-7W alloy with additions of chromium, iron, silicon tantalum, molybdenum, titanium, nickel-vanadium and vanadium [105]. Figure 2.26 indicates the ranking of mass change in oxidation for these alloying element additions to the base alloy (Co-7Al-7W). The trend in the figure shows a parabolic growth behaviour and the alloys have been ranked from the best oxidation resistance as follows: 10Cr > 20Fe > 1Si > 20Ni > 2Ta > Base > 2Mo > 2Ti > 6Ni-4V > 2V as shown in Figure 2.26 (a).

The back-scattered electron (BSE) image in Figure 2.26 (b) represents the image of the base alloy (Co-7Al-7W) after just 20 hours of oxidation at 800 ºC. It is clear to note that this alloy is oxidising rapidly in the transient stage where the thickness of the outer oxide scale is measured as 36 μm. There were two distinct oxide layers formed in the base alloy; the porous outer layer consists of cobalt-rich oxide, and the inner layer consists of cobalt, aluminium and tungsten. The region between the inner oxide layer and the substrate has precipitated an intermetallic phase Co_3W, similar to that reported by Klein et. al [94].

Since the alloy with 10 at. % of chromium yields the best oxidation resistance, a small grained specimen of the oxide scales in this alloy was studied further in the high-resolution TEM to obtain an accurate result of the oxides chemistry. With 10 at. % additions of chromium, the morphology of the oxides has changed completely. The oxide scale grown on the surface is very thin, up to 1.3 μm.

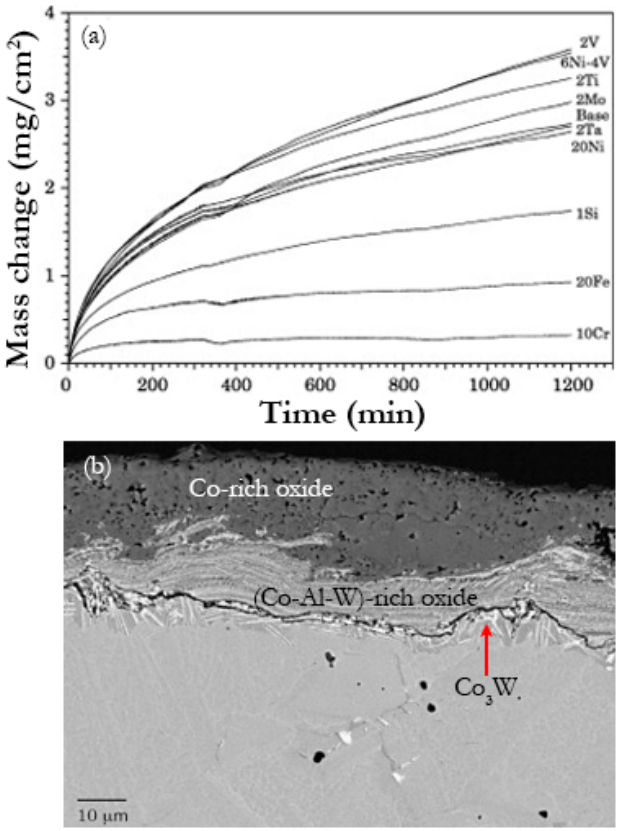


Figure 2.26: Isothermal oxidation of Co-7Al-7W (base alloy) at 800 ºC for 20 hours showing (a) plot of mass change data with other alloying additions in the base alloy (b) BSE image of the oxide scale formed in the base alloy. Figure adapted from [105].

Yan et al. also found that multilayer oxide scales were formed in Co-Al-W alloys containing chromium. The addition of chromium changes the morphology of oxide scale formation where multiple layers of oxides were formed instead of the typically formed cobalt-rich oxides, such as CoO and Co_3O_4, which are not protective. Three layers of oxides were found; the outermost layer was Al_2CoO_4, the middle layer was enriched in chromium and contained CrO_2 and Cr_2O_3, and the innermost layer was Al_2O_3. It is believed that these three layers adhere well to the substrate and each other at high temperature. These three layers also show low oxygen diffusivity and are protecting the alloys at high temperature.

2.6 Alloying of Co-Al-W Superalloys

Since the discovery by Sato et al., many groups have ventured into finding the optimum phase metallurgy in the Co-Al-W ternary system. Due to the similarity of nickel superalloys to this current study, the addition of alloying elements to the Co-Al-W ternary system is based on nickel base alloys research. In nickel base superalloys; titanium, vanadium, niobium and tantalum are the γ′ forming elements, which increase the γ′ solvus temperature and γ′ volume fraction. Whereas chromium, iron nickel, molybdenum and rhenium strengthen the γ matrix but may reduce the γ′ volume fraction [106].

2.6.1 Elemental effects on properties

There were many attempts to increase the γ′ solvus temperatures and volume fraction of the Co-Al-W system but these attempts required a sacrifice in terms of phase stability of the alloy. Figure 2.27 summarises the effect of alloying elements in various compositions of ternary Co-Al-W base alloy on the γ′ volume fraction and solvus temperature [24]. As the basic rule, the γ′ solvus temperature will increase when more aluminium and tungsten are added.

Although alloying additions have been shown to achieve a high γ′ solvus temperatures with stable microstructures following the findings by Sato et al. [5], few studies have been conducted to examine the influence of aluminium and tungsten in the Co-Al-W alloys on the γ′ volume fraction. By increasing the amounts of aluminium from 8.9 to 9.3 (at. %) and tungsten from 6.9 to 10.4 (at. %) in the Co-Al-W alloys, the volume fraction of the cuboidal γ′ precipitates increased from 20% to 80%, [5]. The size of the γ′ cuboids ranged from 100 nm to 200 nm, and the γ′ precipitates became agglomerated as the γ′ size increased [90]. However, tungsten is proven to form more γ′- Co_3(Al-W) phase than aluminium, due to the fact that aluminium has higher solubility in the matrix than tungsten [107]. Therefore, alloys with more tungsten than aluminum will more readily form stoichiometric γ′. Moreover, the volume fraction and solvus temperature increases as tungsten is added.

Similar to nickel-base superalloys, many researchers have attempted to develop the Co-Al-W alloys by adding the γ′ formers (Ti, Nb, Ta, V) to improve the γ′ volume fraction and solvus temperature [95], [108]. Tantalum is proven to increase the γ′ solvus temperature by up to 100 ºC, making it the second highest solvus temperature in Co-Al-W ternary system so far after iridium [103], [109]. Vanadium also develops the same effect but only in the Co-9Al-7W base alloy [110]. An adverse

effect of vanadium occurred in Co-9Al-10W alloy where both γ′ solvus temperature and volume fraction decreased [103], [109].

Meanwhile, other elements such as iron, chromium, nickel and rhenium decrease the γ′ volume fraction in the Co-9Al-7W alloy and have very little effect on the γ′ solvus temperature [110]. Refractory elements (Mo, Nb, Ta) are reported to form the TCP phase, μ (Co_7W_6) [95], [98]. The μ phase is reported to also contain the refractory elements from the matrix and has been shown to be unfavorable to high temperature performance because of its plate-like morphology [103].

Ooshima et al. [110] evaluated the efficiency of various elements (Fe, Cr, Ta, Mo, Ti, V, Ni, Nb and Re) in increasing the γ' solvus temperature. Based on the findings, all of these elements increase the γ' solvus temperature except for rhenium. Of all the investigated elements, tantalum was observed to be the most effective in increasing the γ' solvus temperature.

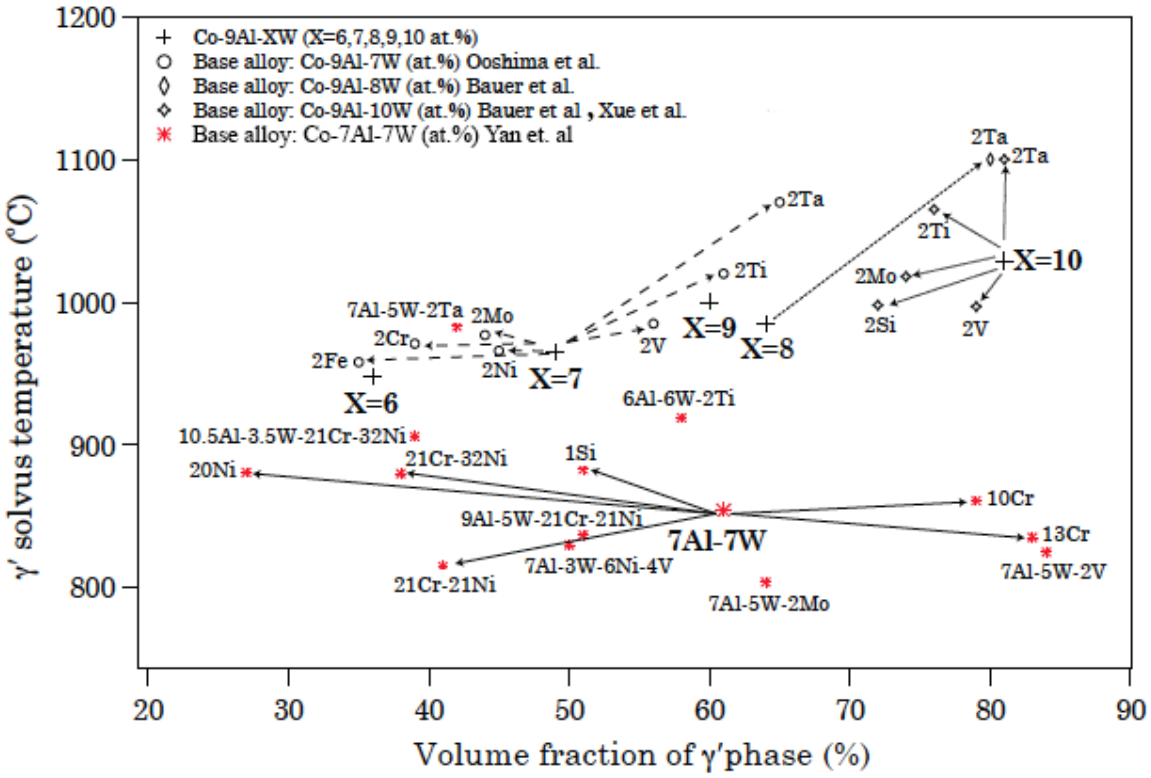


Figure 2.27: Effect of alloying additions and substitutions on the γ′ solvus temperature and volume fraction of secondary γ′, compared to the literature. Figure adapted from [24].

Shinagawa et al. [117] constructed phase diagrams containing 10, 30, 50 and 70 at. % of nickel. It was found that nickel increases the γ' solvus temperature and expands the γ' phase field and found a link between the typical γ'-Ni_3Al and γ'-$Co_3(Al,W)$. It was found that with an increase of nickel in the

quarternary Co-Ni-Al-W alloy, the phase field of γ/γ' also increases. It also shifts the tungsten content to lower atomic percentage, which is beneficial for the density of the alloy. Moreover, when nickel content is more than 50 at. %, no more tungsten is necessary to precipitate the γ' phase. This shows that the solubility of tungsten in the γ' decreases in the Co-Ni-Al-W alloy. Tungsten is more soluble in the matrix by transforming into a γ former rather than a γ' former. The results also show that nickel additions can restore the cuboidal microstructure when nickel content is less than 50 at. %.

Chromium additions are desirable, as the formation of Cr_2O_3 is usually protecting the surface from further oxidation. However, according to Yan et al., beyond 10 at. % of chromium decreases the γ' solvus temperature and the desirable morphology can no longer be achieved without the presence of unwanted secondary phase such as CoAl. Chromium addition is found to alter the morphology of the γ/γ' phase into elongated lamellae. It emerges that excessive chromium additions destabilise the γ/γ' microstructure, until at 23 at. % of chromium in the alloy was found with no γ' solvus [105]. The γ' solvus temperature is lowered by as much as 128 ºC when 21 at. % of chromium is added to the base alloy.

Since the addition of nickel altered the γ' solvus temperature and stabilised the microstructure [105], the possible cobalt-nickel quartenary alloy becomes significant by allowing more chromium to be added in the alloy system for oxidation resistance. It is therefore, worth performing more studies to gain the optimum ratio of chromium in the cobalt-nickel alloy without compensating the microstructure.

2.6.2 Summary of alloying additions effects on Co-Al-W superalloy

A summary of different alloying effects in cobalt-base superalloys is classified as below. Note that the range of addition of each element is the minimum and maximum amount compiled from previous studies of Co-Al-W ternary alloy system as indicated in the reference.

Tungsten (3.5 - 10.7 at. %) - The γ' solvus temperature and the γ' volume fraction increases as the amount of tungsten increased. However, an increasing amount of tungsten will greatly increase the density of the alloy and form the undesirable intermetallic phases like Co_7W_6 and Co_3W [12, 14, 16]. A recent study by Yeh et al. [111] has found that a low tungsten content (approximately 5 at. %) allows the formation of alumina above 1000 ºC whilst high tungsten content (10 at. %) slows down the oxidation rate at 900 ºC.

Aluminium (6.0 – 10.5 at. %) - Aluminium is a major constituent of the γ' phase and also forms a continuous and protective Al_2O_3 film on the material surface, which can increase oxidation resistance at high temperatures. The amount of aluminium should not be too high as it promotes the formation of CoAl, ß-phase with B2 crystal structure [12, 17].

Chromium (2.0 – 21.0 at. %) - According to Sato et al. [5], chromium partitions to the γ phase. Hence, chromium leads to decreasing γ/γ' volume fraction and γ/γ' lattice misfits. Also, addition of 16 at. % of chromium decreases the γ' solvus temperature as reported by Bauer et al. [112]. The content of Cr has to be balanced with elements capable of increasing the γ' solvus temperature such as nickel [105].

Nickel (9.0 – 32.0 at. %) - Yan et al. [95] added nickel into the Co-Al-W-Cr alloys to allow higher chromium additions to be made without destabilising the γ/γ' microstructure. Also, it has been found in the same study that an increasing amount of nickel decreases the lattice misfit. Klein et al. [99] has reported that the addition of nickel to increase the γ' solvus temperature seems to be inappropriate due to the low oxidation resistance. According to them, adding nickel leads to higher mass gain and oxide layer thickness.

Titanium (2.0 – 4.0 at. %) - Similar to nickel base superalloys, titanium partitions to the γ' phase, which increases the γ' solvus temperature and the volume fraction and therefore enhances the mechanical properties at high temperatures [98], [103], [108].

Iron (2.0 – 20.0 at. %) - Iron has a destabilising effect on the γ/γ' microstructure, it decreases the γ' volume fraction by partitioning to the γ phase. Both Bauer et al. and Yan et al. [95], [112] reported that after 16 at. % of iron, alloys not contain the γ/γ' microstructure at all and the oxidation behaviour is very poor.

Tantalum (0.2 – 2.0 at. %) - Addition of tantalum is effective for stabilisation of the γ' phase as tantalum partitions more strongly to the γ' phase and increases the volume fraction of γ'. It is reported to have the best solvus temperature, 1100°C after iridium [110]. However, Klein et al. [98] found that 2 at. % of tantalum impairs the oxidation resistance of the alloy, much less Al_2O_3 can be detected in the inner oxide layer [5], [95], [108], [110], [112].

Silicon (1.0 - 2.0 at. %) - Silicon enhances the oxidation resistance at elevated temperatures, above 900 °C, not only because of SiO_2 formation but also due to the beneficial effect of silicon on the formation of protective Al_2O_3. Silicon that precipitates at the matrix and grain boundaries may also act as diffusion barriers. According to Klein et al. [99], addition of 2 at.% of silicon enhances the oxidation resistance and slightly increases the γ' solvus temperature as well as the γ' volume fraction.

Boron (0.04 – 0.32 at. %) - Boron is an element that can be included to strengthen grain boundaries of the cobalt base superalloys. Higher contents of boron can be important, and in some cases critical, as they can lead to undesirable boron dispersions that can have an embrittling effect. Boron is generally segregated in the γ phase grain boundaries and contributes to the improvement in the high temperature strength of the alloys. Klein et al. [94] found the formation of boron-rich phases at grain boundaries and in the inner oxide layer, which greatly improves the oxide layer adhesion.

Niobium (2.0 – 4.0 at. %) - Niobium is added to increase the γ' solvus temperature of Co–Al–W base alloys [103], [110]. This element has a common characteristic of being a γ' forming element that increases the volume fraction of the γ' phase. Klein et al. [98] added niobium to improve the mechanical properties of Co-Al-W alloys, but the addition of niobium is reported to yield a very thick oxide layer due to cracks after oxidation at 900°C.

Molybdenum (1.0 – 4.0 at. %) - According to Suzuki et al. [113], molybdenum is added as a solid solution strengthener in the cobalt matrix and it also promotes stability to the γ' phase. Molybdenum can, for example, influence lattice dislocations between the γ matrix and the γ' phase and the morphology of γ' under creep loading. Recent studies by Yan et al. [95] and Klein et al. [98] shows that molybdenum does not promote good oxidation resistance in the Co-Al-W as the thickness of oxide layer is reported to be more than 100 μm.

Iridium (2.0 at. %) - According to Bauer et al. [112], the addition of iridium is proven to increase the γ' solvus temperature to 1137 ºC, the highest of all, possibly due to the fact that the melting temperature is 2446°C, but discontinuous precipitation at grain boundaries takes place and the whole γ/γ' microstructure is transformed into lamellae of Co_3W and CoAl.

2.7 Concluding Remarks

This literature review has revealed a few key components in gas turbine engine including the requirements for materials used in the current climate. Nickel base superalloys are extensively used in most of the components that require high temperature applications. Hence, there is the need to develop this current alloy or find the new alternative to replace the increasing demand in the aeroengine industry.

This chapter also presents the preferred processing route for disc manufacturing. The powder metallurgy route was chosen and will be used throughout this research to eliminate segregation during rapid solidification, which will then lead to good mechanical properties. In addition to that, the phases of carbides were also discussed, and previous studies have shown that the precipitation of carbides starts from the as-atomised state and further continue to develop in the later HIP stage. Therefore, it is very important to identify and control the types of carbides that could be detrimental to the alloy. It is worthwhile to carry out any new methods of eliminating or controlling the amount of carbide precipitates by tailoring the microstructure using different HIP temperatures.

A large part of this literature review discussed the isothermal oxidation in nickel base superalloys via mass gain route. Most of the literature utilised mass gain experiments to obtain the oxidation kinetics. However, there is no clear indication of the mechanism of oxide formation (anions and cations transport in the alloy during high temperature oxidation). The use of isotopic oxidation in combination with FIB-SIMS analysis was excellent in evaluating the transport mechanisms in previous studies. It is therefore regarded as the most suitable method, which will be utilised in this study. The same goes to FIB cross sections. Instead of measuring the mass gain in each oxidised sample, the oxide thickness and sub-surface damage will be utilised in this study in order to gain a more accurate comparison of the extent of damage in a certain alloy.

The discovery of Co-Al-W ternary γ/γ' alloy has opened a new venture on finding the suitable compositions as well as understanding its behaviour. It is a promising alloy and could be the next generation material for polycrystalline disc alloy. However, various issues have to be addressed in this alloy system, for example, the density. The density is very high compared to nickel base superalloys due to tungsten. The first few oxidation results also proved lacking, as the oxide thicknesses were very substantial and some cases of spallation also occurred. It is known that nickel gives a very positive effect on this ternary system. The same goes for niobium and titanium. Chromium has to be added in a careful amounts to increase the oxidation resistance but at the same time not too much to destabilise the microstructure. The basis of this current study has been established and the detail investigations will be discussed in the next chapters.

3 Materials and Characterisation Techniques

3.1 The V208 Alloys Series

The V208 alloys series are classed as experimental alloys and are early development alloys with a target operating temperature greater than 800 °C and an entry into service 10 years in the future.

3.1.1 Materials and specimen

The alloy powder was manufactured by vacuum induction melting and inert gas atomisation by ATI Powder Metals, Pittsburgh, PA, USA. It was sieved using 270 mesh - 53 μm and then consolidated by hot isostatic pressing (HIP) for 4 hours at 1050 °C by ATI Powder Metals, Pittsburgh, PA, USA. The compositions of the V208 alloys are shown in Table 3.1. The alloys were subsequently removed from the cans and each billet was cut into two cylindrical pieces, each 75mm in diameter and 75mm high. They were then isothermally forged at 1050 °C by ATI Ladish Forging, Cudahy, WI, USA. Alloys V208A and V208B were reduced to 30 mm whereas V208C and V208D were reduced to 15mm. After forging, the material was subjected to a heat treatment of 1050 °C for 30 minutes, above their respective γ' solvus temperatures with a subsequent aging step at 900 °C for 16 hours. Several different cuboidal blanks were cut from the forgings using electric discharge machining (wire EDM) from which the samples for the various tests were machined as shown in Figure 3.1.

Table 3.1: Measured compositions of the V208 alloys series in at. %

Alloy	Co	Ni	Cr	Al	W	Ta	Ti	Nb	C	B	Zr
V208A	42.03	31.93	11.78	9.86	3.04	0.98	-	-	0.13	0.20	0.04
V208B	33.66	32.15	17.36	12.45	3.06	0.99	-	-	0.11	0.18	0.04
V208C	36.08	34.24	14.81	10.49	3.04	0.95	-	-	0.15	0.20	0.04
V208D	39.71	29.38	17.04	9.53	3.04	0.95	-	-	0.15	0.17	0.04
V208E	40.43	29.00	15.14	9.99	2.77	0.81	1.53	-	0.11	0.17	0.04
V208F	40.97	30.04	14.92	9.56	2.34	0.74	-	1.08	0.14	0.16	0.04

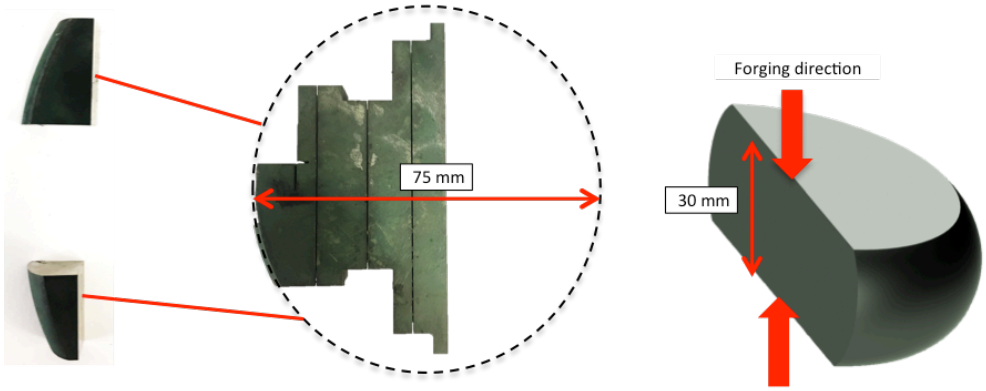


Figure 3.1: Blanks specimens cut from a pancake using wire EDM (left) and forged pancake showing the forging directions to the final thickness (right).

3.1.2 Sample preparation for oxidation experiments

The samples for the oxidation experiments were cut to 5 by 5 by 5 mm using silicon carbide blades on a Struers Accutom 50 saw. After cutting, the top surface of each sample was ground with a series of silicon carbide grinding papers with increasing grit sizes (from 200 to 2000 grit sizes) using a Struers Tegrapol-15. Sharp edges were chamfered at approximately 45° by about 0.5 mm on all edges and corners. Then the same surface was polished with appropriate polishing pads containing diamond paste starting from 6 μm to 1 μm finishing to achieve a highly polished surface. The length, width and height of each sample were measured using a micrometer (accuracy up to 0.001 mm). The weight of each sample was measured using a micro balance (accuracy ~ 0.01 mg) before and after the experiment. Then the samples were thoroughly cleaned with acetone in an ultrasonic cleaner for 5 minutes and dried by blowing with compressed air.

3.2 The Two-Stage Oxidation Experiments

This research project was based on the two-stage oxidation experiment utilizing oxygen isotopes for tracer studies [69], [114], [115], which involves an isotopic oxidation experiment involves exposing a specimen initially under a conventional $^{16}O^-$-enriched gas and later in the last 24 hours, $^{18}O^-$-enriched gas was introduced. The ^{18}O acts as a tracer species, which is detectable by SIMS and distinguishable from the ^{16}O. The transport mechanisms can then later be extracted through the counts of each species in the internal and external oxide regions.

3.2.1 Isotopic oxidation experiments

Oxidation experiments were carried out in an isotopic exchange oxidation rig. The samples were placed in-line on a quartz crucible in a quartz tube, which was then evacuated to a pressure of less than 5 x 10^{-7} mbar. In order to examine the mechanism of oxide formation, two-stage experiments were carried out using oxygen-18 ($^{18}O_2$) at a partial pressure of 0.2 atm. The samples were first exposed in research-grade oxygen (99.9995%), (referred to as $^{16}O_2$) at pO_2 = 200 mbar (0.2 atm). This is to simulate the partial pressure of oxygen in air. After programming to the correct temperature and ramp rate, the tube furnace is rolled on, ensuring that the sample sits in the hot-zone of the furnace, and is finally sealed with ceramic fibre at both ends for insulation. The exchange furnace was then evacuated before introducing the $^{18}O_2$-enriched oxygen also at pO_2= 200 mbar directly from the bottle into the annealing chamber. The samples were then fast-cooled in air by rolling off the exchange furnace before recovering the $^{18}O_2$ gas. Later, the samples were taken out of the quartz tube along with the crucibles, which contain any spalled oxide. Care was taken when removing the samples from the tube to avoid damage to the oxides. Figure 3.2 shows a schematic of the apparatus used to carry out isotopic oxidation experiments. The importance of recovering the $^{18}O_2$ is due to the high cost of the gas. A platinum thermocouple, placed next to the sample, connected to a PC with a data-logging system continually monitors the temperature. The data-logger records the temperature and the pressure over two-second time intervals for the duration of the exposure.

Generally, the tracer element $^{18}O_2$ gas diluted with each use and for the present experiments the level of $^{18}O_2$ gas was approximately 54%. An example of a similar experiment to study the concentration of $^{18}O_2$ gas was conducted by Ooi [115], where a silicon wafer was used as a substrate, heat treated at 1150 °C for 3 hours. FIB-SIMS was then used to determine the concentration of $^{18}O_2$ in relation to $^{16}O_2$.

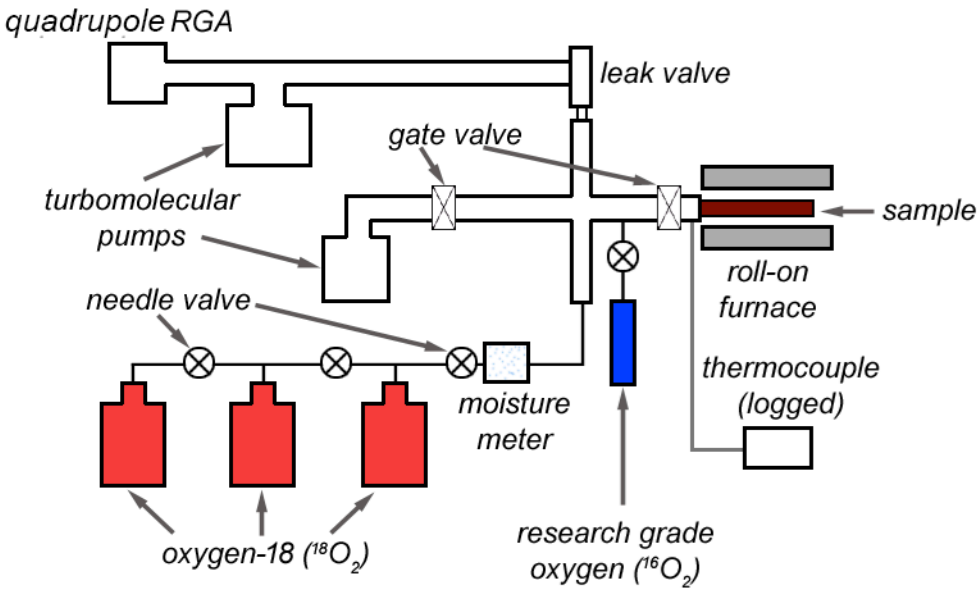


Figure 3.2: Schematic diagram of the isotopic exchange furnace used in isotope exchange experiments-Figure adapted from Alibhai [116].

The sequence of the two-stage oxidation experiment is shown in Figure 3.2, where the first stage is varied from 200 hours to 300 hours but the second stage was always 24 hours. In order to have sufficient $^{18}O^-$ signal generated during the SIMS study, the second stage should be long enough to show the effect of $^{18}O_2$ as a tracer. However, it should not be so long as so as not to exceed the number of hours used in the first stage of oxidation during the experimental design.

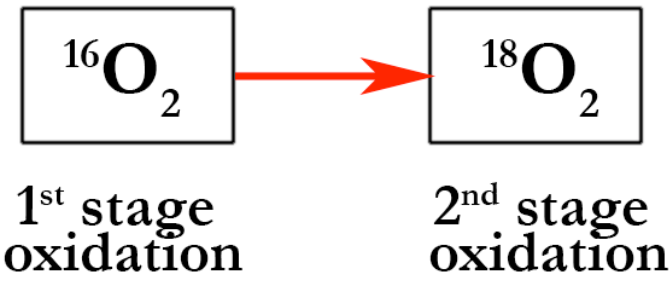


Figure 3.3: The sequence of a two-stage oxidation experiment.

3.2.2 Heating and cooling rate

The preliminary oxidation tests for all V208 alloy samples were performed at 800 ºC for 200 hours. The temperature was chosen in order to assess high temperature oxidation of next generation alloy for disc applications. As previously mentioned, the oxidation tests were carried out in a two-stage oxidation experiment, where the tracer oxygen was introduced in the last 24 hours. Figure 3.4 explains the cycle where the two-stage oxidation experiments were carried out. Temperature rapidly increased to 800 ºC when the quartz tube entered the roll-on furnace. The temperature usually reached the target after 5 – 10 minutes as measured by a thermocouple placed just 3 mm from the sample boat in the reaction tube. After 176 hours, the furnace was rolled back from the reaction tube thereby rapidly cooling the sample in air. The reaction tube was then re-evacuated before allowing the $^{18}O_2$-enriched gas to fill the annealing chamber. Then, after 24 hours of oxidation in oxygen-18, the sample is again rapidly cooled in air. The $^{18}O_2$ gas in the reaction tube was then recovered back due to the high cost price of the gas. The thermocouple was connected to the PC with a data logging system that continually monitors the temperature. The same sequence follows in the exchange rig for oxidation temperature at 850 ºC for 200 hours.

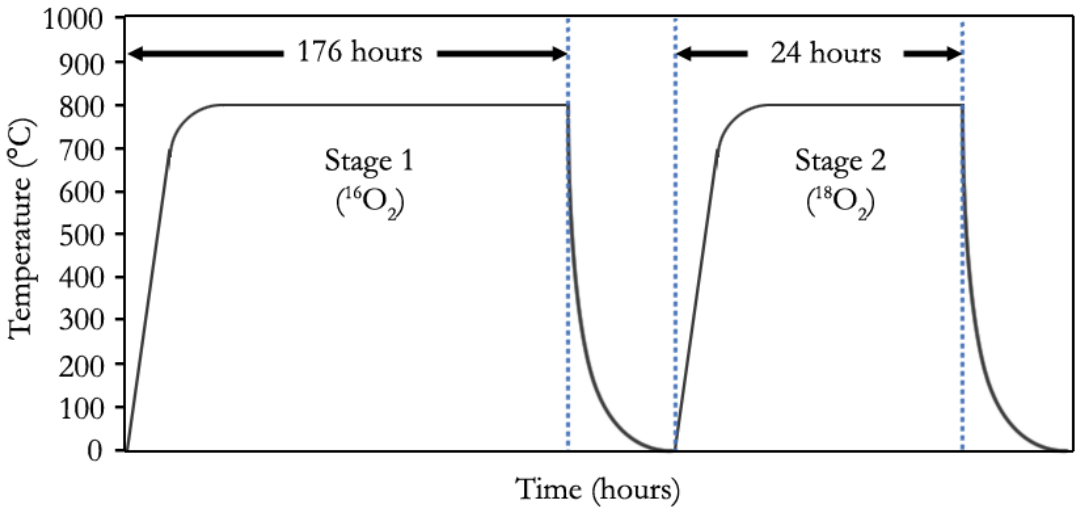


Figure 3.4: The temperature profile during the two-stage oxidation experiment.

3.2.3 Long-term oxidation in air

Long-term isothermal oxidation experiments were carried out on the V208 series alloys in order to establish the specific alloy, which had good oxidation resistance and stable underlying microstructure. V208 C was selected to undergo oxidation tests in air to study the stability of oxides at long-term exposures. The oxidation temperature was set at 800 °C and the samples were oxidized in a box

furnace under atmospheric conditions for 400, 1000 and 2000 hours. The samples were placed in alumina crucibles and were taken out from the furnace and exposed to laboratory air.

3.3 The Two-Stage HIP Process for the As-Atomised Powder

As part of the next generation alloy production for disc applications, a particular V208 alloy (V208 A) was subjected to characterisation throughout production, starting from powder particles analysis of the carbides and prior particle boundaries (PPB). The two-stage HIP process was performed in the laboratory to match the actual powder processing by ATI Powder Products, Robinsons, US. The as-HIPed powder particles were then analysed in the FIB-SEM to obtain a cross-sectional view of the particles, STEM EDX for particles' chemical compositions, and TEM analysis for the morphology of carbide particles. The as-received powder particles were manufactured by vacuum induction melting and inert gas atomisation (sieved using 270 mesh – 53 μm). Figure 3.5 shows typical surface features of V208 A powder particles.

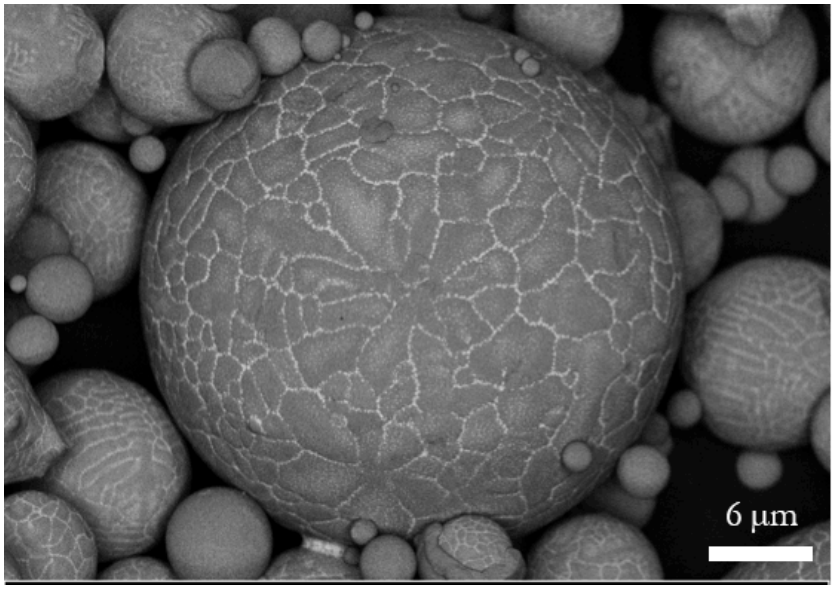


Figure 3.5: Initial microstructure of powder particles with dendritic structure and satellite particles viewed in EsB-SE mode.

3.3.1 Two-stage HIP

The two-stage HIP was performed in a vacuum furnace in argon atmosphere at temperatures shown in Figure 3.6. The powder particles were placed in an alumina crucible prior to heat treatment at 900 ºC for 4 hours and then ramp up to 1050 ºC for another 4 hours. At each stage, small samples were studied by obtaining a cross-section view using FIB-SEM to study the evolution of internal particle

structure (carbides and PPB) during the two-stage HIP. STEM EDX was performed to study the carbides in the interdentritic regions.

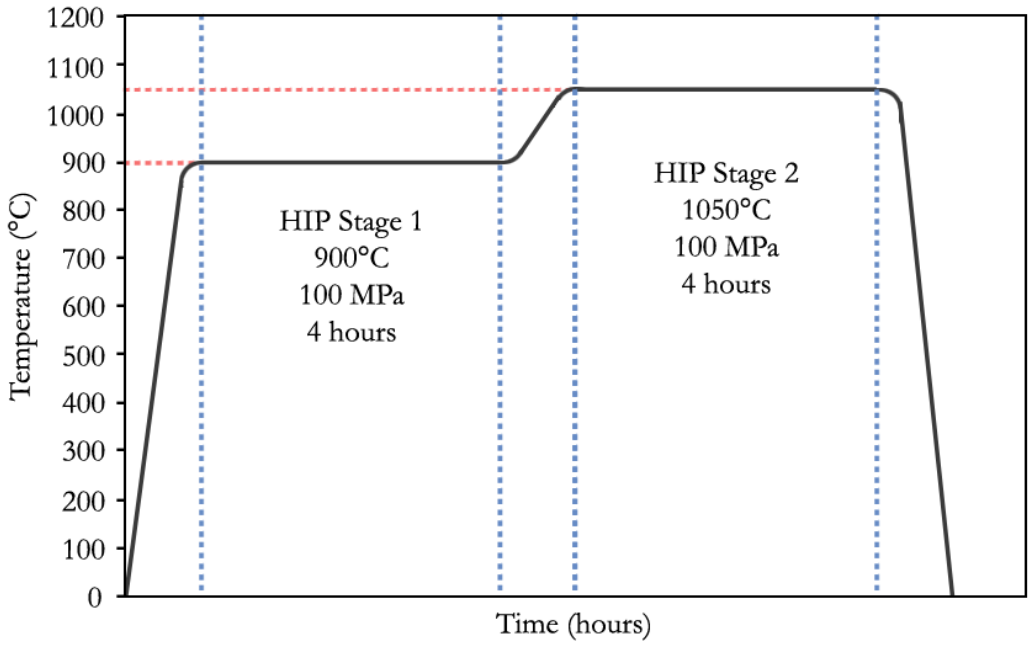


Figure 3.6: The two-stage HIP performed on alloy V208A powder particles.

3.4 Effect of Shot-Peening on Oxidation

The selected V208 alloys with varying amounts of chromium and aluminium (V208 B – D) were further investigated for oxidation resistance under surface stress at a higher oxidation temperature (850 ºC). The alloys were selected due to their superior oxidation resistance and stable underlying microstructures. The samples for oxidation were prepared by cutting 10 x 20 x 5 mm pieces using Struers Accutom precision saw. After mounting in Bakelite, two surfaces (10 x 20 mm) of each sample were ground with a series of silicon carbide grinding papers with increasing mesh sizes (starting from 200 to 2000) using a Struers Tegrapol-15 followed by polishing using a 1µm diamond suspension. The samples were broken out from the Bakelite and the edges were chamfered. The samples were sent to the Metal Improvement Company, Derby, for shot-peening to a specification of 6 – 8 Almen intensity using 110H cast steel shot, to 200% coverage by a conventional nozzle set-up. The samples were cleaned with acetone and soft-tissue to remove any contamination. A two-stage oxidation experiment was carried out at 850 ºC for 200 hours as described in Section 3.2.2 above. Both surfaces (polished and shot-peened) were examined under FIB-SEM and FIB-SIMS to identify any effect of shot-peening on oxidation.

3.5 Scanning Electron Microscopy

The microstructure and the chemical composition of the samples were examined using a Zeiss Auriga scanning electron microscope equipped with an Oxford Instruments EDX detector. The morphologies of the oxide surfaces were characterised using secondary electron mode (SE). A thin platinum strip with dimensions of 25 x 2.5 x 1.5 µm was deposited on the surface of each of the oxidised samples prior to milling. Trenches milled using a focused ion beam (FIB) were viewed in energy selective backscatter (EsB) mode at 36° relative to the sample surface viewing angle. The viewing angle was then corrected during imaging by opting for tilt correction in the user interface. SE mode was chosen to capture microstructure at 1.48 kV acceleration voltage at a working distance of 5 mm. EsB mode was used to identify different phases via atomic mass contrast with 1.48 kV acceleration voltage. All chemical analyses of the samples were performed using EDX in the SE mode using a 15 – 20 kV acceleration voltage. To improve experimental accuracy, each spectrum was collected from at least 5 points.

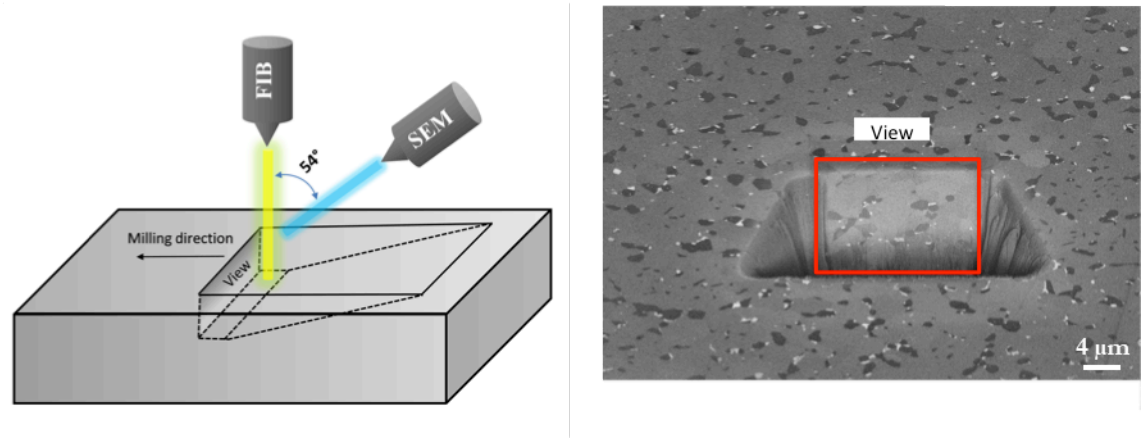


Figure 3.7: Schematic of a trench FIB milling (left) and a microstructure of a trapezium-shaped crater (right) in secondary electron mode using a FIB-SEM (Auriga 40).

3.5.1 FEG-SEM with EDX

Most of the V208 alloy series exhibit a fairly thin oxide layer of sub-µm scale oxide layer (see Chapter 4), which was examined using a conventional metallographic sample preparation (cutting, mounting, grinding, polishing). Unfortunately, this procedure can damage the scale by removal of oxide. Moreover, the surface features of the oxide layers were difficult to relate to a specific area of interest. Therefore, in this thesis, all of the oxidised samples were examined by using focused ion beam milling to produce cross-sections normal to the surface of the sample.

A focused ion beam FEG SEM (Zeiss, Auriga 40) was used to mill cross sections normal to the sample surface to examine the near surface microstructure and oxide film to identify any correlations with specific surface features (see Figure 3.7).

In this system, the sample was put on a holder and adjusted to the eucentric height, at which point the focused area was maintained independent of the stage tilt. The coincidence location between the ion and electron gun was achieved using manipulation of beam shift to image the same area in both SEM and FIB mode. Subsequently, a platinum strip was deposited on the area of interest to prevent the top surface from damage induced by ion milling. The sample was tilted to 54 degrees so that the FIB is perpendicular to the sample surface for milling. The first milling of the trench was performed at 4 nA ion beam current and then the current was reduced to 1 nA to obtain a neat trench.

In general, a trapezium-shaped crater was first formed next to the platinum strip to prevent the re-deposition on the crater walls during milling (Figure 3.8) with a typical milling condition of 30 kV and 4 nA. The resulting rough cross-section was polished with a low-current beam (in the range of 600 pA and 240 pA at 30 kV) to achieve a smooth wall surface. This smooth wall of the crater was imaged using conventional imaging in the SEM (SE, BSE, in-lens SE), as well as low-energy back scattered mode that offered compositional imaging at low accelerating voltage, ideal for non-conducting oxides. Imaging was performed at 36° from the surface as shown in Figure 3.8. Since the viewing is at an angled position, tilt correction must be applied to stretch the images to their true vertical field height.

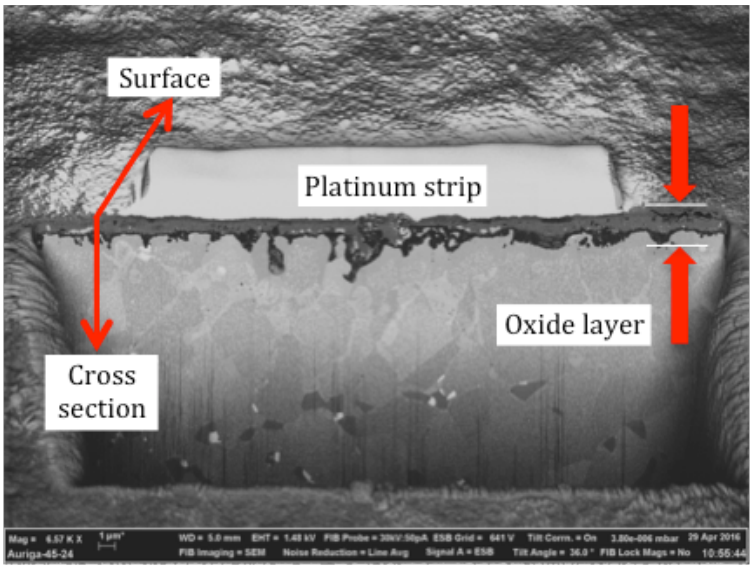


Figure 3.8: A trench of an oxidised sample viewed in BSE mode showing the platinum strip on the surface protecting the oxide scale.

3.5.2 Quantification of Oxidation Products - The Damage Depth Analysis

A typical method which was commonly used for quantifying the oxidation performance of nickel-base superalloys is to measure the mass gain. However, previous work has suggested that damage depth resulting from oxidation is more appropriate in evaluating the influence of oxidation on mechanical performance [65], [117], [118].

Figure 3.9 shows the schematic of a cross section of the oxidised samples with major oxidation damage characteristics near the surface. The outermost layer which is usually referred to as the surface oxide, is labeled as oxide scale, followed by the oxide alloy interface region, called the oxide intrusion and lastly the γ'-depleted zone. The thickness of the damage layers was evaluated as an average value of the thicknesses measured across each area. A number of measurements were taken from at least two cross-sections to provide an average value of thicknesses as well as areas using the open source software ImageJ. All measurements were obtained from a BSE image, which has a distinct benefit of showing specific oxide scales in terms of their atomic mass contrasts.

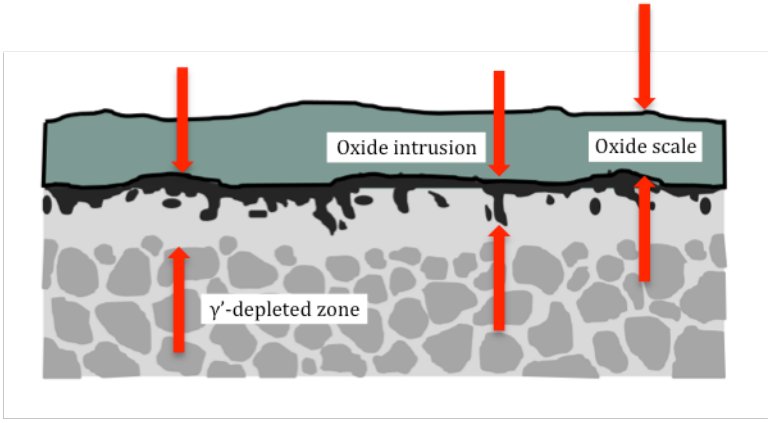


Figure 3.9: Schematic of the damage depth analysis on cross-sections of oxidised samples.

An example of quantification of internal oxide area was completed in BSE mode using ImageJ as shown in Figure 3.10. First, the external/internal oxide is carefully traced in EsB mode in SEM. Then the image threshold is adjusted to match the desirable phase contrast (regions shaded in red). Later the image is converted into 8 bit/16 bit before being converted into binary. Then finally the sum of pixels in the shaded region is calculated to provide the area. This method is applied to each layer of oxide with similar contrasts.

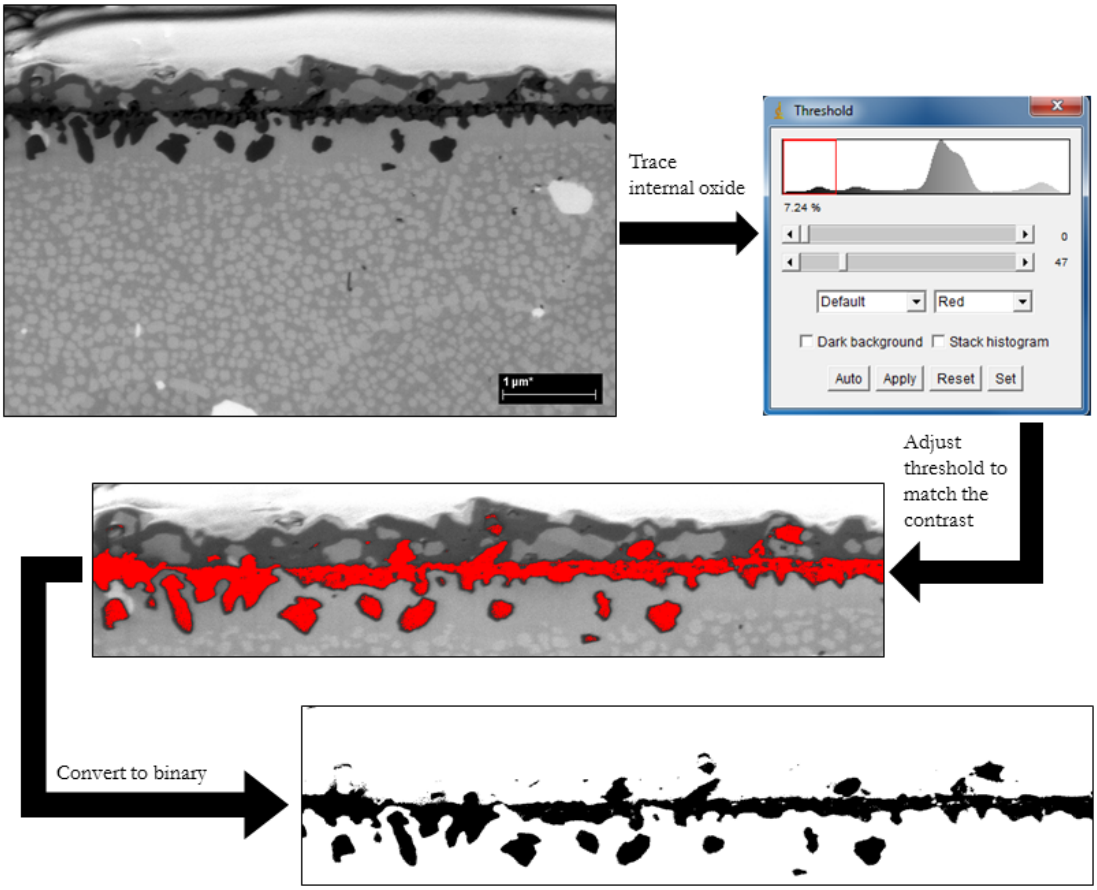


Figure 3.10: Schematic of the process to determine the internal oxide area beneath the external scale.

3.5.3 Energy-selective Backscatter (EsB) mode in FIB-SEM

A specific advantage of the crossbeam FIB-SEM (Auriga 40) is that imaging and sample preparation on a nanoscopic scale is possible. A live cross-section milling and imaging is useful to view the morphology of the phases in 3D using slice and view mode.

The energy selective backscatter (EsB) only allows a specific energy band of backscatter electrons to be selected for imaging. In this case, an energy filtering grid located at the front entry system was adjusted in its potential range from 0 to 1500 volts. When the electrons passing the grids, only backscatter electrons with energies greater than the grid can be detected. Moreover, the threshold voltage at the filtering grid can also be set to reject electrons with specific energies.

The Energy selective Backscattered (EsB) Detector fitted in Auriga 40 is suitable for clear compositional contrast. It is an annular shaped in-column detector that is located above the In-lens detector as shown in Figure 3.11. The ability to detect BSE makes sub-surface information and nano-

scale composition visible. To prevent detection of secondary electrons, a filtering grid is installed in front of the EsB detector.

By switching on the filtering grid voltage, the secondary electrons will be rejected and only BSE will be detected. Below the energy of 1.5 kV, the filtering grid has the additional function of selecting the desired energy of the BSE. This means the threshold energy of inelastically scattered BSE can be selected to enhance contrast and resolution.

The benefits of using the in-lens BSE detector are sub-surface information is visible. Additionally, the low kV BSE imaging is able to examine non-conducting samples without the need for conductive coatings.

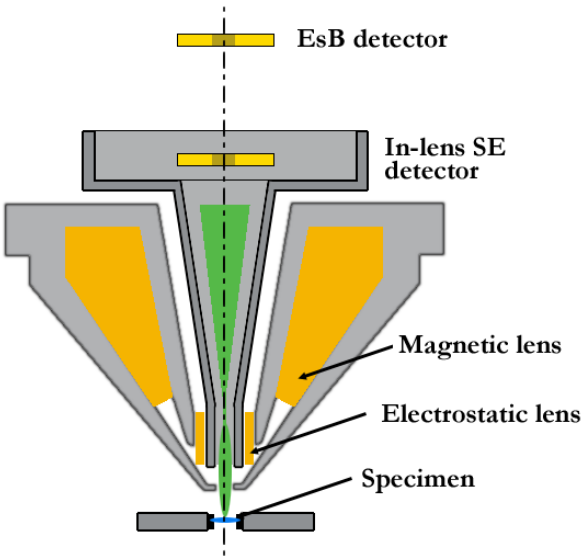


Figure 3.11: A schematic diagram of a cross-section of the electron optical column in the Zeiss Auriga 40.

Figure 3.12 shows the non-linear behavior of the backscatter coefficient, in which below an incident energy of approximately 5 keV, the extent of the reduction in high atomic number elements is stronger than for the elements with low atomic number [119].

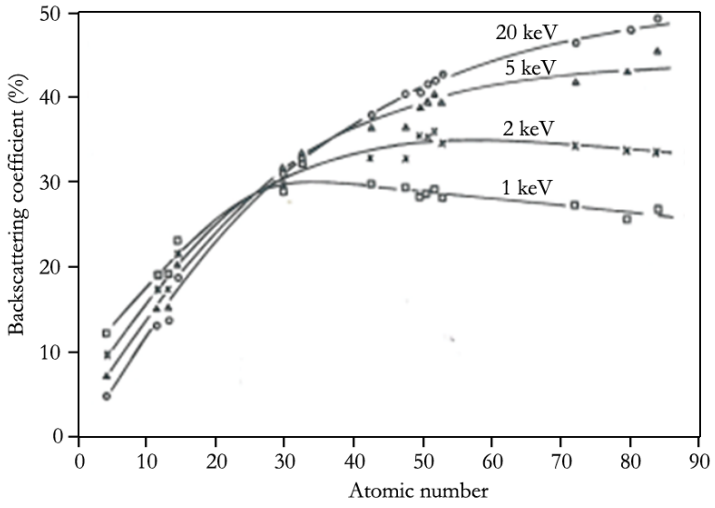


Figure 3.12: The backscattering coefficient as a function of atomic number (Z) in the range of 1-20 keV electron energies. Figure adapted from [119].

The brighter contrast represents the high Z elements whilst the darker contrast arises from the low Z elements below the incident energy of 5 eV. Additional lenses and beam boosting is required at these low voltages to amplify the resulting electron signal and to maintain the brightness of the electron probe.

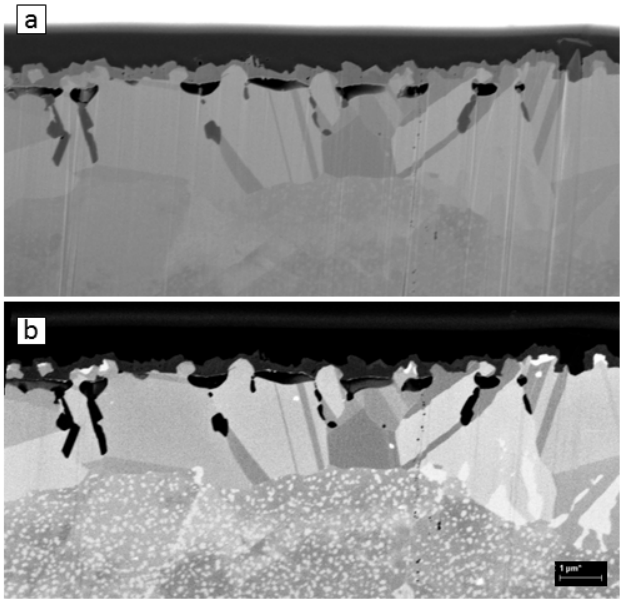


Figure 3.13: Cross-sectional microstructure of the thin oxide scale formed on an oxidised sample (exposed at 850 °C in vacuum atmosphere for 200 hours) acquired at the same area: (a) secondary electron mode and (b) EsB mode.

Figure 3.13 shows clearly the microstructure of the high Z contrast γ' precipitates underneath the oxidised surface in EsB mode. These $Co_3(Al,W)$ precipitates were unable to be observed in the general SE mode due to the small difference in compositional contrast. In addition to that, the conventional BSE mode will not give the same contrasts as a result of poor signal-to-noise ratio due to the interaction volume of high energy electrons produced at high accelerating voltage. Therefore EsB is a much more powerful tool to distinguish a microstructural feature with a smaller compositional contrast through adjusting the energy slit range of emitted BSEs from the sample.

3.6 Focused Ion Beam (FIB) Techniques

The FIB technique is used for high resolution SIMS work on the oxide scale grown on the surface of the alloy; it uses a fine beam of positive gallium ions. It is well known that the FIB imaging is largely different than the SE images from the SEM. The advantage of FIB with SIMs for this study is gained from the mass transport mechanisms in the oxide scale grown on the alloy. The results will be described later.

3.6.1 Overview of instrumentation

The basic setup of the FEI FIB200-SIMS microscope is shown in Figure 3.14. The production of the primary ion beam comes from a Ga^+ liquid metal ion gun (LMIG) with a beam diameter of 5nm, suitable for milling and imaging. Ga^+ is excited and emitted through an aperture to achieve an appropriate beam current which varied from 1 pA to 20 nA, affecting the image resolution. Generally, low beam currents are used for imaging and high currents are used for milling or sputtering. The beam strikes the surface of sample in a high vacuum chamber (10^{-7} mbar), and secondary electrons and ions are emitted from the surface as shown in Figure 3.15. It is crucial to note that the ability to perform in-situ microscopy and SIMS without having to remove the sample from the vacuum between the two gives this technique a significant advantage. Secondary electrons sputtered from the sample surface yield high-resolution images whilst secondary ions will give information of mass spectra, depth profiles and secondary ion images.

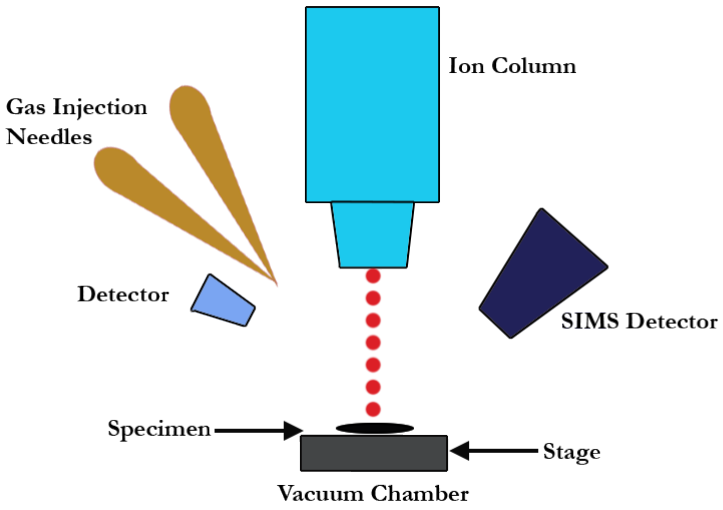


Figure 3.14: Schematic of the basic setup of the FEI FIB200-SIMS.

Bombarding with Ga+ on a sample surface will provide sputtered secondary ions and electrons accompanied with atomic scale erosion on the sample surface. As shown in Figure 3.15, the incident beam will strike the sample surface, producing a series of elastic collisions. The atomic displacements from the bombardment cause ejection of an atom as a sputtered particle. In general, the number of sputtered particles will increase with the number of collisions taking place closest to the surface. It is crucial to note that not all collisions remain elastic and secondary electrons will be ejected which are beneficial for imaging. The ejected ions can be positive, negative or neutral ions. The effectiveness of the primary ion beam to sputter charged particles is known as the ionization yield [71], [120]. The depth of ion penetration will affect the sputtering rate, in other words, less sputtering takes place if the ions penetrate deeper into the sample. This is proven by denser materials having greater stopping power, which therefore possess higher sputtering yields [121].

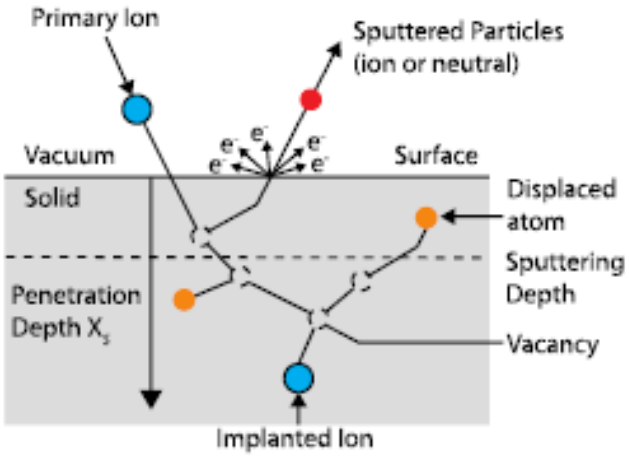


Figure 3.15: Schematic of the sputtering process in FIB-SIMS. Figure adapted from [122].

3.6.2 Alloy cross-section preparation by FIB

The surface roughness due to the ion beam milling will limit the resolution of the oxide scale thickness particularly in samples with thin oxides. Therefore, to overcome this limitation, a tapering of oxide method called the bevelling method was used to characterise thin oxides. The bevelling method was performed via cross sectioning using FIB milling at a steep angle (typically at 60º). Tapering of the oxide scale produced elongated oxide layers, which allows more accurate analysis to be performed. Figure 3.16 illustrates the schematic of how milling at an angle exaggerates the true thickness (x_{true}) of the oxide scales.

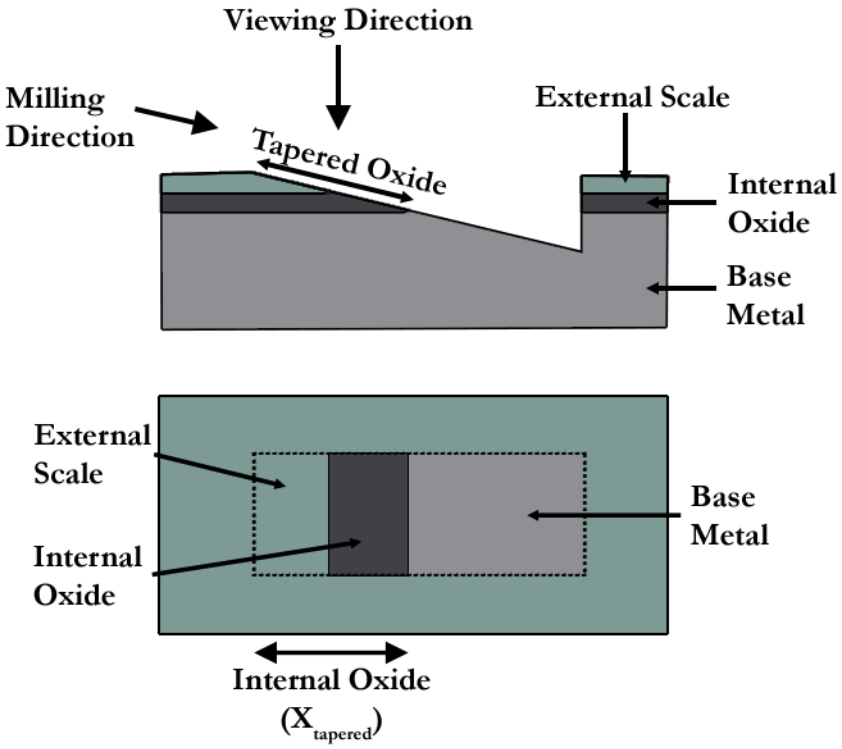


Figure 3.16: Schematic of the FIB bevelling method used in the preparation of cross-sections for oxidised samples.

Essentially, the tapered oxide thickness viewed at zero tilt angle is tangential from the true thickness. Equation 3.1 simplifies the relationship:

$$X_{true} = X_{tapered} tan\theta \qquad \text{Equation 3.1}$$

The tangential oxide scales created using the FIB is important during the SIMS mapping by increasing the quantity of data collected in the oxide scale region, especially for low counts of oxygen-18. Since the kinetics were the slowest in most of the V208 alloy series at 800 ºC for 200 hours, the exaggeration of the true oxide scales which are typically less than a micron thick is necessary.

The preparation of cross-sections are normally started by milling a 60 x 40 μm ramp at an angle 60º from the surface using a 20 nA beam current. Subsequently, for polishing, a low beam current was used (1 nA) to produce a smooth crater. The thickness of the oxide layer will stretch out typically by a factor of 4 from the true thickness.

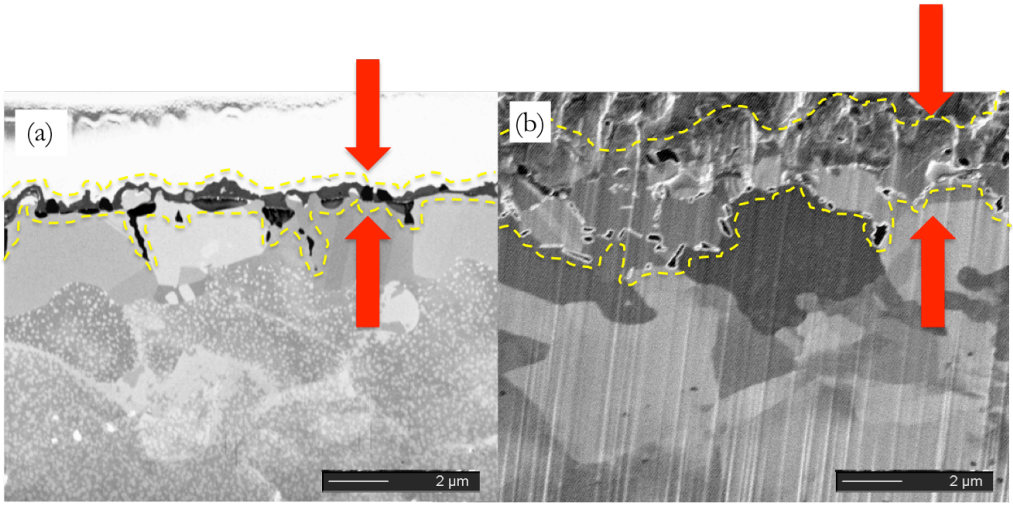


Figure 3.17: Cross-section microstructure of a thin oxide scale for (a) typical SEM image of a true oxide scale and (b) tapered oxide scale at 60° bevelling angle in FIB mode

The actual comparison of a typical SEM image showing the true oxide scale compared with a tapered oxide of the same sample is shown in Figure 3.17. This novel tapering method is very effective in determining the distribution of elements (particularly oxygen isotopes) in the oxide scales as well as internal oxides using SIMS oxide mapping.

3.6.3 FIB-SIMS elemental mapping of oxide scales

The FEI FIB200 microscope used in this study is equipped with a SIMS detector enabling an in-situ milling and mapping of oxide scales. The isotope maps of each species ($^{16}O^-$ and $^{18}O^-$) generated is powerful in revealing the oxidation mechanism. Figure 3.18 shows a FIB-SE image of a ramp containing a polished area chosen to perform further SIMS mapping.

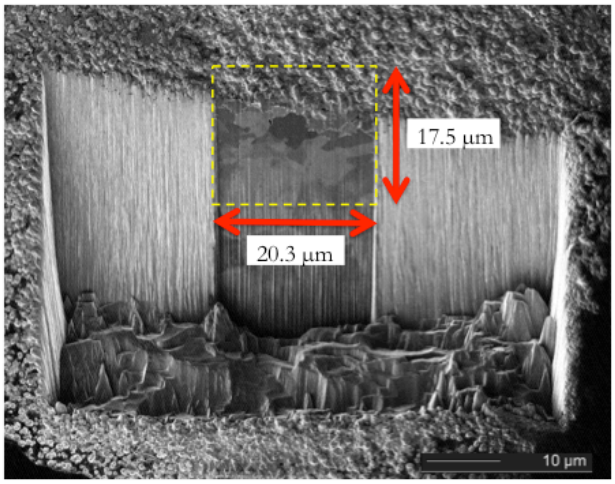


Figure 3.18: Example of a FIB ramp prepared containing a polished area for SIMS analysis

A typical primary ion beam width of 30 nm at 100 pA viewing current was used to obtain a 20 – 25 µm lateral width, which was varied depending on the thickness of the oxides. The acquisition of the $^{16}O^-$ and $^{18}O^-$ maps is different in terms of their beam current dwell time. Typically, the map of $^{18}O^-$ was taken first to minimise the damage after ion beam exposure. Also, due to the high counts of $^{16}O^-$ in nature compared to $^{18}O^-$, mapping of $^{16}O^-$ was relatively simpler than $^{18}O^-$. For the mapping area used, the dwell time for $^{16}O^-$ and $^{18}O^-$ were 2 ms and 4 ms respectively. The relevant experimental chapters provide the specific details of the FIB-SIMS mapping conditions (i.e. beam current, maps area, dwell time).

Figure 3.19 shows a FIB-SE image of a specified area to map each species of oxygen after oxidation at 850 °C for 200 h. The $^{18}O^-$ map was taken prior to the $^{16}O^-$ map with twice the dwell time. In order to standardize the variations when obtaining the maps, the $^{16}O^-$ matrix was normalised to match the $^{18}O^-$ matrix by multiplying it by 2 in MATLAB. Thereafter, an isotopic fraction map of oxygen-18 can be calculated based on the normalised counts of each species.

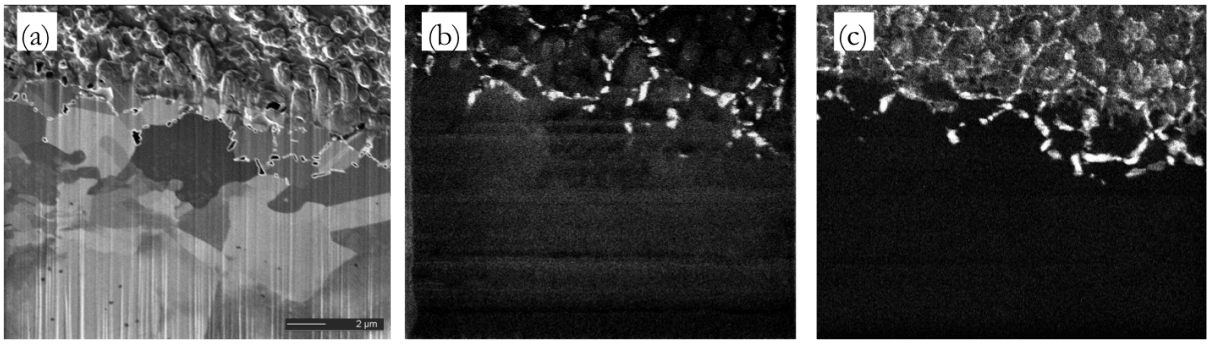


Figure 3.19: An example of a typical FIB-SIMS mapping after oxidation at 850 ºC for 200 h showing (a) FIB-SE image of a map area (b) The $^{16}O^-$ map after 2 ms dwell time and (c) The $^{18}O^-$ map after 4 ms dwell time.

The use of isotopic fractions *f* as shown in Equation 3.2 is appropriate to study the mechanism of oxide formation during the last 24 hours of the oxidation. Neglecting the contribution of $^{17}O^-$, which has a natural abundance of 0.00037, the isotopic fraction (*f*) was calculated as follows:

$$f = \frac{I_{^{18}O^-}}{I_{^{16}O^-} + I_{^{18}O^-}} \qquad \text{Equation 3.2}$$

where the $^{16}O^-$ and $^{18}O^-$ intensities obtained from the FIB-SIMS maps, normalised to the total counts. Also, the $^{18}O_2$ gas-phase concentration (54%) and the $^{18}O_2$ natural abundance (0.24%) gives the corrected isotopic fraction $f_{\text{corrected}}$, given by:

$$f_{corrected} = \frac{f_{18} - 0.0024}{0.54 - 0.0024} \qquad \text{Equation 3.3}$$

Application of Equation 3.3 on point-wise basis of the $^{16}O^-$ and $^{18}O^-$ maps, to form an isotopic fraction (*f*) maps, highlights regions of isotopic enrichment.

3.7 Transmission Electron Microscopy (TEM)

The TEM foil preparation used required the use of FIB in-situ lift out and thinning. The FIB-TEM foils provide a rapid means of preparing electron transparent cross-sections from a specific site of interest. Various TEM analyses were performed on these thin foils. This method was chosen instead of the conventional electro-jet polishing as oxidised samples are non-conductive and the surface oxide layer could possibly be removed.

3.7.1 FIB in-situ lift out

The work was done using an FEI Helios NanoLab DualBeam FIB-FEGSEM operated at 30 keV beam current and a platinum gas injection system was used for surface protection. The process includes many steps and Figure 3.20 describes the whole process. To prepare a specimen for TEM, the site of interest was carefully chosen in the SEM mode. A platinum strip of size 15 μm by 2.5 μm by 1.5 μm was deposited on the surface of interest. Two trenches were made using a high beam current (21 nA) on both side of the platinum strip to simultaneously mill to produce a trench of 10 μm deep as shown in Figure 3.20. A wall of 20 μm by 4 μm thick was produced. The wall was then milled to 2 μm thick using a lower beam current (6.5 nA) in order to produce a smoother surface. Subsequently, the sample was tilted to a step angle of 7° to cut the lamellae on one side and suspend by the other side. The lamella is left attached to the sample on one corner before welding an Omniprobe needle close to the other end. Once the ligament was cut, the lamellae should detach from the sample, and was moved near to a 3-post copper grid. After attaching the lamellae to the copper grid by depositing a platinum strip, a series of milling steps were performed to achieve the desired thickness (250 nA thickness). The polishing takes place by varying the beam current (240 down to 120 pA) and voltages (5 kv down to 2 kV) until electron transparency is observed. The final polished sample should be in the range of 80 – 100 nm thick with a slight translucent appearance in the SE mode.

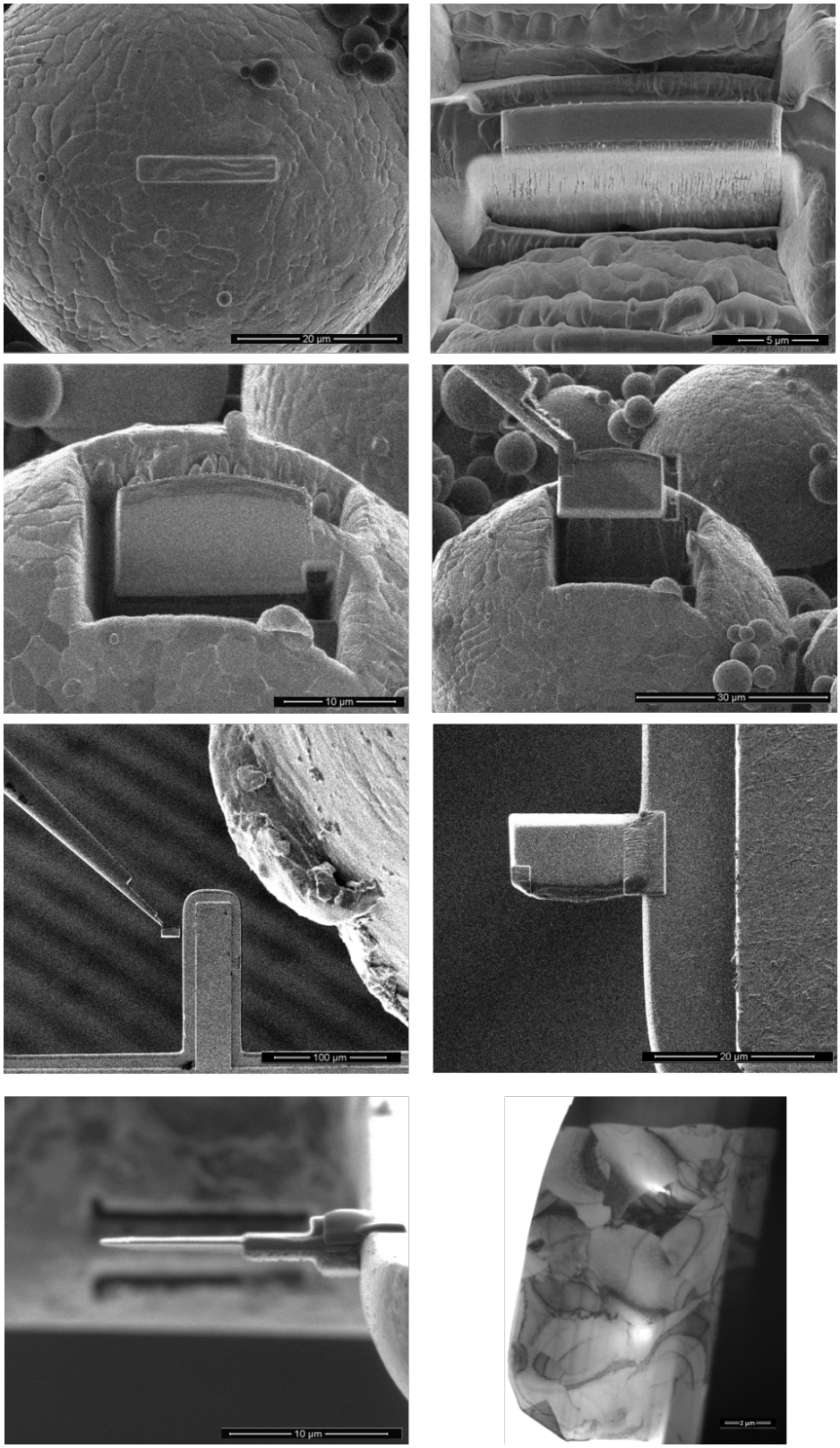


Figure 3.20: TEM sample preparation using the FIB in-situ lift out preparation method.

3.7.2 TEM examination

TEM examinations were performed to examine particles, oxide scales, internal oxides, secondary phases, and topologically closed-packed phases. EDX analyses were performed in both STEM and TEM mode to obtain the chemical information. Prior to the analysis, all TEM foils were cleaned using a plasma system (Gatan, Model 950 advanced plasma system) for 5 minutes. Imaging of the TEM foils was performed using a JEOL JEM 2100F at 200 keV field emission gun (FEG) TEM/STEM. EDX analyses were performed using an energy dispersive X-ray spectroscope (EDX, INCA Oxford). Bright field and dark field images were taken over most regions of all samples to examine and capture microstructure images.

3.7.3 High-resolution TEM

In the case of thin oxide scales, a conventional TEM has a limitation of having a large beam size, therefore, an advanced TEM was used to obtain high-resolution lattice images for small-grained FIB specimens. An FEI Titan 80/300 TEM/STEM fitted with a monochromator and an image aberration corrector was used. Frequency domain images (diffraction patterns) were obtained via Fast Fourier Transform (FFT) using the ImageJ software package. Point EDX analyses were carried out in STEM mode to determine the local chemical compositions in the foils.

4 The V208 Series – Overview

4.1 Introduction

The V208 alloy series were down-selected from an ingot melt alloy series developed by Knop [123], where different ratios of cobalt and nickel were studied to find the optimum ratio of base alloy at a target service temperature of 800 ºC. Tungsten was reduced to 3 at. % from the literature [5] and 1 at. % of tantalum was added to increase the γ' solvus temperature. The amount of these refractory elements was reduced to allow more aluminium to be added and at the same time greatly improving the density of the alloys. The high contents of nickel were chosen to increase the γ'-phase field and to ensure a stable γ/γ' microstructure as well as allowing more additions of chromium without destabilising the microstructure. The varying ratio of Co:Ni produced different types and volume fraction of γ', with cobalt and nickel promoting the precipitation of $Co_3(Al,W)$ and Ni_3Al respectively.

In addition to that, the alloys should possess a good oxidation resistance, hence, chromium was added in varying amounts starting from 12 at. % to 17 at. % and aluminium was varied between 10 at. % to 12 at. %. The findings suggested that high fractions of chromium lead to the formation of undesired phases (which will be discussed later in this chapter) and reduce the γ' solvus temperature regardless of the amount of nickel added. Aluminium was found to reduce the density of the alloys and improve the oxidation resistance. The best Co:Ni ratios were 1:1 and 1:3 and the optimum chromium and aluminium content were 15 to 17 at. % and 10 – 12 at. % respectively.

Titanium was added in one of the alloys as it was assumed to be beneficial for the formation of γ' and stacking fault energy as in the nickel base superalloys. Niobium was added since it partitions to the γ' and changes stacking fault energy nearly as well as tantalum, but without as much of a density penalty. These sets of compositions are comparable to the current nickel base superalloys such as RR1000 [124] and Udimet 720 [125] in terms of oxidation resistance. Compression tests were performed on one of the alloys and it is clear that the present alloys exhibit high strength compared

to the alloys tested by Suzuki et al. [126]. Therefore, further optimisation to improve the mechanical and oxidation properties by eliminating the disadvantages of ingot melt production was planned.

Further development of these alloys has lead to the production of larger forgings using the powder metallurgy route. Six alloys were tailored for the V208 series with the aims of achieving better properties for the next generation high temperature alloys. After the initial screening tests, larger billets of selected alloys were produced using the powder metallurgy route as described in Section 3.1.1. The nominal compositions of these alloys with their γ'-solvus temperatures and density are tabulated in Table 4.1 with 0.15 at. % of carbon, 0.18 at. % of boron and 0.04 at. % of zirconium are added as grain boundary strengtheners. The γ'-solvus temperatures were measured by Mulvey using differential scanning calorimetry (DSC) whilst the densities were measured under ASTM standards using the Archimedes' principle method [127].

Table 4.1: Nominal compositions of the V208 alloy series (in at. %), density (in g/cm^3), and solvus temperature (in ºC).

Alloy	Co	Ni	Cr	Al	W	Ta	Ti	Nb	γ' solvus	Density
V208A	42	32	12	10	3	1	-	-	1010	8.5
V208B	33.5	33.5	17	12	3	1	-	-	990	8.3
V208C	36	35	15	10	3	1	-	-	1000	8.52
V208D	40	29	17	10	3	1	-	-	1010	8.4
V208E	40	31	15	9	2.7	0.8	1.5	-	1030	8.53
V208F	40	31	15	10	2.25	0.75	-	1	990	8.56

4.1.1 Mechanical testing

A parallel PhD project looking at the mechanical properties of the V208 alloy series has been conducted by Mulvey [127]. The project focused on V208 E – F, whilst Knop's PhD was based on the early development of V208 series, which are V208 A – D [123]. Alloy V208 A – D was subjected to tensile and low cycle fatigue testing at 650 ºC with tests being performed by Knop. The same test parameters were applied to alloy V208 E – F later by Mulvey. The results are tabulated in Table 4.2.

Table 4.2: Tabulated conditions and results for yield stress and LCF testing at 650 ºC for all V208 alloys at different percentages of their yield stress [123], [127]. LCF tests were conducted using a 0.25 Hz trapezoidal waveform with an R-ratio of 0.05.

Alloy	Yield σ at 650 ºC (MPa)	Testing Stress (MPa)	% Yield σ	Cycles to Failure
V208A	860	851	99 %	17,334
V208B	940	1081	115 %	10,830
V208C	735	845	115 %	280,158
V208D	810	932	115 %	316,961
V208E	737	774	105 %	277,334
V208F	727	774	107 %	273,657

By referring to both findings, the performance of these alloys can be ranked by their yield stress at 650 ºC, which follows the following sequence, from lowest to highest:

V208 F → V208 C → V208 E → V208 D → V208 A → **V208 B**

The sequence for performance in terms of % yield stress is as follows:

V208 A → V208 E → V208 F → **V208 B,C,D**

Lastly, the performance based on cycles to failure follows the sequence below:

V208 B → V208A → V208 F → V208 E → V208 C → **V208 D**

According to Mulvey, there is a clear indication that the additions of titanium and niobium to V208 E and F caused a reduction in fatigue resistance as they exhibited shorter fatigue lives at lower loading stresses compared to V208 D, which has a similar base chemistry. These mechanical test results in conjunction with the results of the oxidation experiments conducted in this study will be the basis for down selection of the three best performing alloys in the V208 series for further studies of work. From a mechanical property perspective, alloy B, C and D outperformed the rest of the alloys in majority of the mechanical properties tested.

4.1.2 Comparisons of the as-received microstructures

As previously described in Section 3.1.1, the V208 alloys were manufactured using the powder metallurgy route and then isothermally forged at sub-solvus temperature (1050 °C). After forging, the material was solutionised above their respective solvus temperature for 30 minutes. Then, aging takes place at 900 °C for 16 hours for V208 A – D, which was done at the forging facility. The V208 E and F were developed at a later stage where heat-treatment processing had been improved to a two-stage aging process, starting at 950 °C for 16 hours then cool down to 850 °C for the second aging for 4 hours. This improvement was meant to develop the serrated grain boundaries and to bring up the tertiary γ' precipitates. The corresponding micrographs are shown in Figure 4.1

All of the V208 alloys series have a polycrystalline microstructure with γ/γ' volume fraction between 50 – 55 % [123]. The microstructure also contains carbide precipitates, secondary phases and TCP phases, which will be discussed in the next section. The dark and bright contrast particles viewed in the EsB-SE mode show the aluminium-rich secondary phases and tungsten-rich TCP phases, respectively. These dark and bright contrast particles can be clearly seen at higher magnification, as discussed later in section 4.1.3. The purpose of a low magnification view of these as-received microstructures is to compare the distribution of these particles in the bulk, which were found to mostly populate the grain boundaries. These particles are usually nucleated at the grain boundaries and co-exist with the γ' particles surrounded by the γ'-depleted region. These phases have been found in many previous studies of the ternary, quaternary and quinary systems [5], [91], [92], [96], [97], [103], [105] and proved that the γ' is metastable between 900 ºC to 1000 ºC and dissolves in the heat treatment process to form γ, Co_3W and CoAl. Based on the as heat-treated microstructures, it seems that the addition of chromium (up to 17 at.%) destabilised the microstructure and promoted the formation of β-CoAl, as seen in Figure 4.1 (b) and (d).

The volume of β-CoAl increases as aluminium increases from 10 at. % to 12 at. %. It was found that tantalum, titanium, niobium and tungsten are partitioned to the χ phase, as reported by Omori et al. [97]. However, the χ-Co_3W phase is observed in all six alloys (Figure 4.1), appearing as bright contrast particles and no significant addition of alloying elements are found to influence this formation except for the fact that this DO_{19} phase is rich in cobalt and tungsten. It is found that the formation of Co_3W phase is a reaction between the γ and the Co_7W_6 phase upon cooling [91], [97], [128]–[130]. Both of these intermetallic precipitates are detrimental to the mechanical properties of the alloys and should be minimised. Therefore, it is important to understand the effect of alloying additions on the phase equilibria. On the other hand, there are no significant differences in terms of morphology by varying the Co:Ni ratio.

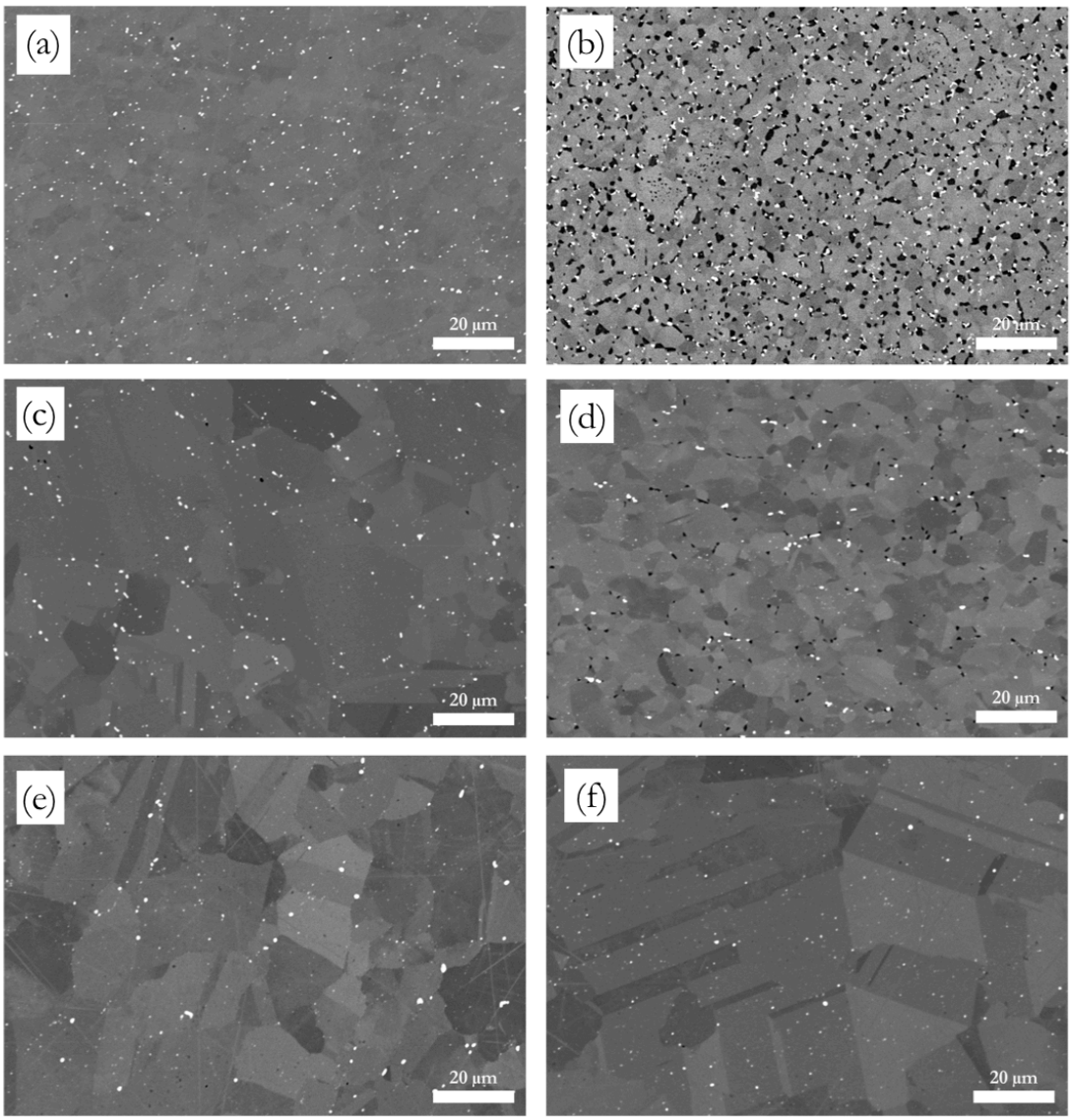


Figure 4.1: EsB-SE micrographs of alloy (a) V208 A (b) V208 B (c) V208 C (d) V208 D (e) V208 E and (f) V208 F, showing the polycrystalline microstructures with several phases in bright and dark contrasts in the as-HIP, forged, and heat-treated conditions.

4.1.3 Phase equilibria in the bulk

Sato et al. claimed that the γ' phase is metastable at 1000 ºC, decomposing into γ, β and χ phases [5]. Likewise, the surface morphologies obtained from the as heat-treated (refer to Figure 4.2) sample of V208 B shows spherical γ' precipitates, χ-Co_3W and β-CoAl within the polycrystalline grains. It is also important to note that near the intermetallic phase, there is a γ' free region. The energy selective back-scattered electron (EsB) mode is beneficial to acquire the right amount of contrast to distinguish these three phases in the bulk. It is presumed that in all V208 alloys, secondary phases are

observed after heat treatment. The elemental maps in Figure 4.2 shows the high intensity of aluminium and nickel enriching the dark contrast particles. This dark contrast phase, which has previously been observed by many [90], [91], [103], [105], [128], [131] is a B2-ordered intermetallic, formed during cooling from solution heat treatment at 1300 °C. However, the β-phase is rich with the base metal, cobalt, instead of nickel in most previous studies. Yan et al. observed the formation of β-phase containing a high percentage of nickel instead of cobalt in 1:1, Co:Ni ratio alloy studied [105]. Many researchers have found the formation of B2-(Ni,Co)Al in the ternary system of Co-Ni-Al and it seems that nickel is partitioned to the B2 intermetallics [132], [133]. It is also notable that nickel is almost equally distributed in the γ and γ' phases and substitutes for more than 50% of the cobalt in the quinary system studied by Sato et al. [5] as observed in nickel and cobalt maps in Figure 4.2. Meanwhile, the bright contrast in Figure 4.2 is purely formed based on the concentration of refractory elements, mainly tungsten in the alloy. The maps of cobalt and tungsten are proving that the TCP phase is found in the high-Z region is Co_3W. Oohashi et al. investigated the influence of tungsten concentrations (from 9 at. % to 11.75 at. %) where the Co_3W arose when the tungsten content increases [93]. Xue et al. reported that the levels of titanium and vanadium also promoted the formation of Co_3W in the Co-9Al-10W base alloy [103]. It is very common to find these three phases γ, B2 and DO_{19} in contact with each other to form a three phase-region with a trace of γ' precipitates appeared in the surrounding.

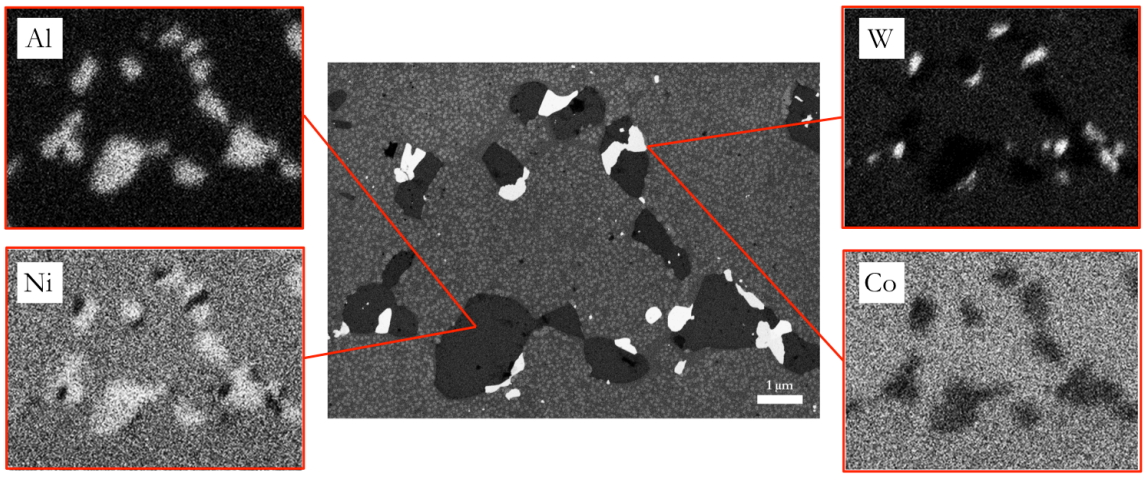


Figure 4.2: EsB-SE micrograph of alloy V208 B with EDX elemental maps showing the intensity of dark and bright contrast particles

4.2 The As-Atomised Powder Particles

The high temperature and high pressure nature of HIP can lead to various complications in terms of microstructural stability such as phase changes, segregation, localised or complete recrystallization and re-precipitation of phases [134], [135].

The surface of the powder after the HIP step is important, as it is the preferential site for the formation of oxides and carbides that forms PPB precipitate networks. It has been found in previous studies that segregation of elements (0.48 at. % of manganese in steel) to the powder surfaces to form oxide can occur while the powder particle is still in the liquid condition. Norell et al. suggested that this shows liquid state diffusion must have taken place [43]. In addition, copper, zinc, and sulphur were also found to segregate to the surface. Therefore, it is important to study the as-atomised powder particles to determine the particle distributions, morphology and overall structure.

Figure 4.3 (a) shows a typical structure of dendrites in large and small as-atomised particles. The dendritic surface structure is a typical example of rapid cooling during powder processing. Some particles show an agglomeration of two or more particles, particularly the smaller particles (~10 μm), which tend to agglomerate to the larger particles through electrostatic forces. It is quite common to find the larger particles with satellite particles frozen on the surface. Large powders (>53 μm for 270 mesh powder) tend to show more dendritic structure than the small powders. According to May et al., agglomeration is viewed as an issue due to the fact that it prevents particles from forming a rounder shape, which in turn creates a deformation in the part during HIPing as the voids between the particles are closed up [136]. Figure 4.3 (a) also shows that a frozen liquid alloy can collide with the solid particles creating a film spread over the surface. This film can entrap gas and produce porosity in the final component.

Figure 4.3 (b) is an example of a FIB trench on a large powder particle, which was used to study the internal particle structure. The trench revealed the grain structure with bright contrast particles (high Z) along the grain boundaries. These bright contrast particles are presumed to be the carbides as suggested by many workers [28], [43], [137], [138].

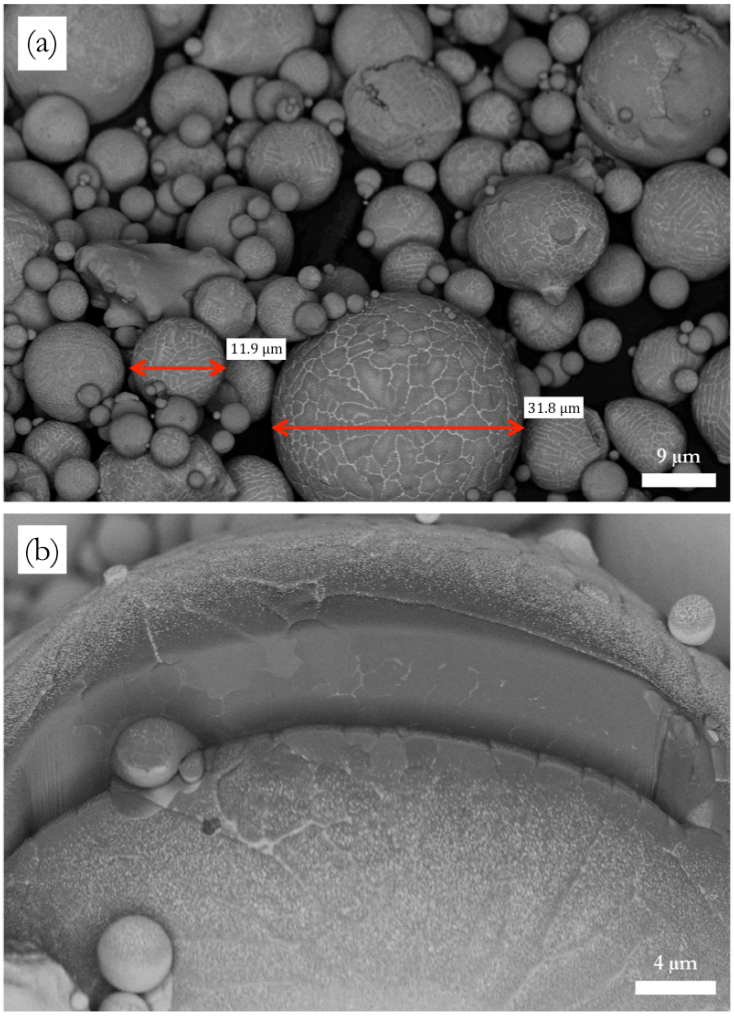


Figure 4.3: The as-atomised powder particles in EsB-SE mode showing (a) typical powder distribution and (b) a FIB trench on one of the particle surfaces together with satellite particles.

4.2.1 Carbide precipitates

In order to minimise the problem of PPB, a two stage HIP powder processing was introduced to study the influence of HIP temperature on the carbide precipitates. Carbon is added as a grain boundary strengthener. It can segregate to the grain boundaries possibly during solidification. The carbide precipitates were first studied in the as-atomised state to identify the types of carbides observed. Figure 4.4 (a) shows a FIB cross-section of carbide particles and film along the grain boundaries of the as-atomised powder particle. The EsB-SE mode shows the bright contrast along the grain boundaries consisting of particles and film. Further imaging was done at higher magnification (STEM bright field) to study the morphology of these precipitates. It was found that there were two types of carbide morphology present. Figure 4.4 (b) shows the carbide film has

formed along the grain boundaries and Figure 4.4 (c) shows the carbide particles found can be intergranular and transgranular.

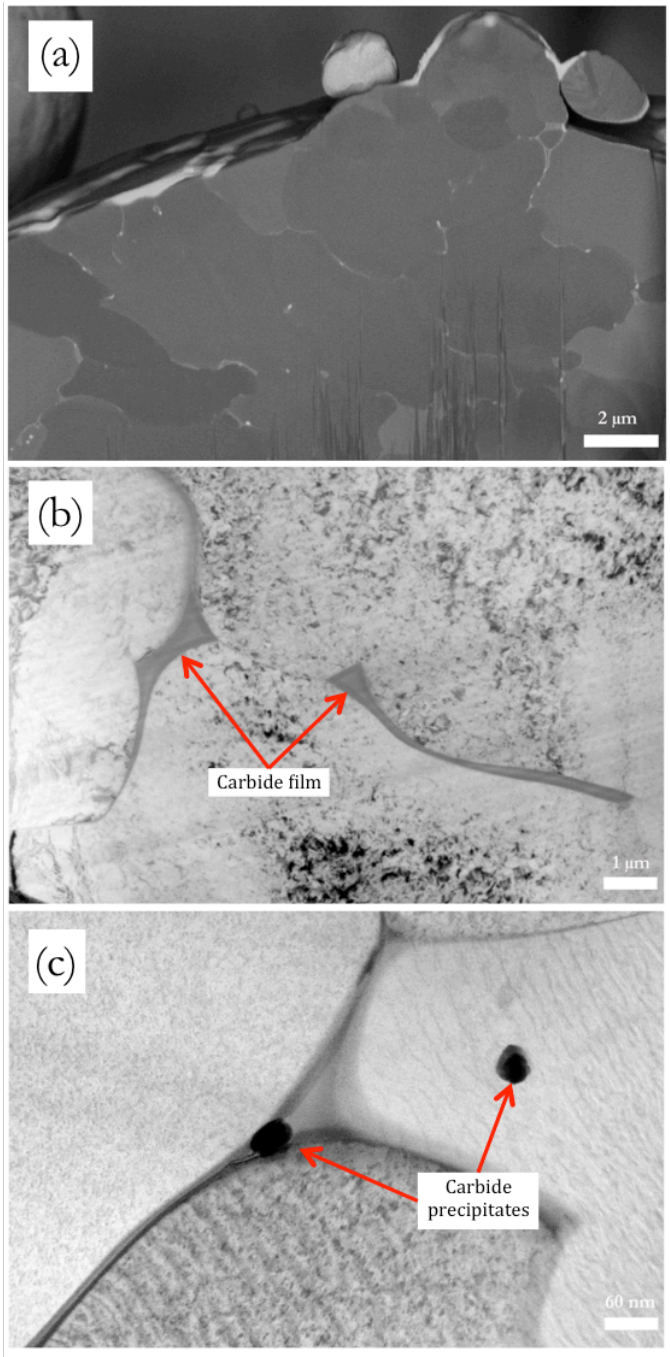


Figure 4.4: The as-atomised powder particle of alloy V208 A showing the (a) EsB-SE micrograph of the FIB cross-section and STEM bright field image of (b) Carbide film along the grain boundary (c) Carbide particles inside the film and in the grain.

The two types of carbide formed in the as-atomised stage are suspected to be the $M_{23}C_6$ and MC carbides. The $M_{23}C_6$ carbides are mainly formed along the grain boundaries at a relatively low

temperature for carbides, between 760 ºC to 980 ºC, and are known to be rich in chromium [26]. Different morphologies of $M_{23}C_6$ carbides have been observed in superalloys, such as continuous $M_{23}C_6$ carbide films [139], discrete $M_{23}C_6$ particles [140], [141] and nano-scaled $M_{23}C_6$ particles [142]. This type of carbide is controversial as there can be two types; one is the blocky shaped at the grain boundaries and have a beneficial effect on rupture strength, and secondly, the depletion of chromium from the matrix to form carbides will hinder the formation of protective oxides, namely Cr_2O_3, due to the lack of chromium [18]. The second type of carbide is the MC carbide that is usually coarse and mostly rich in titanium, niobium, hafnium, and tantalum. This type of carbide is believed to precipitate during processing just after the solidification [18].

Rao et al. studied the as-atomised powder particles of Inconel 718 and found that Al_2O_3 and TiO_2 are decorating the PPB due to the high oxygen content during HIPing [138]. Precipitation of titanium and niobium rich MC carbides was also observed at the PPB and the interior of the grains [143]. These fine particles were presumed to have occurred during the slow cooling stage of HIPing.

The carbides were characterised via elemental analysis and are presented in Figure 4.5 and Figure 4.6. The elemental analysis of the carbide film (Figure 4.5) shows high counts of tantalum, chromium and tungsten. There is an obvious depletion of zirconium in the carbide film, where this element is found in the triangular region. The reason for this phenomenon is unknown and the depletion of zirconium outside the triangular region could possibly be due to the decomposition of other carbides such as M_6C or MC which can form the $M_{23}C_6$ carbide film during high temperature exposure. The reaction below shows the primary M_6C carbide decomposing into $M_{23}C_6$ and solute element [142], [144]–[146]:

$$M_6C \rightarrow M_{23}C_6 + \text{Metal} \ (>1000\ ^\circ C) \qquad \text{Equation 4.1}$$

The other reason could possibly be due to the fact that zirconium has a significantly low solubility in the nickel-base superalloys, and hence zirconium may likely be enriched in the residual liquid as the solidification proceeds [147]. Huang et al. studied the effect of zirconium content on LC superalloys where the element was found to be enriching the grain boundaries and go into solid solution in the carbide and matrix, changing the primary MC carbide morphology and inhibiting the formation of script/film carbides [148].

The STEM EDX results in Figure 4.6 revealed that there is a spheroidal-shaped carbide particle precipitating inside the film in the interdendritic region of the powder particle. This carbide is rich in tantalum and zirconium and has the morphology of MC carbide. Jiang et al. found tantalum, titanium and zirconium MC carbides as the primary carbides in the cobalt-base superalloys which are metastable and degenerate into secondary carbide particles $M_{23}C_6$ which contribute significantly to the strength after aging at 800 ºC for 100 hours [149].

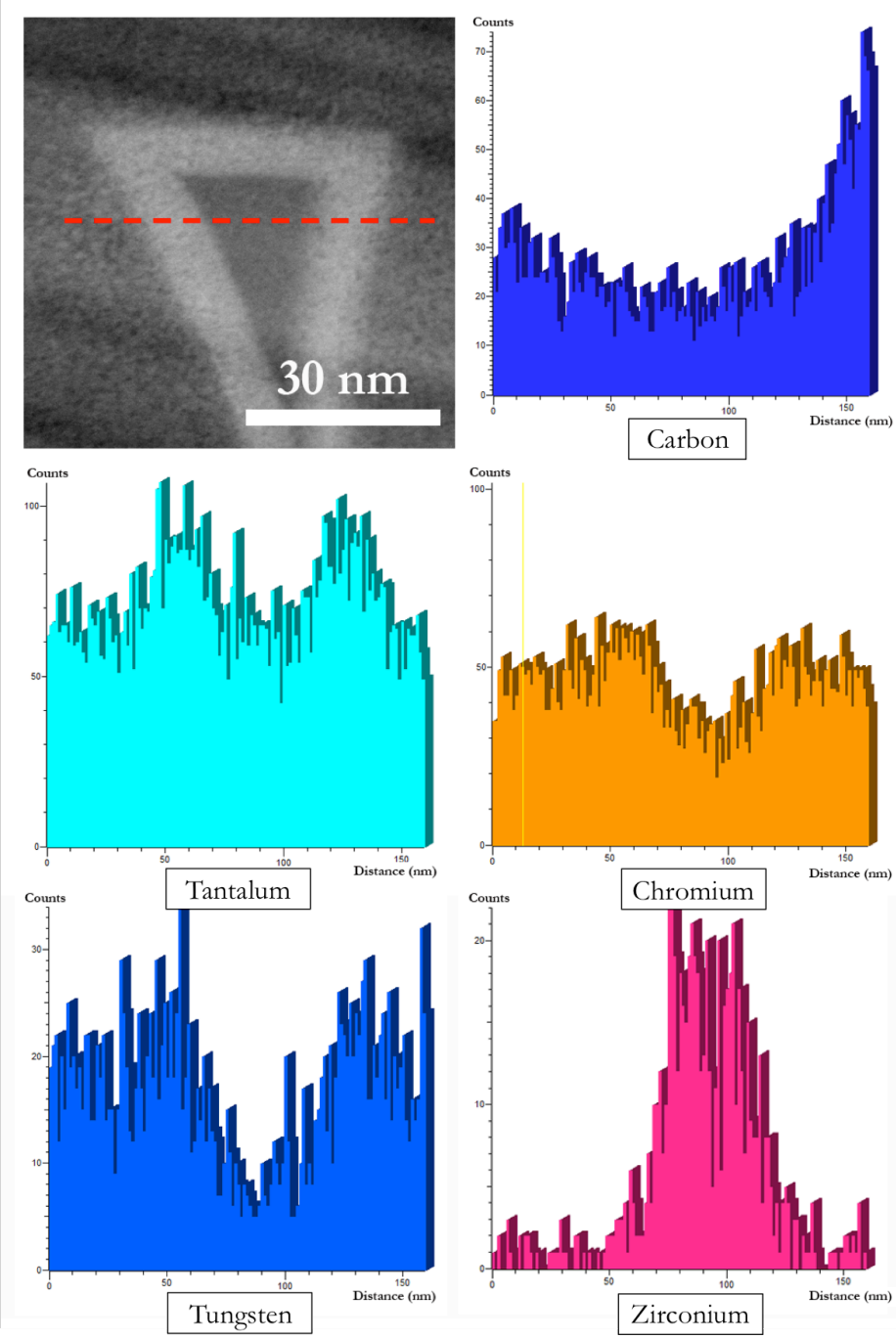


Figure 4.5: STEM bright field image of carbide film in alloy V208 A (dashed red line shows the length of the direction of the EDX line scan) with elemental mapping results showing tantalum, chromium, and tungsten rich and the zirconium rich region outside the film.

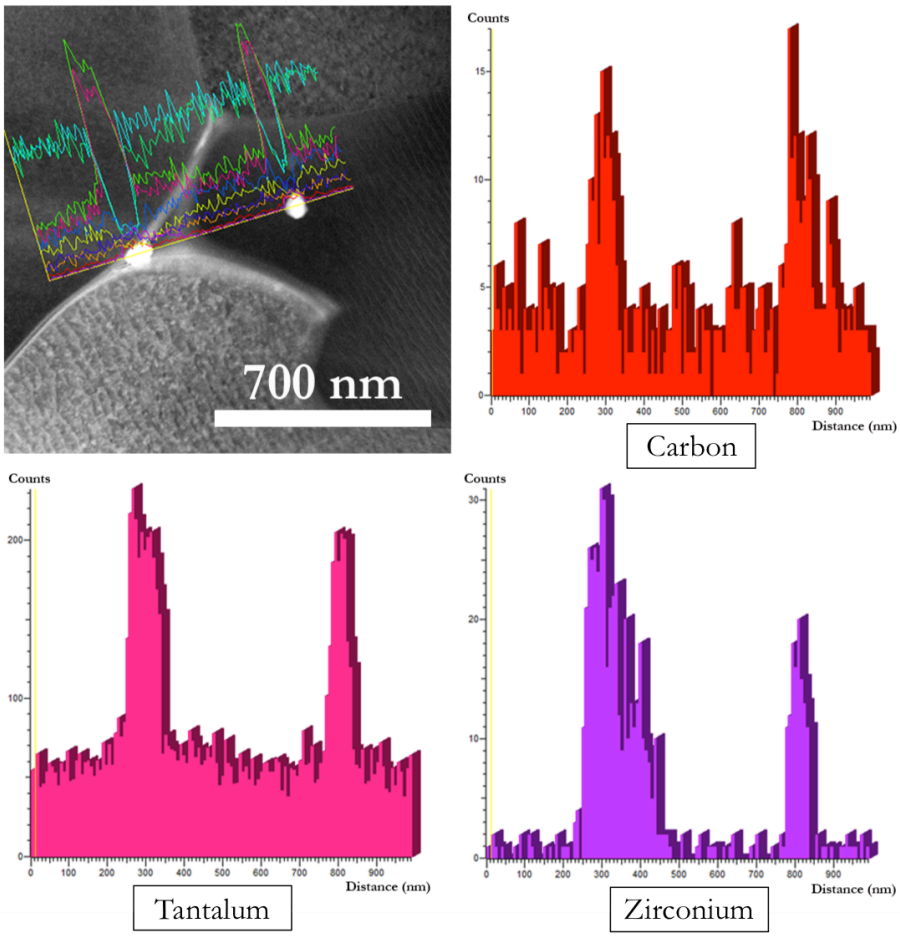


Figure 4.6: STEM bright field image of carbide particles in alloy V208 A (the colour peaks show the direction of the EDX line scan) with elemental mapping results showing high counts of tantalum and zirconium in the particles.

4.3 The Two-Stage HIP Powder Processing

Several studies have optimised the consolidating temperatures to precipitate the carbides. It is generally agreed that the as-atomized powder surfaces contain carbides, borides, nitrides, and oxides. It is speculated that these precipitates may prevent optimum diffusion bonding during consolidation and that the oxides are sites for carbide and boride nucleation and growth during heat treatments [45]. Aubin et al. looked at the extent of PPB decoration which is mainly determined by the carbon and oxygen content; at higher carbon content, slight decorations appear in the as-HIP condition and is further accentuated after heat-treatment [34]. Hack et al. used an intermediate temperature of heat treatment to precipitate $M_{23}C_6$ instead of MC before HIPing [150].

The two-stage HIP powder processing was explained in the previous chapter (see Section 3.3), where the as-atomised powder particles were consolidated in the laboratory to study the effect of heat-treatment (HIP) temperatures on carbide precipitates. According to previous studies, the $M_{23}C_6$ carbides mainly formed at the grain boundaries at a relatively low temperature and precipitated directly from the matrix. Therefore, the powder particles were subjected to three types of exposure in order to determine the morphology of the carbides produced. The first stage proved that after heat-treatment at 950 ºC for 4 hours, fine precipitates of $M_{23}C_6$ carbides at the grain boundaries were formed as shown in Figure 4.7 (a).

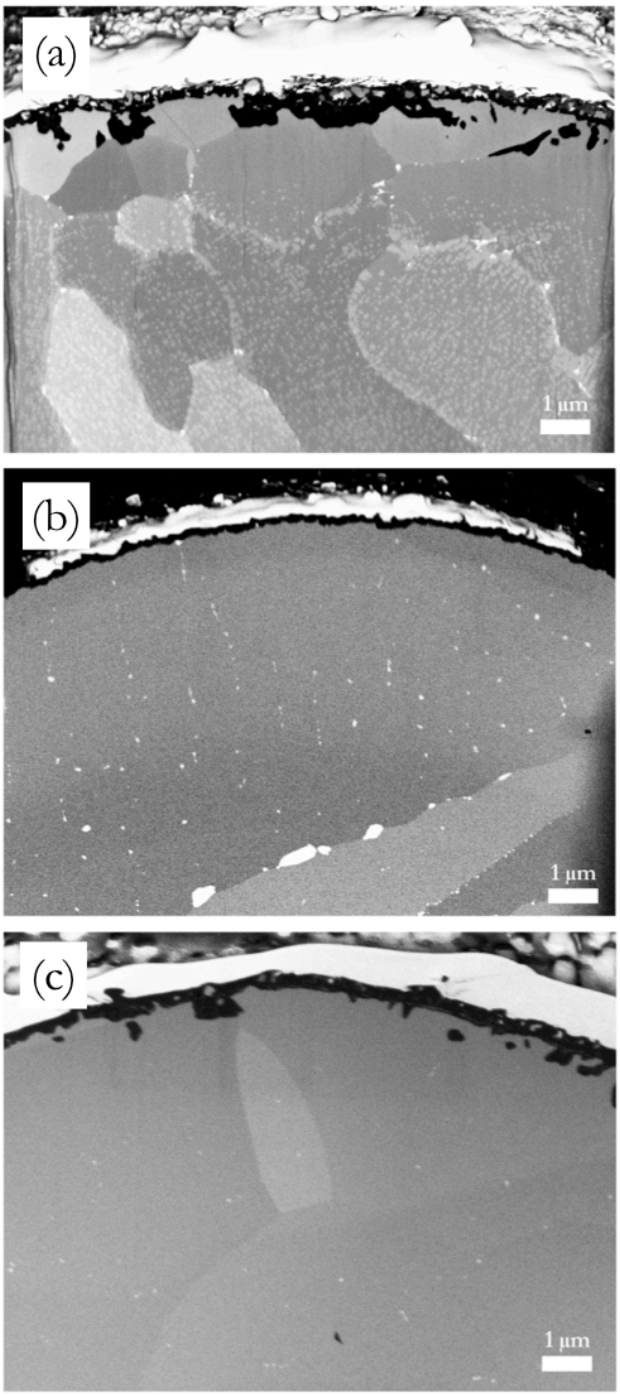


Figure 4.7: EsB-SE micrographs of FIB-sectioned powder after heat treatment at (a) 950 ºC for 4 hours and cooled to room temperature (b) 1050 ºC for 4 hours and cooled to room temperature and (c) 950 ºC for 4 hours and 1050 ºC for 4 hours then cooled to room temperature.

The second stage is to show how a typical sub-solvus HIP temperature, that was normally performed during the actual powder processing at 1050 ºC, is producing carbides that are coarse and blocky (mainly MC) along the grain boundaries as shown in Figure 4.7 (b).

Zhang et al. has investigated the precipitation of nano-scaled $M_{23}C_6$ carbides in intergranular regions (particularly in the dendritic core region) in directionally solidified Ni-base superalloys during high temperature creep [142]. Zhang suggested that the stability of the nano-scaled carbide in the matrix was high and very difficult to coarsen since the carbon content in the matrix is limited after the formation of MC and $M_{23}C_6$ at the grain boundaries.

Bai et al. found two types of $M_{23}C_6$ morphologies at the grain boundaries at different temperatures. The first type is coarse lamellar $M_{23}C_6$ where the lamellae lie almost perpendicularly to the grain boundaries (650 – 900 ºC), and the other is discrete $M_{23}C_6$ carbides (1000 ºC) [145].

Therefore, the fine carbides in the matrix after a two-stage HIP powder processing as shown in Figure 4.7 (c) should be considered as stable precipitates and that the first stage of the HIP at 950 ºC for 4 hours has stabilised the carbide particles before reaching the actual sub-solvus HIP temperature.

Note that the two-stage HIP experiment performed at Imperial College London consisted of thermal exposure of as-atomised powder particles of alloy V208 A mimicking that of a two-stage HIP process. Based on this preliminary finding, Mulvey later performed subsequent experimentation using a two-stage HIP for alloy V208 C on the HIP facility at the University of Birmingham [127]. According to his findings, the effect of the two-stages produced the same resultant effect on the carbide precipitates as the initial heat treatment experiments, thus proved that the two-stage HIP cycle is a success. From the results of this work, the two-stage HIP process is to be applied to all future alloy developments for cobalt base superalloys.

4.4 Oxidation Behaviour of the V208 Alloy Series

In order to compare the oxidation behaviour of the V208 alloy series, the initial oxidation treatment was performed at 800 ºC for 200 hours. The variation of Co:Ni ratio, chromium and aluminium content and titanium and niobium addition will be compared in terms of oxidation performance.

As mentioned in the previous chapter (Section 3.5.1), the 90º trenches were made on the surfaces of samples using FIB milling after oxidation at 800 ºC for 200 hours to investigate the initial cross-sectional microstructure for all the V208 alloy series for comparison.

Based on the results after high temperature oxidation in Figure 4.8, in can be shown from the microstructures that all the V208 alloys are producing multi-layered oxide structures. The oxide layers are roughly divided into 2 to 3 types of oxides, depending on the compositions. For example, sample V208A oxidised very rapidly after 200 hours by producing a thick outer scale with mixed oxides of Ni-Co-Al-Cr in the middle layer and lastly protected by a very thick continuous dark contrast layer as shown in Figure 4.8 (a). The EDX analysis has found that the outer layer is $(CoNi)O_2$, the two types of middle layer to be $Cr(Co,Ni)_3O_2$ and $Ni(Al,Cr,Co)O_4$ and lastly a continuous alumina in dark contrast.

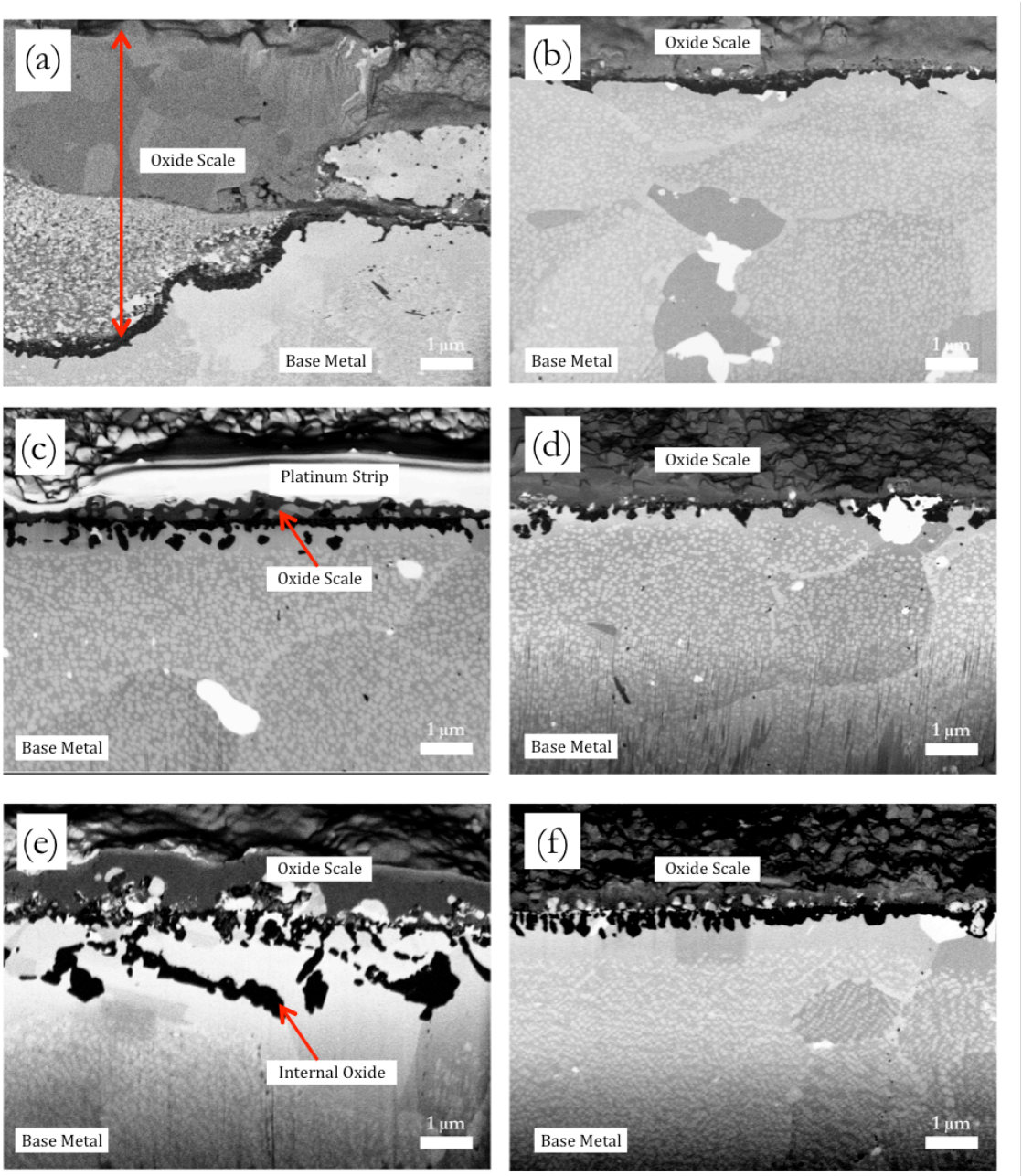


Figure 4.8: Cross-sectional microstructures in EsB-SE mode of (a) V208 A (b) V208 B (c) V208 C (d) V208 D (e) V208 E (f) V208 F after oxidation at 800 ºC for 200 hours.

The rest of the alloys exhibit a two-layer oxide structure with varying thickness. For V208 B, C, D and F, the oxide scale is very thin on the surface with thickness from 0.7 µm to 3 µm. Just beneath this top surface oxide formed a continuous layer of alumina (the dark contrast layer) enriching the oxide alloy interface. A narrow γ'-depleted region (~900 nm) existed beneath this oxide layer. As compared to V208 A and V208 E, the width of the γ'-depleted region is less. The width of γ'-depleted region for V208 A and E is found to be larger due to the dissolution of chromium and aluminium to the surface during oxidation.

Internal oxidation massively occurred in sample V208 E (with 1.5 at. % titanium addition). Just beneath the top surface oxide some dark contrast protrusions extending into the substrate existed with a size range of 2 – 3 μm. The outer scale of this sample is thicker (doubled in thickness) as compared to the other V208 alloys.

Despite the rapid cooling by rolling off the furnace in the two-stage oxidation experiment (see 3.2.2), there was no spallation of oxide scale grown on the surface of any of the V208 alloy series after 800 ºC for 200 hours. A possible explanation for this is that the oxide layer might be too thin to be affected by the thermal stress [56].

4.5 Discussion

The main purpose of this chapter is to examine the effect of alloying compositions on the oxidation resistance and the stability of the underlying microstructure in the V208 alloy series. Many previous studies have suggested that the addition of chromium, titanium and niobium has a positive effect on the Co-Al-W ternary system [95], [98], [99], [105], [151]. Oxidation experiments have been carried out by few studies and the cobalt base superalloys were viewed as comparable to the current nickel base superalloys in terms of their oxidation resistance. The effect of alloying elements on the oxidation resistance and the stability of the underlying microstructure will be discussed in this section.

4.5.1 The effect of alloying additions on the oxidation behaviour

A multi-layered oxide microstructure was formed on all V208 alloy series with varying morphology of oxides and thicknesses. Table 4.3 summarised the effect of alloying elements on the oxidation resistance by comparing their damage depth thicknesses. According to this comparison, alloy V208 A and E possess poor oxidation resistance by having the most oxidation damage on the scale region as well as in the substrate. It can be justified that the Co:Ni ratio has no significant influence on the formation of protective oxides. The shortage of chromium (the only alloy that has 12 at. % chromium) in alloy V208 A, however, seems to result in the rapid formation of nickel oxide on the surface and mixed spinels underneath the layer. This phenomenon is not observed in any other V208 alloys. The fast diffusion of nickel cations outward form the substrate forming a rapid growth of nickel oxide and spinels causes the alloy to oxidise very rapidly without a sufficient chromia level to protect the substrate from further oxidation.

This shortage of chromium proved to be particularly damaging to the Ni-Cr-Al system in forming a protective oxide. This can be justified by Wagner's theory called the 'third-element effect' [54] as discussed in Chapter 2.4.2.

Table 4.3: The damage depth comparisons in terms of Co:Ni ratio, chromia, alumina, titanium and niobium additions.

Alloy	Co:Ni	Cr	Al	Ti	Nb	Oxide scale (μm)	Oxide intrusion (μm)	γ'-depleted zone (μm)
V208A	1.3:1	12	10	-	-	4.04	3.63	3.26
V208B	1.0:0	17	12	-	-	0.64	0.51	0.89
V208C	1.0:0	15	10	-	-	0.74	0.68	0.74
V208D	1.3:1	17	10	-	-	0.90	0.80	1.50
V208E	1.3:1	15	9	1.5	-	1.49	2.10	3.23
V208F	1.3:1	15	10	-	1.0	0.59	0.98	1.22

Titanium seems to inhibit the formation of a continuous protective alumina in the case of V208 E, instead forming an internal oxide by allowing the oxygen species to attack the substrate via grain boundaries. The oxidation occurs via diffusion of oxygen inwards to form alumina in the grain boundary regions. It is worthy of note that only 1.5 at. % of titanium is sufficient to completely change the oxidation mechanism into inward diffusion of oxygen, forming internal branches of non-protective alumina. Other possible reason is the lower aluminium content in this alloy (9 at. %), which plays an important role in forming a protective alumina on the surface.

Regarding the other alloys in the V208 series with 15 – 17 at. % of chromium and 10 – 12 at. % of aluminium, a two-layered oxide structure was formed, with outer chromia scale and underneath it is a continuous layer of protective alumina appearing in the dark contrast. The damage depths for these alloys are very low which proves that sufficient amount of chromium and aluminium in the system has resulted in the formation of strong and dense barriers, which inhibit the movement of metallic elements to the surface as well as oxygen to the substrate.

The depth of oxide scale and γ'-depleted region in V208 A and E (poor oxidation resistance) proved that the metallic elements in the substrate (nickel, chromium and aluminium) decompose to form oxide layers on the surface. The reaction will not reach equilibrium as in the case of V208 A and E due to the limitation of protective oxides on the surface. In this case, bigger γ'-depleted region is formed near the oxide-alloy region. According to the results in Table 4.3, all of the alloys exhibit a sub-μ oxide scale except for V208 A and E, which yield more than three times the average scale of the rest of the alloys. This finding proved that chromium plays a more important role in protecting

the alloy compared to alumina where a reduction of chromium allows the oxygen to diffuse in the bulk alloy more rapidly.

4.5.2 The effect of alloying additions on phase stability in the bulk

The χ-DO_{19} phase is found in all V208 alloy series appearing in bright contrast (high-Z), which indicates a high amount of heavy elements such as tungsten and tantalum. Cobalt seems to partition to this phase but no significant addition of cobalt seems to directly contribute to forming this phase. Unlike the TCP phase, the β-B2 phase is found only at high percentage of chromium (>17 at. %), which in this case shows that this percentage is too high. Even though it is beneficial to forming a protective chromia layer, the detrimental effect of this β-phase should not be underestimated. It is worthy to note that both of the phases do not alter the oxidation resistance and did not change in morphology after oxidation tests were performed. It is worth noting that both χ-DO_{19} and β-B2 phases have not been presented in the early studies by Klein et al. [94], Sato et al. [152] and Pollock et al. [101]. The presence of these metastable phases, however, are acknowledged based on the equilibrium reaction studies done by Shinagawa et al. [90] and Miura et al. [91] as discussed in Section 2.5.3. However, there are limited examples showing the morphology of these phases. The χ-DO_{19} phase can easily be mistaken with the carbides precipitates, which in this case, also appeared bright in the EsB mode. A more detailed explanation on the similarity and differences among these phases will be presented in the next chapter (Section 5.1.1).

Table 4.4: Comparison of the phases present in the bulk in V208 alloy series after heat-treatment.

Alloy	Co:Ni	Cr	Al	B2-phase	DO_{19}-phase
V208A	1.3:1	12	10	-	✓
V208B	1.0:0	17	12	✓	✓
V208C	1.0:0	15	10	-	✓
V208D	1.3:1	17	10	✓	✓
V208E	1.3:1	15	9	-	✓
V208F	1.3:1	15	10	-	✓

4.6 Conclusions

A polycrystalline microstructure with γ/ γ' precipitates with some secondary (β-phase), TCP (χ-phase) and carbides were observed in the as heat-treated condition for all V208 alloy series. Alloy V208 B with the most aluminium content was found to have the lowest density. Addition of chromium (V208 B and F) has proved to lower the γ'-solvus temperature. In addition, a high percentage of chromium (up to 17 at. %) also destabilised the microstructure by forming the β-phase in alloy V208 B and D.

The carbides were formed in the as-atomised state ($M_{23}C_6$ and MC carbides) and continued to change in morphology after exposure at high-temperatures, such as HIPing and forging. Two types of carbides were formed in the as-atomised condition, the $M_{23}C_6$ carbides (M: chromium, tantalum and tungsten) and the MC carbides (M: tantalum and zirconium). The two-stage HIP process proved to be beneficial in refining the carbide particles along the grain boundaries and in the transgranular region. Much finer carbides were formed which is presumed to be the fine $M_{23}C_6$ carbide precipitates, by taking the transformation temperature as a guide. The understanding on this particular carbide formation should be continued in order to examine the type of carbides formed after the actual HIPing process as well as the effect on mechanical properties.

After oxidation at 800 ºC for 200 hours, the V208 alloy series formed a multi-layered oxide structure with various thicknesses depending on the compositions of chromium and aluminium. The alloy with the very least amount of chromium (V208 A) possesses a poor oxidation resistance and forms a complex multi-layered oxide with spinels. On the other hand, alloys with sufficient chromium (>15 at. %) produced a very thin oxide scale in sub-micron depth and a continuous alumina layer at the oxide/alloy interface. Titanium seems to greatly alter the oxidation performance by forming a thicker oxide scale and showed internal oxidation. The niobium addition seems to have a good effect on the oxidation performance as well as the underlying microstructure.

The results of this study have been used to down-select the top three best performing alloys in terms of their mechanical properties, phase stabilities, and oxidation resistance, shown in Table 4.5. The down-selection process has been conducted by screening the results for mechanical properties performed by Mulvey [127] in a parallel PhD study of the V208 alloys combined with the previous study performed by Knop [123]. The alloys were ranked from 1 to 6; 1 being the best performing alloy, and 6 being the least performing alloy. Note that number 1 was given for all three alloys that have the same result in both % yield stress and cycles to failure column. It should also be noted that all variables were given equal weight in the sum used for selection.

Table 4.5: The sum of ranking numbers based on mechanical properties, phase stabilities and oxidation performance.

Alloy	Yield σ at 650 °C (MPa)	% Yield σ	Cycles to Failure	OS (μm)	OI (μm)	GD (μm)	β	χ	Sum
A	2	6	4	6	6	6	0	1	31
B	1	1	6	2	1	2	1	1	15
C	5	1	1	3	2	1	0	1	14
D	3	1	1	4	3	4	1	1	18
E	4	5	1	5	5	5	0	1	26
F	6	4	4	1	4	3	0	1	23

Based on the accumulated rankings for each individual property, the following sequence can be made in terms of best performing alloy, starting from the lowest performing:

V208 A → V208 E → V208F → V208D → V208B → V208C

The top three best performing alloys, V208 B, C and D are selected for further investigations, which will be discussed in the next two chapters.

The initial understanding on the cobalt-nickel base superalloys in terms of their phase equilibria and the types of oxide formed is very crucial to elucidate the beneficial effect of nickel, chromium and aluminium in the alloy system. A more in-depth study on the mechanism of oxide formation in this alloy series will be discussed in a later chapter, particularly on the types and morphology of oxide formed in this alloy.

5 Specific V208 alloys – The Variation of Co:Ni Ratio and Chromium and Aluminium Contents on the Oxidation Behaviour

5.1 Introduction

One of the primary factors that limits the service life of a component for high temperature applications is oxidation, which can lead to the loss of load-bearing capacity in a component by the reduction of metallic cross section [153]. Oxidation of Co-Al-W alloys at 800 ºC typically produces a multi-layered oxide structure, with cobalt-rich oxide in the outer layer, a mixed oxide of Co-Cr-Al in the middle layer, whilst the inner layer is suggested to be a protective layer of Al_2O_3 [94], [98], [103], [105], [154], [155]. The aluminium is usually depleted at the oxide/alloy interface to form a continuous layer of Al_2O_3 on the surface. The effects of alloying elements on oxidation behaviour of Co-Al-W base superalloys have been investigated by many researchers [94], [95], [98], [99], [154], [156], [157].

The oxidation behaviour of cobalt-base superalloys can be improved by suitable alloying strategies. For this, different alloying elements, such as nickel, aluminium, and chromium have been added to Co-Al-W ternary alloys in varying amounts to improve the oxidation behaviour. Since the current understanding of the oxide formation mechanism in Co-Al-W alloys is limited, there is a need to focus on the difference in the oxidation sequence with varying alloy compositions. The V208 alloys have been created to have varying amounts of chromium and aluminium and cobalt-nickel ratio. Based on the results presented in Chapter 4, the three main alloys that exhibit good overall properties have been selected for further investigations. To further investigate the mechanism of oxidation in these alloys, it is best to classify them based on their chromium-aluminium and cobalt-nickel ratio. Since elements such as chromium and aluminium contribute to good oxidation properties, it is important to find the best ratio of the two at longer oxidation exposures, from 200 to 2000 hours.

At the end of this chapter, the alloy that possesses the best oxidation properties will be considered to have the optimum chromium-aluminium ratio. This ratio will then be suggested for use in future alloy

design. Further investigation on the effect of the cobalt-nickel ratio to oxidation behavior of these alloys will also be validated. Note that in the previous chapter, only one oxidation temperature has been studied and therefore a more comprehensive range of temperature and exposure times are studied.

This chapter will evaluate the effects of alloying elements, particularly nickel, aluminium and chromium, on the oxidation behaviour of Co-Al-W superalloys. The use of oxygen isotopes to study the transport mechanisms during high temperature oxide scale growth is essential to improving the understanding of the oxide scale. Later in this chapter, the effect of alloying elements on the oxidation behaviour of the cobalt-base superalloys and their impact on the changes in the underlying microstructures after oxidation from 200 hours to 2000 hours at 800 °C will be discussed.

Table 5.1 summarises the nominal composition of the selected alloys (V208 B, C and D) with varied nickel, aluminium, and chromium content. The abbreviations of the alloys are changed from this chapter onwards to allow an easy differentiation of the major alloying elements. Note that the first two alloys have the same Co:Ni ratio (1:1) whilst the third alloy has 1.3:1 Co:Ni ratio. Hence 1.3Co is utilised in the alloy abbreviation.

Table 5.1: Nominal compositions of the investigated alloys and utilised abbreviations in at. %.

Alloy	Co	Ni	Cr	Al	W	Ta
17Cr-12Al	33.5	33.5	17	12	3	1
15Cr-10Al	36	35	15	10	3	1
1.3Co-17Cr-10Al	40	29	17	10	3	1

5.1.1 Alloys characteristics in the as-received condition

Electron back-scattered diffraction (EBSD) - As previously described in Section 3.1.1 and 4.1.1, the alloys were manufactured via powder metallurgy route, forged, and heat-treated. The average grain size in each material condition was calculated from electron backscatter diffraction (EBSD) derived data using the equivalent grain diameter method and disregarding twin boundaries. 1453 grains were detected with an average grain size of approximately 2.5 μm, as shown in Figure 5.1. The grain size distribution was obtained by fitting a Weibull distribution to the cumulative distribution function, giving an average grain size comparable to powder metallurgy nickel base superalloys. The grain structure of as-HIPed, forged and heat-treated samples were examined using EBSD as shown in Figure 5.2.

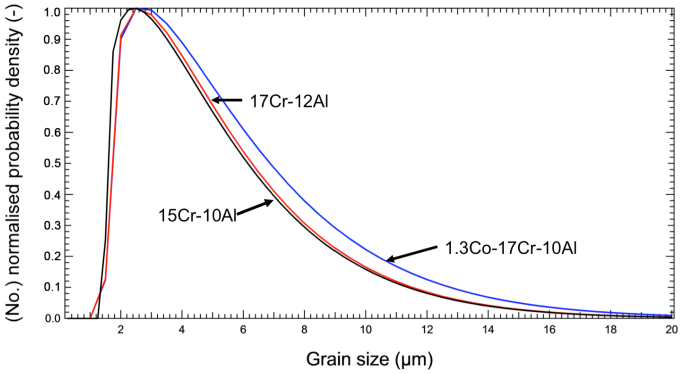


Figure 5.1: The grain size distributions obtained via EBSD using a 0.5 μm step size, 3.6 x 10^5 points, 1453 grains.

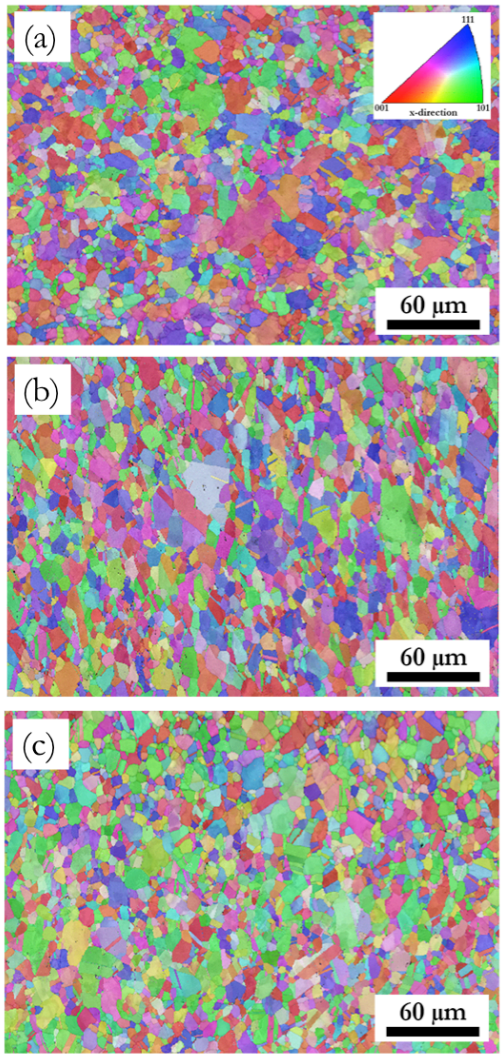


Figure 5.2: Inverse Pole Figure (IPF) coloured map, overlaid with band contrast, electron backscatter diffraction (EBSD) images of the microstructure in (a) 17Cr-12Al (b) 15Cr-10Al (c) 1.3Co-17Cr-10Al.

Energy selective back-scatter (EsB-SEM) - The EsB-SEM micrographs in Figure 5.3 show the FIB cross-section of the base alloys after HIP, forging and heat treatment with γ/γ' grains, sub-μm carbides, the secondary phase NiAl (β phase) and the topological-closed-packed (TCP) Co_3W (χ phase). Based on previous studies [90], [92], [103], [105], it is found that these two phases, B2 (β phase) and DO_{19} (χ phase), form adjacent to each other and can be recognised by their morphology and atomic number contrast. In the present case, these precipitates were examined using STEM-EDX in the TEM later in this chapter which, lacking precise crystallography information, is not completely definitive, but does provide enough information to confirm these preliminary phase assignments. The presence of such secondary phases may be detrimental to the mechanical performance and so it is important to understand the effect of chromium and aluminium additions on the phase equilibria [90]. It is essential to note that 17 at. % of chromium leads to the formation of the β phase, as observed in Figure 5.3 (a) and (c). The reduction of chromium to 15 at. % eliminates the formation of β phase but still forms the χ phase.

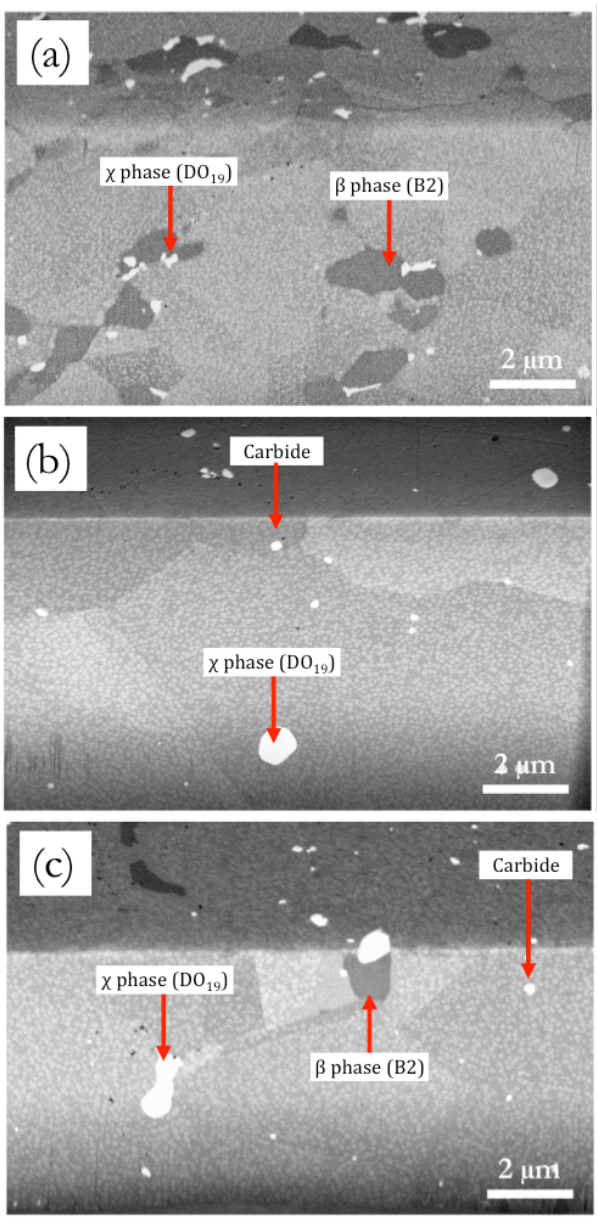


Figure 5.3: EsB-SEM micrographs of as-HIPed, forged and heat-treated alloy (a) 17Cr-12Al (b) 15Cr-10Al (c) 1.3Co-17Cr-10Al showing the polycrystalline grains with a fine γ/ γ' microstructure, carbide precipitates, β phase and χ phase mostly found along the grain boundaries.

Secondary precipitates - The bright contrast particles in Figure 5.3 (b) are corresponding to the heavy elements in the phases; there are two types of particles that can be distinguished in terms of their morphology: i) the χ phase ii) the carbides particles. An example of these particles at a higher magnification can be seen in Figure 5.4. The χ phase in Figure 5.4 (a) and (c) is usually more than 1 µm in size and has a unique elongated shape. In comparison to that, the carbides that also appear bright in the bulk metal are typically smaller (<0.5 µm) and have a spherical shape. The carbides are usually nucleated along the grain boundaries as is clearly shown in Figure 5.4 (d).

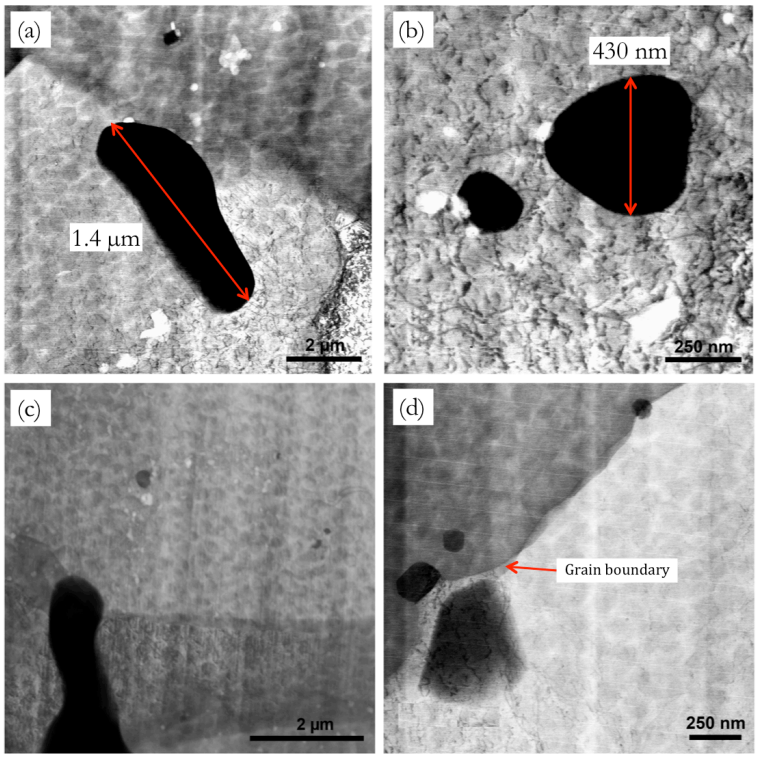


Figure 5.4: STEM-BF image of alloy 15Cr-10Al after oxidation at 800 ºC for 200 hours showing the different morphology of secondary phases in the bulk (a) and (c) showing the χ phase in 1-2 µm size (b) and (d) showing the carbides precipitates in less than 0.5 µm diameter.

The chemical analysis of these precipitates was discussed in the previous chapter (Section 4.1.2 for the χ phase and Section 4.2.1 for the carbides). The χ phase that was analysed in Section 4.2.1 consists of cobalt and tungsten (Co_3W) and it is formed together with the β phase. However, a further investigation in STEM-EDX has confirmed that the χ phase that formed individually in alloy 15Cr-10Al contains cobalt, tungsten and tantalum (Co_3(W-Ta)) as shown in Figure 5.5.

Kobayashi et al. [158] have studied the effect of tantalum on the thermodynamic stability of the γ' phase in Co-Al-W alloy. The study suggested that tantalum is a strong Co_3W phase stabiliser at 900 ºC instead of partitioning to the γ or γ' phase. The chemical analysis indicates that tantalum partitions preferentially into the phases in the order:

$$Co_3W \rightarrow \gamma' \rightarrow CoAl \rightarrow \gamma$$

It is crucial to note that tantalum partitioning in Co_3W is found in the low chromium content alloy (<15 at. %) without the presence of β phase.

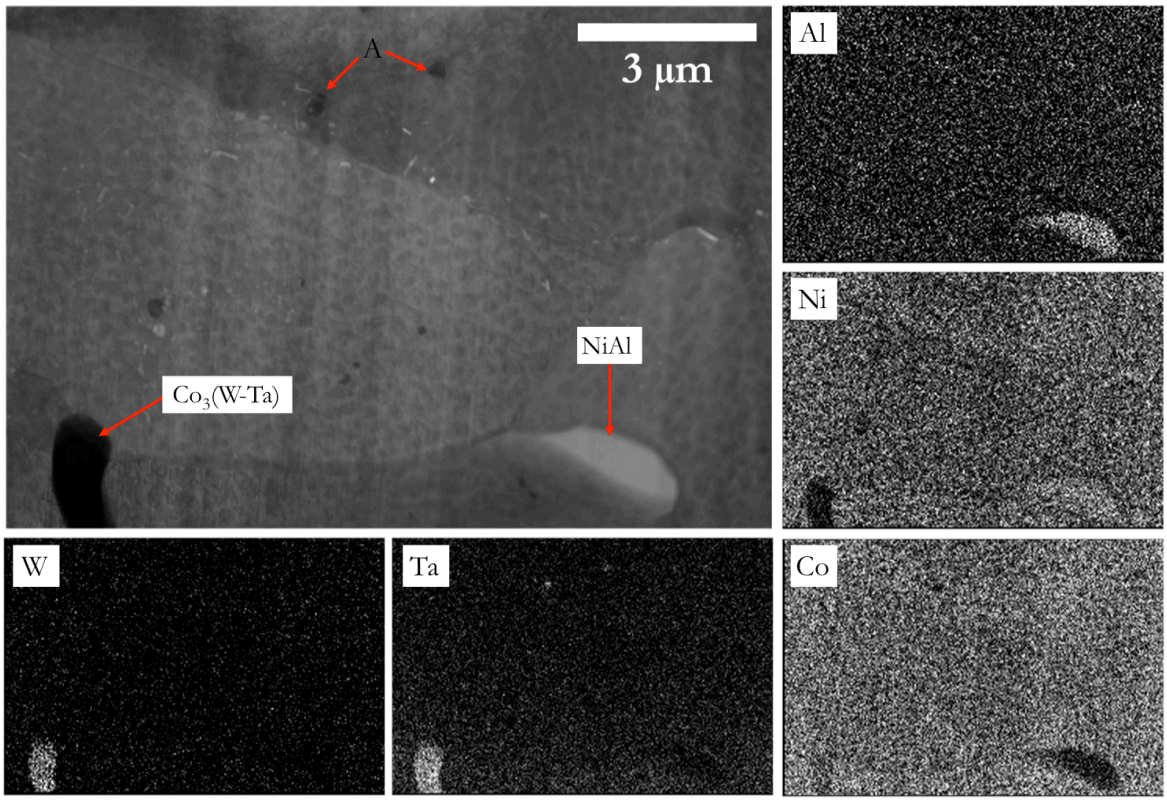


Figure 5.5: STEM-BF image of alloy 15Cr-10Al after oxidation at 800 ºC for 200 hours with the EDX maps highlighting the carbides as particles A, χ phase (Co_3(W-Ta)) and the β phase (NiAl).

The other particles appearing in bright and dark contrast in Figure 5.5 and Figure 5.6 are related to the carbide particles found in the as-atomised condition (see Section 4.2.1). As suggested in STEM-EDX spectrum in Figure 5.6, the particle is rich in tantalum and zirconium. The chemical composition of that particular spectrum is tabulated in Table 5.2

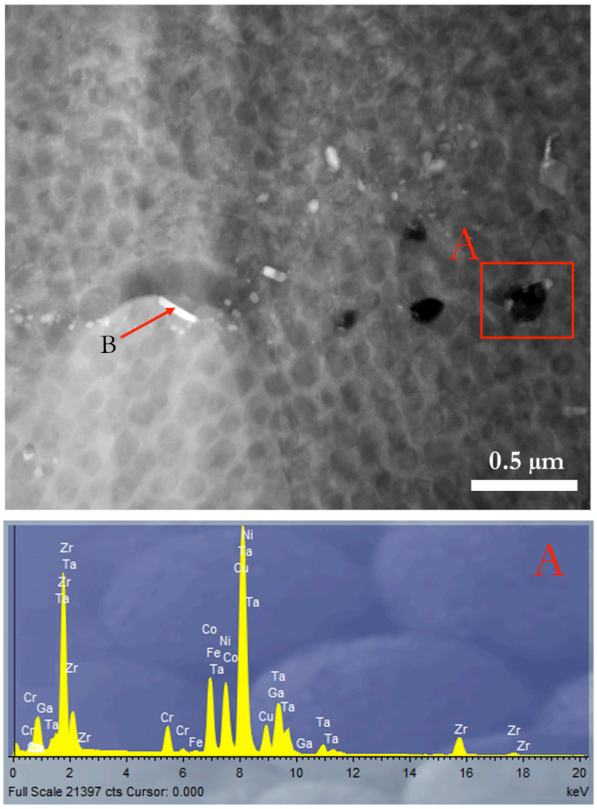


Figure 5.6: STEM-BF image of alloy 15Cr-10Al after oxidation at 800 ºC for 200 hours showing particle A and particle B in the bulk metal. The STEM-EDX point analysis spectrum corresponds to particle A.

However, particle B in Figure 5.6 consists of the bulk elements, namely aluminium, chromium, nickel, and cobalt. The interaction volume could be a limiting factor in this case. However, owing to the size (<20 nm) or volume fraction of the particles, their influence on material properties is negligible.

Table 5.2: Chemical compositions of particle A and particle B in alloy 15Cr-10Al after oxidation at 800 ºC for 200 hours obtained by STEM-EDX point analysis (at. %).

Particle	C	O	Al	Cr	Co	Ni	W	Ta	Zr
A	2.6	0.6	11.3	5.9	23.3	36.2	4.5	11.7	5.0
B	1.4	0.6	11.3	15.2	23.3	36.2	3.7	1.1	0.4

5.1.2 The surface oxide morphology

To examine the surface topography of the oxide, electron micrographs were acquired in SEM in secondary electron mode from the surface oxide, adherent on the substrate. The external scales formed during oxidation for 400 hours at 800 ºC were imaged in the SEM as shown in Figure 5.7. The representative surface oxide structure observed in all three alloys features two distinct external scale morphologies. The morphology of the oxide indicated as A and B in Figure 5.7 consists of (A) 1-2 μm sized polygonal shape with facets and steps and (B) a nodular shaped oxide forming on top that is assumed to be more porous than the other.

As determined by SEM-EDX analysis, the approximate compositions of the two scales are (A) aluminium-rich oxide (approximately 22Al-10(Co-Ni)-68O (at.%)) and (B) chromium-aluminium-rich oxide (approximately 12Al-12Cr-12(Co-Ni)-64O). The facetted aluminium-rich oxide formed preferentially on grain boundaries whilst the nodular chromium-aluminium-rich oxide formed on the remaining grain surfaces.

Comparing the approximate compositions of the two surface oxides, scale B, which forms on the top, consists of chromium and more cobalt and nickel than scale A, as expected thermodynamically (based on Ellingham-Richardson diagram). These key elements will form on the surface before the formation of aluminium-rich oxide in scale A [15-16]. Elements such as nickel and aluminium are the γ' forming elements in the cobalt-base superalloys. The surface oxide compositions suggest that the decomposition of the γ' precipitates, results in migration of aluminium and nickel towards the surface, to form oxides and create a γ'-depleted zone in the sub-surface region.

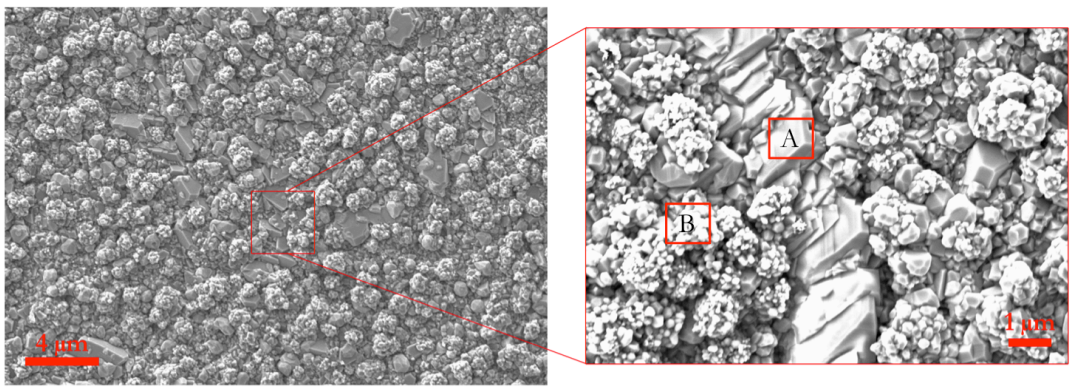


Figure 5.7: SEM images of the surface morphology of alloy 15Cr-10Al after oxidation in air at 800 ºC for 400 hours. Figure on the left is showing the two types of oxide scale found on the surface labelled as scale A and scale B.

5.2 Oxidation of the Specific V208 Alloys

In order to elucidate the oxidation behaviour of the specific V208 alloys, the scale and near surface microstructure were studied using in-situ cross-sections produced using ion-beam milling. The thicknesses of the oxide scale, internal oxide and γ'-depleted zone were compared after oxidation at 800 ºC for 200 hours and 300 hours. The spalled oxide on the surface was studied to investigate the spallation mechanism.

5.2.1 Oxide cross-section morphologies

Figure 5.8 shows the EsB-SEM microstructures of oxidised 17Cr-12Al, 15Cr-10Al, 1.3Co-17Cr-10Al after 200 hours and 300 hours of oxidation at 800 ºC. Alloy 17Cr-12Al proved to have a very good oxidation resistance, forming a continuous Al_2O_3 layer with a very thin external oxide. The underlying bulk metal contained a very fine γ/γ' structure as well as coarse intermetallic β phase (NiAl) and χ phase (Co_3W).

200 hours oxidation - As the chromium content is reduced from 17 at. % to 15 at. % as well as the reduction of aluminium content from 12 at. % to 10 at. %, good oxidation resistance is still observed (Figure 5.8 (17Cr-12Al)). Alloy 15Cr-10Al is also forming a continuous Al_2O_3 layer together with blocky internal oxide (Figure 5.8 (15Cr-10Al)). The χ phase is rich in tungsten and tantalum, Co_3(W-Ta). The γ' volume fraction in the bulk is reduced as most of the aluminium has diffused out towards the surface to form a protective Al_2O_3 layer. As the proportion of cobalt is increased to give Co:Ni ratio of 1.3:1, whilst chromium is increased to 17 at. %, the formation of non-continuous Al_2O_3 layer resulted as well as an increase in the thickness of the external scale as shown in Figure 5.8: EsB-SEM micrographs of cross-sectional of the oxidised V208 alloys at 800 ºC classified into their main compositions vs. the oxidation time (200 hours and 300 hours).

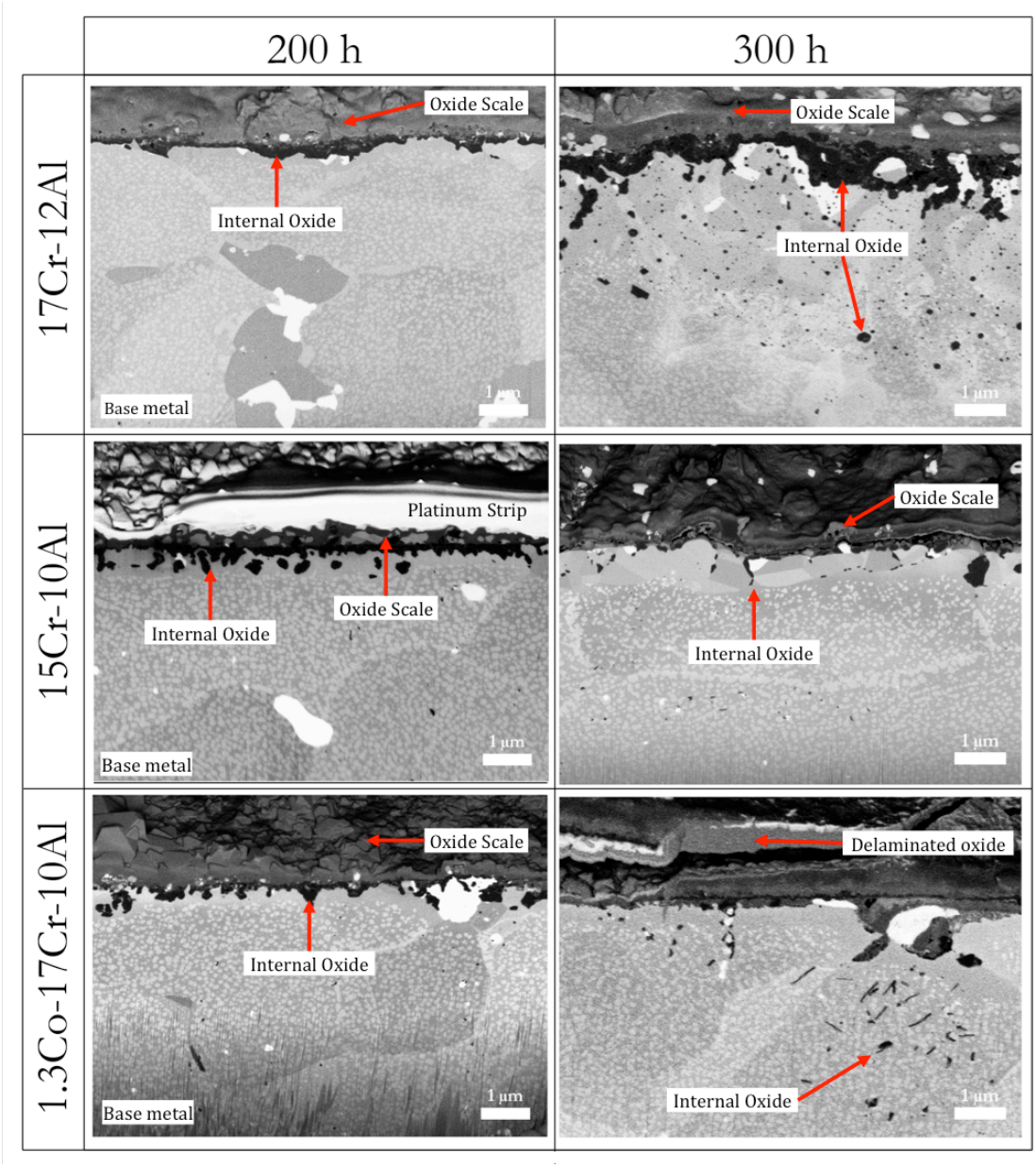


Figure 5.8: EsB-SEM micrographs of cross-sectional of the oxidised V208 alloys at 800 ºC classified into their main compositions vs. the oxidation time (200 hours and 300 hours).

300 hours oxidation - After 300 hours of oxidation at 800 ºC, thicker oxides were formed on the surface as shown in Figure 5.8 (300 h). Major changes can be seen in the scale thickness of the external scale and the formation of recrystallised grains in the γ'-depleted zone. Alloy 17Cr-12Al forms a large amount of internal oxide Al_2O_3, though there is a thick external oxide layer on the surface. The formation of internal alumina proved that the external scale is not protective, it allows oxygen to diffuse through and form internal oxide via grain boundaries.

The unique observation in alloy 15Cr-10Al is the recrystallised grains that formed in the γ'-depleted zone. The internal oxide was mostly found to form on the surface as well as intergranularly in the region of recrystallised grains. Despite the thin oxide scale thickness of this alloy being consistent in comparison to the other two alloys, the presence of voids between the external and internal oxides is of concern.

An issue of even greater concern is the spallation of the external scale, which in this case, was observed in alloy 1.3Co-17Cr-10Al. A trench was FIB milled in an area where the oxide had spalled, as seen in Figure 5.8. A thin external oxide that is almost completely delaminated can be seen on the surface. Even though there was no trace of spalled oxide in the crucible, delamination of external scale is an early sign of spallation. Also, there is an uncommon phase in the bulk with a plate-like morphology, which has the same contrast in EsB-SEM mode as the Al_2O_3 scale. Often in nickel superalloys, aluminium nitride (AlN) can co-occur with alumina internal oxides [17-18], but in the present case no nitrogen signal was detected in STEM-EDX examination, which will be discussed later in this chapter.

5.2.2 Spallation behaviour of surface scale

The surface of the spalled oxide was examined in the SE mode as shown in Figure 5.9.

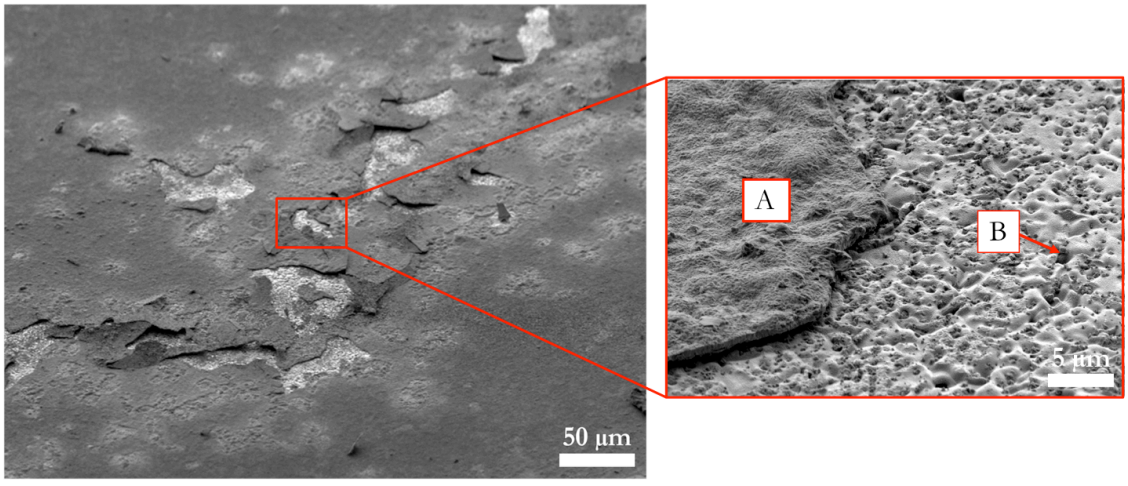


Figure 5.9: Electron micrographs (SE mode) of the surface oxide and the exposed surface after spallation occurred in alloy 15Cr-10Al after oxidation for 1000 hours at 800 ºC in air and the magnified view of the scale that is still intact (scale A) and exposed surface after spallation (surface B).

The area of examination was chosen to include both exposed surface (surface B) and the surface that was not well adhered to the substrate (scale A). The surface of the exposed area is full of particles, which is deemed to be the remainder of the spalled oxide, labelled as B in Figure 5.9.

The EDX point analysis of both scale A and surface B is tabulated in Table 5.3. The chemical compositions indicate that both have the same compositions, which is alumina. The evolution of the surface scale in this alloy indicates that the alumina-rich oxide is forming outward into a less adherent scale after oxidation at 800 ºC from 200 hours to 300 hours (Figure 5.8) and finally spalled after 1000 hours (Figure 5.9). The spallation mechanism can be explained by the famous study by Evans et al. where the spallation occurs under compressive in-plane stress in the oxide layer via buckling [58].

Table 5.3: EDX chemical compositions of the delaminated surface oxide (point A) and the particles on the surface (point B) for alloy 15Cr-10Al after oxidation at 800 ºC for 1000 hours in air.

Point EDX	C	O	Al	Cr	Co	Ni	W
Point A	8.2	63.1	21.2	2.5	2.8	1.5	0.2
Point B	11.2	43.4	22.0	6.0	10.6	5.6	1.0

5.3 Selected Alloy – 15Cr-10Al

5.3.1 Long-term oxidation

Since alloy 15Cr-10Al has less external oxide, a continuous internal Al_2O_3 layer, and a stable underlying microstructure, it was selected for long-term oxidation trials for 400 hours, 1000 hours and 2000 hours in air. After long-term oxidation at 800 ºC for 400 – 2000 hours, severe internal oxidation took place in the oxide/alloy region as seen in Figure 5.10. After 1000 hours, the oxide scale is producing a crack and started to delaminate for the surface, leaving the exposed surface unprotected. This caused rapid internal oxidation as observed in Figure 5.10 with plate-like alumina forming in the bulk metal. One important observation in the bulk metal concerns the γ' shape and volume fraction near the surface region. Due to the diffusion of aluminium towards the surface to form a protective Al_2O_3 layer, the γ' shape has evolved to become spherical-like and less in volume in the bulk.

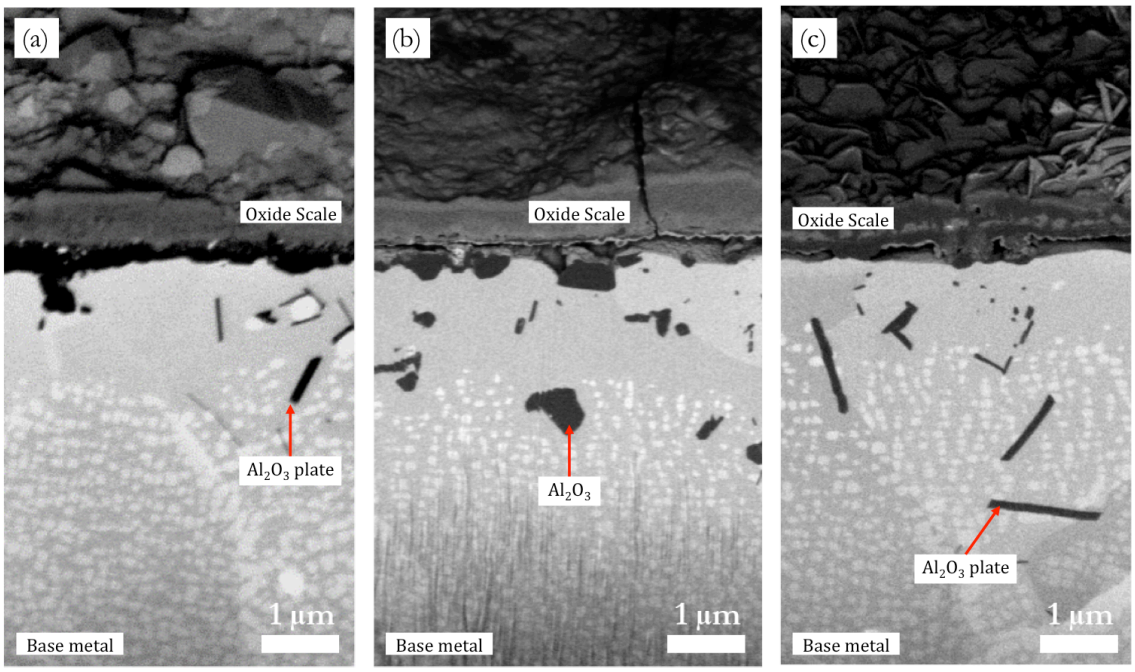


Figure 5.10: EsB-SEM micrographs of alloy 15Cr-10Al after oxidation at 800 ºC for (a) 400 hours (b) 1000 hours (c) 2000 hours showing the cross-sections with external and internal oxides, voids, crack, γ'-depleted zone, alumina plates and a γ/ γ' microstructure in the base metal.

A STEM-EDX analysis was performed to obtain the elemental maps of alloy 15Cr-10Al after oxidation at 800 ºC for 1000 hours to determine the plate-like composition of the phase as shown in Figure 5.11. The maps of chromium and aluminium were observed on the oxide scale area and a

point EDX on plate A (see Figure 5.11) was found to be rich in Al_2O_3, with no nitrogen found as reported by previous studies [159], [160]. Particle B and C in Figure 5.11 were found to be the χ phase, Co_3(W-Ta) and the Ta-Zr carbide respectively.

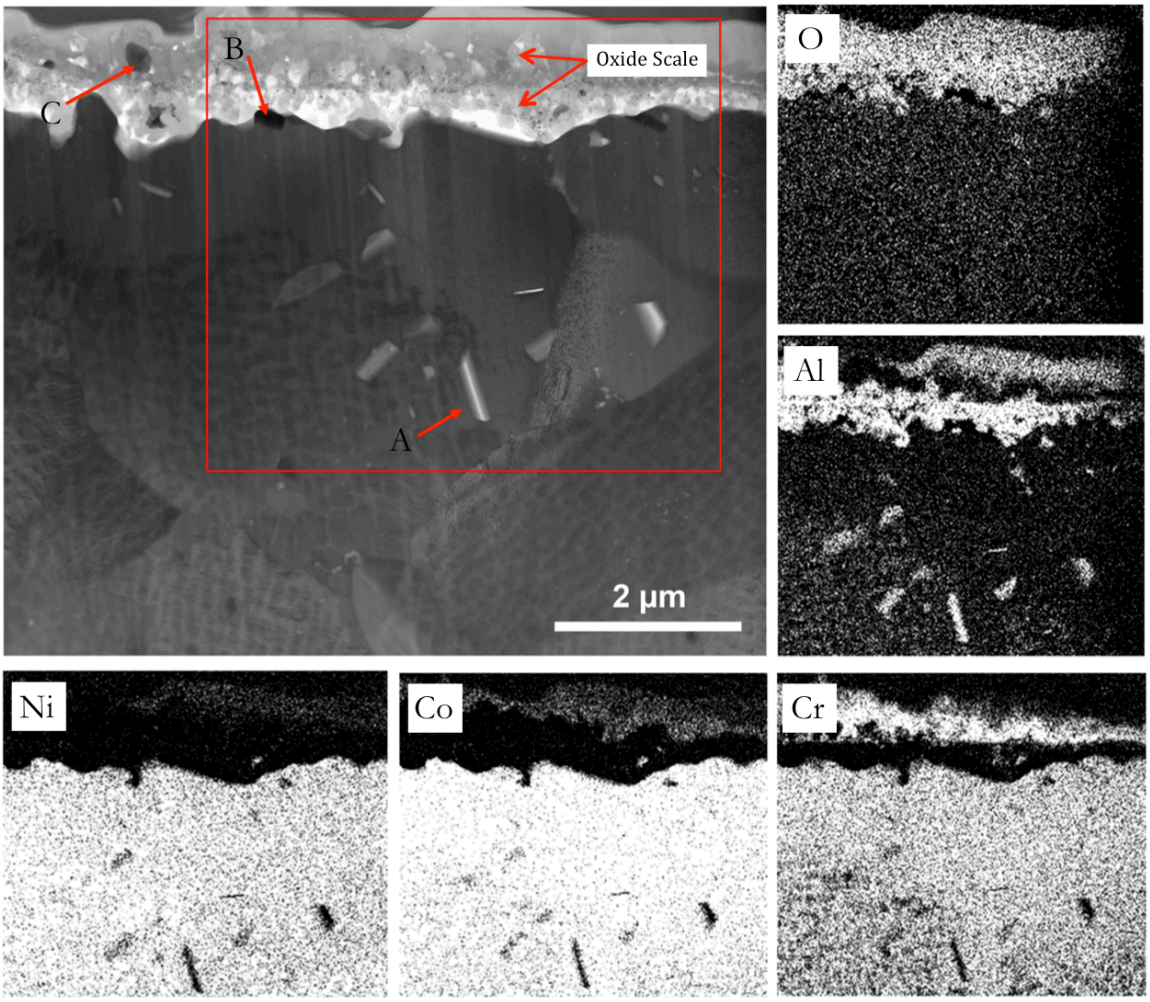


Figure 5.11: STEM-EDX image of alloy 15Cr-10Al after oxidation at 800 ºC for 1000 hours and their elemental maps showing the distributions of elements forming the oxide scales, plate A, particles B and particle C as well as the base metal.

5.3.2 FIB-SIMS elemental mapping of $^{16}O^-$ and $^{18}O^-$

Typically, the studies of oxidation mechanism using isotopic oxygen are conducted using SIMS analysis. The distribution of the tracer oxygen by SIMS is easily acquired by oxygen mapping on the cross-section (ramp) of the sample. In this case, where the oxide is very thin, producing a tapered oxide can elongate the scale. The analysis results will have clear and more reliable information on the distribution of the isotopic tracer as well as other elemental distributions. Tapered sections of the

surface scales were analysed in SIMS to examine the elemental distribution in the scale. The distribution of the tracer oxygen ($^{18}O_2$) is a crucial indicator of the oxide growth mechanism [69].

Figure 5.12 shows a FIB cross-section of the surface layers in alloy 15Cr-10Al following exposure at 800 ºC for 200 hours (176 hours in $^{16}O_2$ and the remaining 24 hours in $^{18}O_2$). The FIB-SE image of the tapered oxide shows the surface of oxide, a section through the oxide scale containing alumina (dark contrast), the internal oxides, and the base metal.

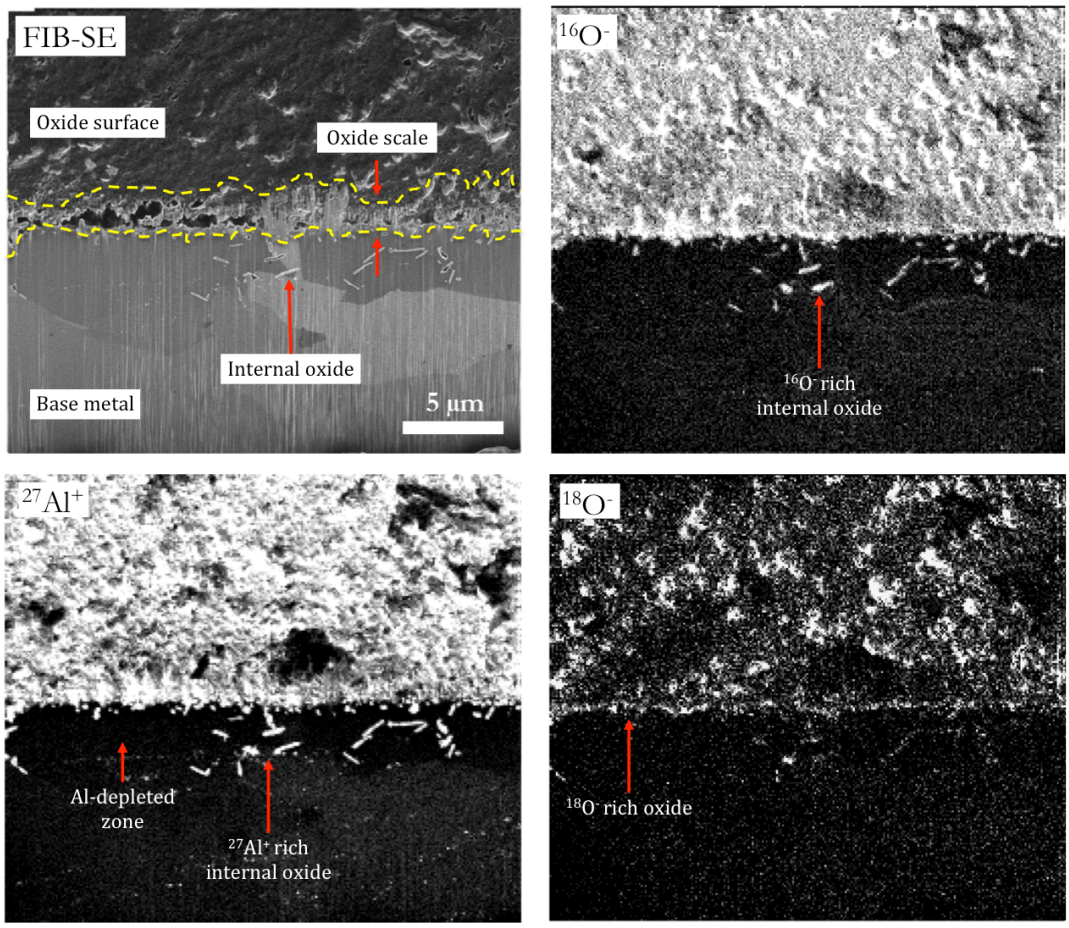


Figure 5.12: FIB-SIMS oxide ramp for alloy 15Cr-10Al following exposure in oxygen (200 mbar) at 800 ºC for 200 hours (a) FIB-SE image showing the oxide scale and internal oxide (b) FIB-SIMS elemental mapping of $^{16}O^-$ (b) FIB-SIMS elemental mapping of $^{27}Al^+$ (c) FIB-SIMS elemental mapping of $^{18}O^-$

Figure 5.12 (b) – (d) show the FIB-SIMS $^{16}O^-$, $^{27}Al^+$ and $^{18}O^-$ elemental maps obtained on the tapered oxide. The FIB-SIMS maps of $^{16}O^-$ and $^{18}O^-$ show the relative distributions of the species. By normalising the pixel intensities to the maximum counts in each array, the $^{16}O^-$ map represents the oxide growth that occurs in the first part of the two-stage exposure. Note that the high intensity of $^{16}O^-$ signals in the outer oxide layer and some in the internal oxide correlate to the $^{27}Al^+$ signal, which is deemed to be the formation of protective Al_2O_3. The $^{18}O^-$ ion distribution indicates that the oxide

is enriched at the surface closest to gas-oxide region, oxide scale (Al_2O_3 layer) and the internal oxide region.

This phenomenon indicates that the new oxide is formed at the oxide-alloy region as well as gas-oxide interface. This finding is in line with the oxidation mechanism of nickel base superalloy (particularly RR1000) as reported by Foss et al., where Cr_2O_3 typically grows through outward cationic diffusion which explains the new oxide at the gas-oxide region [20-21]. Therefore, it is reasonable to assume that the oxide grows through both inward diffusion of oxygen anions (oxygen) and outward diffusion of cations (chromium).

5.3.3 Isotopic fraction (f) maps and intensity peaks

In order to eliminate any instrumental ionisation effect, the isotopic fraction was calculated from both FIB-SIMS maps of $^{16}O^-$ and $^{18}O^-$. The isotopic fraction f was calculated as the fraction of the detected oxygen signals I due to $^{18}O^-$,

$$f = \frac{I_{18_O-}}{I_{16_O-} + I_{18_O-}} \qquad \text{Equation 5.1}$$

Note that the isotopic fraction is normalised relative to the natural abundance (0.26%) and the tracer gas concentration at the time the experiment was taking place (54%). In Figure 5.13 (a), the blue regions indicate low $^{18}O^-$ enrichment, whereas the red regions imply high enrichment. It can be seen in Figure 5.13 that the $^{18}O^-$ enrichment is localised, at the oxide-alloy interface (Al_2O_3) and in the internal oxide (plate-like Al_2O_3) regions. The $^{16}O^-$ and $^{18}O^-$ intensity peaks in Figure 5.13 (b) show high intensity at the oxide-alloy interface. Hence, the new oxide is still forming at the Al_2O_3 region in the second stage exposure. The peak $^{16}O^-$ and $^{18}O^-$ intensity at the oxide-alloy interface suggests that there was an accumulation of oxygen species at the oxide-alloy interface, particularly in the Al_2O_3 region. Note that after both peaks, the enrichment does not fall to zero. This can be regarded as 'noise', since no internal oxidation takes place beyond this point, as indicated in Figure 5.13 (b).

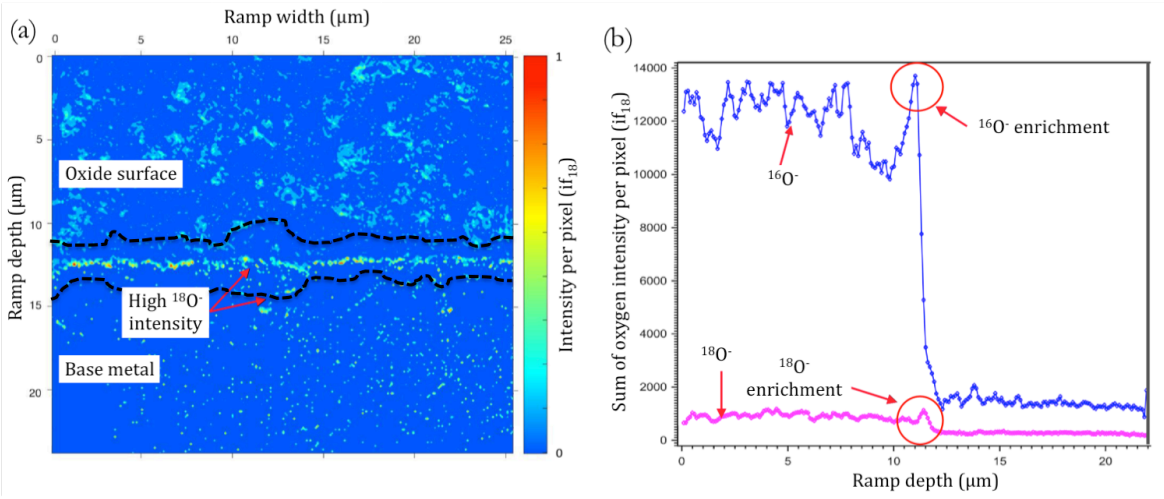


Figure 5.13: Isotopic enrichment of $^{18}O^-$ in alloy 15Cr-10Al after oxidation at 800 ºC for 200 hours showing (a) isotopic fraction (*f*) map (b) $^{16}O^-$ and $^{18}O^-$ intensity peaks along the depth profile. The isotopic enrichment map is based on the same FIB-ramp area as in Figure 5.12.

5.3.4 STEM-EDX analysis

Based on the micrograph of alloy 15Cr-10Al after oxidation at 800 ºC for 200 hours in Figure 5.8, STEM-BF elemental maps were obtained to better understand the types of oxide formed. The STEM-BF image of alloy 15Cr-10Al in Figure 5.14 is consistent with the scales as seen in Figure 5.8, where there are two types oxide formed; i) is the external oxide ii) the internal oxide in different EsB-SEM contrasts. The scale was comprised of outer chromium-rich oxide (scale 1) and inner aluminium-rich oxide (scale 2). Due to the accuracy limitations of STEM-EDX analysis, the crystal structures of the oxides were determined using high resolution TEM (HRTEM) for stoichiometric determination, which will be discussed in the next section.

It is also noted from the STEM-EDX maps in Figure 5.14 that chromium and cobalt partitions to the γ matrix, whilst aluminium, nickel and tungsten partitions to the γ' precipitates.

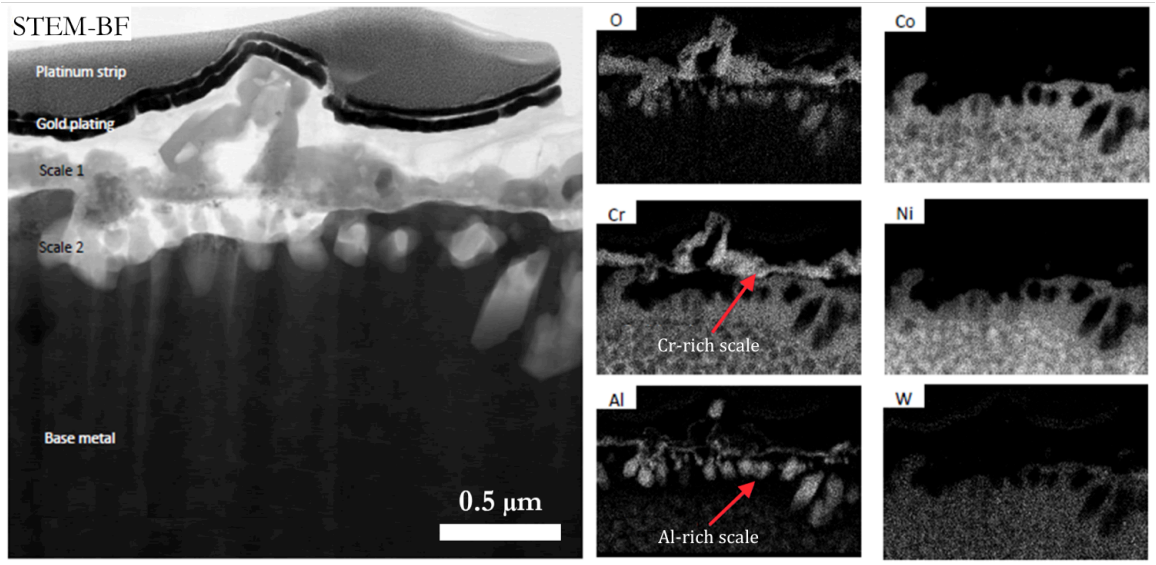


Figure 5.14: STEM-BF image of alloy 15Cr-10Al oxidised for 200 hours at 800 ºC showing a chromium-rich oxide scale (scale 1), an aluminium-rich internal oxide (scale 2).

A STEM dark field (DF) image of the same alloy was acquired in order to study the mechanism of oxide fomation after a long-term exposure (300 hours). Figure 5.15 is in agreement with the EsB-SEM result in Figure 5.8, where delaminated external oxide and recrystallisation can be clearly observed in the γ'-depleted zone. The external aluminium-rich oxide was formed through the outward migration of aluminium from the bulk, particularly through the grain boundaries of the recrystallized grains. Between the scale and the base metal, a cavity is present along the interface and ligaments of aluminium-rich scale, which contained some Cr_2O_3, support the scale. It appears that surface scale is too thin to support a stress; therefore cavity formation occurs prior to spallation. In any case such cavity formation would seem to be deleterious to the oxidation performance of the alloy. By comparing the STEM-EDX results after oxidation for 200 hours and 300 hours, it can be clearly seen that the aluminium is migrating outwards which protects the surface from oxidising further.

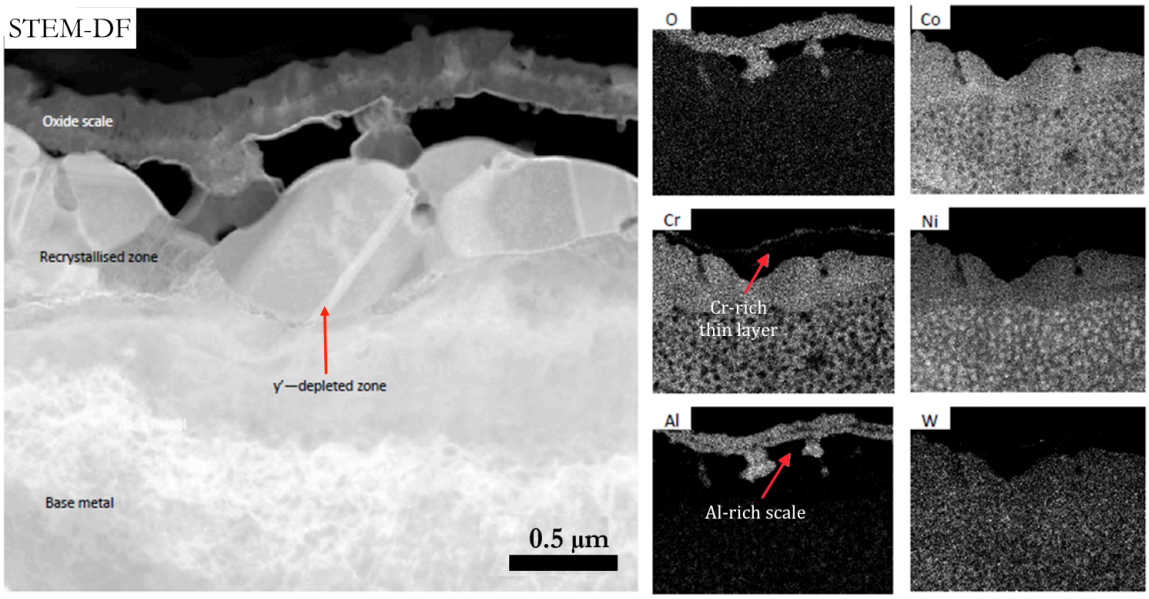


Figure 5.15: STEM-DF image of alloy 15Cr-10Al oxidised for 300 hours at 800 ºC showing a delaminated aluminium-rich oxide scale with a thin layer of Cr_2O_3 and recrystallized region at the γ'-depleted region.

5.3.5 High resolution TEM examination

The EsB-SEM micrograph in Figure 5.8 and STEM-EDX maps in Figure 5.14 of alloy 15Cr-10Al, oxidised for 200 hours at 800 ºC, provide initial indication of the compounds that form in this alloy series during oxidation. There were two distinct types of oxides known; i) a chromium-rich external scale and ii) an aluminium-rich internal oxide. However, it is difficult to determine the crystal structures using selected area diffraction patterns as the oxides grains were too fine.

Therefore, to identify the oxide compounds present in these layers, pseudo-diffraction patterns were obtained from individual grains in the TEM. The inter-planar spacings were measured from Fast-Fourier transforms (FFT) of the lattice images. The calculated lattice constants were compared to the literature values and thus the chemical identities of the oxides were determined. This approach is similar to the work of Yan et al., where different layers of oxides with mixed spinels were successfully identified in a Co-7Al-7W-10Cr (at. %) alloy [95].

The compositions of the two layers of oxides in alloy 15Cr-10Al were determined by point EDX in STEM-BF and the average values were calculated. To confirm the oxide phase, high-resolution phase contrast lattice imaging was performed and the points noted as A, B and C in Figure 5.16 are the small-grained areas where the oxides were examined. The frequency domain images in Figure 5.17 were compared to simulated diffraction pattern generated using the Crystal Maker software.

By measuring the angles and distances between the spots in the frequency domain images and comparing them to the simulated diffraction patterns, the oxides labelled in Figure 5.16 are identified as A: Co_3O_4, B: Cr_2O_3, and C: Al_2O_3. The different oxide layers are also shown, in the same TEM foil, in Figure 5.14, which uses a different contrast optimisation.

The average lattice constant of Co_3O_4 was measured to be 8.06 Å, which is close to the lattice constant in the literature 8.17 Å [161]. The Cr_2O_3 has a hexagonal structure with average measured lattice constants of a = 4.97 Å and c = 13.56 Å. The lattice constants in the literature are a = 4.96 Å and c = 13.59 Å [162]. The inner layer of the oxide is confirmed to be Al_2O_3 with an average calculated lattice constant of a = 4.29 Å and c = 12.24 Å. These measured lattice constants matched the trigonal structure found in the literature, with average lattice constants of a = 4.76 Å and c = 12.99 Å [163].

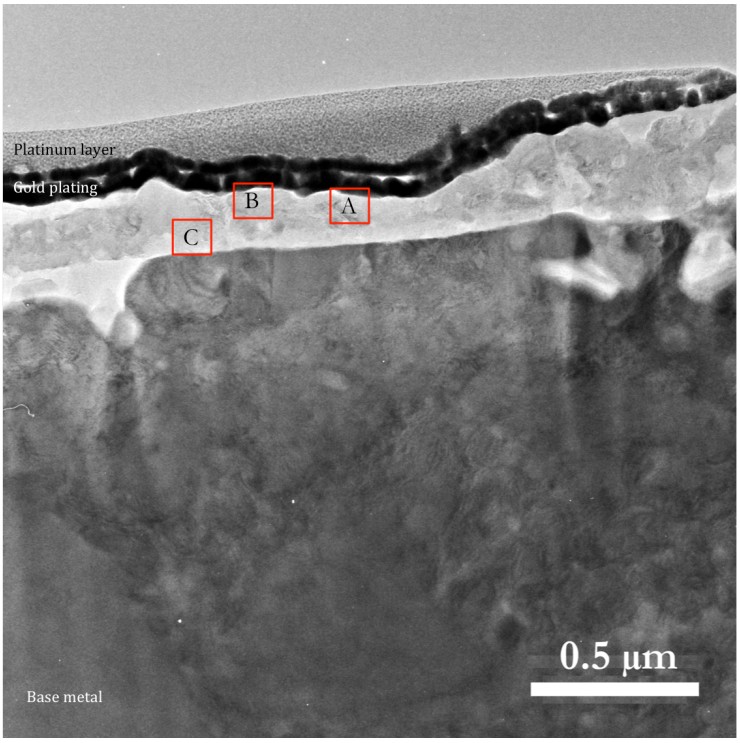


Figure 5.16: Overview of the oxidised alloy 15Cr-10Al after 200 hours at 800 ºC obtained from a FIB-milled TEM foil using STEM-BF imaging mode. Lattice images of grains in region A, B and C were obtained using HRTEM and frequency domain images were obtained using FFT in ImageJ.

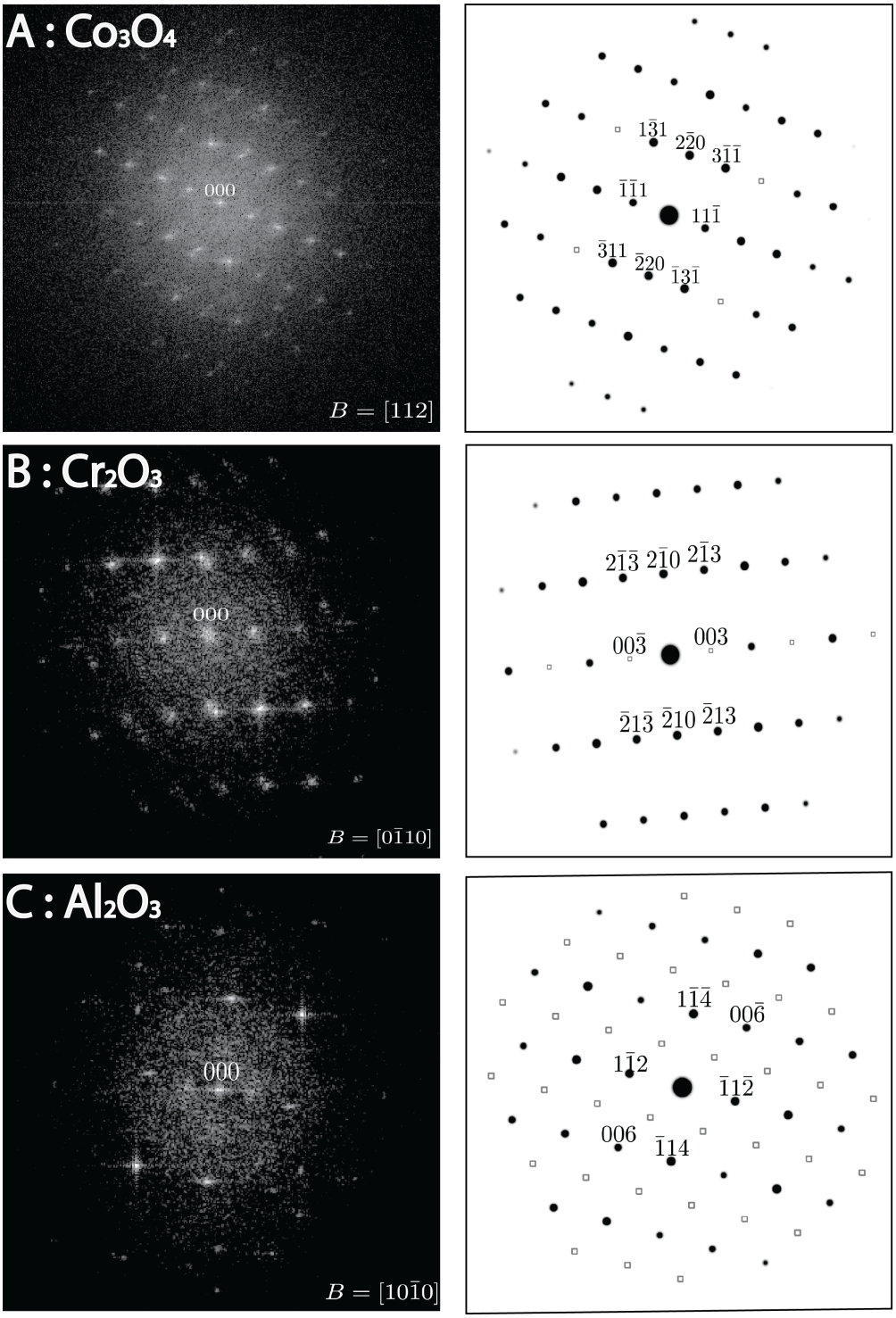


Figure 5.17: Frequency domain images (left) from the oxide scales in alloy 15Cr-10Al oxidised for 200 hours at 800 ºC with a labelled zone axis and the corresponding simulated diffraction patterns (right). Note: systematic absences are represented by squares.

5.4 Discussion

The objective of the work presented in this chapter is to select the optimal Co:Ni ratio and the optimum fractions of chromium and aluminium for obtaining the best oxidation resistance while maintaining a stable underlying microstructure. A typical cross-sectional microstructure of an oxidised sample can be divided into five zones: (1) the external scale (2) the internal oxide (3) the γ'-depleted zone (containing ultra-fine precipitates of γ' or sometimes recrystallised grains) (4) the round edged γ' precipitates below that and (5) the typical cuboidal precipitates in the bulk alloy (as well as the intermetallics β phase (NiAl) and χ phase (Co_3W or $Co_3(W\text{-}Ta)$).

After 200 hours of oxidation at 800 ºC, all three alloys exhibited a similar oxide morphology in which there were two external oxides (chromium-rich and aluminium-rich scales) of sub-μm thickness and internal alumina, Figure 5.8. Distinctions between the three alloys could only be made after 300 hours of oxidation at 800 ºC. The differences noted: (a) the external oxides were thickest in alloy 17Cr-12Al, (b) the internal oxide intrusions formed in alloy 15Cr-10Al and (c) the external oxide delamination was observed in alloy 1.3Co-17Cr-10Al.

Alloy 1.3Co-17Cr-10Al oxidised more rapidly compared to the other two alloys based on the thickness of the scales. Even with 10 at. % of aluminium and higher chromium content (17 at. %), the alloy exhibits poor oxidation resistance. The only possible reason for this is the amount of cobalt. As we change the Co:Ni ratio from 1:1 to 1.3:1, the oxidation resistance is reduced. Furthermore, as the chromium content was increased to 17 at. %, the β phase was found in the bulk, which is undesirable for mechanical properties.

The FIB-SIMS mapping reveals that there is $^{16}O^-$ and $^{27}Al^+$ enrichment at the oxide-alloy interface (oxide intrusion) and that the new oxide ($^{18}O^-$ -enrichment) is also formed in the vicinity of the metal-oxide interface. Nevertheless, it can be concluded from the maps that $^{16}O^-$ is observed in the inner part of the oxide scale, enriching the alumina scale and subsequently limiting further diffusion of $^{18}O^-$. The transport mechanism during oxidation at 800 ºC for 200 hours is outward cationic transport (chromium and aluminium) and inward anionic transport via grain boundaries [69].

The HRTEM results are in agreement with the established thermodynamic rules of partial pressure of oxygen [50], where at high oxygen partial pressure, the outer oxide layer Co_3O_4 forms first then Cr_2O_3 underneath and lastly Al_2O_3 developing the internal oxide at low oxygen partial pressure with low diffusivity of oxygen compared to the other two oxides.

5.4.1 The effect of Cr:Al ratio in Co-Ni base superalloys in terms of phase stability and oxidation resistance

It is crucial to find the optimised content of chromium and aluminium in the alloy compositions for the purpose of oxidation resistance whilst maintaining the desired mechanical properties by controlling the formation of secondary phases. Therefore, Figure 5.18 relates the optimum atomic ratio of Cr:Al to the oxidation damage depth (in μm thickness) after 200 hours and 300 hours of thermal exposure. The data suggest that the overall best Cr:Al atomic ratio is 1.5:1. As the exposure time increased, the external oxide (Cr_2O_3) is not protective and the internal oxidation occurs to a greater depth, forming plate-like Al_2O_3 in the bulk material. At the same time, alumina grows outward forming external scale that in some cases delaminates from the surface.

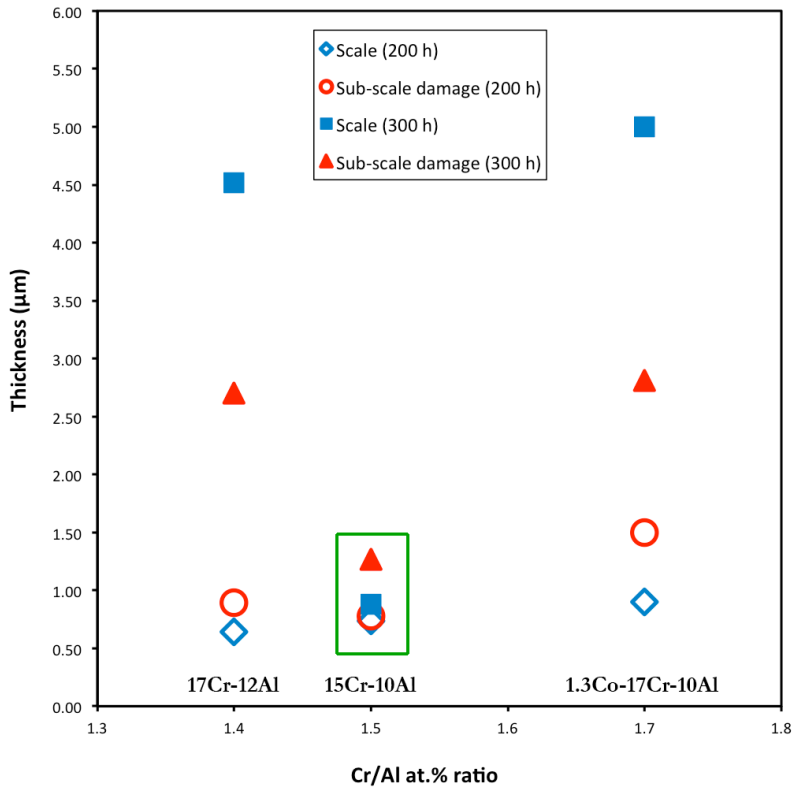


Figure 5.18: Variation of oxidation damage depth with Cr:Al atomic ratio.

5.4.2 Mechanism of oxide formation in Co-Ni base superalloys

This study of oxidation for Co-Ni base superalloys at 800 ºC, from 200 hours to 2000 hours has led to the identification of a change in mechanism of oxide formation from transient oxidation period to long-term exposures. Figure 5.19 shows the schematic representation of the mechanism established.

Transient oxidation (< 100 hours) – Although the early stage of oxide formation (typically below 100 hours in nickel base superalloys) is not studied in this research, it is believed that at transient oxidation period, Co_3O_4 is formed at the early stage of oxidation. HRTEM result in section 5.3.5 proved that there is a small grain of Co_3O_4 region found on the outer scale after oxidation at 800 ºC for 200 hours, which is likely to be the remainder product from the transient oxidation period. Furthermore, due to the high nickel content in this alloy, NiO is also predicted to be formed on the surface in the early stage of oxidation.

Steady-state oxidation (200 – 300 hours) – At this stage, stable and protective oxides have formed on the surface. These oxides, chromia and alumina, are fully developed after oxidation at 800 ºC for 200 hours. Chromia is forming on the surface and alumina is forming as internal oxides. During the formation of alumina, a precipitate-free region can be found underneath the internal oxide. This is due to the depletion of aluminium from the precipitates to form alumina at the oxide-alloy interface. Between 200 hours and 300 hours, recrystallisation started to occur at this precipitate-free region. Internal oxidation can be found along the grain boundaries of the recrystallized grains, which act as diffusion paths for cations to migrate towards the surface to form oxides.

Delamination and spallation (400 hours) – Delamination of oxide scale started from void or cavity formation between the oxide-alloy interface. This is due to the poor adherence of oxide scale to the metal surface and the oxide scale is thin. In this case, the oxide scale, which is chromia, started to buckle and spall, exposing the underneath layer, alumina. Moreover, due to the prolonged oxidation time, internal oxides (alumina) grew thicker, there were more intergranular alumina formed and this formation went deeper into the bulk. This phenomenon is caused by the grain growth in the recrystallised region. Plate-like alumina can also be found deep in the bulk metal.

Re-growth of exposed surface (>1000 hours) – At this stage of exposure, the exposed alumina on the surface started to develop into facetted morphology. It is believed that the surface is still protected from rapid oxidation, however, the oxidation rate will not be as slow as when chromia is present. Internal oxidation is less, due to cations migrating outward to form alumina on the surface.

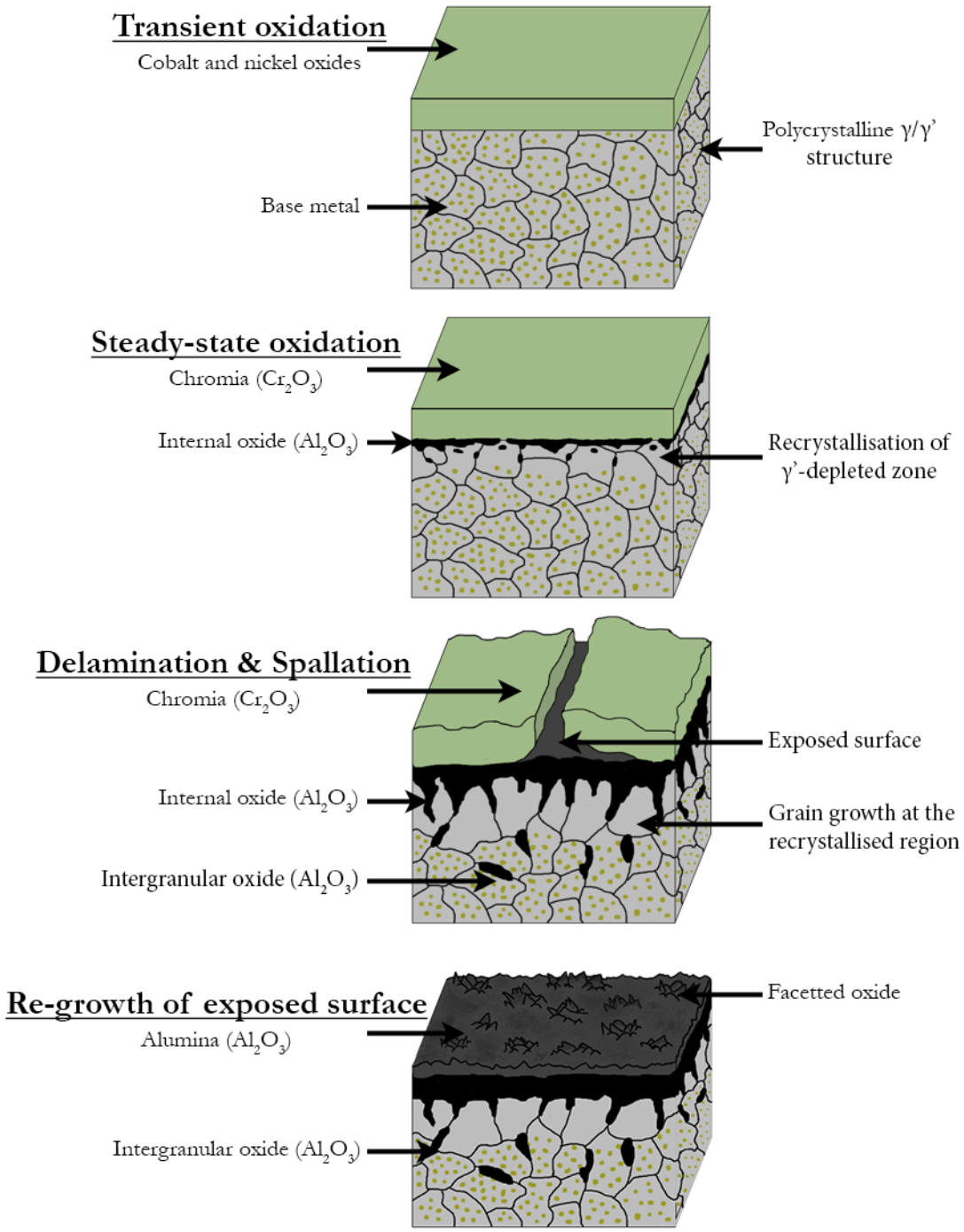


Figure 5.19: Schematic representation of the mechanism of oxide formation in 15Cr-10Al alloy after oxidation at 800 ºC from early stage oxidation (transient period) to 2000 hours (re-growth).

5.5 Conclusions

In this study, the experimental evidence suggested that oxidation-resistant, protective oxide scales can be formed in Co-Ni superalloys. The following conclusions can be drawn in terms of chromium and aluminium content; 15 at. % of chromium and 10 at. % of aluminium produced a multilayer oxide scale and internal alumina which is protective and limits the inward diffusion of oxygen at 800 ºC for 200 hours. A very thin sub-μm oxide scale was formed in all of the alloys after oxidising for 200 hours at 800 ºC. However, a high percentage of chromium and cobalt caused further oxidation of the samples at longer exposure times.

Significant internal oxidation was observed, with plate-like alumina forming during long-term oxidation, even with optimal Cr:Al ratio. Alloy 15Cr-10Al maintained a two-phase γ/γ' microstructure with minimal secondary phase formation.

6 Specific V208 alloys - The Effect of Shot-Peening on the Oxidation Behaviour

6.1 Introduction

According to the previous chapter, the optimisation of chromium and aluminium percentage in the V208 alloys played an important role in achieving the most stable protective oxide layer. Consequently, in this chapter, further studies have been made to examine the effect of shot-peening on the oxidation performance. It is known that shot-peening is useful in extending the service life of a component through the introduction of compressive stresses in the surface. Several studies have found positive effects of cold work on the surface finish, which promotes the formation of protective oxide layers on the surface [164]–[167].

The formation of short diffusion paths for transport of oxygen or other species (cations) after shot-peening increases the formation of chromium oxide thereby protecting the surface from oxidising. This phenomenon is observed at above 700 ºC for low chromium content (12 at. %) steels and RR1000 (15 at. %) [70], [72], [165], [78]. According to Wagner's theory of oxidation, the diffusion of cations and anions mainly influence the growth rate of oxide scales [54]. This can be explained by the fact that cold working near the surface influences the microstructure, in a way that dislocations and grain boundaries are assisting the diffusion of cations to the surface and form a protective oxide through the diffusion paths.

Shot-peening in a nickel base superalloy (RR1000) increased the surface hardness and roughness resulting in an increase in the number of dislocation density near the surface as well as an altered microstructure [72], [77], [75]. The hardness values were considerably higher near the surface region and recrystallisation occurred in the near surface region, establishing more outward diffusion paths of cations via grain boundaries. Based on the study performed by Naraparaju et al., the reliability of having a positive effect on shot-peening in oxidation resistance is only accountable when the chromium content is high enough to form a chromia layer on the surface [165]. The increased chromium supply through dislocations leads to a change in the kinetics of oxidation, which strongly

affects the subsequent stability of the formed passive oxide scales. However, the effect of higher temperature was observed in low chromium content steels (12 at. %) after oxidation at 750 ºC where shot-peening considerably increased the diffusion of chromium to the surface.

Shot-peening could be expected to have a similar result in the selected V208 alloys and the effect of chromium and aluminium content will be discussed later in this chapter.

6.2 Oxide Cross-Section Morphology

A typical oxide cross-section morphology is shown in Figure 6.1 for both polished and shot-peened specimens after oxidation at 850 ºC for 200 hours. The EsB-SE micrograph of a polished specimen in Figure 6.1 (a) shows oxides in dark contrasts consisting of external and internal oxides. The external and internal oxides are known to be chromia and alumina (from the previous chapter), and it was found that an increase in temperature gradually increases the thickness of the scales. The oxides are adherent to the surface, protecting it from further oxidation. The alumina intrusion formed intergranularly.

Discontinuous precipitates were observed in the base metal in the region near the γ'-depleted zone. The phenomenon of discontinuous precipitates in nickel-base superalloys have been reported by many, in which the metastable parent microstructure is transformed by boundary precipitation and interfacial migration with high degree of super-saturation of some elements in the γ/γ' alloy [168], [169]. The reaction most commonly observed at the grain boundaries in polycrystalline materials. It is worthy of note that this phenomenon is only observed in the V208 alloy series above 850 ºC oxidation temperature.

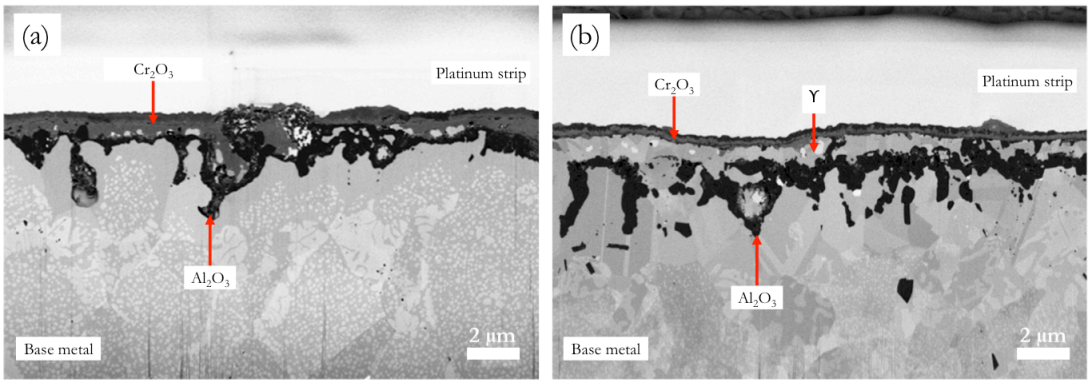


Figure 6.1: EsB-SE cross-section micrographs of alloy 17Cr-12Al after oxidation at 850 ºC for 200 hours for (a) polished surface (b) shot-peened surface.

Figure 6.1 (b) shows the effect of shot-peening on the surface and sub-surface structure in alloy 17Cr-12Al. Figure 6.2 shows the EDX elemental mapping of alloy 17Cr-12Al after shot-peening which revealed the high intensity of cobalt, chromium and tungsten found in between the external scale and internal oxide. The presence of these elements comprising the base metal (γ) between the external scale and the internal alumina proved that sub-surface damage from shot-peening has occurred to a minimal extent (less than 2 µm thick). Continuous alumina is still forming at the oxide-alloy region and internal oxidation is observed both intergranularly and intragranularly at a deeper range in the base metal, twice as thick compared to the polished specimen. Recrystallisation occurred at the γ'-depleted zone where the region is doubled to more than 5 µm deep. This extensive γ'-depleted zone formation is caused by the depletion of aluminium as a result of sub-surface alumina formation.

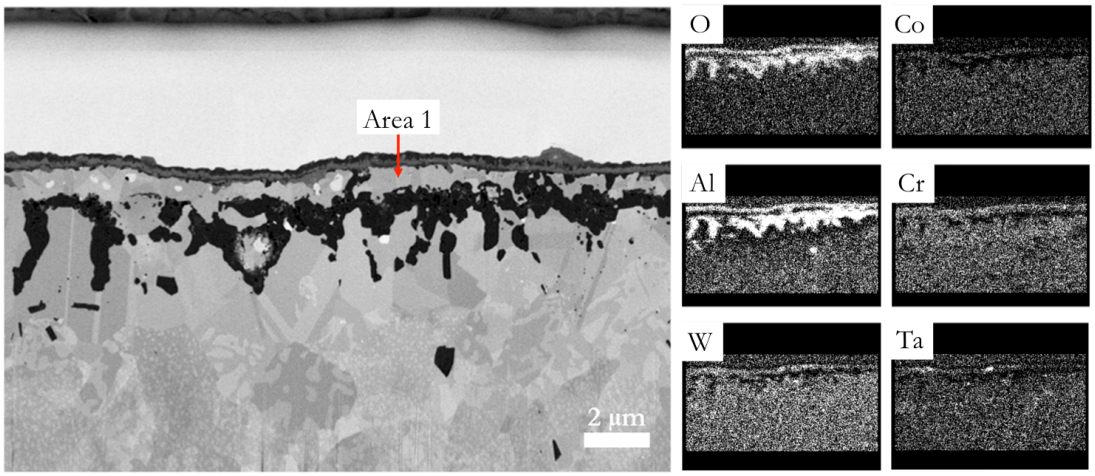


Figure 6.2: EsB-SE cross-section micrograph of alloy 17Cr-12Al after oxidation at 850 ºC for 200 hours and the elemental maps from the EDX analysis.

Despite the superior oxidation resistance of alloy 15Cr-10Al at 800 ºC for 200 hours (as discussed in the previous chapter), spallation of surface oxide was found in the case of the shot-peened specimen when the oxidation temperature was increased to 850 ºC. Figure 6.3 shows the SE micrographs of the surface oxide after oxidation at 850 ºC for 200 hours. The surface morphology of the polished specimen does not exhibit any signs of spallation. This is not the case in the shot-peened specimen, the less adherent external scale is exposing the underlying surface to further oxidation. A trapezium-shaped crater was prepared at the region indicated in Figure 6.3 (b) and is taken as the representative result for a shot-peened specimen in the case of spalled oxides.

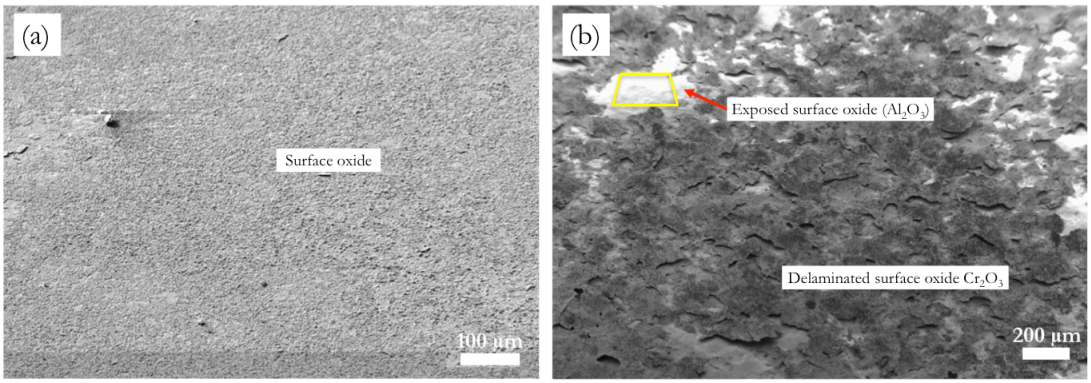


Figure 6.3: SE micrographs of the surface oxide of alloy 15Cr-10Al after oxidation at 850 ºC for 200 hours for (a) polished specimen (b) shot-peened specimen.

The effect of shot-peening on the underlying microstructure of alloy 15Cr-10Al can be seen in Figure 6.4. Higher oxidation temperature (850 ºC) does not yield a significant drop in terms of oxidation resistance in the polished condition for alloy 15Cr-10Al. However, the delamination of the surface

oxide has exposed the underlying oxide layer in the shot-peened condition. Shot-peening has increased the tendency of the surface oxide to delamination and spallation. The morphology of the internal oxide and the underlying γ'-depleted region is similar to the shot-peened specimen of alloy 17Cr-12Al.

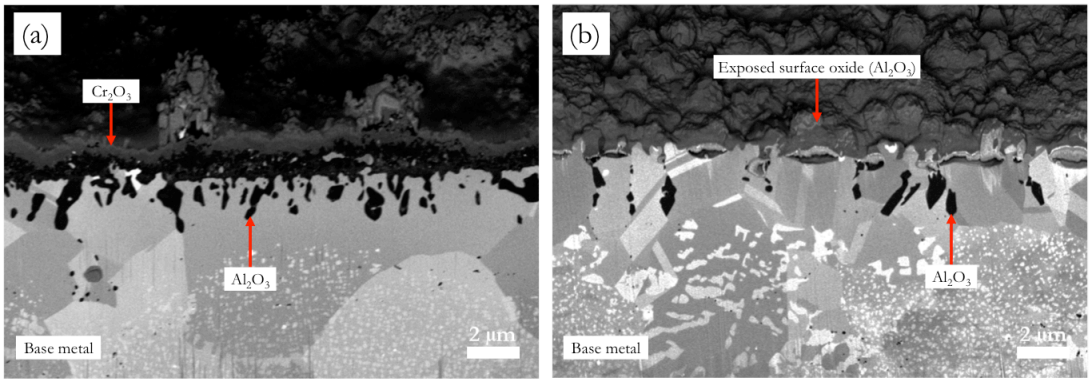


Figure 6.4: EsB-SE cross-section micrographs of alloy 15Cr-10Al after oxidation at 850 ºC for 200 hours for (a) polished surface (b) shot-peened surface.

Similar behaviour is reported in alloy 1.3Co-17Cr-10Al, where shot-peening has caused surface oxide spallation at 850 ºC for 200 hours as shown in Figure 6.5. It is worthy of note that in both cases of spallation, the amount of aluminium is 10 at. %, regardless of the high chromium content in alloy 1.3Co-17Cr-10Al.

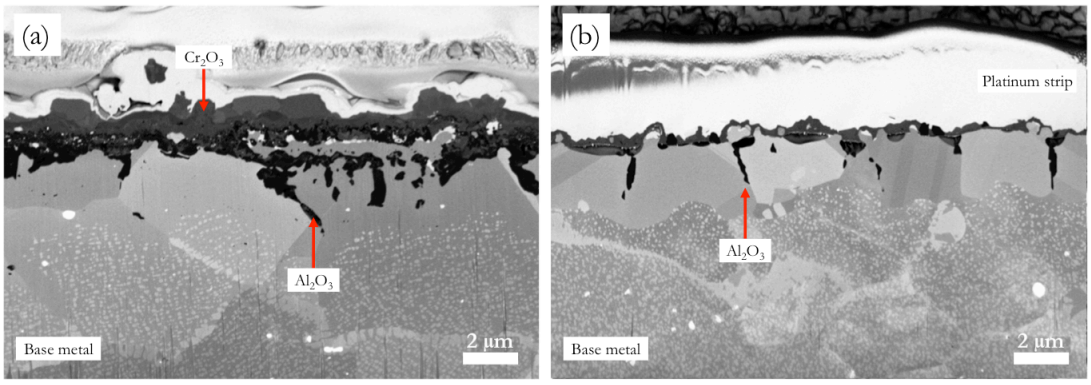


Figure 6.5: EsB-SE cross-section micrographs of alloy 1.3Co-17Cr-10Al after oxidation at 850 ºC for 200 hours for (a) polished surface (b) shot-peened surface.

6.3 FIB-SIMS Analysis

Figure 6.6 – 6.8 tabulates the FIB-SIMS cross-sections with their corresponding $^{16}O^-$ and $^{18}O^-$ elemental maps obtained after the pixel intensities have been normalised to the total counts in each array and the upper dashed yellow line represents the surface of the external oxide. The $^{16}O^-$ maps represent the oxide growth that occurs in the first part of the two-stage exposure and the $^{18}O^-$ represents the new oxide formed in the last 24 hours of the total oxidation time.

6.3.1 Elemental mapping of $^{16}O^-$ and $^{18}O^-$

Figure 6.6 shows the cross-sectional oxide morphologies of alloy 17Cr-10Al after oxidation at 850 ºC for 200 hours. Note that the $^{18}O_2$ exposure is in the last 24 hours of the oxidation time. The cross-sections, which are the projected depth of true oxide thickness, reveal the formation of an adherent external oxide scale with underlying internal oxides fingers at the bulk grain boundaries for the polished specimen. Similar observation can be found in the shot-peened condition, however, the internal oxide is thicker and regions of γ at the external-internal oxide can be found. Following this finding, this area is free of $^{16}O^-$ enrichment as shown in the $^{16}O^-$ map. The $^{16}O^-$ can be found enriching the external scale (Cr_2O_3) and the internal oxide (Al_2O_3). The same goes for the polished specimen where $^{16}O^-$ is enriching the external and internal oxide. No significant $^{18}O^-$ intensities were found at the oxide-alloy region.

Comparison of the $^{16}O^-$ and $^{18}O^-$ ion distributions for both polished and shot-peened specimens indicates that the external scale contains $^{16}O^-$-rich regions at the surface and within the internal oxide, forming a protective layer which inhibits further diffusion of oxygen at the later stage. No new oxides were formed at the gas-oxide interface or at the oxide-alloy interface. It can be concluded from the $^{18}O^-$ maps that the diffusion of $^{18}O^-$ is severely limited by the existing oxide scale

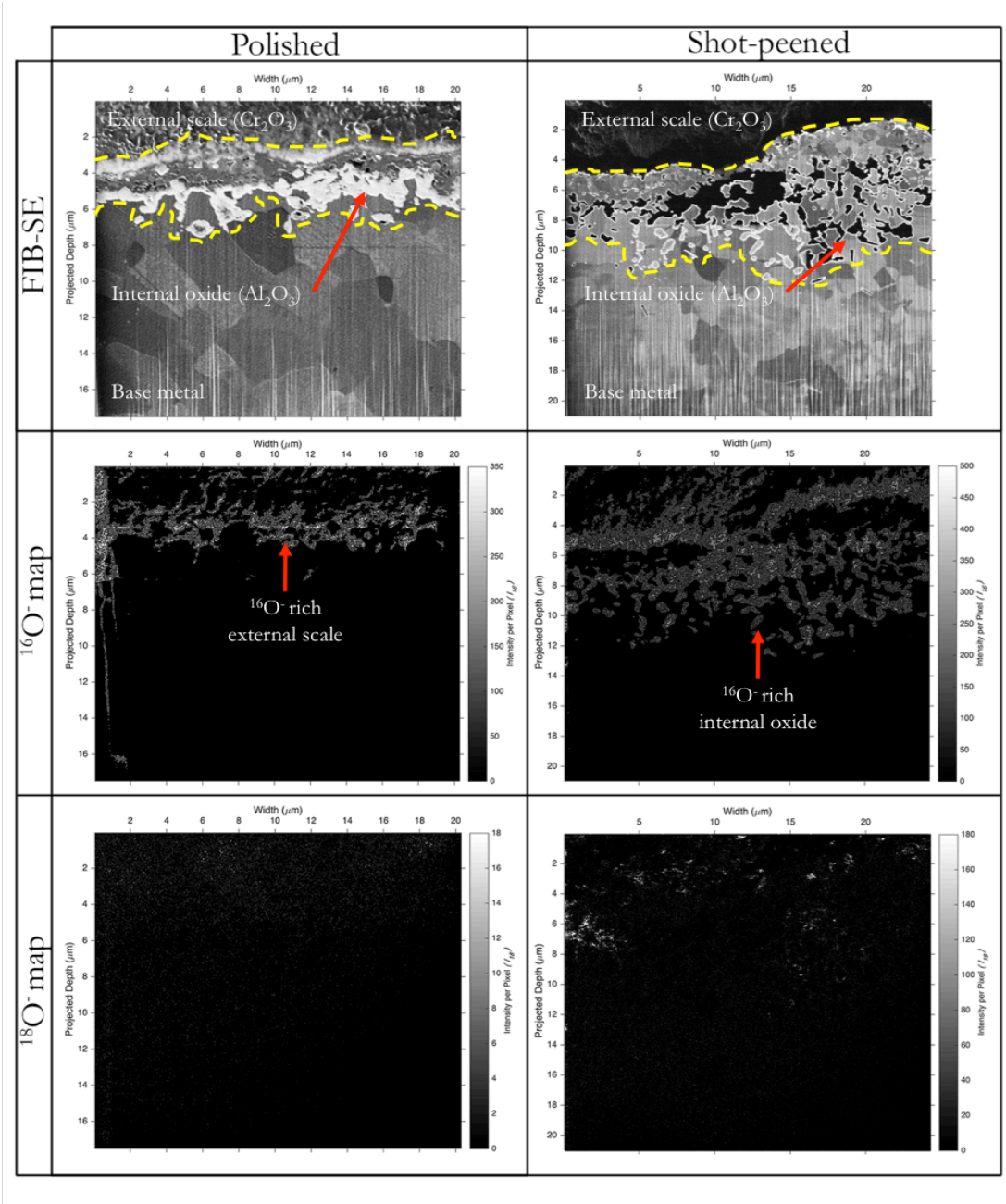


Figure 6.6: FIB-SEM oxide cross-sections of alloy 17Cr-12Al after oxidation at 850 ºC for 200 hours in polished and shot peened conditions with their corresponding $^{16}O^-$ and $^{18}O^-$ maps.

Figure 6.7 summarised the effect of shot-peening on alloy 15Cr-10Al, as previously discussed in sub-chapter 6.2. The oxidation resistance of this alloy remains excellent in the as-polished condition since there is no significant new oxide intrusion in the internal layer, which proves that this sample has developed a protective oxide layer. The external scale in the shot-peened condition, though, has exposed the underlying oxide (Al_2O_3) to further oxidation. Comparing the intensity of the $^{18}O^-$ signal at the gas-oxide and oxide-alloy interface with the intensity of $^{16}O^-$, the increase in $^{18}O^-$ concentration shows that the new oxide is forming at these regions. This proves that oxygen transport is taking

place through the external oxide to form new oxide at the oxide-alloy interface, but at the same time new oxide forms at the gas-oxide interface.

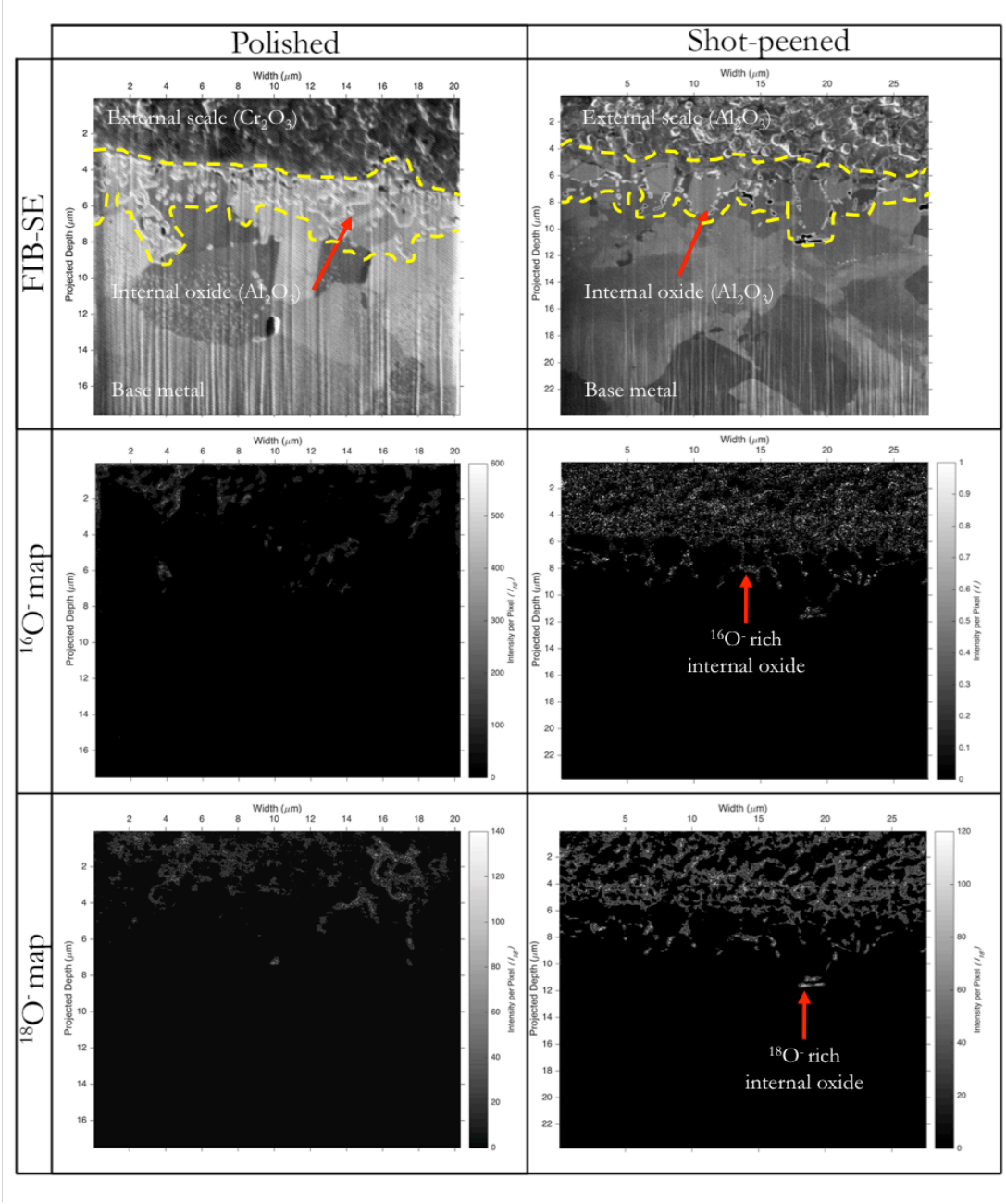


Figure 6.7: FIB-SEM oxide cross-sections of alloy 15Cr-10Al after oxidation at 850 °C for 200 hours in polished and shot peened conditions with their corresponding $^{16}O^-$ and $^{18}O^-$ maps.

The FIB-SIMS map is a useful tool to identify the diffusion paths. The maps reveal the dominant oxygen transport paths as well as regions of new internal oxidation. The observation in the shot-peened specimen showing $^{18}O^-$ enrichment along the grain boundaries of the recrystallised zone demonstrates the dominant oxygen transport paths. Many have reported the same observation,

which indicates the preferential oxygen diffusion along the grain boundaries as previously suggested for nickel-base alloys [65], [66], [115], [170]–[173].

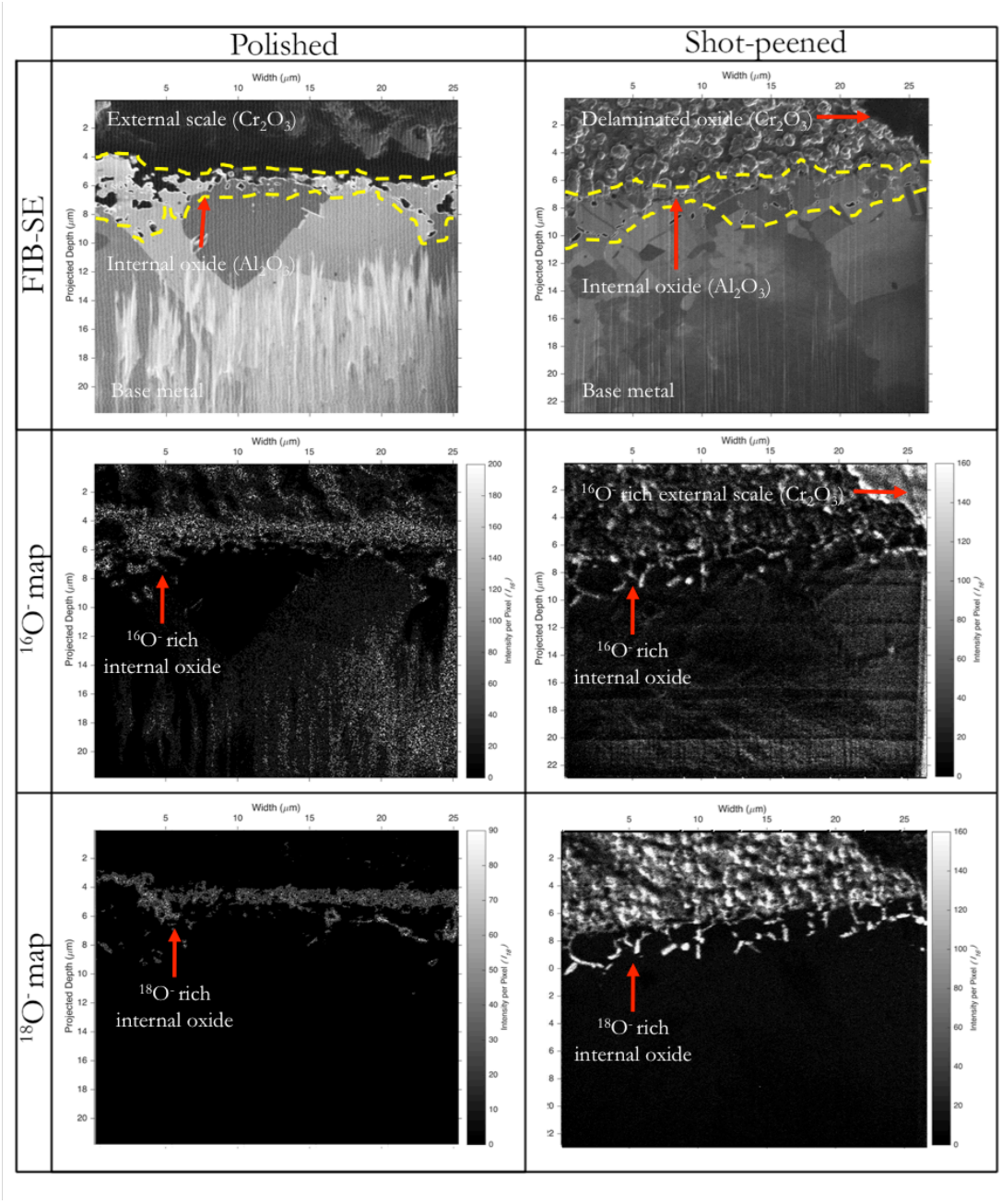


Figure 6.8: FIB-SEM oxide cross-sections of alloy 1.3Co-17Cr-10Al after oxidation at 850 °C for 200 hours in polished and shot peened conditions with their corresponding $^{16}O^-$ and $^{18}O^-$ maps.

The intensity of both $^{16}O^-$ and $^{18}O^-$ in alloy 1.3Co-17Cr-10Al in the as-polished condition are relatively high compared to the other two alloys as shown in Figure 6.8. These concentrations suggested that the external scale and the internal scale are protecting the alloy in the first stage of oxidation. The new oxide that formed in the last 24 hours of oxidation shows that there is a build-up

of oxygen at the front end of the internal oxide. It could be that the build-up of oxygen is at the front end of the internal oxide interface and reaction takes place with the aluminium flux from the bulk metal. The shot-peened specimen shows the absence of external scale due to spallation along with a piece of a delaminated scale as indicated (Cr_2O_3). Similar to the shot-peened specimen for alloy 15Cr-10Al, this alloy exhibits lower concentration of $^{16}O^-$ compared to $^{18}O^-$, which shows that the old oxide has spalled in the first stage of oxidation. The key finding in these SIMS maps is in the shot-peened condition where the $^{16}O^-$ intensity is found enriched at the delaminated oxide, and at the last 24 hours of this oxidation, the exposed surface is oxidising forming the new oxide via diffusion paths along the grain boundaries. Shot peening has induced stresses on the sample surface and hence opening up the oxygen diffusion paths at the oxide alloy interface.

A clear understanding of the spallation of the external scale can be seen in Figure 6.9, where the $^{16}O^-$ species are found enriched on the surface of the delaminated oxide and the $^{18}O^-$ is enriching the inner scale layer in the subsequent stage. It can be estimated that the spallation occurs towards the end of the oxidation period.

The spallation of oxide scale usually takes place during cooling when the stress develops in the scale as a result of thermal expansion differences between the scale and the metal surface. Generally, a compressive stress existed in the oxide scale during cooling down and this causes the scale to spall away through delaminating and cracking, which can be seen in this case.

A few commercial nickel-base superalloys yield spallation of oxide scale during cooling after oxidation at 1150 ºC and 1200 ºC [164], [174]–[176]. The oxidation of NiAl alloy at 1100 ºC exhibits spallation of surface oxide by the formation of voids and cavities beneath the alumina scale [66], [67], [177]. In most cases of spallation, the starting point is in between the oxide scale and the metal surface.

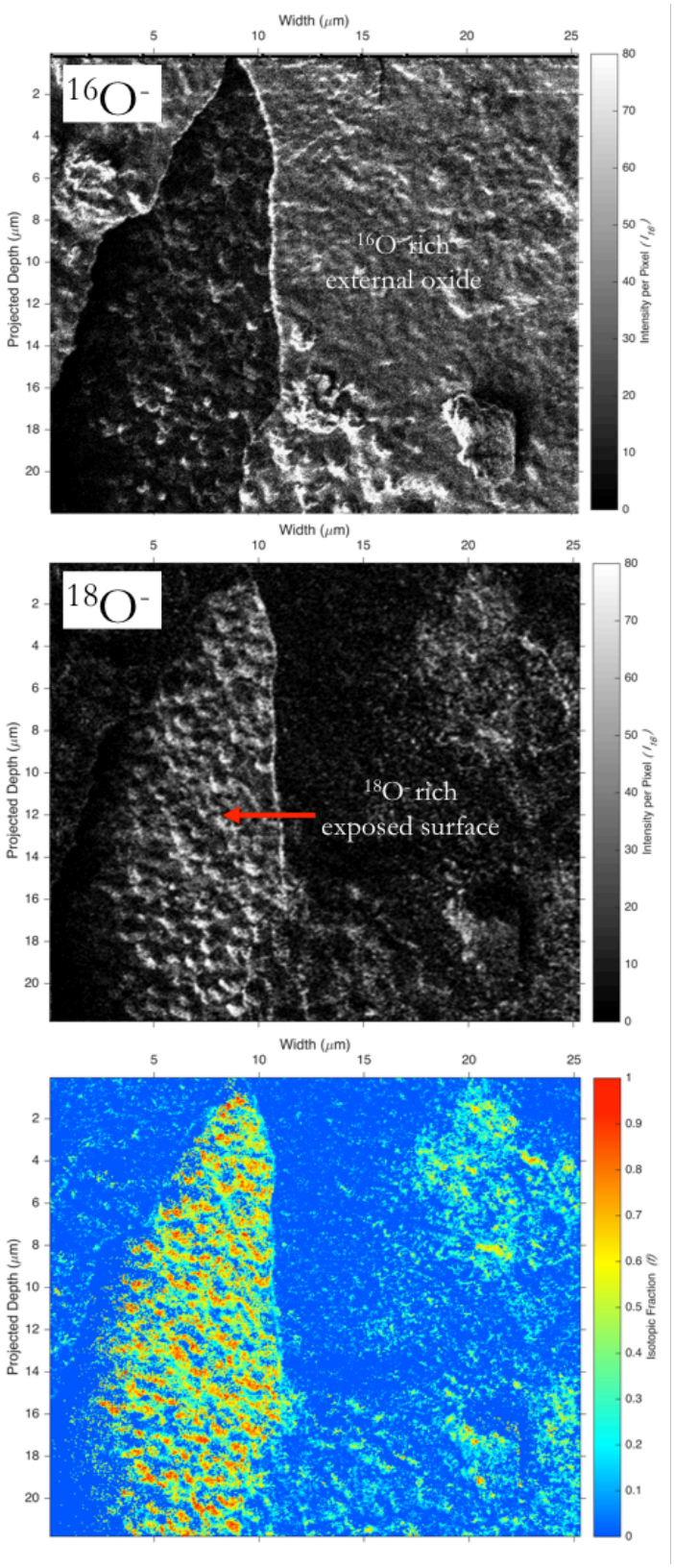


Figure 6.9: Comparison of the $^{16}O^-$ and $^{18}O^-$ enrichment on the surface topography of the spalled oxide of alloy 1.3Co-17Cr-10Al after oxidation at 850 ºC for 200 hours. The isotopic fraction map of $^{18}O^-$ at the bottom shows the new oxide formed.

6.3.2 Isotopic fraction map

A typical isotopic fraction map (f), as shown in Figure 6.10 consists of 512 sampling points across the x-axis and 442 sampling points across the y-axis. Each pair of $^{16}O^-$ and $^{18}O^-$ FIB-SIMS elemental maps (512 x 442 pixels) were used in the calculation of the isotopic fraction maps (f). Hence, the isotopic fraction map can be considered to have 512 vertical depth profiling lines across the map. The interface at the oxide-alloy region is quantified by aligning the 512 horizontal lines to construct 512 vertical depth-profiling lines. The peaks on the right-hand side correspond to the concentration of $^{18}O^-$ residing at the oxide/alloy interface. The use of Matlab software allows the manipulation of data in the SIMS maps.

The FIB-SIMS maps presented are useful to determine the mechanism of oxidation and finding the oxygen transport via tracer analysis. -. The isotopic fraction (f) was calculated as the fraction of the detected oxygen signals I due to $^{18}O^-$,

$$f = \frac{I_{^{18}O^-}}{I_{^{16}O^-} + I_{^{18}O^-}} \qquad \text{Equation 6.1}$$

Figure 6.10 – 6.12 are the isotopic fraction maps and the depth profiling graphs, following normalisation to the gas phase concentration and background concentration of $^{18}O_2$ (refer to Chapter 3), for the polished and shot-peened specimens oxidised for 200 hours at 850 °C. Note that these isotopic fraction maps and depth profiling graphs were constructed from the previous $^{16}O^-$ and $^{18}O^-$ maps in Figure 6.6 Figure 6.8.

The blue regions indicate low $^{18}O^-$ enrichment, whereas red regions imply high enrichment. The peaks along the x-axis in the depth profile indicate the thickness of the projected oxide. The thickness and regions of the external scales and internal oxides can be estimated by using the depth profile. In the case of alloy 17Cr-12Al, there have been significantly low fractions of $^{18}O^-$ in the external oxide (EO) as well as in the internal oxide (IO), which indicate that the alloy is producing a protective oxide layer that limits the diffusion of anions and cations at the oxide-alloy interface. The depth profile however, shows the counts of $^{18}O^-$ at the interface, proving that there are still diffusion activities on the surface and the oxide-alloy interface, but the intensity is very low (less than 30). Note that the depth profile peak does not fall to zero even when there is no intensity of $^{18}O^-$ can be found in the map, this can be regarded as 'noise', since no internal oxidation takes place beyond this point.

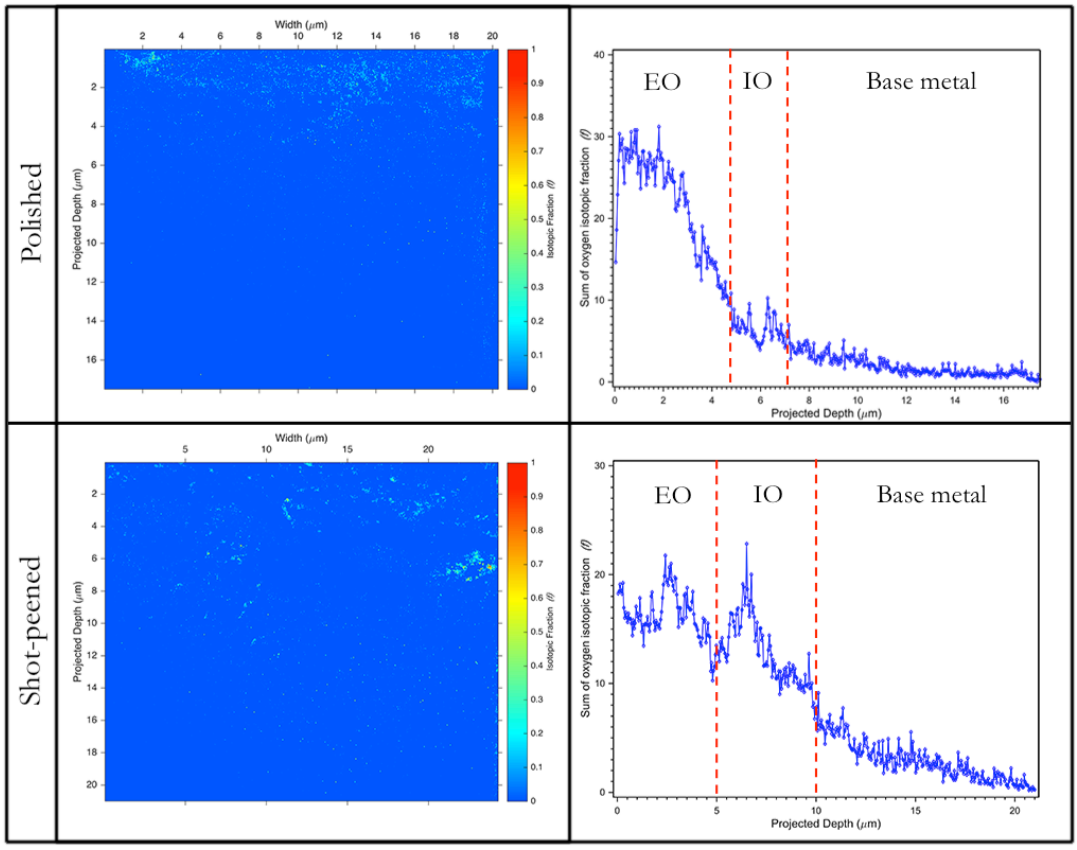


Figure 6.10: $^{18}O^-$ isotopic fraction (f) map of alloy 17Cr-12Al after oxidation at 850 ºC for 200 hours in polished and shot-peened condition with their corresponding depth profile graphs.

The enrichment of $^{18}O^-$ can clearly be seen in the isotopic fraction maps in Figure 6.11 in both polished and shot-peened conditions. There are two regions clearly displaying significant $^{18}O^-$ enrichment. The first of these is at the surface, where outward cationic transport gives further external oxidation at the gas-oxide interface. The second region is at the internal oxide where new grain boundary internal oxide growth via inward anionic transport of oxygen.

In the polished condition, the enrichment of $^{18}O^-$ did not give a clear internal oxidation region, the range of oxide intrusion is in between 6 – 8 μm. However, in the shot-peened specimen, due to the spallation of the external scale, the new oxide is forming on the surface and internally, the boundaries where the internal oxide starts can be seen in the figure.

The peak enrichment between 250 and 300 at the first 5 μm depth indicates the exposed surface oxide and the peak enrichment of 30 – 100 at the 6 -10 μm depth clearly shows the internal oxidation region. The enrichment declines rapidly from 300 to 100 after 2 μm. This decline region denotes the oxygen diffusion through the external oxide. A small region of 2 μm in length immediately

follows. Previous studies recognized these regions can short-circuit diffusion via dislocations or grain boundaries [116].

There are two regions clearly exhibiting significant $^{18}O^-$ enrichment. The first of these is at the surface where outward cationic transport gives further external oxidation at the gas-oxide interface. The second region is the new grain boundary internal oxide growth at the boundary of the oxide-alloy interface.

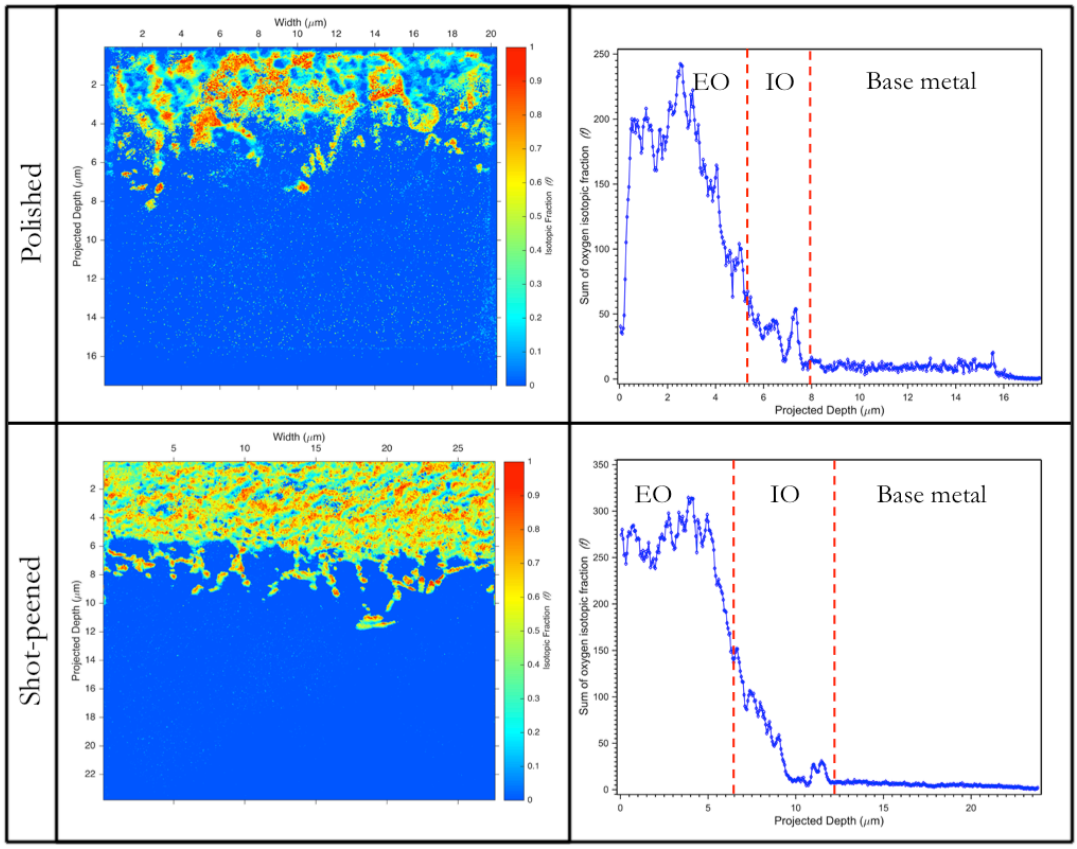


Figure 6.11: $^{18}O^-$ isotopic fraction (f) map of alloy 15Cr-10Al after oxidation at 850 ºC for 200 hours in polished and shot-peened condition with their corresponding depth profile graphs.

The isotopic fraction map obtained from the FIB-SIMS techniques not only revealed the graphical diffusion path of the $^{18}O^-$ through alumina grain-boundaries but also helped in quantifying the amount of $^{18}O^-$ that has actually diffused through grain-boundaries channels and accumulated at the oxide-alloy interface.

The peak enrichment in the as-polished specimen is high at the intermediate depth profile as shown in Figure 6.12. The enrichment of $^{18}O^-$ is at the highest point at 5 μm depth (100), where in this case, represent the internal oxide front. The enrichment declines rapidly to 40 (counts) at the internal

oxide region. This decline denotes the oxygen diffusion through the external scale into the bulk metal region.

The shot-peened condition in alloy 1.3Co-17Cr-10Al exhibits a similar pattern to the spalled behaviour in alloy 15Cr-10Al. Due to the spallation of the external scale, the new oxide is forming on the surface and internally, the boundaries where the internal oxide diffusion paths can be seen Figure 6.12. The intensity of $^{18}O^-$ is also in the same range, 200 – 300 at the external scale and 30 – 100 at the internal oxide region. One important observation to note is the complete absence of $^{18}O^-$ intensity in the isotopic fraction map of shot-peened specimen, where the absence is showing the region of the delaminated external scale, which was grown and spalled in the first stage of oxidation.

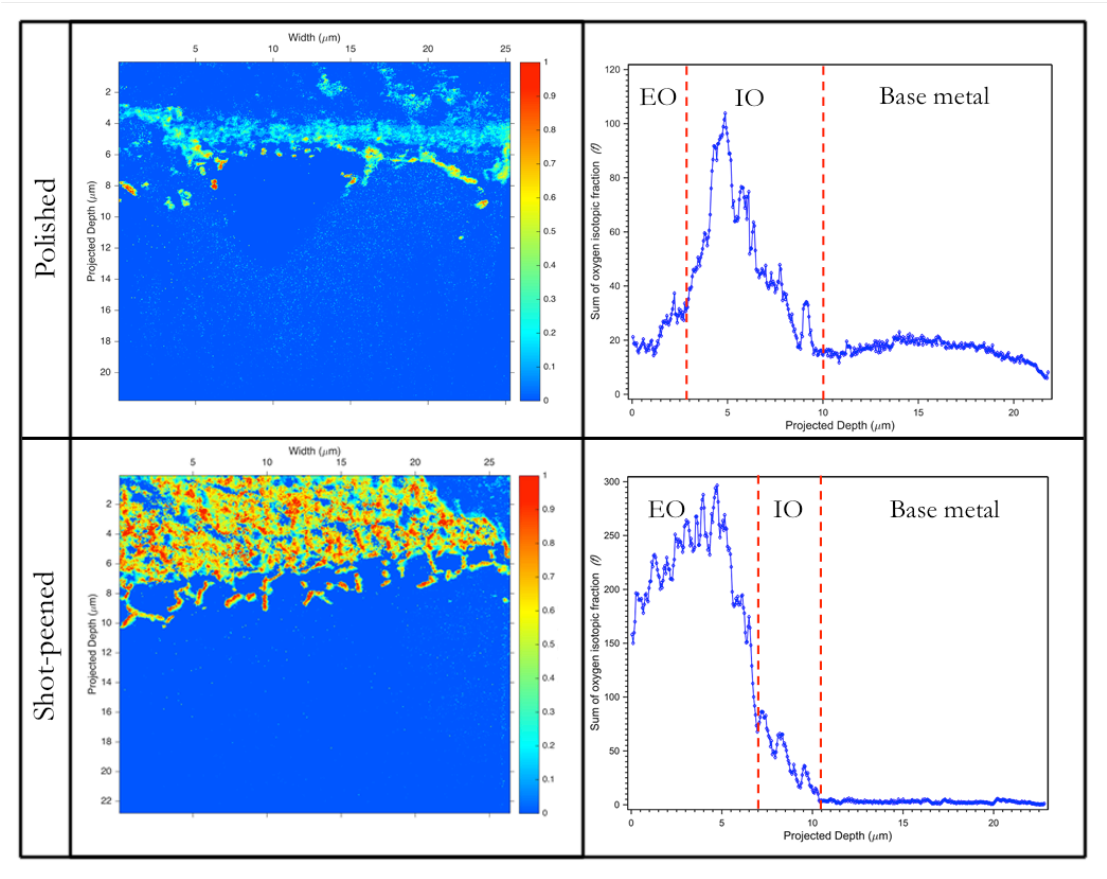


Figure 6.12: $^{18}O^-$ isotopic fraction (f) map of alloy 1.3Co-17Cr-10Al after oxidation at 850 °C for 200 hours in polished and shot-peened condition with their corresponding depth profile graphs.

6.4 Discussion

Based on the previous studies in nickel-base superalloys, the external oxide growth observed in both the polished and shot-peened specimen in the selected V208 alloys follows that observed for other superalloys tested at approximately the same temperatures [70], [72], [118], [124], [125], [178]. The overall oxide sequence, from the outermost scale to the internal oxide follows the thermodynamic rules, starting from $Cr_2O_3 \rightarrow Al_2O_3$.

The early assumption discussed earlier in this chapter explained that according to previous studies done in the oxidation of shot peened specimens, the cold work on the surface creates easy diffusion paths for chromium, which in turn allows rapid formation of a dense protective oxide layer at the oxide-alloy surface. Previous studies have concluded that during heating and in the initial hours, the dislocations introduced by shot peening can serve as fast diffusion paths, and later grain boundaries will be important for the supply of chromium and the formation of a protective oxide layer [165].

According to Foss et al., shot peening on RR1000 modifies the morphology of the oxide and accelerates the oxidation kinetics. The oxide grows through simultaneous inward diffusion of oxygen and outward diffusion of titanium and chromium. A similar study was done to examine the effect of chromia growth on shot-peened RR1000 and it was found that at 700 - 750 ºC, shot peening increases the chromia growth rate but at 800 °C, shot peening appears to improve oxidation resistance after a rapid formation of chromia layer on the surface. The effect of chromium and aluminium percentage in the V208 alloy series is crucial in examining the influence of surface stress on oxidation resistance.

Table 6.1 compares the current Co-Ni base superalloys to the previous nickel base superalloys. The comparisons are based on the thicknesses of oxide scales, oxide intrusion and γ'-depleted zone reported for alloy RR1000, ME3 and Udimet 720. Based on these results, the oxide scale in polished ME3, RR1000 and Udimet 720 are reported to be thicker, between 1.1 and 2.4 μm, compared to the Co-Ni base superalloys studied, between 0.8 to 1.1 μm. The same is true for oxide intrusion, where polished RR1000 and Udimet 720 are deeper, between 2.2 to 3.9 μm, compared to Co-Ni base superalloys studied, between 1.6 to 2.0 μm. Shot-peening did have a greater damage depth in both cobalt and nickel base superalloys. Previous studies in RR1000 proved that shot-peening in RR1000 produces a thicker oxide scale thickness, approximately 2.5 μm, whereas for Co-Ni base superalloys, the thickness as low as from 0.3 to 0.7 μm. The same trend occurs in the internal oxide region, where in RR1000, the oxide intrusion goes as deep as from 3.5 to 7.4 μm, compared to Co-Ni base superalloys, which extended just up to 2 μm.

Table 6.1: Cobalt and nickel base superalloys comparisons polished and shot-peened condition after oxidation between 800 and 850 °C for 200 hours.

Polished	17Cr-12Al (800 °C, 200 h)	15Cr-10Al (800 °C, 200 h)	1.3Co-17Cr-10Al (800 °C, 200 h)	ME3 (815 °C, 200 h) *Sudbrack et al. [118]	RR1000 (800 °C, 200 h) *Cruchley et al. [72]	Udimet 720 (800 °C, 200 h) *Gabb et al. [179]
Oxide scale	1.1	0.8	0.9	1.6	2.4	1.1
Oxide intrusion	1.6	2.0	1.8	3.2	-	3.3
γ'-depleted zone	2.6	4.4	4.0	5.0	-	-
Shot-peened	17Cr-12Al (800 °C, 200 h)	15Cr-10Al (800 °C, 200 h)	1.3Co-17Cr-10Al (800 °C, 200 h)	RR1000 (800 °C, 200 h) *Cruchley et al. [72]	RR1000 (800 °C, 200 h) *Foss et al. [70]	-
Oxide scale	0.4	0.7	0.3	2.4	2.5	-
Oxide intrusion	2.2	1.6	1.6	-	3.5	-
γ'-depleted zone	5.7	4.2	2.6	-	-	-

6.4.1 The effect of chromium and aluminium content

The comparison of damage depth thickness based on the chromium and aluminium content is plotted in Figure 6.13. According to the chart, shot peening has little effect on the oxide scale and oxide intrusion thickness but may have an effect on the γ'-depleted zone. This seems to be the case in alloy 17Cr-12Al where the γ'-depleted zone region is doubled compared to the polished condition, this is likely a consequence of recrystallization.

Due to the spallation of the surface oxide in alloy 15Cr-10Al and alloy 1.3Co-17Cr-10Al, the oxide scale thicknesses are incomparable. One important aspect to note in these cases is that the alumina intrusion is less in the case of shot-peening compared to the polished condition. This could be an indication that before spallation happens, these two alloys exhibit superior oxidation resistance by forming a protective external scale chromia. Since shot-peening increases the tendency of recrystallization at the γ'-depleted zone, a network of diffusion paths regions created by shot peening near the surface is supplying chromium to the surface, which is causing a dense and compact

protective oxide layer to be formed. It is only after the spallation occurs which delaminates the external scale that an inward diffusion of oxygen started at the sub-surface region.

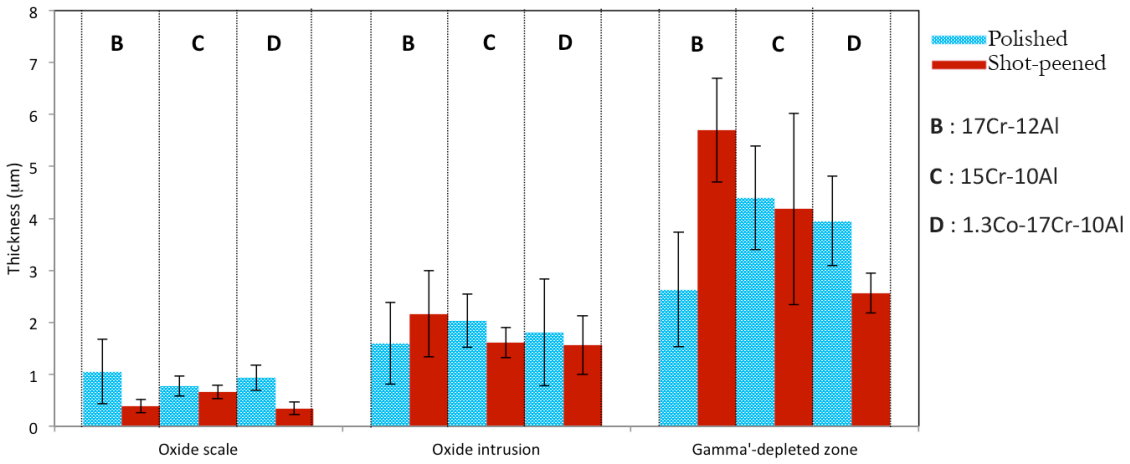


Figure 6.13: The damage depth thickness of the selected V208 alloy series in the polished and shot-peened condition after oxidation at 850 ºC for 200 hours.

When aluminium is reduced from 12 to 10 at. %, the effect of shot peening leads to spallation of the surface oxide. This could be the case where there is scarcity in the supply of aluminium to the surface to form alumina, which protects the surface oxide from spallation.

The following quantification in terms of damage depth areas in Figure 6.14 is plotted to further investigate the extent of external scale and internal oxide before and after shot-peening. The drop in both external and internal oxide in shot-peening specimen of alloy 15Cr-10Al and 1.3Co-17Cr-10Al indicated the spallation that occurs on the external scale. As previously mentioned, the comparison is insignificant due to the loss of external scale when spallation occurs. Shot-peening does not alter the thickness of chromia (external scale) in alloy 17Cr-12Al. No growth of chromia is reported in this study.

However, it can be gathered that shot-peening modifies the morphology of the oxide scale susceptibility to cracking and spalling and γ'-depleted zone and in turn accelerates the oxidation kinetics.

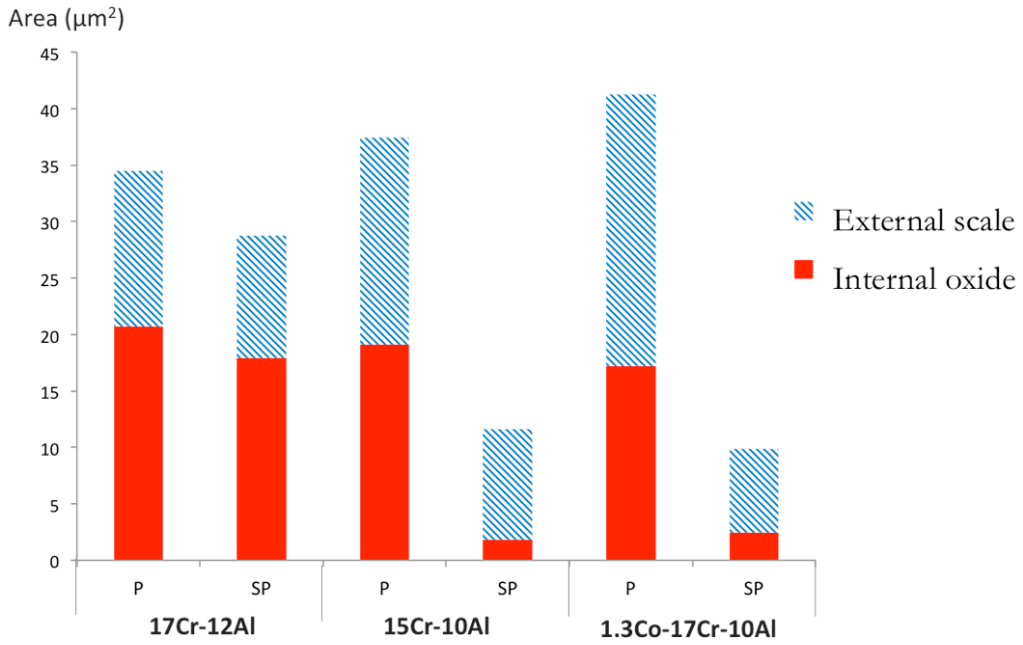


Figure 6.14: The quantification of damage depth areas highlighting the external scale and internal oxide areas in the polished and shot-peened specimens.

6.5 Conclusion

This chapter investigated the oxidation behaviour of polished and shot-peened selected V208 alloys under isotopic oxidation conditions at 850 ºC for 200 hours. Characterisation mostly used FIB microscopy and FIB-SIMS elemental mapping, with supplementary SEM analysis providing further evidence. The following conclusions are applicable to this study.

- Spallation occurs in the shot-peened specimens of alloy 15Cr-10Al and alloy 1.3Co-17Cr-10Al.
- New oxide is forming on the exposed surface after spallation occurs.
- Compositions of the oxides are both similar in the as-polished and shot-peened condition where the external scale is Cr_2O_3 and internal oxide is Al_2O_3
- Shot-peening enhances recrystallisation at the sub-surface region and causes a larger γ'-depleted zone in all alloys.
- Shot-peening does not increase the formation of oxide (protective oxide areas smaller than polished)
- Shot-peening does not affect oxidation resistance directly but it does promote the spalling of the surface oxide, leaving a less protective scale.
- Shot-peening influences the $^{18}O^-$ inward diffusion in alloy 15Cr-10Al and 1.3Cr-17Cr-10Al.

7 Conclusions and Further Work

The main objective of this study was to investigate the oxidation of cobalt-nickel base superalloys as well as studying the basic phase metallurgy of this newly developed alloy. The preliminary study of this alloy started with optimising the ratio of cobalt and nickel as key base elements. In order to achieve excellent corrosion resistance, the levels of aluminium and chromium are also optimised to match the properties possessed by the current polycrystalline nickel base superalloys utilised for disc material. Therefore, an initial screening of the alloys started by characterising the typical microstructure of the base metal in the as-received condition, after solution heat treatment and aging.

The alloying elements played an important role in producing a stable underlying microstructure. With the aid of SEM equipped with EsB detector, various secondary phases that precipitated in the bulk can be distinguished by their contrasts. It has been observed in the early stages of screening that an excessive level of chromium (17 at. %) does influence the stability of the underlying microstructure. Alloys with high amounts of chromium co-exist with a three-phase precipitate structure during solidification, that is the γ'-Co_3(Al, W), β-CoAl and DO_{19}-Co_3W. Without an excessive amount of chromium (less than 15 at. %), the alloy shows a two-phase precipitate structure, that is γ'-Co_3(Al, W) and DO_{19}-Co_3W. These secondary phases can be easily distinguished by the dark and bright contrasts, which corresponds to β-CoAl and DO_{19}-Co_3W, respectively. The substitution of nickel as part of the base alloy instead of high cobalt shows no significant effect on the stability of the underlying microstructure. The addition of titanium and niobium also has no significant effect on the underlying microstructure.

In the case of carbides precipitates, the V208 alloy series contain two types of carbides; the $M_{23}C_6$ carbides in discreet and film form and the blocky MC carbides. One interesting finding in this cobalt base superalloy, which is not often found in nickel base superalloys is the presence of metallic elements that constitute the MC carbides. It seems that 0.04 at. % of zirconium is enough to make it the main metallic constituent (M) in MC carbides along with tantalum. The modification of the HIP cycle has proven to alter the morphology of the carbides particles. Since the carbide particles transformation is happening in the HIP cycle, the precipitation of carbides can be controlled by changing the HIP temperatures from 1050 ºC to 950 ºC (to precipitate the $M_{23}C_6$) in the first stage

and later to 1050 ºC in the second stage. It has been proven in previous studies of nickel base superalloys that the two-stage HIP has effectively changed the types of carbides that formed in the alloys.

The addition of alloying elements such as chromium, titanium, and niobium in the Co-Ni base superalloy started to play an important role when the alloys are exposed at elevated temperatures (between 800 to 850 ºC) for a prolonged time (from 200 hours to 2000 hours). Firstly, the Co-Ni base superalloy in this study oxidises by forming a protective oxide layer, predominantly Cr_2O_3 and Al_2O_3. These oxides are so thin (mainly sub-µm thickness) that they make the alloy superior in oxidation resistance to nickel base superalloys. A 12 at. % of chromium content is too low to form a stable oxide on the surface, instead, a mixed spinel consisting of nickel-aluminium-chromium is formed, which is not protective. Whereas, a 15 at. % of chromium is enough to protect the substrate by forming protective oxide layers. Niobium has a good influence on high temperature oxidation whilst titanium is bad for oxidation. 1.5 at. % addition of titanium is adequate to double the oxide thickness of the base alloy.

Good oxidation resistance is not just achieved by forming suitable oxides at high temperatures but also depends on prolonged exposure times and some surface oxides can eventually lead to spallation. The mechanism of oxide formation has been established in this particular study and concludes that with prolonged exposure time (from 200 hours to 2000 hours), the surface oxide changes into spikey-facetted morphology and eventually spalls in less than 1000 hours. Whereas, in the sub-surface region, recrystallization started to occur at 300 hours, allowing faster diffusion of cations outward and anions inward. Eventually, a greater level of internal oxidation will occur by the formation of a plate-like alumina deep in the bulk metal. Nevertheless, the damage depth is still within an acceptable level, comparable to that of nickel base superalloys.

The results for oxidation damage depth analysis have been compiled and compared with those for nickel base superalloys used in similar disk applications. The comparison with RR1000, ME3 and Udimet 720 in polished and shot-peened condition at 800 ºC to 850 ºC for 200 hours shows that Co-Ni base superalloys are superior to any of these nickel base alloys.

Overall, the results of this work suggests that V208C is a suitable base composition for further investigation and comprises a 1:1 cobalt-nickel ratio, 15 at. % chromium, 10 at. % aluminium, 3 at. % tungsten and 1 at. % tantalum. This alloy was found to outperform the current nickel base superalloys in terms oxidation resistance at operating temperatures between 700 to 800 ºC. It is therefore suggested that the alloy is suitable for further investigation to obtain a more comprehensive understanding of the alloys mechanical properties, in particular creep and dwell fatigue crack growth properties to determine its suitability for turbine disc applications.

Further optimisation of the compositions is advised to further improve phase stability by removing the unwanted DO_{19}-Co_3W phase. This can be achieved through a proper heat-treatment procedure as well as finding the balance between tungsten and tantalum in the alloy. For example, the addition of tantalum as an alternative to tungsten will remove this DO_{19}-Co_3W phase. It is proven in this study that tantalum will form Ta-Zr carbides and at the same time, partitions to the γ' phase in cobalt base superalloys. In addition, mechanical properties could be improved by optimising the percentage of grain boundary strengtheners, such as carbon, boron and zirconium.

In terms of shot-peening, V208C was not necessarily the best performing alloy with spallation observed at a temperature of 850 ºC following 200 hours exposure. However, the results of V208B, which showed the best performance following shot-peening, showed increasing the aluminium content to 12 at. % to be beneficial in withstanding the higher temperature with compressive stresses on the surface and could be readily applied to V208C.

Lastly, for future alloy processing, it is recommended that a two-stage HIP process be applied in the next generation alloy studies for turbine disc applications as it showed a refinement in carbide composition and distribution. However, the phase structure of the population of carbides should be confirmed with a selected area diffraction patterns or with a more focused high-resolution TEM study.

This study has shown the great potential for finding an alternative material for nickel base superalloys. The results are promising and in the case of oxidation resistance, it can be concluded that the alloys studied in this thesis possesses superior oxidation properties compared to nickel base superalloys. These alloys are capable of working at high temperatures, between 700 and 800 ºC and not deteriorate significantly over time in a corrosive environment.

7.1 Suggestion for Further Work

Even when the mechanisms of oxide formation in this V208 alloy series have been established, there are a few grey areas that need to be better understood. For example:

The reasons for the formation of detrimental secondary phases such as Co_3W and CoAl, which arise in the bulk metal during solidification, should be studied thoroughly. It is very likely that these phases originate from the PPB and carbides during the HIP stage. Even though the two-stage HIP has successfully produced finer carbides along the grain boundaries, there is still the need to evaluate the types of carbides after the two-stage HIP via diffraction pattern analysis to determine their crystallographic structure. The evaluation would be important in order to eliminate the detrimental phases in the bulk metal during heat treatment.

Boron is a popular grain boundary strengthener and it has also been found to be beneficial in resistance to oxidation. However, its role in the present alloys is still uncertain and no previous studies have explained how it works in protecting the alloy from oxidation. An in depth study of the effect of boron on both oxidation resistance and grain boundary strengthening should be carried out.

Previous studies by Klein et al. also suggested that tungsten aids the formation of alumina on the surface by increasing the diffusivity of aluminium towards the surface. Therefore, it is presumed that the TCP phase, Co_3W, supports this mechanism. It is worth looking at the areas where this phase is present and then studying the formation and thickness of alumina on top of this phase.

Even though the spallation behaviour in this alloy has been observed and documented, there is still uncertainty as to why spallation occurs earlier for some alloys than for others. It is believed that aluminium and chromium levels play an important role in the development of stresses that occur in the surface oxide.

References

[1] G. Crook and M. Horlor, editors. *The Jet Engine*, 5th edition. London, Rolls-Royce plc, 2005.

[2] R. C. Reed, *The Superalloys: Fundamentals and Applications*. Cambridge University Press, 2006.

[3] C. T. Sims, N. S. Stoloff, and W. C. Hagel, editors. *Superalloys II*. John Wiley & Sons, Inc., 1987.

[4] N. Cumpsty, *Jet Propulsion*. University of Cambridge, UK, 1997.

[5] J. Sato, T. Omori, K. Oikawa, I. Ohnuma, R. Kainuma, and K. Ishida. Cobalt-Base High-Temperature Alloys. *Science*, 312:90–91, 2006.

[6] NASA Glenn Research Centre. (2017, Jan 12). Ideal Brayton Cycle [Online]. Available: https://www.grc.nasa.gov/www/k-12/airplane/brayton.html

[7] H. Bhadeshia. (2017, Jan 13). The Rolls-Royce Trent Engine [Online]. Available: https://www.msm.cam.ac.uk/phase-trans/mphil/Trent1/index.htm

[8] J. C. Williams and E. A. Starke, Progress in structural materials for aerospace systems, Acta Materilia, 51:5775–5799, 2003.

[9] Rolls-Royce plc. (2017, Jan 13). Rolls-Royce Civil Aerospace [Online]. Available: http://www.rolls-royce.com/products-and-services/civil-aerospace/products/future-products/ultrafan.aspx

[10] M. Dareki, C. Edelstenne, and T. Enders. (2017, Jan 14). Flightpath 2050: Europe's Vision for Aviation (2011) [Online]. Available: http://ec.europa.eu/transport/sites/transport/files/modes/air/doc/flightpath2050.pdf

[11] C. Lambert. (2017, Jan 14). SBAC Aviation and Environment Briefing Papers 8: Advanced Materials (2012) [Online]. Available: http://www.sustainableaviation.co.uk/wp-content/uploads/2015/09/SBAC-Aviation-and-Environment-Briefing-Paper-%E2%80%93-ACARE-Explained.pdf

[12] S. C. Armand. Structural optimisation methodology for rotating disks for aircraft engines, NASA technical memorandum, Cleveland, Ohio. 4693, Nov., 1995.

[13] T. Gabb, J. Telesman, A. Garg, and J. Gayda. The effects of heat treatment and microstructure variations on disk superalloy properties at high temperature, in *Superalloys 2008*, pages 121-130, Warrendale, PA, 2008. The Minerals, Metals and Materials Society (TMS).

[14] SkyBrary. (2017, Jan 13). Uncontained Engine Failure [Online]. Available: http://www.skybrary.aero/index.php/Uncontained_Engine_Failure.

[15] European Aviation Safety Agency. (2017, Jan 12). Design specification for large airplanes (Amendment 12: CS-25.903) [Online]. Available: https://www.easa.europa.eu/system/files/dfu/CS-25%20Amdt%2012.pdf

[16] National Transport Safety Board. (2017, Jan 14). Update on Uncontained Engine Failure Accident Involving a Wide Body Jetliner (2016) [Online]. Available: https://www.ntsb.gov/news/press-releases/Pages/pr20161104.aspx

[17] S. Carey and A. Pasztor. (2017, Jan 14). Unusual Failure in American Airlines: Jet Engine Prompts Investigation, The Wall Street Journal (2016) [Online]. Available: https://www.wsj.com/articles/disc-in-engine-turbine-failed-on-american-airlines-jetliner-1477864909

[18] C. T. Sims and W. C. Hagel, editors. *The Superalloys*. New York: John Wiley & Sons, Inc., 1972.

[19] B. Geddes. *Superalloys: Alloying and Performance*. A S M International, Materials Park, OH, 2010.

[20] M. J. Donachie. *Superalloys: A Technical Guide*, ASM International, Materials Park, OH, 2002.

[21] D. L. Klarstrom. Wrought cobalt- base superalloys. *Journal of Materials Engineering Performance*, 2:523–530, 1993.

[22] M. J. Donachie. *Superalloys Source Book*. ASM International, Materials Park, OH, 1984.

[23] J. R. Davis. *ASM Specialty Handbook: Nickel, Cobalt, and Their Alloys*. ASM International, Materials Park, OH, 2000.

[24] H. Yan. Co-Al-W based alloys for turbine disc applications. PhD dissertation, Department of Materials, Imperial College London, London, 2014.

[25] L. Z. He. Effect of carbides on the creep properties of a Ni-base superalloy M963. *Materials Science and Engineering: A*, 397:297–304, 2005.

[26] H. Kitaguchi. (2012). Microstructure-property relationship in advanced Ni-based superalloys [Online]. Available: http://www.intechopen.com/books/metallurgy-advances-in-materials-and-processes/microstructure-property-relationship-in-advanced-ni-based-superalloys.

[27] R. C. Reed. (2017, Jan. 18). Powder Metallurgy and Superalloys, Materials Technology [Online]. Available: http://iweb.tms.org/SUP/SUP-0701-5.pdf.

[28] G. H. Gessinger. *Powder metallurgy of superalloys*. Stoneham: Michigan, Butterworth Publishers, 1984.

[29] C. Briant. *Impurities in Engineering Materials*. New York, USA: Marcel Dekker Inc., 1999.

[30] G. Raisson. Evolution of PM nickel base superalloy processes and products. *Powder Metallurgy*, 51:10–13, 2008.

[31] H. Atkinson and S. Davies. Fundamental aspects of hot isostatic pressing: An overview. *Metallurgical and Materials Transaction: A*, 31:2981–3000, 2000.

[32] C. Qiu. Net-shape hot isostatic pressing of a nickel-based powder superalloy. PhD dissertation, College of Engineering and Physical Sciences, University of Birmingham, UK, 2010.

[33] Y. Ning, Z. Yao, M. W. Fu, and H. Guo. Recrystallization of the hot isostatic pressed nickel-base superalloy FGH4096. *Materials Science and Engineering: A*, 528:8065–8070, 2011.

[34] C. Aubin, J. H. Davidson, and J.P.Trottier. The Influence of Powder Particle Surface Composition on the Properties of a Nickel- based Superalloy Produced by Hot Isostatic Pressing. in *Superalloys 1980*, Metals Park, Ohio: ASM International, 345–356, 1980.

[35] F. V. Lenel. International Powder Metallurgy Conference and Exhibition. *JOM*, 36:48, 1984.

[36] D. R. Chang, D. D. Krueger, and R. A. Sprague. Superalloy Powder Processing, Properties, and Turbine Disk Applications. in *Superalloys 1984*, Metals Park, Ohio: ASM International, 245–273, 1984.

[37] Q. Bai, J. Lin and G. Tian. Review and Analysis of Powder Prior Boundary (PPB) Formation in Powder Metallurgy Processes for Nickel-based Super Alloys. *Journal of Powder Metallurgy and Mining*, 4:127, 2015.

[38] J. S. Crompton and R. W. Hertzberg. Analysis of second phase particles in a powder metallurgy HIP nickel-base superalloy. *Journal of Materials Science*, 21:3445–3454, 1986.

[39] C. L. Qiu, M. M. Attallah, X. H. Wu, and P. Andrews. Influence of hot isostatic pressing temperature on microstructure and tensile properties of a nickel-based superalloy powder. *Materials Science and Engineering: A*, 564:176–185, 2013.

[40] L. Zhang, H. Liu, X. He, and G. Zhang. Thermal evolution behavior of carbides and γ' precipitates in FGH96 superalloy powder. *Materials Characterisation*, 67:52–64, 2012.

[41] M. Dahlen, N. G. Ingesten, and H. Fishchmeister. Parameters influencing particle boundary precipitation in superalloy powders. *Modern Development in Powder Metallurgy*, 14:3–14, 1981.

[42] W. Ma, G. Liu, B. Hu, Y. Zhang, and J. Liu. Effect of Hf on carbides of FGH4096 superalloy produced by hot isostatic pressing. *Materials Science and Engineering: A*, 587:313–319, 2013.

[43] M. Norell, L. Nyborg, and M. Friesel. Segregants at Prior Particle Boundaries in Powder Metallurgical Martensitic Stainless Steel. *Powder Metallurgy*, 41:31–39, 1998.

[44] M. M. Allen, R. L. Atheby, and J. B. Moore. Application of Powder Metallurgy to Superalloy Forgings. Pratt & Whitney Aircraft Report GP68-234, 27 November 1968.

[45] R. Thamburaj, W. Wallace, Y. N. Chari, and T. L. Prakash. Influence of Processing Variables on Prior Particle Boundary Precipitation and Mechanical Behaviour in PM Superalloy APK1. *Powder Metallurgy*, 27:169–180, 1984.

[46] S. Hu, B. Li and H. Zhang. Stabilization of non-equilibrium carbides in powder superalloy Rene 95. *Acta Metallurgica Sinica*, 27:131–135, 1991.

[47] J. C. Scully. The fundamentals of corrosion. *Materials Corrosion*, 42:54, 1991.

[48] D. Young. High Temperature Oxidation and Corrosion of Metals. Cambridge,:UK, Elsevier, 2008.

[49] A.S. Khanna. Introduction to High Temperature Oxidation and Corrosion. Materials Corrosion, 54:346–347, 2003.

[50] T. Ellingham. Transactions and Communications. Journal Society of Chemical Industries, 63:125, 1944.

[51] V. S. Sastri, E. Ghali, and M. Elboujdaini. *Corrosion Prevention and Protection: Practical Solutions.* Ontario:Canada, Wiley, 2012.

[52] D. Jones. Principles and prevention of corrosion. *Materials and Design*, 14:207, 1993.

[53] C. S. Giggins and F. S. Pettit. Oxidation of Ni-Cr-Al Alloys Between 1000 °C and 1200 °C. Journal Electrochemical Society, 118:1782–1790, 1971.

[54] C. Wagner, "Passivity and inhibition during the oxidation of metals at elevated temperatures," *Corros. Sci.*, vol. 5, no. 11, pp. 751–764, 1965.

[55] H. E. Evans. Stress effects in high temperature oxidation of metals. *Journal of International Material Review*, 40:1–40, 1995.

[56] H. E. Evans. Modelling oxide spallation. *Materials High Temperature*, 12:219–227, 1994.

[57] A. T. Donaldson and H. E. Evans. Oxidation-induced creep in Zircaloy-2. III. The average stress in the oxide layer. *Journal of Nuclear Materials*, 99:57–65, 1981.

[58] H. E. Evans. Cracking and spalling of protective oxide layers. *Materials Science and Engineering: A*, 121:139–146, 1989.

[59] H. E. Evans. Spallation of oxide from stainless steel AGR nuclear fuel cladding: mechanisms and consequences. *Materials Science and Technology*, 4:414–420, 1988.

[60] R. Prescott and M. J. Graham. The formation of aluminum oxide scales on high-temperature alloys. *Oxidation of Metals*, 38:233–254, 1992.

[61] J. K. Doychak. The evolution and growth of alumina scales on beta-NiAl. PhD dissertation, Dept. of Metallurgy and Materials Science, Case Western University, Ohio, 1986.

[62] B. H. Kear, F. S. Pettit, D. E. Fornwall, and L. P. Lemaire. On the transient oxidation of a Ni-15Cr-6Al Alloy. *Oxidation of Metals*, 3:557–569, 1971.

[63] D. P. Garriga-Majo, B. A. Shollock, D. S. McPhail, R. J. Chater, and J. F. Walker. Novel strategies for evaluating the degradation of protective coatings on superalloys. *International Journal of Inorganic Materials*, 1:325–336, 1999.

[64] J. Jedlinski, "Comments on the use of the two-stage-oxidation method and surface-analytical techniques in studying growth processes of oxide scales," *Oxidation of Metals*, 39:61–68, 1993.

[65] B. Foss. Oxidation and oxygen transport in a commercial polycrystalline Ni-based superalloy under static and loading conditions. PhD dissertation, Department of Materials, Imperial College London, London, 2014.

[66] T. N. Ooi. High temperature oxidation of platinum alimunide coated CMSX-4. PhD dissertation, Department of Materials, Imperial College London, London, 2007.

[67] J. Jung. Investigation of the effect of lanthanum on the oxidation of CMSX-4. PhD dissertation, Department of Materials, Imperial College London, London, 2014.

[68] K. Reddy, J. L. Smialek, and A. R. Cooper. 18-O Tracer studies of Al_2O_3 scale formation on Ni-Cr-Al alloys. *Oxidation of Metals*, 17: 429–449, 1982.

[69] S. Chevalier, G. Strehl, J. Favergeon, and F. Desserrey. Use of oxygen isotope to study the transport mechanism during high temperature oxide scale growth. *Material High Temperature*, 20, 2003.

[70] B. J. Foss, M. C. Hardy, D. J. Child, D. S. McPhail, and B. A. Shollock. Oxidation of a Commercial Nickel-Based Superalloy under Static Loading. *JOM*, 66:2516–2524, 2014.

[71] A. Benninghoven. Surface analysis by Secondary Ion Mass Spectrometry (SIMS). *Surface Science*, 300:246–260, 1994.

[72] S. Cruchley, M. P. Taylor, R. Ding, M. C. Hardy, D. J. Child, and H. E. Evans. Comparison of Chromia Growth Kinetics in a Ni-based Superalloy, with and without Shot-peening. *Corrosion Science*, vol. 100, pp. 242–252, 2015.

[73] M. Kobayashi, T. Matsui, and Y. Murakami. Mechanism of creation of compressive residual stress by shot peening. *International Journal of Fatigue*, 20:351–357, 1998.

[74] A. Karabela, L. G. Zhao, J. Tong, N. J. Simms, J. R. Nicholls, and M. C. Hardy. Effects of cyclic stress and temperature on oxidation damage of a nickel-based superalloy. *Materials Science and Engineering: A*, vol. 528, no. 19–20, pp. 6194–6202, 2011.

[75] J. L. Evans.Effect of Surface Roughness on the Oxidation Behavior of the Ni-Base Superalloy ME3. J. Mater. Eng. Perform., vol. 19, no. 7, pp. 1001–1004, 2010.

[76] L. Tan, X. Ren, K. Sridharan, and T. R. Allen. Effect of shot-peening on the oxidation of alloy 800H exposed to supercritical water and cyclic oxidation. *Corrosion Science*, vol. 50, no. 7, pp. 2040–2046, 2008.

[77] D. J. Child, G. D. West, and R. C. Thomson. Assessment of surface hardening effects from shot peening on a Ni-based alloy using electron backscatter diffraction techniques. *Acta Materilia*, 12:4825–4834, 2011.

[78] S. Cruchley, M. P. Taylor, H. E. Evans, P. Bowen, M. C. Hardy, and S. Stekovic. Microstructural Characterisation of High Temperature Oxidation of Nickel Base Superalloy RR1000 and the Effect of Shot-Peening. in *Superalloys 2012*, Seven Springs: PA, John Wiley & Sons, Inc., pp. 751–758, 2012.

[79] S. Cruchley, M. P. Taylor, H. E. Evans, M. C. Hardy, and D. J. Child. Characterisation of subsurface oxidation damage in Ni based superalloy, RR1000. *Materials Science and Technology*, 30:1884–1889, 2014.

[80] S. Cruchley, H. E. Evans, M. P. Taylor, M. C. Hardy, and S. Stekovic. Chromia layer growth on a Ni-based superalloy: Sub-parabolic kinetics and the role of titanium. *Corrosion Science*, 75:58–66, 2013.

[81] W. Betteridge and S. W. K. Shaw. Development of superalloys. *Materials Science and Technology*, 3:682–694, 1987.

[82] W. Betteridge, *Cobalt and its Alloys*. Chichester:UK, Ellis Horwood Limited, 1982.

[83] T. Omori, Y. Sutou, K. Oikawa, R. Kainuma, and K. Ishida. Shape memory and magnetic properties of Co-Al ferromagnetic shape memory alloys. *Materials Science and Engineering: A*, 440:1045–1049, 2006.

[84] J. Grin, U. Burkhardt, M. Ellner, and K. Peters. Crystal structure of orthorhombic Co_4Al_{13}. *Journal of Alloys and Compounds,* 206:243–247, 1994.

[85] P. Zięba, G. Cliff, and G. W. Lorimer. Discontinuous precipitation in cobalt-tungsten alloys. *Acta Materialia*, 45:2093–2099, 1997.

[86] J. Dutkiewicz and G. Kostorz. Structure of martensite in Co_3W alloys. *Materials Science and Engineering: A*. 132: 267–272, 1991.

[87] P. Viatour, J. M. Drapier, and D. Coutsouradis. Stability of the gamma prime- Co_3Ti compound in simple and complex cobalt alloys. *Cobalt*, 3: 67, 1973.

[88] P. Viatour, J. M. Drapier, D. Coutsouradis, and L. Habraken. Structure and properties of CM-7, A wrought precipitation- hardening cobalt-base alloy. *Cobalt*, 51:67, 1971.

[89] R. D. Dragsdorf and W. D. Foreing. The intermetallic phases in the cobalt–tantalum system. *Acta Crystallogrraphica*, 15: 531–536, 1962.

[90] K. Shinagawa, T. Omori, J. Sato, and K. Ishida. Phase Equilibria and Microstructure on γ' phase in Co-Ni-Al-W System. *Materials Transactions,*vol. 49, no. 6, pp. 1474–1479, 2008.

[91] S. Miura, K. Ohkubo, and T. Mohri. Mechanical Properties of Co-Based L12 Intermetallic Compound Co3(Al,W). *Materials Transactions,* 48: 2403–2408, 2007.

[92] S. Kobayashi, Y. Tsukamoto, T. Omori, and K. Ishida. Determination of phase equilibria in the Co-rich Co–Al–W ternary system with a diffusion-couple technique. *Intermetallics*, 17:1085–1089, 2009.

[93] T. Oohashi, N. L. Okamoto, K. Kishida, K. Tanaka, and H. Inui. Microstructures and Mechanical Properties of $Co_3(Al,W)$ with the $L1_2$ Structure. *MRS Proceedings*, vol. 1128, 2008.

[94] L. Klein, Y. Shen, M. Killian, and S. Virtanen. Effect of B and Cr on the high temperature oxidation behaviour of novel γ/γ' strengthened Co-base superalloys. *Corrosion Science*, 53:2713–2720, Sep. 2011.

[95] H. Y. Yan, V. A. Vorontsov, and D. Dye. Effect of alloying on the oxidation behaviour of Co-Al-W superalloys. *Corrosion Science*, vol. 83, pp. 382–395, 2014.

[96] H.-Y. Yan, V. A. Vorontsov, J. Coakley, N. G. Jones, H. J. Stone, and D. Dye. Quaternary Alloying Effects and the Prospects for a New Generation of Co-Base Superalloys. in *Superalloys 2012*, Seven Springs: PA, John Wiley & Sons, Inc., pp. 704-715, 2012.

[97] T. Omori, J. Sato, I. Ohnuma, R. Kainuma, and K. Ishida. Partition behavior of alloying elements and phase transformation temperatures in Co–Al–W-base quaternary systems. *Intermetallics*, vol. 32, pp. 274–283, 2013.

[98] L. Klein, A. Bauer, S. Neumeier, M. Göken, and S. Virtanen. High temperature oxidation of γ/γ' -strengthened Co-base superalloys. *Corrosion Science*, vol. 53, no. 5, pp. 2027–2034, 2011.

[99] L. Klein, M. S. Killian, and S. Virtanen. The effect of nickel and silicon addition on some oxidation properties of novel Co-based high temperature alloys. *Corrosion Science*, vol. 69, no. 0, pp. 43–49, 2013.

[100] A. Mottura, A. Janotti, and T. M. Pollock. Alloying Effects in the γ' Phase of Co-Based Superalloys. in *Superalloys 2012*, Seven Springs: PA, John Wiley & Sons, Inc., pp. 683-693, 2012.

[101] A. Suzuki, J. Zhu, M. Tsukane, J. Dibbern, and T. M. Pollock. New Co-based γ/γ' high-temperature alloys. *JOM*, vol. 62, no. 1, pp. 58–63, 2010.

[102] N. Vermaak, A. Mottura, and T. M. Pollock. Cyclic oxidation of high temperature coatings on new γ'-strengthened cobalt-based alloys. *Corrosion Science*, vol. 75, pp. 300–308, 2013.

[103] F. Xue, M. Wang, and Q. Feng. Alloying Effects on Heat-Treated Microstructure in Co-Al-W-Base Superalloys at 1300 °C and 900 °C. in *Superalloys 2012*, Seven Springs: PA, John Wiley & Sons, Inc., pp. 813-821, 2012.

[104] Y. D. Chen and R. N. Noufi. Electrodeposition of Nickel and Cobalt Oxides onto Platinum and Graphite Electrodes for Alkaline Water Electrolysis. *Journal of Electrochemical Society*, vol. 131, no. 4, pp. 731–735, 1984.

[105] H.-Y. Yan, V. A. Vorontsov, and D. Dye. Alloying effects in polycrystalline γ/γ'-strengthened Co-Al-W base alloys. *Intermetallics*, vol. 48, pp. 44–53, 2014.

[106] H. T. Pang and P. A. C. Reed. Fatigue crack initiation and short crack growth in nickel-base turbine disc alloys - the effects of microstrcuture and operating parameters. *International Journal of Fatigue*, vol. 25, pp. 1089–1099, 2003.

[107] S. Meher, H.-Y. Yan, S. Nag, D. Dye, and R. Banerjee. Solute partitioning and site preference in γ/γ' cobalt-base alloys. Scripta Materilia, vol. 67, no. 10, pp. 850–853, Nov. 2012.

[108] A. Suzuki, K. Blance, C. Schaeffer, and A. J. E. Pazhayannur Subramaniam. Alumina-Forming Cobalt-Nickel base alloy and method of making an article thereform. Patent US9034247. June 9, 2011.

[109] A. Bauer, S. Neumeier, F. Pyczak, and M. Goken. Microstructure and creep strength of different γ/γ'-strengthened Co-base superalloy variants. *Scripta Materilia*, vol. 63, no. 12, pp. 1197–1200, 2010.

[110] M. Ooshima, K. Tanaka, N. L. Okamoto, K. Kishida, and H. Inui. Effects of quaternary alloying elements on the γ' solvus temperature of Co–Al–W based alloys with fcc/$L1_2$ two-phase microstructures. *Journal of Alloys and Compounds,* vol. 508, no. 1, pp. 71–78, 2010.

[111] A.-C. Yeh, I.-T. Ho, S.-C. Wang, and C.-F. Cheng. Effects of Si Addition on the High Temperature Strength and Oxidation Behavior of y'-Bearing Co-Based Superalloys. in *Superalloys 2012*, Seven Springs: PA, John Wiley & Sons, Inc., pp. 149-157, 2016.

[112] A. Bauer, S. Neumeier, F. Pyczak, and M. Goken. Creep Strength and Microstructure of Polycrystalline Gamma Prime - Strengthened Cobalt-Base Superalloys. in *Superalloys 2012*, Seven Springs: PA, John Wiley & Sons, Inc., pp. 695-703, 2012.

[113] A. Suzuki, A. J. Elliott, M. F. X. Gigliotti, K. B. Morey, J. C. Schaeffer, and P. Subramanian. Alumina-forming cobalt-nickel base alloy and method of making an article therefrom. Patent US9034247. June 9, 2011.

[114] S. N. Basu and J. W. Halloran. Tracer Isotope Distribution In Growing Oxide Scales. *Oxidation of Metals*, vol. 27, no. 3–4, pp. 143–155, 1987.

[115] T. N. Ooi, D. S. McPhail, R. J. Chater, and B. A. Shollock. Isotope exchange studies of oxidation mechanisms in nickel-base superalloys using FIB-SIMS techniques. *Surface and Coatings Technology*, vol. 201, no. 7, pp. 3885–3888, 2006.

[116] A. A. Alibhai, R. J. Chater, D. S. McPhail, and B. A. Shollock. Use of isotopic tracers and SIMS analysis for evaluating the oxidation behaviour of protective coatings on nickel based superalloys. *Applied Surface Science*, vol. 203–204, pp. 630–633, 2003.

[117] S. Cruchley, H. Y. Li, H. E. Evans, P. Bowen, D. J. Child, and M. C. Hardy. The role of oxidation damage in fatigue crack initiation of an advanced Ni-based superalloy. *International Journal of Fatigue*, vol. 81, pp. 265–274, 2015.

[118] C. Sudbrack, S. Draper, T. Gorman, J. Telesman, T. Gabb, and D. Hull. Oxidation and the Effects of High Temperature Exposures on Notched Fatigue Life of an Advanced Powder Metallurgy Disk Superalloy. in *Superalloys 2012*, Seven Springs: PA, John Wiley & Sons, Inc., pp. 863-872, 2012.

[119] L. Reimer and C. Tollkamp. Measuring the backscattering coefficient and secondary electron yield inside a scanning electron microscope. *The Journal of Scanning Microscopy*, vol. 3, no. 1, pp. 35–39, 1980.

[120] L. A. Giannuzzi and F. A. Stevie, *Introduction to focused ion beams: Instrumentation, theory, techniques and practice*. Orlando:Florida, Springer, 2005.

[121] J. F. Ziegler, M. D. Ziegler, and J. P. Biersack. SRIM - The stopping and range of ions in matter (2010). *Nuclear Instruments and Methods in Physics Research Section B: Beam Interactions with Materials and Atoms*, vol. 268, no. 11–12, pp. 1818–1823, 2010.

[122] R. Levi-Setti, P. H. La Marche, K. Lam, T. H. Shields, and Y.-L. Wang. Secondary ion imaging in the scanning ion microscope. Nuclear Instruments and Methods in Physics Research Section B, vol. 218, no. 1, pp. 368–374, 1983.

[123] M. Knop. Development of Co-Ni Superalloys. PhD dissertation, Department of Materials, Imperial College London, 2015.

[124] M. P. Taylor and H.E. Evans and S. Stekovic and M.C. Hardy. The oxidation characteristics of the nickel-based superalloy, RR1000, at temperatures of 700–900°C. *Materials at High Temperature*, vol. 29, no. 2, pp. 145–150, 2012.

[125] J. H. Chen, P. M. Rogers, and J. A. Little. Oxidation behavior of several chromia-forming commercial nickel-base superalloys. *Oxidation of Metals*, vol. 47, pp. 381–410, 1997.

[126] A.Suzuki and T. M. Pollock. High-temperature strength and deformation of γ/γ' two-phase Co-Al-W-base alloys. *Acta Materialia*, vol. 56, no. 6, pp. 1288–1297, 2008.

[127] P. Mulvey. Alloying Effects and the Development of Co-Ni Superalloys. PhD dissertation, Department of Materials, Imperial College London, 2017.

[128] S. Kobayashi, Y. Tsukamoto, and T. Takasugi. Phase equilibria in the Co-rich Co-Al-W-Ti quaternary system. *Intermetallics*, vol. 19, no. 12, pp. 1908–1912, 2011.

[129] H.-Y. Yan, J. Coakley, V. a. Vorontsov, N. G. Jones, H. J. Stone, and D. Dye. Alloying and the micromechanics of Co–Al–W–X quaternary alloys. *Materials Science and Engineering: A*, vol. 613, pp. 201–208, Sep. 2014.

[130] M. S. Titus, A. Suzuki, and T. M. Pollock. High Temperature Creep of New $L1_2$ Containing Cobalt-Base Superalloys. in *Superalloys 2012*, Seven Springs: PA, John Wiley & Sons, Inc., pp. 823-832, 2012.

[131] K. Ishida. Intermetallic Compounds in Co-base Alloys-Phase Stability and Application to Superalloys. *MRS Proceeding*, vol. 1128, pp. 1106–1128, 2008.

[132] R. Kainuma, M. Ise, C.-C. Jia, H. Ohtani, and K. Ishida. Phase equilibria and microstructural control in the Ni-Co-Al system. *Intermetallics*, vol. 4, pp. S151–S158, 1996.

[133] W. H. Tian, M. Hibino, and M. Nemoto. Crystal structure and morphology of Co precipitates in B2-ordered (Ni,Co)Al. *Intermetallics*, vol. 6, no. 2, pp. 121–129, 1998.

[134] R. D. Kissinger, S. V Nair, and J. K. Tien. Hot Isostatic Consolidation of P/M Superalloys. *MRS Proc.*, vol. 28, 1983.

[135] E. Arzt, M. F. Ashby, and K. E. Easterling. Practical applications of Hot Isostatic Pressing diagrams: Four case studies. *Metallurgical and Materials Transaction: A*, vol. 14, no. 1, pp. 211–221, 1983.

[136] J. R. May, M. C. Hardy, M. R. Bache, and D. D. Kaylor. Microstructure and Mechanical Properties of an Advanced Nickel-Based Superalloy in the as-HIP Form. *Advance Materials Research*, vol. 278, pp. 265–270, 2011.

[137] G. A. Rao and M. Kumar. High performance stainless steel via powder metallurgy hot isostatic pressing. *Materials Science and Technology*, vol. 13, no. December, pp. 1027–1032, 1997.

[138] G. A. Rao, K. S. Prasad, M. Kumar, M. Srinivas, and D. S. Sarma. Characterisation of hot isostatically pressed nickel base superalloy Inconel 718. *Materials Science and Technology*, vol. 19, no. 3, pp. 313–321, 2003.

[139] A. K. Koul and R. Castillo. Assessment of service induced microstructural damage and its rejuvenation in turbine blades. Metall. Trans. A, vol. 19, no. 8, pp. 2049–2066, 1988.

[140] T. J. Garosshen, T. D. Tillman, and G. P. Mccarthy. Effects of B , C , and Zr on the Structure and Properties of a P/M Nickel Base Superalloy. *Metallurgical and Materials Transaction: A*, vol. 18, no. January, pp. 69–77, 1987.

[141] L. Z. He, Q. Zheng, X. F. Sun, G. C. Hou, H. R. Guan, and Z. Q. Hu. $M_{23}C_6$ precipitation behavior in a Ni-base superalloy M963. *Journal of Materials Science*, vol. 40, no. 11, pp. 2959–2964, 2005.

[142] D. Wang, J. Zhang, and L. H. Lou. Formation and stability of nano-scaled $M_{23}C_6$ carbide in a directionally solidified Ni-base superalloy. *Materials Characterisations*, vol. 60, no. 12, pp. 1517–1521, 2009.

[143] L. Chang, W. Sun, Y. Cui, and R. Yang. Influences of hot-isostatic-pressing temperature on microstructure, tensile properties and tensile fracture mode of Inconel 718 powder compact. *Materials Science and Engineering: A*, vol. 599, pp. 186–195, 2014.

[144] L. Jiang, R. Hu, H. Kou, J. Li, G. Bai, and H. Fu. The effect of $M_{23}C_6$ carbides on the formation of grain boundary serrations in a wrought Ni-based superalloy. *Materials Science and Engineering: A*, vol. 536, pp. 37–44, 2012.

[145] G. Bai, J. Li, R. Hu, T. Zhang, H. Kou, and H. Fu. Effect of thermal exposure on the stability of carbides in Ni–Cr–W based superalloy. *Materials Science and Engineering: A*, vol. 528, no. 6, pp. 2339–2344, 2011.

[146] W. H. Jiang, X. D. Yao, H. R. Guan, Z. Q. Hu, and W. H. Jiang. Secondary carbide precipitation in a directionally solified cobalt-base superalloy. *Metalurgical and Materials Transaction: A*, vol. 30, no. 3, pp. 513–520, 1999.

[147] Y. Murata, K. Suga, and N. Yukawa. Effect of transition elements on the properties of MC carbides in IN-100 nickel-based superalloy. *Journal of Materials Science*, vol. 21, no. 10, pp. 3653–3660, 1986.

[148] H.-E. Huang and C.-H. Koo. Effect of Zirconium on Microstructure and Mechanical Properties of Cast Fine-Grain CM 247 LC Superalloy. *Materials Transactions,* vol. 45, no. 2, pp. 554–561, 2004.

[149] W. H. Jiang, X. D. Yao, H. R. Guan, and Z. Q. Hu. Secondary M_6C Precipitation in a Cobalt–base Superalloy. *Journal of Materials Science*, vol. 18, no. 4, pp. 303–305, 1999.

[150] G. A. J. Hack, J. W. Eggar, and C. H. Symonds, *Powder Metallurgy Superalloys*, 2nd ed. Shrewsbury, England: Metal Powder Report Publishing Services Ltd., 1980.

[151] L. Klein and S. Virtanen. Electrochemical characterisation of novel γ/γ'-strengthened Co-base superalloys. *Electrochimica Acta*, vol. 76, pp. 275–281, 2012.

[152] J. Sato, T. Omori, K. Oikawa, I. Ohnuma, R. Kainuma, and K. Ishida, "Cobalt-Base High-Temperature Alloys," *Science (80-.).*, vol. 312, no. 5770, pp. 90–91, 2006.

[153] M. P. Brady, I. G. Wright, and B. Gleeson. Alloy design strategies for promoting protective oxide-scale formation. *JOM*, vol. 52, no. 1, pp. 16–21, 2000.

[154] Y. T. Xu, T. D. Xia, J. Q. Yan, and W. J. Zhao. Effect of alloying elements on oxidation behavior of Co-Al-W alloys at high temperature. *Chinese Journal of Non-Ferrous Metals*, vol. 20, no. 11, pp. 2168–2177, 2010.

[155] L. Klein and S. Virtanen. Corrosion properties of novel γ'-strengthened Co-base superalloys. *Corrosion Science*, vol. 66, pp. 233–241, 2013.

[156] A. Bauer, S. Neumeier, F. Pyczak, R. F. Singer, and M. Goken. Creep properties of different ' -strengthened Co-base superalloys. *Materials Science and Engineering: A*, vol. 550, pp. 333–341, 2012.

[157] M. Ooshima, K. Tanaka, N. Okamoto, K. Kishida, and H. Inui. Effects of quaternary alloying elements on the γ' solvus temperature of Co-Al-W based alloys with fcc/$L1_2$ two-phase microstructures. *Journal of Alloys and Compounds*, vol. 508, no. 1, pp. 71–78, 2010.

[158] S. Kobayashi, Y. Tsukamoto, and T. Takasugi. The effects of alloying elements (Ta, Hf) on the thermodynamic stability of γ'-Co_3(Al,W) phase. *Intermetallics*, vol. 31, pp. 94–98, 2012.

[159] Y. Z. Liu, X. B. Hu, S. J. Zheng, Y. L. Zhu, H. Wei, and X. L. Ma. Microstructural evolution of the interface between NiCrAlY coating and superalloy during isothermal oxidation. *Materials and Design*, vol. 80, pp. 63–69, 2015.

[160] K. Yuan, R. L. Peng, X.-H. Li, S. Johansson, and Y.-D. Wang. Simulation of oxidation-nitridation-induced microstructural degradation in a cracked Ni-based superalloy at high temperature. *MATEC Web Conference*, vol. 14, p. 16004, 2014.

[161] P. J. Brown and J. B. Forsyth, The crystal structure of solids: Structures and Properties of Solids, New York: Edward Arnold, 1973.

[162] R. Newnham and Y. Haan. Refinement of the α Al_2O_3, Ti_2O_3, V_2O_3 and Cr_2O_3 structures. *New Crystal Structure* (Zeitschrift fur Kristallographie), 117:235-237, 1962.

[163] L. Lutterotti and P. Scardi. Simultaneous structure and size-strain refinement by the Rietveld method. *Journal of Applied Crystallography*, 23:246-252, 1990.

[164] H. J. Grabke, E. M. Muller-Lorenz, S. Strauss, E. Pippel, and J. Woltersdorf. Effects of Grain Size, Cold Working, and Surface Finish on the Metal-Dusting Resistance of Steels. *Oxidation of Metals*, vol. 50, no. 3, pp. 241–254, 1998.

[165] R. Naraparaju, V. B. Trindade, H.-J. Christ, and U. Krupp. Effect of shot peening on high temperature oxidation behaviour of boiler steel: experimental results and simulation. *Corrosion Engineering Science Technology*, vol. 44, no. 3, pp. 211–217, 2009.

[166] X. Ren, K. Sridharan, and T. R. Allen. Effect of grain refinement on corrosion of ferritic-martensitic steels in supercritical water environment. *Materials and Corrosion*, vol. 61, no. 9, pp. 748–755, Sep. 2010.

[167] B. Hutchinson and N. Ridley. On dislocation accumulation and work hardening in Hadfield steel. *Scripta Materilia*, vol. 55, no. 4, pp. 299–302, 2006.

[168] E. Hornbogen. Systematics of the cellular precipitation reactions. *Metallurgical and MaterialsTransaction: A*, vol. 3, no. 11, pp. 2717–2727, 1972.

[169] J. D. Nystrom, T. M. Pollock, W. H. Murphy, and A. Garg. Discontinuous cellular precipitation in a high-refractory nickel-base superalloy. *Metalurgical and Materials Transaction: A*, vol. 28, no. 12, pp. 2443–2452, Dec. 1997.

[170] D. P. Whittle, Y. Shida, G. C. Wood, F. H. Stott, and B. D. Bastow. Enhanced diffusion of oxygen during internal oxidation of nickel-base alloys. *Philosophical Magazine: A*, vol. 46, no. 6, pp. 931–949, 1982.

[171] Y. Shida, F. H. Stott, B. D. Bastow, D. P. Whittle, and G. C. Wood. Development of preferential intergranular oxides in nickel-aluminum alloys at high temperatures. *Oxidation of Metals*, vol. 18, no. 3–4, pp. 93–113, 1982.

[172] F. H. Stott, Y. Shida, D. P. Whittle, G. C. Wood, and B. D. Bastow. The morphological and structural development of internal oxides in nickel-aluminum alloys at high temperatures. *Oxidation of Metals*, vol. 18, no. 3–4, pp. 127–146, 1982.

[173] C. H. Konrad, L. Fuhrmann, R. Völkl, and U. Glatzel. Internal oxidation with significant contribution of oxygen diffusion through the oxide phase. *Corrosion Science*, vol. 63, pp. 187–192, 2012.

[174] T. M. Pollock and S. Tin. Nickel-Based Superalloys for Advanced Turbine Engines: Chemistry, Microstructure and Properties. J. Propuls. *Power*, vol. 22, no. 2, pp. 361–374, 2006.

[175] K. Kawagishi, H. Harada, A. Sato, A. Sato, and T. Kobayashi. The oxidation properties of fourth generation single-crystal nickel-based superalloys. *JOM*, vol. 58, no. 1, pp. 43–46, 2006.

[176] M. Göbel, A. Rahmel, and M. Schütze. The cyclic-oxidation behavior of several nickel-base single-crystal superalloys without and with coatings. *Oxidation of Metals*, vol. 41, no. 3–4, pp. 271–300, 1994.

[177] H. J. Grabke. Oxidation of NiAl and FeAl. *Intermetallics*, vol. 7, no. 10, pp. 1153–1158, 1999.

[178] A. Encinas-Oropesa, G. L. Drew, M. C. Hardy, J. Leggett, J. R. Nicholls, and N. J. Simms. Effects of oxidation and hot corrosion in a nickel disc alloy. in *Superalloys 2008*, Seven Springs: PA, John Wiley & Sons, Inc., pp. 609–618, 2008.

[179] T. P. Gabb, J. Telesman, P. T. Kantzos, J. W. Smith, and P. F. Browning. Effects of High Temperature Exposures on Fatigue Life of Disk Superalloys. in *Superalloys 2004*, Seven Springs: PA, John Wiley & Sons, Inc., pp. 3-6, 2004.